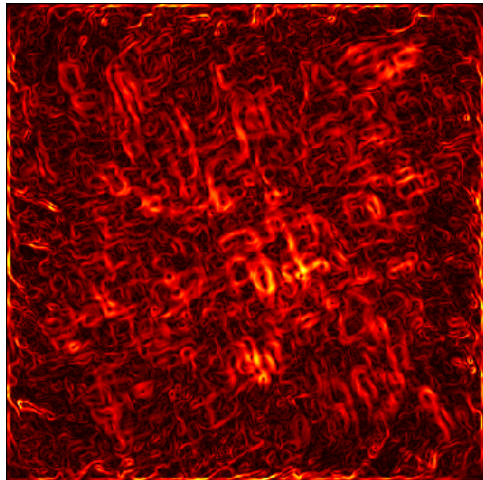


THEORY AND SIMULATION OF LOW PRESSURE PLASMA TRANSPORT PHENOMENA

Application to the PEGASES thruster

Romain Lucken¹

A thesis presented for the degree of
Doctor of Philosophy



Laboratoire de Physique des plasmas
UMR CNRS 7648, École polytechnique, Sorbonne Université,
Université Paris-Sud, Observatoire de Paris
Route de Saclay 91128
Palaiseau France

June 18, 2019

¹Email: roman.lucken@lpp.polytechnique.fr

Abstract

The field of low temperature plasma physics has emerged from the first fundamental discoveries in atom and plasma physics more than a century ago. However, it has soon become very much driven by applications. One of the most important of them in the first half of the XXth century is the "Calutron" (California University Cyclotron") invented by E. Lawrence in Berkeley, that was part of the Manhattan project, and operated as a mass spectrometer to separate uranium isotopes. In a 1949 report of the Manhattan project, D. Bohm makes two observations that are fundamental for low-temperature plasma physics.

- The ions must have a minimum kinetic energy when they enter the plasma sheath estimated to T_e [eV]/2 ;
- Plasma transport across a magnetic field is enhanced by instabilities.

His concern was already to gain understanding of transport phenomena to optimize system efficiency with respect to parameters such as pressure, magnetic field strength, discharge power and geometry. The field has also considerably benefited from the development of the microelectronics industry since the 1990s. Plasma electric propulsion is used on military satellites and space probes since the 1960s and has gained more and more interest for the last 20 years as space commercial applications were developing. However, the same questions as the ones D. Bohm was faced with, namely multi-dimensional transport, plasma sheath interaction, and instabilities, arise. Theory and simulation are even more important for electric space propulsion design since testing in real conditions involves to launch a satellite into space.

In this work, we derive the multi-dimensional equations of the isothermal plasma transport, we establish a sheath criterion that causes the magnetic confinement to saturate in low-temperature, weakly ionized plasmas, and we model the electron cooling through the magnetic filter of the Plasma Propulsion with Electronegative Gases (PEGASES) thruster. All the theories are driven and validated with extensive Two-dimensional (2D) Particle-In-Cell (PIC) simulations, using the *LPPic* code

that was partially developed in the frame of this project. Finally, the simulation cases are extended to an iodine Inductively-Coupled Plasma (ICP) discharge with a new set of reaction cross sections.

Acknowledgments

ANR chaire CINES GENCI CERFACS Anne Bourdon Pascal Chabert Trevor Lafleur
Vivien Croes Antoine Tavant Florian Marmuse Victor Desangles Thomas Charoy
Ane Aanesland Mike Lieberman Allan Lichtenberg Benjamin Estèves Guillaume
Bogopolsky David Tordeux Thierry Magin Roberto Martorelli Alejandro Laguna
Constance Duchesne Jean-Luc Raimbault Ozgur Gurcan Catherine Jegu Christiane
Chevalier Dominique Fontaine Matthieu Berthomier Nicolas Sissourat Dan Goebel
Yannis Laplace

Dana and Leroy

Damien Giolito Vincent Marsat Victor Gabella

Alice et Edouard, Mike et Isabelle Lucken Jean-Pierre et Michèle Joseph-Marie
et Yana Tanguy Lagree Paul Champion Thomas Franzini Marion Lemoine Pierre-
Antoine Poncet

Claudia Verheyen

Contents

Abstract	iii
Acknowledgments	v
Symbols and abbreviations	xi
List of Acronyms	xi
Nomenclature	xiii
0.0.1 Real and imaginary parts	16
Introduction	17
Plasma physics for space propulsion	17
Low temperature plasma	21
Particle-in-Cell simulation	23
The PEGASES thruster	25
Outline of the thesis	28
1 Weakly ionized plasma	29
1.1 Particle approach: theory and simulation	30
1.2 Kinetic theory and collisions	33
1.2.1 Boltzmann equation	33
1.2.2 Electron-neutral reactions	35
1.2.3 Ion-neutral reactions	36
1.2.4 Momentum transfer collision frequency	42
1.3 Introduction to ICP theory and simulation	45
1.3.1 Heating mechanism	45
1.3.2 Fluid equations of the plasma transport	47
1.3.3 Numerical parameters of the PIC simulation	50
1.3.4 First run example	52
1.4 Observation of the main features of a plasma discharge	56
1.5 Sheath theory	60

1.6	Global models of a plasma discharge	64
2	Isothermal transport models	69
2.1	Motivation	70
2.2	One-dimensional (1D) transport solutions	71
2.2.1	Differential equation for the plasma velocity	71
2.2.2	The problem of ion-neutral momentum transfer collision frequency	72
2.2.3	Boundary conditions and mathematical solution	74
2.2.4	The high D_a limit (low pressure <i>and</i> low magnetic field) .	79
2.2.5	The low D_a limit (high pressure <i>or</i> high magnetic field) .	79
2.3	2D transport modeling in the non-magnetized case	81
2.3.1	Equations of ion transport	81
2.3.2	The temperature equation	83
2.3.3	h factor in 2D	85
2.3.4	Comparison with 2D PIC simulation	88
2.3.5	Discussion	101
3	Cross field transport	107
3.1	2D PIC simulation of a magnetized plasma column	108
3.1.1	Context	108
3.1.2	Simulation parameters	109
3.1.3	Description of the steady state	109
3.1.4	Magnetic drifts	112
3.1.5	Magnetized sheath	114
3.1.6	Parametric studies with the magnetic field and the pressure	116
3.2	The collisional resistive drift instability	122
3.2.1	Model introduction	122
3.2.2	Dispersion relation in a homogeneous plasma	123
3.2.3	Dispersion relation in an inhomogeneous plasma	127
3.2.4	Solutions of the dispersion relations	132
3.2.5	Comparison with the PIC simulations	133
3.3	Transport theory at high magnetic field	145
3.3.1	2D isothermal model	145
3.3.2	Saturation of the magnetic confinement	151
3.3.3	Instability-enhanced transport	159
3.3.4	Discussion on the marginal stability	162

4 Magnetic filter	167
4.1 Why studying magnetic filters?	168
4.1.1 Applications	168
4.1.2 Literature review on magnetic filter studies	168
4.1.3 The PEGASES experiment	168
4.2 2D PIC simulations of a magnetic filter with argon	169
4.2.1 Simulation parameters	169
4.2.2 Simulation results	169
4.3 Reduced geometry	173
4.4 PIC model validation	175
4.4.1 Comparison with experiments	175
4.4.2 Comparison with previous fluid simulations	175
4.5 Identifying the main drivers of a magnetic filter	177
4.6 Influence of the localized heating	177
4.6.1 Influence of the power	177
4.6.2 Influence of dielectric boundaries	177
4.6.3 Influence of the gas pressure	184
4.6.4 Effect of the magnetic field	184
4.7 1D fluid model of a magnetic filter	184
4.7.1 Model assumptions	184
4.7.2 Model equations	184
4.7.3 Numerical scheme	188
4.7.4 First results with no heat flux	189
4.7.5 The role of the heat flux	189
4.7.6 Comparison with PIC simulations	189
4.8 The effect of instability-enhanced plasma transport in the 1D modeling of PEGASES	189
4.9 "Anomalous" heat transport	189
5 Simulation of iodine discharges	191
5.1 Iodine for electric space propulsion	192
5.2 Iodine cross section set	193
5.2.1 Plasma species	193
5.2.2 Electron-neutral reactions	194
5.2.3 Ion-neutral reactions	195
5.2.4 Ion loss mechanisms	196
5.3 2D PIC simulation of an iodine discharge	203
5.3.1 Electronegative gas balance	203
5.3.2 Relaxation oscillations in an iodine plasma	206
5.4 A low power discharge model for iodine	212

5.5	Global model comparison	212
5.6	Simulation of negative ion production through a magnetic filter . .	212
Conclusion		213
Summary	213
A	Refined cross section sets for noble gases	215
B	Simulations at higher magnetic field	221
C	Mathematical functions	223
D	Fortran gas type defintion	225
Bibliography		227

Symbols and abbreviations

List of Acronyms

0D Zero-dimensional

1D One-dimensional

2D Two-dimensional

3D Three-dimensional

AC Alternative Current

amu Atomic Mass unit

BATMAN Bavarian Test Machine for Negative Ions

CCP Capacitively-Coupled Plasma

CMF Center of Mass Frame

CFL Courant – Friedrichs – Lewy

CPU Central Processing Unit

DC Direct Current

EEDF Electron Energy Distribution Function

EEPF Electron Energy Probability Function

ELISE Extraction from a Large Ion Source Experiment

EP Electric Propulsion

EVDF Electron Velocity Distribution Function

- FT** Fourier transform
- GIT** Gridded Ion Thruster
- HT** Hall Thruster
- ICP** Inductively-Coupled Plasma
- ITER** International Thermonuclear Experimental Reactor
- JPL** Jet Propulsion Laboratory
- LEO** Low Earth Orbit
- LHS** left-hand side
- LPP** *Laboratoire de Physique des Plasmas*
- LTP** Low-temperature plasma
- GEO** Geostationary Earth Orbit
- MHD** Magnetohydrodynamics
- MRFEA** magnetized retarding field energy analyzer
- MCC** Monte-Carlo collision
- NBI** Neutral Beam Injector
- PDE** partial differential equation
- PEGASES** Plasma Propulsion with Electronegative Gases
- PIC** Particle-In-Cell
- PPU** Power Processing Unit
- RHS** right-hand side
- RF** Radio-Frequency
- SC** spacecraft
- SEE** Secondary Electron Emission
- sccm** Standard Cubic Centimeters per Minute
- SI** International System of Units
- SPT** Stationary Plasma Thruster

Nomenclature

Physical constants

k_B	Boltzmann constant	$1.38064852 \times 10^{-23}$	J/K
e	Elementary charge	$1.60217662 \times 10^{-19}$	C
ϵ_0	Vacuum permittivity	$8.854187817 \times 10^{-12}$	F/m
g	Gravitational acceleration on the ground	9.81	m/s ²
c	Speed of light	299 792 458	m/s
m_e	Electron mass	9.109×10^{-31}	kg
m_H	Hydrogen atom mass	$1.6726219 \times 10^{-27}$	kg

Dimensional quantities

Unless otherwise stated, all the dimensional quantities are in the International System of Units (SI). Vector quantities are in bold font.

n	Density
\mathbf{v}	Velocity
v_T	Thermal velocity
u_B	Bohm speed
Γ	Flux
\mathbf{J}	Electric current density
T	Temperature, in K
T_e [eV]	Electron temperature, in V
ϕ	Electrostatic potential
\mathbf{E}	Electric field
\mathbf{B}	Magnetic field
ν	Collision frequency
ω	Angular frequency
ω_{pe}, ω_{pi}	Plasma frequencies
ω_{ce}, ω_{ci}	Cyclotron frequencies
K	Reaction rate
m	Particle mass
\mathcal{E}	Reaction threshold energy
\mathcal{W}	Injected power
w	Volume density of injected power
l	Discharge length
L	Gradient length
\mathbf{k}	Wavevector
λ	Wavelength
λ_e, λ_i	Electron and ion mean free paths
ρ_L	Larmor radius
σ	Collision cross section
p	Pressure, in Pa (gas pressure if no subscript)
p [mTorr]	Pressure, in mTorr (gas pressure if no subscript)
F	Thrust
I_{sp}	Specific impulse
I_d	Discharge current
f	Velocity distribution function
f_e	Energy distribution function
f_P	Probability distribution function

Dimensionless quantities

\mathcal{M}	Mach number
η	Hall parameter
h	Edge-to-center plasma density ratio
μ	Ratio of the electron mass over the ion mass
η	Efficiency
γ	Polytropic coefficient
q_f	Particle weight factor

Subscripts

\max	Maximum
av	Average
e	Electrons
i	Positive ions
n	Negative ions
g	Gas
x	x axis
y	y axis
z	z axis
d	Electron drift
$*$	Electron diamagnetic drift
$E \times B$	Electron $E \times B$ drift
a	Instability-enhanced ("anomalous")
eff	Effective
$loss$	Loss energy or power
iz	Ionization
el	Elastic momentum transfer
ex	Inelastic momentum transfer
LH	Lower hybrid
$1D$	1D model
$2D$	2D Two-dimensional model
s	Sheath boundary
B_{ref}	Reference quantities for the dispersion relation
\mathcal{E}_{ref}	Reference quantities for the global and 1D fluid model
th	Thermal quantity

Normalization

- \tilde{x} x variable normalized to $x_{B\text{ ref}}$ (see Chapter 3)
 X x variable normalized to $x_{E\text{ ref}}$ (see Chapter 4)

Derivatives

- | | |
|-----------------|--|
| ∇ | Gradient |
| ∇^2 | Laplace operator |
| $\nabla \cdot$ | Divergence operator |
| $\nabla \times$ | Rotational operator |
| ∂_x | Derivative along x |
| ∂_y | Derivative along y |
| ∂_z | Derivative along z |
| ∂_t | Derivative along t |
| $\frac{df}{dt}$ | Total (Lagrangian) derivative |
| f' | Derivative of a single variable function |

Integrals

- | | |
|-----------------------------|--------------------------------------|
| $\oint_S \cdot d\mathbf{S}$ | Integral over the discharge surface |
| $\iiint_V \cdot dV$ | Integral over the discharge volume |
| $\langle \cdot \rangle$ | Average over a distribution function |

Taylor expansion

The i -th term of the Taylor expansion of the variable X is X_i .

Vector norm

The vector norm is either $\|\cdot\|$, or just the vector quantity in light font.

0.0.1 Real and imaginary parts

- | | |
|-------|----------------|
| \Re | Real part |
| \Im | Imaginary part |

Introduction

Contents

Plasma physics for space propulsion	17
Low temperature plasma	21
Particle-in-Cell simulation	23
The PEGASES thruster	25
Outline of the thesis	28

Plasma physics for space propulsion

At the beginning of the XXth century, when airplanes were hardly flying, Rutherford evidenced the role of electrons and protons as constituents of atoms, opening the way to a new discipline: plasma physics [49]. Plasma physics deals with the collective behavior of electric charges carried by electrons, ions or striped atoms. The neutrality of atoms, that is widely observed at the Earth surface, happens to be just an exception at the scale of the universe. In most conditions of pressure and temperature observed outside of our planet, electrons are not bounded enough to the nuclei, such that matter behaves as a plasma, and not as a standard gas or liquid. The plasma can be accelerated by electric fields, confined by magnetic fields, and heated by electromagnetic waves. These phenomena are essential to understand the structure of astrophysical objects, and in particular the sun and its interaction with the planets of the solar system. For example, on Earth, the confinement of ions of the solar wind around the Earth magnetic field lines can be observed in auroras, and high electric field trigger ionization fronts in lightnings.

Plasma physics lies at the crossing of hydrodynamics, statistical physics, particle physics and quantum chemistry. It inherently tackles physical problems at a *mesoscopic* scale. The observation of natural phenomena was very important for the progress of plasma physics, but perhaps at an equally important level, the fact

that ionized matter can be accelerated, confined and heated by electric and magnetic fields gave birth to many technological applications. The application that has drawn most interest from the scientific community and the governments in the past seventy years is nuclear fusion. Nuclear energy is the densest source of energy currently available. The typical energy released in a chemical reaction is 1 eV while the typical energy released in a nuclear reaction is 1 MeV. So the nuclear energy density per mass unit is typically one million times higher than the chemical energy density per mass unit. This is of great interest both for civilian energy supply, and military applications, including propulsion and weapons. While fission reactions rely on high energy neutron impactors, nuclear fusion of light elements is sustained by the energy of the elements themselves. The typical fusion reaction between deuterium and tritium nuclei can be sustained only under very high temperatures and very high pressures, where the gas behaves as a fully ionized plasma. Research on nuclear fusion has been fundamental for the development of the theories of plasma physics since World War II, both for magnetic confinement fusion (mostly civilian), and inertial confinement fusion (mostly military) applications.

The motivation of the present work is spacecraft (SC) Electric Propulsion (EP). EP is perhaps less fundamental to the future of human kind than nuclear fusion but is a key element for the development of space exploration and for the commercial use of the outer space. It has been successfully tested in the 1960s in Cold War United States and USSR. The idea of using charged particles to generate thrust instead of hot gases appeared almost at the same time as the discovery of the very existence of these particles [33]. In 1920, at the very early stage of plasma physics and soon after the fundamental discoveries of electrons and ions, the first concepts of electric propulsion were patented by Robert H. Goddard [53]. The original idea comes from the very high velocity that ions can reach when accelerated through a moderate electrostatic potential. While the thermal expansion of neutral gases leads to velocities that are typically

$$v_{Tg} = \left(\frac{k_B T_g}{m_g} \right)^{1/2}, \quad (1)$$

the velocity reached by an ion accelerated by an electrostatic potential $\Delta\phi$ is

$$v_i = \left(\frac{2e\Delta\phi}{m_i} \right)^{1/2}. \quad (2)$$

For xenon (131.29 Atomic Mass unit (amu)), with $T_g = 1000$ K and $\phi = 100$ V, $v_{Tg} = 0.25$ km/s and $v_i = 12$ km/s. The velocity achieved by electrostatic acceleration are easily one or two orders of magnitude higher than those reached through thermal expansion. This difference comes from the ratio between the elementary

charge and the Boltzmann constant $e/k_B = 11\,605 \text{ K/V}$: while it is relatively easy to generate a 1 V electrostatic potential, it is much more challenging to sustain a gas reactor at 11\,605 K.

The outer space cannot provide the external forces that could be used for propulsion purposes like on ground, in the air or in the sea. On the contrary, the mass used for propulsion has to be carried on board the SC. According to Newton's third law, the thrust generated by a mass flow at velocity v is

$$F = \dot{m}v_{ex} \quad (3)$$

where v_{ex} is the exhaust velocity of the propellant and \dot{m} is the mass flow rate. This equation can be integrated over time to yield Tsiolkovsky equation of the velocity budget Δv of a space mission

$$\Delta v = v_{ex} \ln \left(\frac{m_0 + m_p}{m_0} \right) \quad (4)$$

where m_0 is the "dry mass" of the SC (its mass without the propellant) and m_p is the mass of propellant available at the beginning of the mission. The two previous equations put emphasis on the very important role of the outlet velocity of the propellant in space propulsion. At a given mass flow rate, a higher thrust can be achieved if the exhaust velocity is higher. Conversely, a smaller mass flow rate can be used to achieve the same thrust, which means that less propellant needs to be carried to space from the ground. Tsiolkovsky equation also shows that a greater velocity budget can be achieved with a greater exhaust velocity, which makes EP a good candidate for deep space exploration. In SC propulsion, the exhaust velocity is usually estimated through the specific impulse

$$I_{sp} = v_{ex}/g \quad (5)$$

where $g = 9.81$ is the gravitational acceleration on the ground. This quantity is particularly convenient for rocket propulsion: when $I_{sp}\dot{m} = m_R$, m_R being the total mass of the rocket, the rocket can take off.

Of course, like for any propulsion technology, an energy source is needed. For most scientific and commercial space missions, the electrical energy is provided by solar panels. The USSR has flown Stationary Plasma Thruster (SPT) technologies powered by a nuclear reactor through a thermionic converter, for example on the Kosmos 1818 surveillance satellite launched in 1987. The development of nuclear electric propulsion systems has slowed down since the end of the Cold War and the consensus on the peaceful use of the outer space and of nuclear energy. The power budget for most electric propulsion systems today is limited by the size of

the solar panels (typically 1 kW/m^2) such that most electric thrusters commercially available are in the $1\text{-}10 \text{ kW}$ range. The current trend is to miniaturize satellites to build constellations of hundreds or thousands of satellites that can provide global connectivity or Earth imaging with a very short revisit period. In-orbit servicing or extra-terrestrial resource extractions tend to draw an interest from the public and private investors since 2016. These applications may require the development of new high power propulsion systems in a not-too-distant future.

The rough characteristics of a plasma thruster can be estimated through very simple analytical models. The main parameters are the discharge current I_d , the acceleration voltage $\Delta\phi$, the mass flow rate \dot{m} , and the type of propellant. In an ideal plasma thruster with only singly-charged ions of mass m_i , each atom that enters the discharge chamber has to be ionized and accelerated, such that

$$\mathcal{W} = \Delta\phi \times I_d = (\mathcal{E}_{\text{ion}} + e\Delta\phi) \frac{\dot{m}}{m_i} \quad (6)$$

where \mathcal{W} is the electrical power and \mathcal{E}_{ion} is the mean energy required to create one ion. The exhaust velocity is estimated by Eq. (2). The specific impulse is

$$I_{sp} = \frac{1}{g} \left(\frac{2e\Delta\phi}{m_i} \right)^{1/2}, \quad (7)$$

and the thrust

$$F = \frac{\mathcal{W}}{\mathcal{E}_{\text{ion}} + e\Delta\phi} (2e\Delta\phi m_i)^{1/2}. \quad (8)$$

This equation shows that the propellant should have a high ion mass and a low ionization energy to maximize the thrust. The kinetic power of the plasma plume is

$$\mathcal{W}_{kin} = \frac{1}{2} \dot{m} v_i^2 = \frac{\mathcal{W}}{1 + \mathcal{E}_{\text{ion}}/(e\Delta\phi)} \quad (9)$$

such that the thruster efficiency is

$$\eta = \frac{1}{1 + \mathcal{E}_{\text{ion}}/(e\Delta\phi)}. \quad (10)$$

In this simple model, the thruster efficiency only depends on the mean energy required to generate one ion \mathcal{E}_{ion} , which is typically of the order of magnitude of the ionization potential \mathcal{E}_{iz} of the propellant (molecule or atom). Due to its inert nature, its high mass, and low ionization energy, xenon is the most commonly used propellant in the field of plasma propulsion.

This model is very much simplified and the art of plasma thruster design is to obtain performances that are close to the ideal situation depicted by Eqs. (7), (8) and (10).

The original designs of Gridded Ion Thruster (GIT) and Hall Thruster (HT) (equivalent to the SPT), which are the two main families of plasma thrusters, are the results of decades of research and technological development mainly in the US and in the former Soviet Union. Nowadays, new thruster designs, even when they are not revolutionary, need to be validated through expensive test campaigns where the thrusters are fired for over 10 000 hours in a vacuum chamber on ground. One of the first approaches of plasma thruster design via modeling was established by D. Goebel and I. Katz at the Jet Propulsion Laboratory (JPL) [56]. Among the main parameters that limit the thruster performances, we can mention

- (1) The *plume angle*. Only the kinetic energy of the beam directed along the thrust axis is useful for the thrust generation. Designing a thruster where the ion beam is narrow is quite important. The GIT technology is typically more efficient to this respect than the HT.
- (2) The *multi-ion generation* also deteriorate the thruster efficiency. A significant amount of doubly-ionized ions can be generated when the electron temperature is too high.
- (3) The most important source of performance losses holds in the discrepancy between \mathcal{E}_{ion} and the ionization energy \mathcal{E}_{iz} . The energy required per ion generated \mathcal{E}_{ion} is necessarily greater than the ionization potential energy \mathcal{E}_{iz} , and it can eventually be much higher. The power conversion from the Power Processing Unit (PPU) to the plasma may not be ideal, which yields what is called in the literature the electrical efficiency. A significant amount of the energy is lost in atomic or molecular excitation levels that naturally decay to the fundamental state by emitting light at various frequencies, including in the visible spectrum, or remain in metastable states. Some of the energy is also lost through elastic collisions with the neutral gas and contributes to gas heating. Finally, the loss of energetic particles at the inner reactor walls may deteriorates the thruster performances as well. The same questions of plasma confinement and transport arise as in problems related to fusion technologies.

An investigation of the phenomena mentioned above requires a deep understanding of Low-temperature plasma (LTP) Physics. In this work, we will focus mainly on point (3), with great emphasis set on transport and power loss phenomena involved in GIT technologies, both with and without magnetic fields.

Low temperature plasma

LTP Physics is a theoretical framework that covers a quite wide range of experiments and applications. The pressure can vary between atmospheric pressure or

above to very low pressures of a fraction of milli-Torr (mT). The milli-Torr will be the typical unit of pressure used throughout this work. In our simulations, the pressure is varied between 0.3 and 100 mTorr. We remind that the Torr unit is defined by

$$1 \text{ Torr} = 1/760 \text{ atm} \approx 1 \text{ mmHg} \approx 133.32 \text{ Pa.} \quad (11)$$

The type of power injection in LTP experiments can be Radio-Frequency (RF), microwave, helicon, or through a Direct Current (DC) discharge. The nature and the applications of LTP vary very widely. However, a few properties are common to every LTP systems. The most fundamental property is that electrons are not in thermal equilibrium with the gas and with the ions. The electron temperature has to be high enough to sustain the discharge through electron impact ionization. In practice, the electron temperature has to be greater than a fraction of the ionization potential, typically a few electron-volts. The temperature of heavy species (gas and ions) is typically lower than 1 eV. If there is such a temperature gap between electrons and ions, it means that electrons and ions cannot be thermalized through Coulomb collisions. This implies that the plasma density cannot be too high. The issue will be addressed more carefully in 1.2. Transport processes are driven by collisions between charged particles and neutrals, but the residence time of a particle inside the discharge is not high enough to achieve thermal equilibrium with the gas. Since interactions between charged particles and neutrals dominate over Coulomb collisions, the gas is often weakly ionized: the electron density is smaller or comparable to the gas density. This also means that the electron temperature cannot be much higher than the ionization potential.

Many chemical processes are enhanced by temperature. However, only the energy of the electrons actually plays a role in the reactivity of a gas because they are responsible for molecular bounds. In LTP, instead of heating a gas to a high temperature to enhance reactivity, only electrons are targeted, which potentially yields a much better power efficiency for chemical processes, and for the generation of metastable species and ions.

At pressures down to 10^3 Pa, the collisional processes are so strong that the fluid velocity of charged species does not exceed the thermal velocity. The properties of the plasma are considered to be local and they can be parametrized by the reduced electric field E/n , where E is the local electric field and n is the gas density. At lower pressure, the particles are more freely accelerated by the electric field, and space derivatives become important to predict correctly the plasma properties.

Particle-in-Cell simulation

As said previously, plasma physics consists in investigating the collective behavior of charged particles. One approach is to treat the plasma as a fluid to derive equations for the statistical properties of this fluid, for instance its local density, fluid velocity, and temperature. As computer power increased in the early 1990's, it became possible to a certain extent to extract these collective properties by simulating the motion of charged particles interacting together. The description of 1 cm^3 of a plasma of 10^{11} cm^{-3} of electron density by pair interactions leads to the computation of $2^{10^{11}}$ interactions at each time step which is completely out of reach even by todays most powerful computing systems. The PIC simulation is based on two fundamental assumptions that allow to reduce massively the computation resources required.

1. The collective behavior of the plasma can be described by the motion of *super-particles* that obey the same physical laws as the particles that they represent but with a statistical weight factor q_f such that the mass of a super-particle that represents q_f electrons of mass m_e and charge $-e$, is $q_f m_e$ and its charge is $-q_f e$. In PIC simulations, no real particle is tracked individually, only sets of hundred thousands of particles are. If the number of super-particles simulated is too low, numerical noise can appear very quickly.
2. The interaction between charged particles is well represented by computing an electric field and sometimes also a magnetic field according to Maxwell's equations from a density of charge and of current. While this seems an obvious consequence of Maxwell's equations, the implementation of this method necessarily underestimates the role of short range Coulomb interactions, due to grid discretization.

The motion of super-particles is directed by the Lorentz force

$$m \frac{d\mathbf{v}}{dt} = q(\mathbf{E} + \mathbf{v} \times \mathbf{B}) \quad (12)$$

where m and q are respectively the mass and the charge of the super-particle.

As illustrated in Fig. 1, all PIC simulations start with an initialization stage where super-particles are distributed in a simulation domain, with initial values of the electric and magnetic fields. Eq. (12) is then integrated over one time step dt . After this initial time step, some of the particles may be collected on the boundaries of the simulation, and subsequently absorbed or re-injected. Depending on reaction cross sections, a subset of the super-particles can undergo collisions leading to scattering, energy loss, and new particle generation. The new distribution of

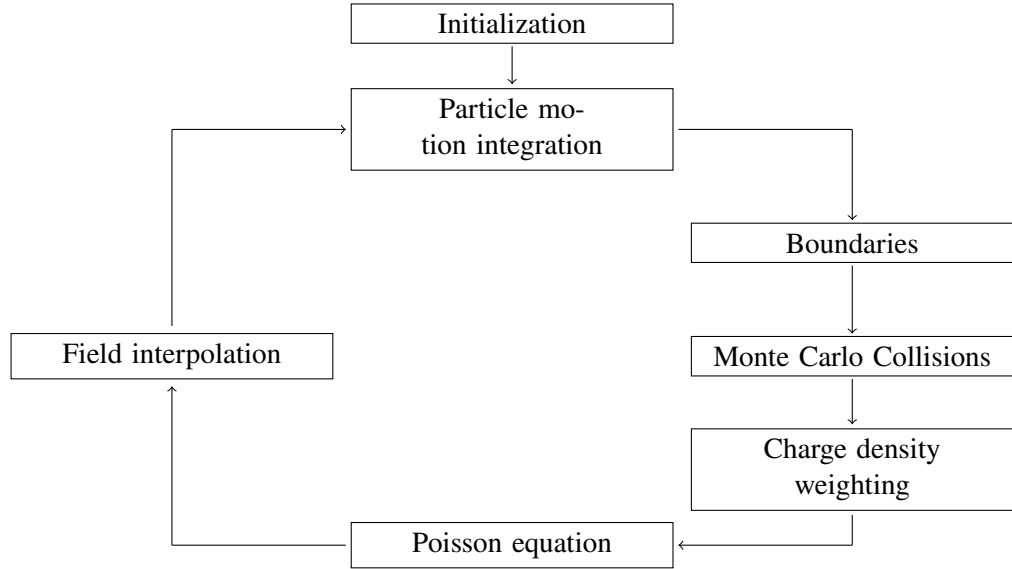


Figure 1: Diagram of the PIC time loop.

super-particles leads to a new charge density map obtained by weighting the particle positions with their charges on grid points. The field equations are then solved (Poisson's equation in the electrostatic case treated in this work) to obtain new electric and magnetic fields that are in turn interpolated at each particle's position to initialize the next time step. The first PIC algorithms for electrostatic simulation of plasmas were implemented in the 1960s and a comprehensive monograph was published by Birdsall and Langdon in 1985 [15]. The present work is the continuation of the doctoral work carried out by V. Croes [35], and his effort to develop a 2D PIC code at *Laboratoire de Physique des Plasmas* (LPP) that would be suited for the simulation of plasma thrusters, supervised by T. Lafleur, P. Chabert and A. Bourdon. This code is called *LPPic* and is developed since 2014. Most of the algorithms implemented in *LPPic* come from Birdsall and Langdon [15]. Nevertheless, the Monte-Carlo algorithms used to describe the collisions between charged particles and the neutral background were developed in the 1990's by Vahedi [128]. Collisions between super-particles and the background of neutral gas necessarily make the simulation stochastic. PIC simulation is a remarkably powerful tool because all the properties of the super-particles and the plasma as a fluid can be extracted. However, the amount of data processed and generated can be overwhelming, and needs to be carefully selected and sorted. Up to the 1990's PIC simulation was mostly used to investigate fundamental processes and was often limited to 1D [125]. Only since the 2000's, 2D and Three-dimensional (3D) PIC simulation of

real systems has become more and more accessible [36, 22], but they also demand more computer engineering to run with massively parallelized codes, and require careful benchmarking [126], validation [23], and convergence study [69].

The PEGASES thruster

The work carried out during these three years was largely motivated by the investigation of the PEGASES thruster, a concept patented at LPP by P. Chabert in 2005 [25]. This thruster is a GIT designed to operate with strongly electronegative gases.

The space environment is a plasma at very low density, ($10^9 - 10^{10} \text{ m}^{-3}$). The surfaces of the satellites form space charge sheaths of several meters with electric fields that tend to accelerate the ions towards the surfaces of the satellite, affecting the local charging of the satellite, and causing erosion on some surfaces,[85] and contamination.

On classical electric propulsion systems, the beam of ion is neutralized by a cathode, which is an external electron source that maintains the charge balance with the ion beam [56]. However, this device does not prevent ions from being collected on the surfaces and their lifetime is limited [55]. Most commonly used cathodes are hollow cathodes and their Physics require a dedicated treatment [105, 104]. Moreover, they can be expensive and difficult to miniaturize.

The main idea of the PEGASES thruster is to generate thrust with two ion beams of opposite sign. The design would tackle at the same time the issues of ion recollection, the plume angle, and would allow one to get rid of the cathode subsystem. As illustrated in Fig. 2(a), the design comprises a planar RF antenna which is located on the side of the gas injection. The inner walls of the thruster are made out of dielectric materials (ceramic and Pyrex). The plasma is generated inductively near the RF antenna and transported towards the double acceleration grid located on the right-hand side of Fig. 2(a) through the magnetic filter formed by permanent magnets. The double grid is polarized alternatively positively and negatively in order to accelerate the positive and negative ions. The ion fluxes were analyzed by a specially designed magnetized retarding field energy analyzer (MRFEA) [80]. The role of the magnetic filter is to cool down the electrons through magnetic confinement. The thruster was made to operate with iodine (I_2), which is a promising candidate for future electric propulsion systems (see Chapter 5), but experiments were also carried out with argon and SF_6 . The thruster can be split in three stages:

- The ionization stage where the electron temperature needs to be high enough to produce ionization;
- The magnetic filter where the electron temperature decreases due to magnetic

confinement, such that they can produce dissociative attachment on the I₂ molecule;

- The acceleration stage where the ions are extracted and expelled at high velocity

The objective is to guarantee that the positive and negative ions can recombine in the plasma plume to form a neutral beam.

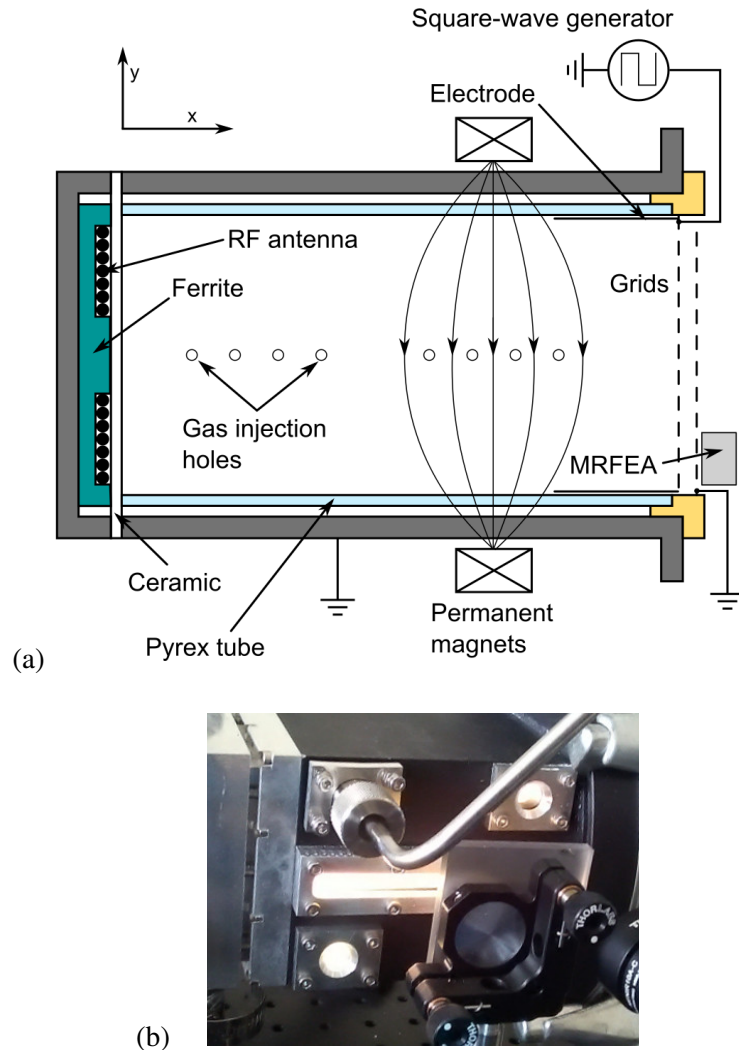


Figure 2: The PEGASES thruster at LPP. (a) Diagram of the system, from Lafleur et al. (2014) [80]. (b) Picture of the system operated with iodine (Experiment by F. Marmuse in 2017)

Outline of the thesis

The first four chapters of the thesis will be dedicated to theory and simulation of transport phenomena in plasmas of noble gas discharges, with a particular emphasis set on the case of argon. In Chapter 1 we introduce the basic definitions and concepts that will be used throughout the Thesis. The general equations of the transport are provided, the PIC simulation method and global models of plasma discharges are described. First simulation results of a helium ICP discharge are qualitatively discussed to illustrate basic plasma theories.

In Chapter 2, some analytical solutions of the isothermal plasma transport in 1D and 2D are given. The 2D theory is compared to the PIC simulation results, and generalized to 3D geometries. Parametric studies with respect to the pressure and the aspect ratio are performed.

Chapter 3 investigates the cross-field transport phenomena with a study of the effect of resistive drift instabilities in low pressure, weakly ionized plasmas. It is shown in this chapter that the magnetic confinement of the plasma completely saturates at high magnetic field.

In Chapter 4, we present simulations of a magnetic filter in both realistic and reduced geometries and compare it to a 1D quasineutral model. The results are also compared with experimental results and 2D fluid simulations performed by other authors.

Chapter 5 is dedicated to the study of an iodine ICP with no magnetic field. The state-of-the art regarding low pressure iodine plasmas is summarized and a cross section set relevant to low pressure, low temperature plasmas is presented. Relaxation oscillations observed in the transient of the PIC simulation are analyzed. Edge-to-center density ratio formulas established for electronegative plasmas are compared with PIC simulation results.

Chapter 1

Weakly ionized plasma

Contents

1.1	Particle approach: theory and simulation	30
1.2	Kinetic theory and collisions	33
1.2.1	Boltzmann equation	33
1.2.2	Electron-neutral reactions	35
1.2.3	Ion-neutral reactions	36
1.2.4	Momentum transfer collision frequency	42
1.3	Introduction to ICP theory and simulation	45
1.3.1	Heating mechanism	45
1.3.2	Fluid equations of the plasma transport	47
1.3.3	Numerical parameters of the PIC simulation	50
1.3.4	First run example	52
1.4	Observation of the main features of a plasma discharge	56
1.5	Sheath theory	60
1.6	Global models of a plasma discharge	64

In this first Chapter of the Thesis, we introduce the particle motion equations, the kinetic equations and the fluid conservation equations that will be used throughout this work. This includes a description of the collision processes between charged particles and atoms in noble gas plasma discharges. Cross section sets and reaction rates are provided for helium, argon, krypton and xenon. The principles underlying low temperature plasma simulation by the PIC method are also presented and the first simulation results of a low density helium ICP discharge are discussed. The equations of global models (Zero-

dimensional (0D)) of low temperature plasma discharges are derived.

1.1 Particle approach: theory and simulation

The motion of a non-relativistic charged particle is described by the integration of Newton's second law with the Lorentz force

$$\frac{d\mathbf{v}}{dt} = \frac{q}{m} (\mathbf{E} + \mathbf{v} \times \mathbf{B}) \quad (1.1)$$

If there is no electric field, the trajectory of a charged particle is a circle and the angular velocity of the particle is the cyclotron frequency

$$\omega_c = qB/m \quad (1.2)$$

where q and m are the charge and the mass of the charged particle respectively, and B is the intensity of the magnetic field. The radius of the circular trajectory is called the Larmor radius ρ_L . If the projection of the particle velocity vector in the plane perpendicular to the magnetic field is v_\perp , then the Larmor radius is

$$\rho_L = v_\perp / \omega_c = \frac{v_\perp m}{qB} \quad (1.3)$$

The magnetic field cannot accelerate a particle in the parallel direction, such that the motion of a charged particle in a magnetic field is an helix. This motion is called the cyclotron motion. When an electric field is added, one can retrieve the same form of equation as for the cyclotron motion by noticing that

$$\frac{d(\mathbf{v} - \mathbf{v}_{E \times B})}{dt} = \frac{q}{m} (\mathbf{v} - \mathbf{v}_{E \times B}) \times \mathbf{B} \quad (1.4)$$

where

$$\mathbf{v}_{E \times B} = \frac{\mathbf{E} \times \mathbf{B}}{B^2} \quad (1.5)$$

is the $E \times B$ drift. The motion of a charged particle in constant and uniform electric and magnetic fields is the sum between the cyclotron motion (helix) and a drift in the direction perpendicular both to \mathbf{E} and \mathbf{B} . The reader can refer to the monograph by Chen [31] for more details about the basics of single particle motion.

The electric and magnetic fields are the sum of the fields generated by each particles, following Coulomb's law for the electric field and Biot-Savart's law for the magnetic field. Computing the binary interactions of each charged particles is very computationally expensive. In practice, the field generated by a large number

of particles is computed using Maxwell's equations using a continuous description of the charge and current densities ρ and \mathbf{j} .

$$\nabla \cdot \mathbf{E} = \rho/\epsilon_0 \quad (1.6)$$

$$\nabla \cdot \mathbf{B} = 0 \quad (1.7)$$

$$\nabla \times \mathbf{E} + \partial_t \mathbf{B} = 0 \quad (1.8)$$

$$\nabla \times \mathbf{B} - \frac{1}{c^2} \partial_t \mathbf{E} = \mu_0 \mathbf{j} \quad (1.9)$$

The plasma densities considered throughout this work do not exceed 10^{17} m^{-3} with electron temperatures that remain below 5 eV. The fluid velocities were always smaller than the electron thermal velocity

$$v_{Te} = \left(\frac{k_B T_e}{m_e} \right)^{1/2} \quad (1.10)$$

This yields currents always lower than $1.5 \times 10^4 \text{ A/m}^2$. For a system of typically 1 cm of size, the induced magnetic field is about 0.2 mT, which corresponds to a Larmor radius of about 3 cm for electron moving at the electron thermal velocity (Eq. (1.10)), which is of the same order of magnitude as the systems investigated in this work. The magnetic field induced by the electron motion is weak and does not affect much the particle trajectory. The effect is even weaker for the ions due to their lower typical velocity. Most often, the fluid velocity of the electrons is at least on order of magnitude lower than the thermal velocity, except in the high magnetic field case that will be discussed in Chapter 3, where the fluid velocity of the electrons comes close to the electron thermal velocity. Moreover, the frequencies investigated are in the range of 1-100 MHz such that the term $\frac{1}{c^2} \partial_t \mathbf{E}$ remains low and does not influence the magnetic field either. In all the models developed in this work, we stand in the magnetostatic assumption, and we further assume that the magnetic field is decoupled from the particle motion equations. The electric field is coupled to the particle motion equations through Gauss' law (Eq. (1.6)). In the magnetostatic limit, Maxwell-Faraday's equation is equivalent to $\nabla \times \mathbf{E} = 0$, which means that that an electrostatic potential ϕ exists such that

$$\mathbf{E} = -\nabla \phi. \quad (1.11)$$

PIC simulation codes feature two co-existing data structures the particles, which are defined by their charge, position and velocity, and a grid of cells. Each cell contains at least the charge density, the electrostatic potential and the electric field. The particle and grid types implemented in the LPPic are given below as an illustration.

```

type particle
!
integer :: numero = 0      !ID number
integer :: charge = 1000   !charge
real(dbleprc), dimension(3) :: V  = [0,0,0] !velocity
(normalized)
real(dbleprc) :: X = 8880 !Position along x
real(dbleprc) :: Y = 8880 !Position along y
real(dbleprc) :: Z = 8880 !Position along z
end type particle
!

type grid
!
! De-normalized charge density
real(dbleprc) :: Rho = 0
! Normalized electric field
real(dbleprc), dimension(2) :: Ej = [0,0]
! Normalized electrostatic potential
real(dbleprc) :: Phi = 0
! Normalized charge density
real(dbleprc) :: p = 0
! Normalized magnetic field
real(dbleprc), dimension(3) :: B = [0,0,0]
! Normalized electron density
real(dbleprc) :: Nume = 0
! Normalized density of heavy species tracked
real(dbleprc), dimension(:), allocatable :: Numh
end type grid
!
```

The particle position is interpolated at the grid cells using a linear weighting method. The contribution of all the charged particles at all the grid cells provides values of the charge density at each grid cell. Eq. (1.6) combined with Eq. (1.11) yields Poisson's equation:

$$\nabla^2 \phi = -\rho/\epsilon_0 \quad (1.12)$$

which is the fundamental law of electrostatics. The Poisson's equation is solved using either Hypre or Petsc numerical solvers in 2D, with either closed boundary conditions in the x and y directions or periodic boundary conditions in the x direction and closed boundary conditions in the y direction. The solvers are interfaced in C language and provide a value of the potential at each grid cell. The electric field is estimated from the electrostatic potential using simple finite differences. The value of the electric potential at each particle's position is interpolated using again a linear

interpolation algorithm. The particles are then displaced by integrating Eq. (1.1) over one time-step dT . In case of a magnetized plasma, the classical Boris scheme is used [18, 15, 35], which consists in splitting the particle motion in two halves, and the rotation due to the magnetic field is performed at $t + dt/2$. In their motion, particles can eventually undergo collisions of various sorts that will be investigated in the next section. The current version of *LPPic* uses a completely explicit scheme [15].

In general the weight factor q_f is defined by

$$q_f = \frac{nV_{simu}}{N_{part}} \quad (1.13)$$

where N_{part} is the number of particles for the considered species and n the initialized density. In 3D V_{simu} is the simulation volume, and the weight factor represents exactly the ratio between the number of physical particles and the number of numerical particles. However, in lower dimension, the super-particles are not exactly points but straight lines (in 2D) or planes (in 1D) because the simulation volume is either a surface area (2D) or a line segment (1D). In the 2D PIC simulations presented here, the weight factor is therefore in m^{-1} .

1.2 Kinetic theory and collisions

1.2.1 Boltzmann equation

The kinetic theory of plasmas is based on equations that apply on the distribution function of each species of a given system. In 3D, the velocity distribution function f takes 7 arguments x, y, z, v_x, v_y, v_z , and t , such that $f(\mathbf{x}, \mathbf{v}, t) d^3x d^3v$ is the number of particles inside a six-dimensional phase space volume $d^3x d^3v$ at (\mathbf{r}, \mathbf{v}) at time t , where $d^3x = dx dy dz$ and $d^3v = dv_x dv_y dv_z$ [84]. If the distribution of particles is not affected by any collision, the distribution function f obeys a continuity equation

$$\partial_t f + \mathbf{v} \cdot \nabla f + \mathbf{a} \cdot \nabla_{\mathbf{v}} f = 0 \quad (1.14)$$

where $\mathbf{a} = \partial_t \mathbf{v}$ and $\mathbf{v} = \partial_t \mathbf{x}$ are the acceleration and the velocity vectors of the flow, respectively, and $\nabla_{\mathbf{v}}$ is the gradient operator with respect to the velocity variables:

$$\nabla_{\mathbf{v}} = \mathbf{e}_x \frac{\partial}{\partial v_x} + \mathbf{e}_y \frac{\partial}{\partial v_y} + \mathbf{e}_z \frac{\partial}{\partial v_z}. \quad (1.15)$$

Assuming that the particles at the position \mathbf{x} all undergo a force field \mathbf{F} , Newton's second law imposes that $\mathbf{F} = m \mathbf{a}$. Moreover, collisions can affect the velocity of some particles, or cause the creation or destruction of some particles at very

short time scales. These effects are accounted for by introducing a collision term in Eq. (1.14)

$$\partial_t f + \mathbf{v} \cdot \nabla f + \frac{\mathbf{F}}{m} \cdot \nabla_{\mathbf{v}} f = \partial_t f|_c. \quad (1.16)$$

Eq. (1.16) is called the Boltzmann equation or the Vlasov equation when $\partial_t f|_c = 0$. While the Vlasov equation can be solved by the method of characteristics, the Boltzmann equation (including collisions) is much more challenging to solve, especially due to the collision term which is difficult to estimate. The *LPPic* contains a Monte-Carlo collision (MCC) subroutine that describes the collisions between charged particles and the neutral gas.

In the following, the density n , and the fluid velocity \mathbf{u} are defined for each species by integrating the distribution functions in the velocity space

$$n(\mathbf{x}, t) = \iiint f d^3 v \quad (1.17)$$

$$\mathbf{u}(\mathbf{x}, t) = \frac{1}{n} \iiint \mathbf{v} f d^3 v. \quad (1.18)$$

The kinetic definition of the temperature is also used

$$T(\mathbf{x}, t) = \frac{m}{3k_B n} \iiint (\mathbf{v} - \mathbf{u})^2 f d^3 v. \quad (1.19)$$

These definitions can be naturally used in the PIC code to extract macroscopic information (either local or global) from the simulation. Isotropic distribution functions can be described using the energy distribution function $f_e(\epsilon)$ or the energy probability distribution function f_P where $\epsilon = \frac{1}{2}mv^2$ is the kinetic energy of the particle. These functions are connected to the velocity distribution function by

$$f_e(\mathbf{x}, \epsilon, t) d\epsilon = f(\mathbf{x}, \mathbf{v}, t) d^3 v \quad (1.20)$$

$$f_P(\mathbf{x}, \epsilon, t) = \epsilon^{-1/2} f_e(\mathbf{x}, \epsilon, t) \quad (1.21)$$

The energy distribution function

$$f_e(\epsilon) = \frac{2N\epsilon^{1/2}}{(k_B T)^{3/2}\pi^{1/2}} \exp\left[-\frac{q\phi + \epsilon}{k_B T}\right] \quad (1.22)$$

is called the Maxwell-Boltzmann distribution function. The probability distribution function f_P is proportional to $\exp(-\frac{\epsilon}{k_B T})$ for a Maxwell-Boltzmann distribution function, which makes it a convenient variable to estimate if a population extracted from experimental or simulation data is Maxwellian.

In terms of velocity, Eq. (1.10) is

$$f(\mathbf{v}) = N \left(\frac{m}{2\pi k_B T} \right)^{3/2} \exp \left[-\frac{q\phi + mv^2/2}{k_B T} \right]. \quad (1.23)$$

This function is a solution of the (stationary) Vlasov equation (1.14) where the only force term is the electrostatic force $qE = -q\nabla\phi$. In Eq. (1.22), N is the density at the position corresponding to $\phi = 0$. One can also show (Lieberman and Lichtenberg 2nd ed. Appendix B [84]) that this distribution function corresponds to the solution of the Boltzmann equation (1.16) with only elastic collisions.

1.2.2 Electron-neutral reactions

The elastic scattering of electrons, electron impact induced excitations and ionization were implemented by V. Croes during his thesis [35] for helium and xenon in two different codes. In this thesis, the code was generalized to read cross section data files exported from the LXCat database, allowing to explore various cross section sets, and with various gases where the chemistry is limited to the same types of reactions as for noble gases. The cross sections are tabulated against the collision energy in eV. All the electron neutral collision cross sections come from the Biagi database retrieved from LXCat [9]. In 2017, the collision module was used for the study of the instability-enhanced electron mobility in the direction of the thrust axis of a HT using PIC simulations in the radial - azimuthal plane, and published in Croes et al. [38, 37]. Similar investigations were also presented with a simplified cross section set for iodine, involving only the same reactions as in the case of a noble gas, in V. Croes' thesis [35]. More complete cross section sets for the iodine chemistry will be detailed in Chapter 5.

The momentum transfer from electrons to the gas is neglected. Therefore, when elastic scattering occurs, the impinging electron keeps the same kinetic energy. The direction of its velocity vector is simply randomized following a uniform probability function over a solid angle of 4π sterad. Ionization and excitation reactions are inelastic collisions so a fraction of the kinetic energy of the impinging electron is transferred to internal energy levels of the target atom in the case of excitation, and used to detach an electron in the case of ionization. After an excitation takes place, the atoms should release their energy by photon emission or remain in a metastable state. Ionization or excitation from excited atomic levels are neglected such that we always make the assumption that the neutral species are in the majority in their fundamental state. After an excitation, the electron is scattered with a random velocity angle and a kinetic energy which is simply $E_k - \mathcal{E}_{e,x}$ here E_k is the kinetic energy of the impinging particle and $\mathcal{E}_{e,x}$ is the energy loss corresponding to the excitation reaction. In the case of an ionization collision, the remaining kinetic energy

$E_k - \mathcal{E}_{e,x}$ is divided in two between the two secondary electrons, which are both scattered with a random velocity angle.

Some cross section sets available on the LXCat database contain many excitation levels that each correspond to real electronic states. However, it is possible to average some neighboring excitation levels into fewer effective inelastic collisions that represent correctly the electron transport. Such simplifications were made by Biagi [9] and all the electron cross section sets used by default in *LPPic* contain between 1 and 4 inelastic collisions with various energy thresholds that do not represent well identified excitation levels of the atom. As shown in the next section, this simplification does not affect the local electron temperature and the electron density.

The cross sections can be integrated over the whole energy space and weighted against a distribution function to yield the reaction rate or reaction rate factor

$$K(\mathbf{x}, t) = \frac{1}{n} \left(\frac{2}{m} \right)^{1/2} \int f_e(\epsilon) \sigma(\epsilon) \epsilon^{1/2} d\epsilon \quad (1.24)$$

It is also useful to introduce the collision frequency defined for particles colliding with a gas of density n_g .

$$\nu = n_g K \quad (1.25)$$

For a Maxwellian distribution function, the reaction rate is

$$K = \left(\frac{2}{k_B T} \right)^{3/2} \frac{1}{(m\pi)^{1/2}} \int \sigma(\epsilon) \epsilon e^{-\frac{\epsilon}{k_B T}} d\epsilon \quad (1.26)$$

The cross section of electron-atom processes selected for *LPPic* are summarized in Fig. 1.1. The MCC subroutine uses the "null collision" method as described in the original paper by V. Vahedi [128] and in V. Croes' thesis [35]. The reaction rates for Maxwellian distribution functions are also provided in Fig. 1.2. These reaction rates are the ones used in the global model of noble gas discharges described in this work. For the sake of comparison, the set of reaction rates for argon estimated by V. Vahedi is provided in Fig. 1.3. It is sometimes convenient to have access to analytical fits of the reaction rates. Some of the fits available in the literature are summarized in Fig. 1.4.

1.2.3 Ion-neutral reactions

The collisional transport of ions across a neutral background can be modeled by decomposing the collisions in two categories: isotropic scattering and backscattering [91]. The cross sections for xenon and argon were validated against experimental data [92, 91], but a simple assumption of Langevin collision cross section using

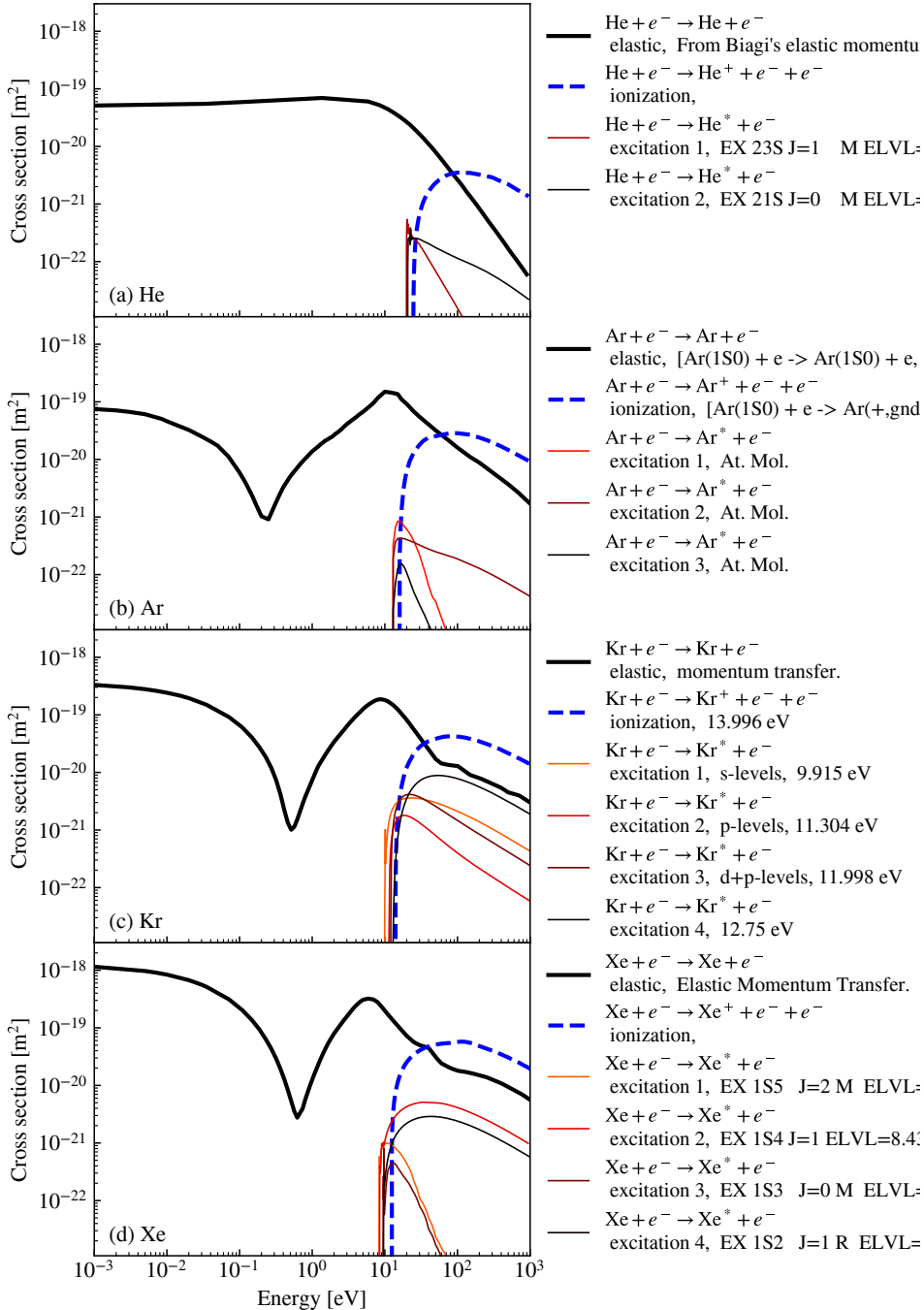


Figure 1.1: Electron-neutral collision cross sections for noble gases used by default in the simulations performed in this work [9].

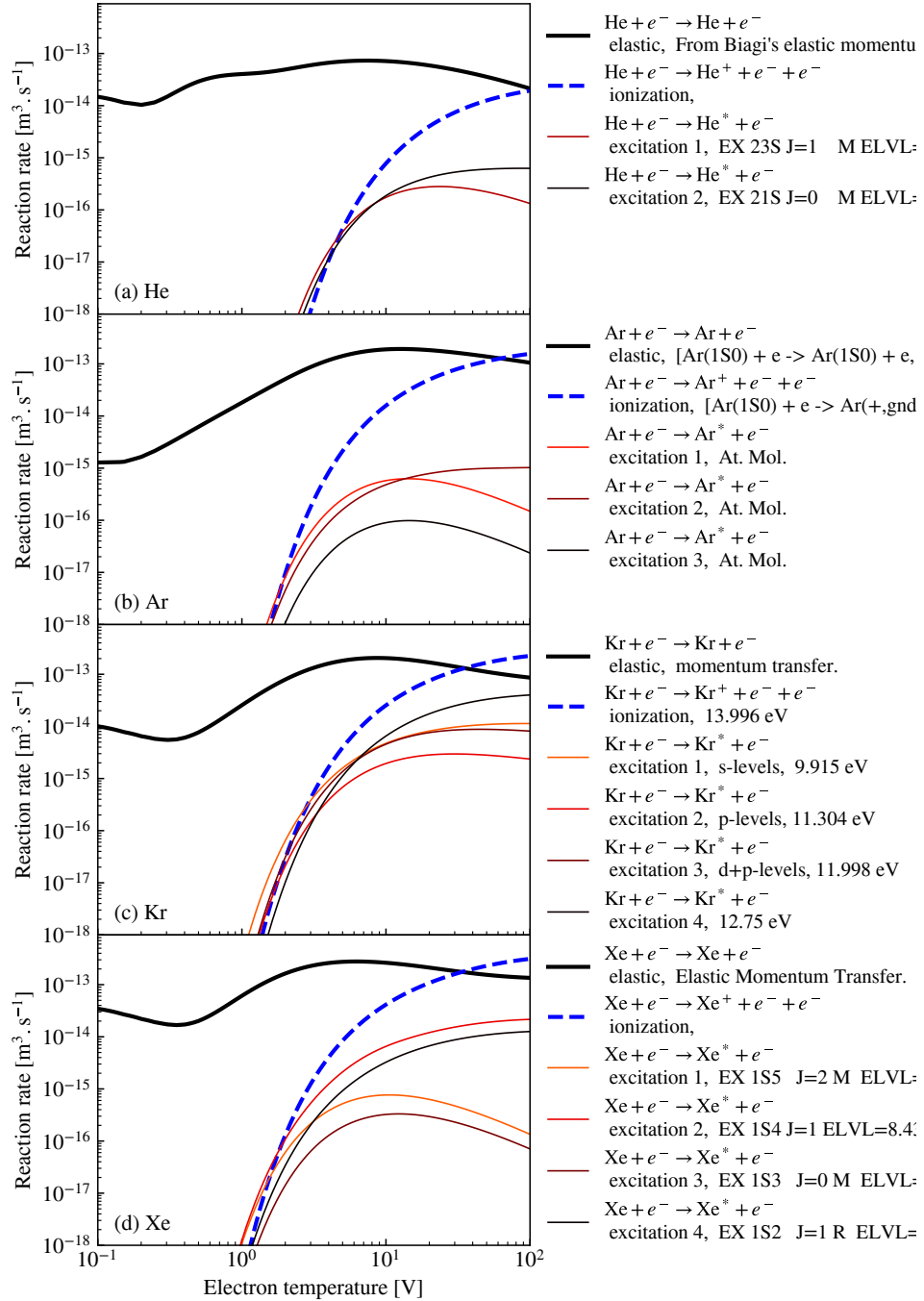


Figure 1.2: Electron-neutral reaction rates for a Maxwellian EEDF and neutral atoms at rest. Numerical integration was performed over the data of Fig. 1.1.

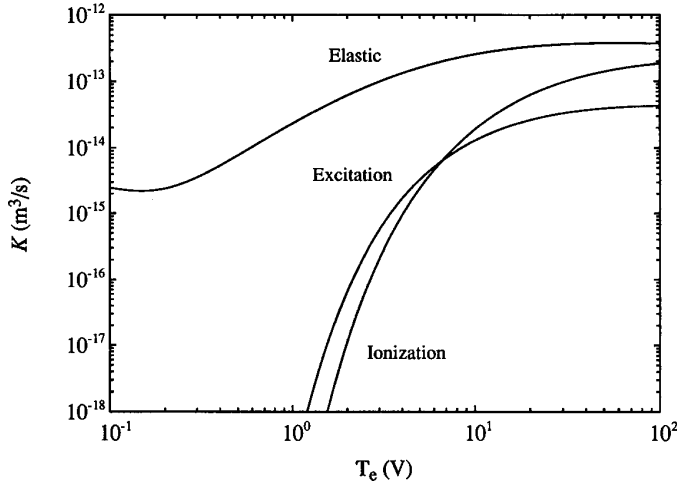


Figure 1.3: Electron-neutral reaction rates for argon [84].

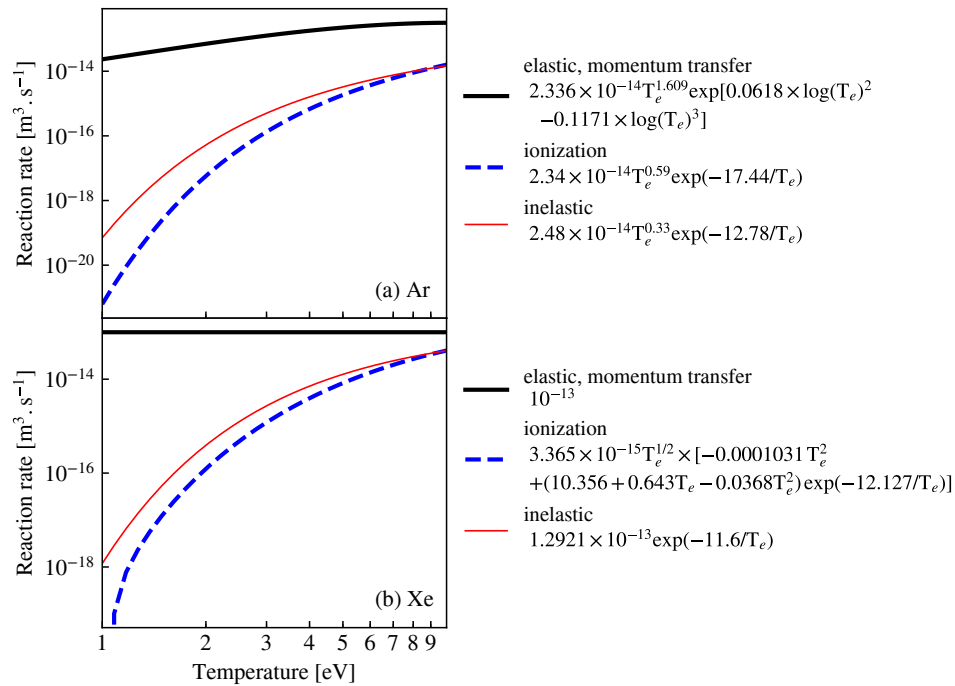


Figure 1.4: Analytical formulas to estimate the electron-neutral reaction rates for argon (a) [84] and xenon (b) [26].

atomic polarisability was chosen in the paper of Piscitelli et al. [92] for xenon. Helium data was also released on LXCat by the group of Phelps, but no data was available for krypton. The Langevin capture cross section corresponds to the polarization of an atom or a molecule by the close approach of an ion [84]:

$$\sigma_L = \frac{1}{v_R} \left(\frac{\pi \alpha_P e^2}{\epsilon_0 \mu} \right)^{1/2} \quad (1.27)$$

where v_R is the relative velocity between the two particles, $\mu = m_1 m_2 / (m_1 + m_2)$ is the reduced mass, and α_P is the relative polarizability of the atom. The values of polarizabilities for noble gases are provided in Table 1.1. Lieberman and Lichtenberg propose an estimate of the charge exchange cross section based on a semi-classical quantum tunneling theory

$$\sigma_{BS} \approx \frac{9}{16\pi} \left(\frac{e}{\epsilon_0 \mathcal{E}_{i,z}} \right)^2 \quad (1.28)$$

where $\mathcal{E}_{i,z}$ is the ionization potential of the atom in electron-volts. This estimate has the advantage of being independent of the impact energy.

Sakabe et al. [103] (1992) proposed an analytical formula that is an improvement of the earlier work of Rapp and Francis (1962) [98], validated with a large set of experimental data for quite high relative impact velocities ($> 10^3$ m/s).

$$\sigma_{BS} \approx (A - B \log_{10} v_R) (\mathcal{E}_{i,z} / \mathcal{E}_{i,z,0})^{-3/2} \quad (1.29)$$

where $A = 1.81 \times 10^{-14}$, $B = 2.12 \times 10^{-15}$, and v_R is the relative velocity in cm/s. $\mathcal{E}_{i,z} = 13.6$ eV is the ionization potential of hydrogen. Fig. 1.5 summarizes the various estimates of reaction cross sections for isotropic scattering and resonant backscattering in noble gas plasmas. Sakabe formula (1.29) provides reasonable estimates of the backscattering cross section for helium, argon, and xenon, except at low energy where it does not apply well for xenon. Sakabe formula was used to run the simulations with krypton in Croes et al. [38]. The constant cross section estimate (Eq. (1.28)) provides also a reasonable order of magnitude but seems to systematically underestimate the backscattering cross section.

The cross sections of two-body collisions provided by the LXCat database are functions of the total energy in the center of mass frame of the collision \mathcal{E}_{CM} . However, the collision frequency is calculated from the velocity of the charged species in the reference frame of the neutrals v , by the formula :

$$v = \sigma n_g v \quad (1.30)$$

where n_g is the density of the neutral gas. The aim here is to determine the relationship between \mathcal{E}_{CM} and v in order to calculate the collision frequency correctly and in a general case.

Let v_{CM} , m_g , and m be respectively the center of mass velocity, the neutral mass, and the charged particle mass. By definition of the center of mass, and since the neutral velocity is zero in the neutral center of mass:

$$(m + m_g)v_{CM} = mv \Rightarrow v_{CM} = \frac{m}{m + m_g}v \quad (1.31)$$

The total kinetic energy in the center of mass frame is the sum of the kinetic energy of the charged particle and the neutral, in the center of mass frame.

$$\mathcal{E}_{CM} = \frac{1}{2}m(v - v_{CM})^2 + \frac{1}{2}m_g v_{CM}^2 \quad (1.32)$$

$$= \frac{v^2}{2(1 + m_g/m)^2} \left(\frac{m_g^2}{m} + m_g \right) \quad (1.33)$$

$$\mathcal{E}_{CM} = \frac{m_g v^2}{2(1 + m_g/m)} \quad (1.33)$$

The velocity of the charged particle in the neutral frame hence writes:

$$v = \left[2\mathcal{E}_{CM} \left(\frac{1}{m_g} + \frac{1}{m} \right) \right]^{1/2} \quad (1.34)$$

And using Eq. (1.30),

$$v = \sigma n_g \left[2\mathcal{E}_{CM} \left(\frac{1}{m_g} + \frac{1}{m} \right) \right]^{1/2} \quad (1.35)$$

Two limiting cases can be of interest.

- When the impinging particle is an electron, the term $\frac{1}{m_g}$ in equation 1.34 is negligible, the velocity becomes $v = \left(\frac{2\mathcal{E}_{CM}}{m_e} \right)^{1/2}$ and the collision frequency:

$$v = \sigma n_g \left(\frac{2\mathcal{E}_{CM}}{m_e} \right)^{1/2}. \quad (1.36)$$

- When the impinging particle has the same mass as the neutral, $m = m_g$, $v = 2(\mathcal{E}_{CM}/m_g)^{1/2}$, and

$$v = 2\sigma n_g \left(\frac{\mathcal{E}_{CM}}{m_g} \right)^{1/2}. \quad (1.37)$$

1.2.4 Momentum transfer collision frequency

In order to better understand isotropic and backscattering collision processes, we propose here a simple explanation for the theoretical framework used in the works of the group of Phelps [91, 92]. More details about binary collisions can also be found in Lieberman and Lichtenberg (2005) [84]. In reality, the scattering angle of a particle colliding with a target particle depends on the impact parameter, and every angle does not have the same probability. This effect is taken into account by introducing the concept of different cross sections $I(v, \theta)$. The quantity

$$I(v, \theta) d\theta n_g v dt \quad (1.38)$$

is the probability for a particle to be scattered with an angle between θ and $\theta + d\theta$ in the time lapse dt against the particles of the gas of density n_g . Only one angular parameter θ is chosen because a binary collision system features a cylindrical symmetry. The cross section σ is the integral over all the scattering angles of the differential cross section.

$$\sigma(v) = 2\pi \int_0^\pi I(v, \theta) \sin \theta d\theta. \quad (1.39)$$

When a process is assumed to be isotropic, the differential cross section does not depend on the angle θ and is

$$I_{\text{isotropic}} = \frac{\sigma}{4\pi}. \quad (1.40)$$

For an elastic process, the kinetic energy of the fictitious particle in the Center of Mass Frame (CMF) is conserved and the momentum transfer in the direction of the initial velocity vector \mathbf{v} in the CMF is $(1 - \cos \theta)\mathbf{v}$. The *momentum transfer cross section* is therefore defined as

$$\sigma_p = 2\pi \int_0^\pi (1 - \cos \theta) I(v, \theta) \sin \theta d\theta. \quad (1.41)$$

For an isotropic process

$$\sigma_p = \sigma \quad (1.42)$$

since $\int_0^\pi \cos \theta \sin \theta d\theta = 0$. All the electron-neutral processes are assumed to be isotropic, such that for all of them, using σ_p or σ is equivalent. Due to charge

Gas	He	Ar	Kr	Xe
Atomic mass [amu]	4.003	39.95	83.8	131.3
Ionization potential [eV]	24.59	15.7	21.75	12.13
Relative polarizability	1.383	11.08	16.74	27.06

Table 1.1: Atomic masses and relative polarizabilities of the noble gases implemented in *LPPic*, from Radzig and Smirnov (1985) [94].

exchange mechanisms that are particularly important at low ion energy, the ion-atom (or ion-molecule) elastic interactions cannot be modeled with an isotropic cross section. The idea of Phelps [91] is to use a differential cross section

$$I = I_{\text{isotropic}} + I_{\text{BS}} \quad (1.43)$$

where

$$I_{\text{BS}} = \frac{\sigma_{\text{BS}} \delta(\theta - \pi)}{2\pi \sin \theta} \quad (1.44)$$

where δ is the delta Dirac function, and I_{BS} and σ_{BS} are the backscattering differential cross section and cross section respectively. σ_{BS} is just chosen to satisfy Eq. (1.39). At high ion energy, a charge exchange reaction is equivalent to a backscattering reaction, since the ion produced at very low velocity in the laboratory reference frame has just the velocity $-v$ in the CMF. Direct integration of Eq. (1.41) leads to the momentum cross section associated with a backscattering reaction

$$\sigma_{p,\text{BS}} = 2\sigma_{\text{BS}} \quad (1.45)$$

In PIC simulations, the cross sections used are the (real) reaction cross sections, while momentum transfer cross sections are usually implemented in fluid models. The relevant quantity for the momentum balance equations of fluid models is actually the *effective momentum transfer cross section* that includes both the elastic and the inelastic processes. As seen in Figs. 1.1 and 1.2, the elastic collisions dominate over all inelastic processes at electron temperatures below a few electron-volts.

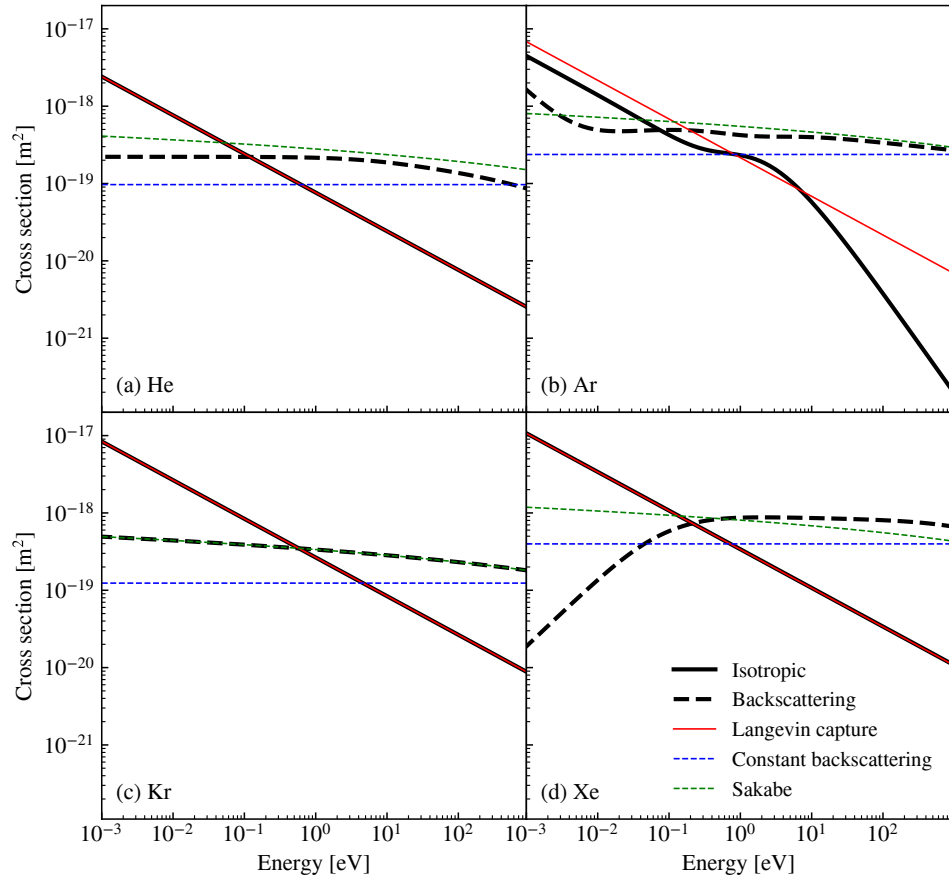


Figure 1.5: Ion-neutral collision cross sections for noble gases. The thick black line represent the values implemented in the *LPPic* simulation code. The solid lines represent estimations of the elastic scattering, and the dashed lines represent resonant charge exchange.

1.3 Introduction to ICP theory and simulation

1.3.1 Heating mechanism

A main driver of this work is the simulation of the PEGASES thruster. The PEGASES source used at LPP is an ICP source with a planar antenna. The planar coil is powered with a sinusoidal RF voltage and produces a magnetic field that can be estimated through Maxwell-Ampere's law (Eq. (1.9)). A sinusoidal electric field is in turn generated in the plasma, according to Faraday's law (Eq. (1.8)). The induced electric field vector is typically in a plane parallel to the planar coil. It accelerates the electrons that gain enough energy to produce ionization and sustain the discharge. The amplitude of the oscillatory electric field decreases with the distance x to the coil due to two factors

1. the magnetic field generated by a planar coil typically decreases as $1/x^3$ when the distance x becomes larger than the radius of the coil;
2. the electric field penetrates only through a typical distance δ_s called the skin depth that depends on the plasma conductivity. This length is also called London's length and is a characteristic of the plasma response to an electromagnetic perturbation [99]

$$\delta_s = c/\omega_{pe} = c \left(\frac{\epsilon_0 m_e}{n_e e^2} \right)^{1/2} \quad (1.46)$$

where c is the speed of light, and

$$\omega_{pe} = \left(\frac{n_e e^2}{\epsilon_0 m_e} \right)^{1/2} \quad (1.47)$$

is the electron plasma frequency. For an homogeneous plasma, the amplitude of the heating electric field satisfies

$$E \propto e^{-x/\delta_s} \quad (1.48)$$

The skin depth is 5.3 cm at 10^{16} m^{-3} of plasma density, and 5.3 mm for a plasma density of 10^{18} m^{-3} . Therefore, for the simulations of small ICP discharges of 3 cm at low plasma density, the geometrical decrease of the electromagnetic field is more important than the skin depth effect, whereas for the real system at high density and with large dimensions (≈ 10 cm), the skin depth effect is the main cause of the limitation of the induced electric field amplitude.

These considerations are very important for the electrostatic simulation of ICP because the shape of the induced electric field cannot be resolved in a self-consistent

manner. The only way to resolve it would be to use a solver for the full set of Maxwell's equations (Eqs. (1.6) to (1.9)), and not only a Poisson's equation solver.

The coupling between the electric circuit and the plasma is not investigated in depth here, the reader can refer to the book of P. Chabert and N. Braithwaite [27] for more details about concepts such as plasma impedance, matchboxes, or power coupling efficiency that are very important experimentally. The method implemented in *LPPic* uses an electric E_z field imposed in the z direction perpendicular to the simulation plane. In order to represent a joint effect of the geometrical decrease of the electromagnetic field produced by the coil, and the skin effect, the magnitude of E_z can vary with the distance x from the coil.

$$E_z = E_0 \max \left[0, \left(1 - \frac{\alpha x}{x_{\max}} \right) \right] \cos(\omega t) \quad (1.49)$$

where ω is the RF frequency, set to $2\pi \times 13.56$ MHz in all simulation conditions, x_{\max} is the distance at the end of the simulation domain (near the acceleration grid), and α sets the linear decrease of the heating electric field with distance. Three different values were tested for α :

- $\alpha = 0$: This corresponds to the situation where the heating electric field is uniform.
- $\alpha = 1$: The electric field reaches 0 right at the end of the simulation domain.
- $\alpha = 3$: The heating occurs only in one third of the simulation domain.

The amplitude of the electric field E_0 is updated at the end of each RF cycle to keep the total power absorbed by the plasma equal to a fixed parameter \mathcal{W}_{abs} . The aim is to reach

$$\mathcal{W}_{\text{abs}} = \frac{l_z \omega_{RF}}{2\pi} \int_t^{t + \frac{2\pi}{\omega_{RF}}} \iint J_z E_z dx dy dt \quad (1.50)$$

at steady-state. The simulation starts with a first estimate of E_0 provided as an input parameter, that should be roughly consistent with the initial plasma density imposed, in order to avoid a too violent behavior of the plasma during the first RF periods that can cause the simulation to crash. This effect can be particularly visible at low pressure and when the heating electric field is more localized. Adjusting the right initial condition can require a little bit of engineering, but once the steady-state is reached, the amplitude of the heating electric field does not vary anymore

and the state of the system does not depend on the initial condition.

$$E_0 = \frac{2\pi\mathcal{W}_{\text{abs}}}{l_z\omega_{RF}} \left(\int_t^{t+\frac{2\pi}{\omega_{RF}}} \iint J_z \max \left[0, \left(1 - \frac{\alpha x}{x_{\max}} \right) \right] \cos(\omega t) dx dy dt \right)^{-1} \quad (1.51)$$

While the heating electric field is in the z direction, the x and y components of the electric field are solved through the solution of Poisson's equation. The particles are free to move in the three directions, such that the electrons respond to the heating electric field and generate a current that can be monitored to keep the power as imposed by Eq. (1.50).

One should keep in mind that this method to model the inductive plasma does not accurately represent the local power balance, because the profile of the heating electric field is fixed *a priori*, but it does preserve the global power balance. Moreover, the instantaneous heating electric field should also vary along the y coordinate, and this effect was completely ignored here.

The configurations simulated in this work are represented in Fig. 1.6 where the RF antenna is schematically represented on the left. Fig. 1.6(a) and (d) correspond to the case $\alpha = 0$, Fig. 1.6(b), (e) and (h) correspond to the case $\alpha = 1$, and Fig. 1.6(c), (f), and (i) correspond to the case $\alpha = 3$.

The scheme can be subject to oscillations during the transient and over-shooting is observed. This can be fixed by adding a successive over relaxation coefficient r to the numerical method, such that the electric field is updated the following way:

$$E_{n+1} = rE_n + (1 - r)E_0 \quad (1.52)$$

where E_0 is defined by Eq. (1.51). We found a significantly smoother transient at low pressure by choosing for example $r = 2/3$, with no significant loss on the convergence time. When the electrons are well confined, either by a relatively high gas pressure or by an external magnetic field, r can be 0.

1.3.2 Fluid equations of the plasma transport

Plasma transport covers all the collective phenomena where electrons and ions move inside a discharge domain, and how they reach the discharge walls. In general, these phenomena can be described by a set of conservation equations, field equations (a subset of Maxwell's equations), and closure equations. The equations presented below are the fluid equations of the plasma, that come from the integration of the various moments of Boltzmann equation [8]. The *continuity equation*

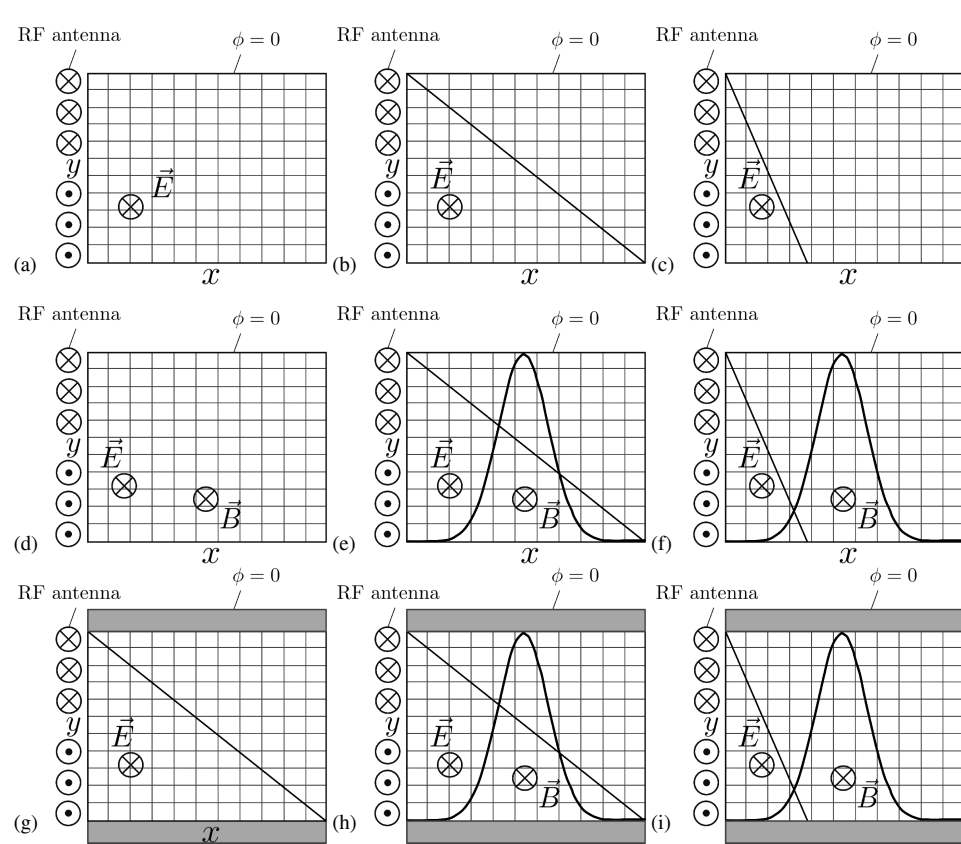


Figure 1.6: Sketches of the various ICP configurations investigated with the 2D PIC model.

for electrons and ions is

$$\partial_t n + \nabla \cdot n = S \quad (1.53)$$

where S represents the local particle source term (or loss term) due to collisions. Eq. (1.53) is valid for both electrons and ions, and can be used with the corresponding density and source terms. For a quasineutral plasma in usual LTP conditions, the source term is identical for electrons and ions and is only due to electron impact ionization. Therefore,

$$\partial_t n_i + \nabla \cdot \Gamma_i = \partial_t n_e + \nabla \cdot \Gamma_e = n_e v_{iz} \quad (1.54)$$

where v_{iz} is the electron impact ionization frequency. The momentum conservation equation contains all the force terms that drive the plasma motion.

$$m (\partial_t \mathbf{v} + \mathbf{v} \cdot \nabla \mathbf{v}) = q (\mathbf{E} + \mathbf{v} \times \mathbf{B}) - \frac{\nabla p}{n} - m \mathbf{v} \nu_m \quad (1.55)$$

where ν_m is the total momentum transfer collision frequency, and

$$p = n k_B T \quad (1.56)$$

is the pressure of the considered species. The loss of momentum due to collisions can be quite complicated to take into account. It is assumed that the plasma is weakly ionized, such that the frequency of charged species is much lower than the density of the neutral gas. Similarly to the PIC model, Coulomb collisions are neglected and only collisions with high density neutral species are taken into account. In general, the collision frequency depends on the energy, and thus the fluid velocity. However, for electrons, the thermal velocity is usually much higher than the fluid velocity, such that the collision frequency becomes a function of the local electron temperature and the neutral gas density. The situation is harder for ions because the fluid velocity can be higher than the thermal velocity. As described in Section 1.2.3, collision cross sections between ions and atoms are quite poorly characterized. However Langevin capture cross sections that describe the isotropic scattering of ions on neutral atoms are proportional to v^{-1} . An approximation that is often made in analytical models is to assume a constant collision cross section (typically 10^{-18} m^2 for argon) and to assume that the ion thermal velocity is the reference velocity for the computation of the total momentum transfer collision frequency.

In the quasistatic approximation, the magnetic field has only a DC component that is imposed by permanent magnets or a coil powered in DC, as it is the case in the PEGASES experiment. Combined with Poisson's equation for the electric field, this set of equations can already be enough to determine the plasma density

if an assumption is made on the electron temperature. The simplest assumption is the isothermal assumption where electrons and ions are assumed to be at a constant temperature, still with $T_e \gg T_i$. Another model that can be used but which is less spread in the community of LTP technologies is the *polytropic* model. This model consists in assuming a relationship between the density and the temperature under the form

$$Tn^{1-\gamma} = cst \quad (1.57)$$

where γ is called the polytropic coefficient. The polytropic law is associated with adiabatic processes for ideal monoatomic gases with three degrees of freedom, and has then the value of 5/3 [8]. The polytropic coefficient can also be used as an empirical coefficient that accounts for first order variations of the temperature inside a discharge due in particular to non-Maxwellian distribution functions.

An energy equation may also be added to the system, for instance to account more precisely for local heating phenomena. It can be written either in terms of total energy or internal energy only. We provide here the form given by P. Bellan, integrated from the Boltzmann equation [8]:

$$\frac{3}{2}\partial_t(nk_B T) + \frac{3}{2}\mathbf{v} \cdot \nabla(nk_B T) + \frac{5}{2}nk_B T \nabla \cdot \mathbf{v} = -\nabla \cdot \mathbf{Q} + v_m n \mathbf{v}^2 - \partial_t w|_c \quad (1.58)$$

where $\partial_t w|_c$ is the rate at which the species transfers its energy through collisions, and

$$\mathbf{Q} = \frac{m}{2n} \iiint (\mathbf{v} - \mathbf{u})^2 (\mathbf{v} - \mathbf{u}) f d^3 v \quad (1.59)$$

is the heat flux. The electron and ion heat fluxes are neglected in the models developed in this work but may be of high interest for future investigations.

1.3.3 Numerical parameters of the PIC simulation

The Debye length

$$\lambda_D = \left(\frac{\epsilon_0 k_B T}{ne^2} \right)^{1/2} \quad (1.60)$$

represents the typical screening distance between charged particles [31] and can be defined for each species. The electron Debye length has to be resolved to guarantee the stability and the accuracy of the simulation. For similar reasons, the time step is constraint by the plasma frequency (Eq. (1.47)). The conditions imposed on the time step and the cell size in plasma simulations using particles are the result of extensive numerical experiments [15, 66] and depend on various numerical choices

such as the particle weighting scheme, or physical parameters, such as the drift velocity. A bilinear weighting scheme is used in *LPPic*, and the commonly accepted criteria in the low-temperature plasma community are

$$\Delta x < \lambda_{De}/2 \quad (1.61)$$

$$\Delta t < 0.2/\omega_{pe} \quad (1.62)$$

where λ_{De} and ω_{pe} are the electron Debye length and electron plasma frequency respectively.

Another stability condition that is not exclusive to PIC simulation is the Courant – Friedrichs – Lewy (CFL) condition that imposes that the typical velocity is not such that particles would "jump" over one cell in a single time step.

$$v\Delta t < \Delta x \quad (1.63)$$

Particles have a velocity distribution function that is not bounded in velocity. The highest typical velocity in LTP is the electron thermal velocity v_{Te} (Eq. (1.10)), such that if the CFL condition has to be fulfilled approximately by a fraction α of the electron population, one can estimate a maximal velocity v_α for the CFL condition. For a Maxwellian distribution function defined by Eq. (1.23), the velocity v_α satisfies

$$\int_0^{v_\alpha} \left(\frac{m_e}{2\pi k_B T_e} \right)^{3/2} \exp \left[\frac{m_e v^2}{2\pi k_B T_e} \right] 4\pi v^2 dv = \alpha \quad (1.64)$$

which is also

$$\operatorname{erf} \left(\frac{v_\alpha}{\sqrt{2} v_{Te}} \right) - \left(\frac{2}{\pi} \right)^{1/2} \frac{v_\alpha}{v_{Te}} \exp \left[-\frac{1}{2} \left(\frac{v_\alpha}{v_{Te}} \right)^2 \right] = \alpha \quad (1.65)$$

where erf is the error function defined by

$$\operatorname{erf}(x) = \frac{2}{\sqrt{\pi}} \int_0^x \exp(-x^2) dx \quad (1.66)$$

One should typically aim for a ratio $v_\alpha/v_{Te} = 2.5$ which fulfills the CFL conditions for $\alpha = 90\%$ of the electrons. The CFL condition of interest for the PIC simulation is therefore

$$v_{Te} \Delta t < 0.4 \Delta x \quad (1.67)$$

1.3.4 First run example

We conclude this section by presenting the first 2D PIC simulation results of an ICP discharge. The numerical and physical parameters are inspired by the 1D benchmark of a helium Capacitively-Coupled Plasma (CCP) discharge published by Turner et al. [126]. The idea of this simulation case is to work towards a series of benchmarks for the 2D PIC simulation of LTP. The helium cross section set described in the previous section is the same as in the case of Turner et al. The numerical parameters of the simulation are summarized in Table 1.2. An excitation frequency of 13.56 MHz is retained because it is the standard frequency delivered by many experimental power supplies. The aim is not to reach exact experimental conditions but to have a simulation case that is clearly defined and whose numerical results can be verified independently by other groups. While plasma reactors for plasma processing can be quite well described by 1D models due to their aspect ratio that can be quite large, plasma thrusters usually have at least an intrinsically 2D geometry. We hence present here first results for a square simulation domain of 3×3 cm size. The absorbed power is 10 kW/m^3 , which is relatively low for laboratory plasmas, and yields a plasma density comprised between 10^{14} and 10^{15} m^{-3} . This low density allows to use a time step and cell sizes that are not too small, which reduces the computation time.

Gas heating and gas depletion phenomena are neglected and the neutral gas is assumed to be of uniform and constant density n_g and temperature T_g . We assume that the gas behaves as an ideal gas, such that the pressure in mTorr is provided as an input parameter:

$$n_g = \frac{0.133p \text{ [mTorr]}}{k_B T_g}. \quad (1.68)$$

The plasma is initialized with uniform densities of electrons and ions of 10^{14} m^{-3} . The super-particles representing electrons are distributed with a Maxwellian distribution function at 4.0 eV, while the ions are initialized with a Maxwellian distribution function at temperature 0.026 eV. All the new ions created by ionization are generated at the same temperature of 0.026 eV, which is approximately equal to the gas temperature (300 K). As illustrated in Fig. 1.7(a), the electrons first leave the plasma before being regenerated by ionization after approximately 0.5 μs . There are always slightly more ions than electrons in the discharge. Fig. 1.7(b) shows the mean kinetic energy of the electrons in the three directions. Since the electrons are accelerated by the heating RF electric field in the z direction, their kinetic energy is higher in the z direction. The kinetic energy of the electrons is transferred from the z direction to the x and y directions through collisions. The system is perfectly symmetrical with respect to x and y , so it can be verified that the mean kinetic energy has the same value along x and y directions. The discrepancy in kinetic

Physical parameters			
Discharge sizes	$l_x = l_y$	30	mm
Neutral pressure	p	30	mTorr
Neutral density	n_g	9.578×10^{20}	m^{-3}
Neutral temperature	T_g	0.026	eV
Frequency	f_{RF}	13.56	MHz
Power density	w	10.0	kW/m^3
Physical time of the simulation	$t_{\text{simulation}}$	$300/f_{RF} = 22.12$	μs
Averaging time	t_{average}	$3/f_{RF} = 0.2212$	μs
Initial conditions			
Plasma density	$n_e = n_i$	1×10^{14}	m^{-3}
Electron temperature	T_e [eV]	4.0	eV
Ion temperature	T_i [eV]	0.026	eV
Particles per cell	$N_{\text{part./cell}}$	100	
Heating electric field amplitude	E_0	1.0	kV/m
Numerical parameters			
Cell size	Δx	150	μm
Time step	Δt	$(2000f_{RF})^{-1} = 3.6873 \times 10^{-11}$	s
Steps to execute	$N_{\text{simulation}}$	600 000	
Steps to average	N_{average}	6 000	
Weighting factor	q_f	22 500	m^{-1}

Table 1.2: Main physical and numerical input parameters of the 2D PIC simulation.

Physical characteristics		
$n_{i\max} \times 10^{14}$	[m ⁻³]	6.21
$n_{e\max} \times 10^{14}$	[m ⁻³]	5.87
T _e [eV]		12.81
J _e	[A/m ²]	1.12
Numerical characteristics		
$\omega_{pe}\Delta t$	0.053	
$\lambda_D/\Delta x$	7	
v _e Δt	0.0085	
v _i Δt	1.4 × 10 ⁻⁵	
N _D	26 566	
N _P	19 760 461	

Table 1.3: Physical and numerical characteristics extracted from the results of the simulation.

energy between the heating direction and the others was observed in all simulation conditions, and the effect was more visible at low pressure. The amplitude of the heating electric field oscillates during the first RF cycles and converges to 543 V/m after 3 μs. The value of the heating electric field amplitude is updated every 2 000 time steps, while the number of particles and the mean kinetic energy are extracted every $N_{\text{average}} = 6\,000$ time steps. The oscillations that are visible in the curve of E_0 should be more visible in the curves showing the number of super particles if the sampling time was the same.

A few numerical parameters are shown in Table 1.3. The maximum ion density is 6.21×10^{14} m⁻³ while maximum electron density is 5.87×10^{14} m⁻³. N_P represents the number of super-particles (both ions and electrons) in memory at the end of the simulation. There are on average 494 particles per cell (both ions and electrons) at steady-state. The Debye length is 1.1 mm and the number of super-particles in a Debye square is N_D = 25 566.

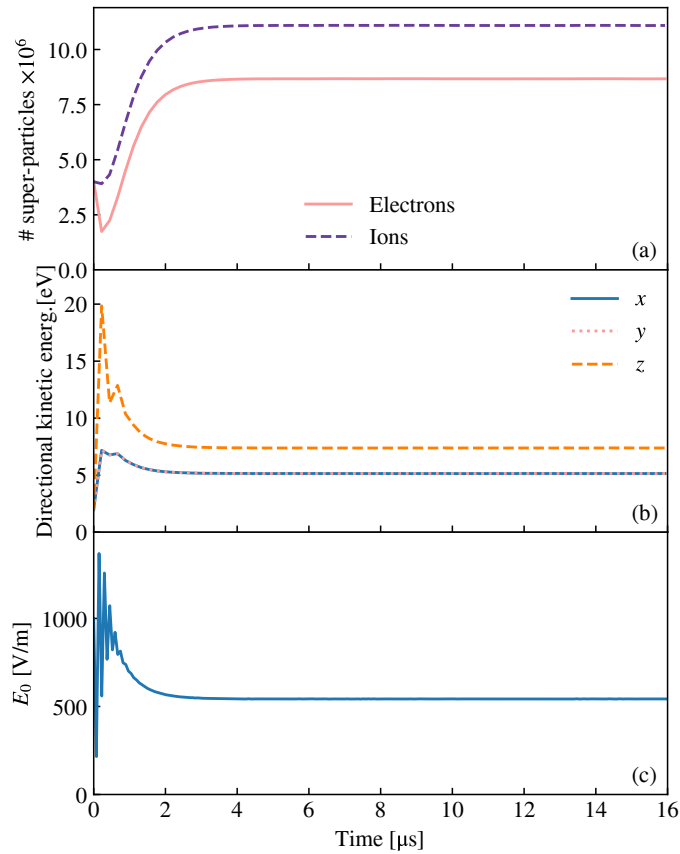


Figure 1.7: Temporal evolution of (a) the number of super-particles of electrons and ions (He^+), (b) the electron kinetic energy along each axis, and (c) the amplitude of the heating electric field (Eq. (1.51)).

1.4 Observation of the main features of a plasma discharge

Fig. 1.9 shows that both the electron and the ion densities decrease smoothly from the center of the discharge to the edges, and the electron density is always below the ion density. Fig. 1.8(c) shows the plasma potential (the walls are grounded to $\phi = 0$) spatial distribution. The plasma potential ϕ is positive, which means that the electrons are confined inside the plasma discharge while the ions are accelerated towards the edge. The plasma potential and the electron temperature (Fig. 1.8) are almost uniform in the middle of the discharge and decrease strongly near the edge, in a region that is called the *sheath*. While the electron and ion densities are almost equal in the center of the discharge, the electrons are repelled by the strong electric field in the sheath and their density becomes much lower than that of the ions. The electron temperature reaches 12.81 eV in the center of the discharge and drops to approximately 6 eV at the wall. Fig. 1.8(d) represents a map of the electron currents. The background color map represents the norm of the current and the arrows represent the direction of the current. The electrons flow from the center of the discharge to the walls, the current points inward due to the negative electron charge. The deceleration of the electrons in the sheath is quite visible.

A few tests were performed to assess the sensitivity of this run to several parameters:

- Case (1) the number of particles per cell ;
- Case (2) the reaction scheme used for inelastic collisions ;
- Case (3) the presence of inelastic collisions.

The electron and ion densities, the electron temperature, and the Electron Energy Probability Function (EEPF) for the 4 cases (including the reference Case (0) presented in the above paragraph) are shown together in Fig. 1.9(a-c). Fig. 1.9(a) and (b) show cuts at $y = 15$ mm of the plasma density and the electron temperature. For Case (1), the initial number of particles per cell was divided by 4. This increases the noise level visible in the ion density and in the electron temperature profiles. As expected, the tail of the EEPF is less well resolved as in the reference Case (0). More interestingly, the gradient in the electron temperature profile is sharper than in the reference case: it is higher in the center and lower at the walls. The mean kinetic energy of the particles and the density profiles are not much affected by the number of particles, but the local temperature is affected. Since we know that the local power balance is not necessarily well resolved in the heating scheme used in the electrostatic PIC simulation as a uniform heating electric field is assumed, this is not a major problem.

In the Case (2), we used a more recent version of the Biagi database for inelastic collisions between electrons and helium atoms [11], and the number of particles per cell was fixed to 100 when the simulation is initialized, as in case (0). This set of cross section includes 49 excitation states that are all detailed in Appendix A. This set of cross section was designed to model correctly the transport of the helium plasma. We remind that the excitation states are not tracked in the PIC model used here, and each excitation reaction is just treated as isotropic scattering with an energy loss for the electron that corresponds to an excitation energy of the atom. Fig. 1.9(a) shows that the ion and the electron densities are statistically the same in the Cases (0) and Case (2). The electron temperature profile is also very similar to the reference case. Even the EEPF shown in Fig. 1.9 are quite indistinguishable down to $10^{-6} \text{ eV}^{-3/2}$. Comparing the EEPF could be used as a method to validate a cross section set that is aggregated from multiple sources.

In order to better sense the role of inelastic collisions, we chose to present a simulation with no excitation reactions at all in Case (3), where the number of particles per cell was kept to 100 at initialization. This simulation case does not represent any possible realistic plasma but aims at pointing out the role of inelastic collisions in the transport equations. As illustrated in Fig. 1.9(a), the ion and electron density profiles have the same shape as in the Case (0) but the maximum density is approximately 30 % higher. This can be explained by the fact that less energy is dissipated in internal levels of the atom and a higher fraction of the injected power is converted into ionization of the helium atoms. Nevertheless, Fig. 1.9(b) shows that the electron temperature has locally almost exactly the same value as in the reference Case (0). To the first order, one can interpret this observation by saying that the electron temperature results from a balance between ionization and ion losses to the walls. These models will be discussed in Section 1.5. All the EEPF presented in Fig. 1.9(c) feature the same shape with a knee at approximately 40 eV. Even in Case (3), when no excitation levels are present, the knee is still visible. This indicates that the knee in the EEPF does not come from excitation reactions, but it should rather come here from wall absorption of electrons that have a kinetic energy higher than the plasma potential.

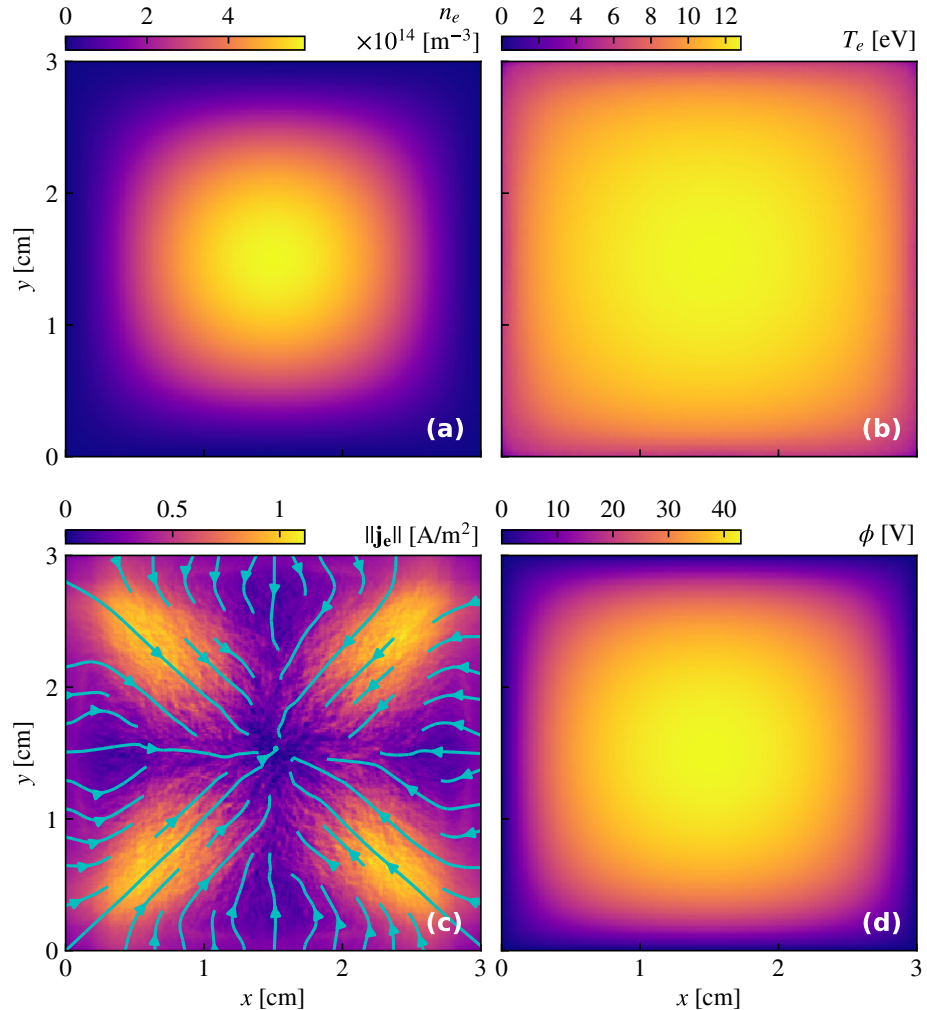


Figure 1.8: 2D plots of the electron density (a), the electron temperature (b), the electron current (c), and the plasma potential (d). The streamlines represent the line of electron currents in the simulation plane. All the data are averaged over the last 6 000 time steps of the simulation.

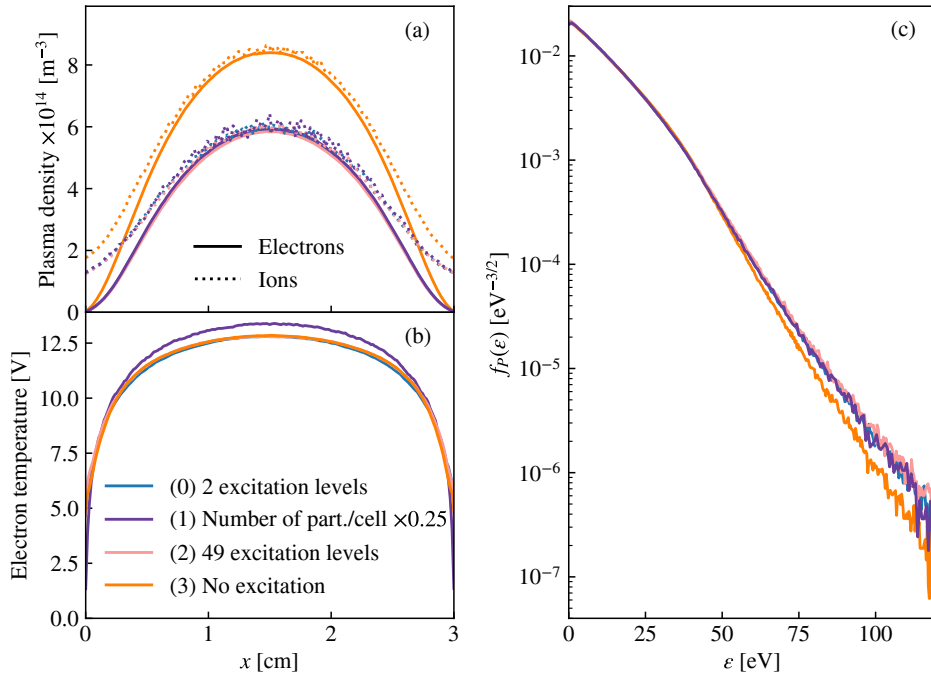


Figure 1.9: PIC simulation results of an ICP helium discharge with various models: refined model with 49 excitation levels, approximate model with 2 excitation levels, and a model with no inelastic collisions except ionization. (a) Electron and ion densities, (b) electron temperatures, (c) EEPF.

1.5 Sheath theory

We have mentioned in Section 1.4, a region called the *sheath* where the ion density becomes higher than the electron density. This is a very important characteristic of LTP. The sheath is a region that separates a quasineutral plasma region from the reactor walls. Quasineutral models are very convenient to handle but break in the sheath region. It is therefore very important to understand how the sheath behaves to feed quasineutral models with the right boundary conditions. Due to their low mass and high temperature, the electrons have typical velocities that are typically much greater than the ion velocity. If electron and ion densities would remain equal up to the walls, the flux of electrons would be much higher than the ion flux, and it would not be possible to sustain a discharge steady-state. At steady-state, in all the simulation conditions studied in this work, the total current leaving the plasma has to be zero in average. The primary characteristic of the sheath is therefore to feature a charge difference between electrons and ions, and subsequently a strong space charge electric field. We have seen in the previous section, for example in Fig. 1.8(b), that the sheath can also be associated to a significant temperature drop. In the next paragraph, we propose to describe a 1D model of a DC sheath with a temperature gradient described by a *polytropic* law.

Polytropic sheath model

In a 1D plasma, a polytropic coefficient can always be locally defined for the electrons by

$$\gamma = 1 + \frac{n_e dT_e}{T_e dn_e} \quad (1.69)$$

In some plasma conditions reached by the PIC simulations, this polytropic coefficient is notably constant throughout the discharge and the value of this constant can lead to a much more accurate description of the plasma properties than classically used isothermal models, while keeping the mathematical framework quite simple. In this case, the electron density and temperature are bounded by the relation

$$T_e/T_0 = (n/N)^{\gamma-1} \quad (1.70)$$

where N and T_0 are reference electron density and temperature respectively, for example taken at the discharge center. Note that the isothermal limit is recovered when $\gamma = 1$. In this paragraph, the role of the magnetic field is neglected.

In a collisionless plasma, the electron momentum conservation equation at steady-state is

$$en_e \nabla \phi - \nabla(k_B T_e n_e) = 0 \quad (1.71)$$

where ϕ is the plasma potential. Eq. (1.71) can be rearranged as

$$\frac{e\nabla\phi}{k_B T_e} = \frac{\nabla T_e}{T_e} + \frac{\nabla n_e}{n_e} \quad (1.72)$$

So

$$e\nabla\phi = \frac{\gamma k_B \nabla T_e}{\gamma - 1} \quad (1.73)$$

which can be integrated into

$$e\phi = \frac{\gamma}{\gamma - 1} k_B (T_e - T_0) \quad (1.74)$$

where it was assumed that the plasma potential is zero at the discharge center.

The electron density is hence:

$$n_e = N \left[1 + \frac{(\gamma - 1)e\phi}{\gamma k_B T_0} \right]^{\frac{1}{\gamma-1}} \quad (1.75)$$

Eqs. (1.70) and (1.71) provide two equations for the three unknown variables n_e , T_e , and ϕ . Additional equations are required in order to solve for the sheath properties. In the sheath, the plasma is not quasineutral so Poisson's equation (Eq. (1.12)) needs to be solved. The simplest way to describe the plasma sheath is to assume a collisionless model for the ions which reduces the ion momentum conservation equation (Eq. (1.55)) to the energy conservation for one ion:

$$\frac{1}{2} m_i (v_i^2 - v_0^2) = -e\phi \quad (1.76)$$

where v_0 is the ion velocity when they enter the sheath. Moreover, ionization is neglected in the sheath because the electron density is expected to be very low (the electrons are repelled by the space charge field). Therefore, the continuity equation has no source term:

$$\nabla \cdot (n_i v_i) = 0 \quad (1.77)$$

which reduces to flux conservation

$$n_i v_i = N v_0 \quad (1.78)$$

In Eq. (1.78), it was assumed that the plasma is quasineutral at the sheath edge:

$$n_e(0) = n_i(0) = N \quad (1.79)$$

The system of equations to be solved is then made of Eqs. (1.12), (1.70), (1.71), (1.76) and (1.78) for the five variables n_e , n_i , T_e , ϕ , and v_i .

The ion velocity v_i can immediately be eliminated by combining Eqs. (1.76) and (1.78). This leads to an expression of n_i as a function of the plasma potential

$$n_i = N \left(1 - \frac{2e\phi}{m_i v_0^2} \right)^{-1/2} \quad (1.80)$$

Replacing n_i , n_e , and T_e with Eqs. (1.74), (1.75) and (1.80) respectively in Poisson's equation leads to the second order differential equation for a 1D system

$$\frac{d^2\phi}{dx^2} = N \left[\left\{ 1 + \frac{(\gamma - 1)e\phi}{\gamma k_B T_0} \right\}^{\frac{1}{\gamma-1}} - \left(1 - \frac{2e\phi}{m_i v_0^2} \right)^{-1/2} \right] \quad (1.81)$$

Let us introduce the normalized potential $\chi = -\frac{e\phi}{k_B T_0}$, the Mach number $\mathcal{M} = v_0 \left(\frac{m_i}{k_B T_0} \right)^{1/2}$, and the normalized position $X = x/\lambda_{De}$, where λ_{De} is the electron Debye length defined by Eq. (1.60). Eq. (1.81) can then be expressed in the normalized form:

$$\chi'' = \left(1 + \frac{2\chi}{\mathcal{M}^2} \right)^{-1/2} - \left[1 - \frac{(\gamma - 1)\chi}{\gamma} \right]^{\frac{1}{\gamma-1}} \quad (1.82)$$

where the symbol $''$ represents the second derivative with respect to the normalized dimension X . After multiplying this equation by the first derivative of the normalized potential χ' the integration yields

$$\frac{\chi'^2 - \chi'(0)^2}{2} = \mathcal{M}^2 \left[\left(1 + \frac{2\chi}{\mathcal{M}^2} \right)^{1/2} - 1 \right] + \left[1 - \frac{(\gamma - 1)\chi}{\gamma} \right]^{\frac{\gamma}{\gamma-1}} - 1 \quad (1.83)$$

where $\chi'(0)$ is the normalized electric field at the sheath edge. In Eq. 1.83, the second term of the right-hand side (RHS) tends towards $e^{-\chi}$ when γ tends towards 1^+ , which is the classical exponential factor when the EEDF is assumed to be Maxwellian with a uniform temperature. In the isothermal electrons limit corresponding to $\gamma \Rightarrow 1^+$, Eq. (1.83) becomes:

$$\frac{\chi'^2 - \chi'(0)^2}{2} = \mathcal{M}^2 \left[\left(1 + \frac{2\chi}{\mathcal{M}^2} \right)^{1/2} - 1 \right] + e^{-\chi} - 1 \quad (1.84)$$

which is in agreement with classical isothermal sheath models [102].

This quantity has to be positive for all χ . Hence, a second order Taylor expansion in χ provides the relation

$$\mathcal{M}^2 > \gamma \quad (1.85)$$

which means that the ion must enter the polytropic sheath with a speed larger than the ion acoustic speed

$$u_0 > \gamma^{1/2} u_B ; \quad (1.86)$$

where

$$u_B = \left(\frac{k_B T_e}{m_i} \right)^{1/2} \quad (1.87)$$

is the Bohm speed.

We find again the more classical Bohm sheath criterion [102, 40] in the case where $\gamma = 1$. In the same way as for the isothermal Debye sheath, we will assume that the sheath criterion is saturated

$$\mathcal{M}^2 = \gamma \quad (1.88)$$

The potential drop ϕ_s in the sheath can then be obtained by equating electron and ion fluxes at the wall. The electron flux can be found by integrating a Maxwellian distribution function over half a sphere. This is called the thermal flux

$$\Gamma_e = \frac{1}{4} n_{e,wall} \left(\frac{8k_B T_{e,wall}}{\pi m_e} \right)^{1/2} \quad (1.89)$$

where the $n_{e,wall}$ and $T_{e,wall}$ are given by Eqs. (1.74) and (1.75) respectively. In this steady-state model, the ion flux is conserved through the sheath, which can be obtained by integrating Eq. (1.53) with no source term. Therefore,

$$\Gamma_i = N \left(\frac{k_B T_e}{m_i} \right)^{1/2} \quad (1.90)$$

The steady-state current equality condition

$$\Gamma_e = \Gamma_i \quad (1.91)$$

yields

$$\left[1 + \frac{(\gamma - 1)}{\gamma} \frac{e\phi_s}{k_B T_0} \right]^{\frac{2}{\gamma-1}} \left[1 - \frac{(\gamma - 1)}{\gamma} \frac{e\phi_s}{k_B T_0} \right] = \frac{4\gamma\pi m_e}{m_i} \quad (1.92)$$

This equation can be solved numerically to find the sheath drop as a function of the electron temperature at the sheath edge T_0 and the polytropic coefficient. A numerical fit was proposed by A. Tavant et al. for argon [119]

$$\frac{e\phi_s}{k_B T_0} \approx 0.70 + 4.1 \times \gamma^{-1.7} \quad (1.93)$$

In the limit where γ equals 1, Eq. (1.92) becomes

$$\frac{e\phi_s}{k_B T_0} = \frac{1}{2} \ln \left(\frac{m_i}{2\pi m_e} \right) \quad (1.94)$$

which is approximately 4.8 for argon. PIC simulation results have shown that γ was always between 1.2 and 1.8.

In summary, when an ion is created in the plasma bulk, it is accelerated to the sheath edge where it reaches the speed $\gamma^{1/2} u_B$. The potential drop that produces the ion acceleration is related to a decrease of the electron density. At the sheath edge, the plasma density is lower than at the discharge center and the space charge electric field becomes very strong.

The electron temperature drop in the sheath is often neglected in fluid models but can be crucial to account correctly for electron impact secondary electron emissions as shown by the work of Tavant et al. [118]. The temperature drop mainly comes from an EEDF effect: as the walls absorb high energy electrons, the EEDF is a concave function of the energy, which implies that mean electron energy decreases when the plasma potential decreases. This effect was investigated in details by Tavant et al. using 1D-3V PIC simulations [119].

1.6 Global models of a plasma discharge

Global models rely on volume-averaged balance equations for the particle densities and energy. The variables are typically the electron and ion densities at the discharge center, the electron temperature, the gas density, and in some cases the gas temperature. All the global models studied here assume two temperatures: one for the electrons, and one for the heavy species ($T_g = T_i$). The models are always quasineutral, such that we will assume in this section

$$n_e = n_i = n . \quad (1.95)$$

The set of equations here is applicable for a plasma with only one ion species, following for example the work of P. Chabert et al. [26]. More details about global models of thrusters operated with molecular gases (e.g. iodine) will be given in Chapter 5 and can also be found in Grondein et al. [59].

The particle balance equation is obtained by integrating the continuity equation (Eq. (1.54))

$$\iiint_V \partial_t n dV + \oint_S \Gamma_i \cdot dS = \iiint_V n v_{iz} dV \quad (1.96)$$

and illustrated in Fig. 1.10(a). Let N be the plasma density at the discharge center. The ion flux at the walls is normalized to the Bohm flux SNu_B through the h factor

defined by

$$h = \frac{\oint_S \Gamma_i \cdot d\mathbf{S}}{SNu_B} \quad (1.97)$$

We also introduce the normalized mean plasma density

$$\tilde{n} = \frac{1}{V} \iiint_V \frac{n}{N} dV \quad (1.98)$$

such that Eq. (1.96) becomes

$$\frac{dN}{dt} = n_g K_{iz} N - \frac{hSu_B}{V\tilde{n}} N \quad (1.99)$$

where we have substituted the collision frequency by its expression $K_{iz}n_g$, K_{iz} being the reaction rate factor provided for instance by Fig. 1.2 as a function of the electron temperature.

Low pressure global models often make the assumption of a Maxwellian Electron Velocity Distribution Function (EVDF). The equation for the internal energy of the electrons is an integral form of Eq. (1.59)

$$\partial_t \iiint_V \frac{3}{2} nk_B T_e dV = \mathcal{W}_{\text{abs}} - \mathcal{W}_{\text{loss}} \quad (1.100)$$

where \mathcal{W}_{abs} stands for the power absorbed by the plasma which is a control parameter, and $\mathcal{W}_{\text{loss}}$ aggregates all the volume and surface power losses

$$\mathcal{W}_{\text{loss}} = \iiint_V nv_{iz} e \mathcal{E}_{iz} \gamma_i + 3 \frac{m_e}{m_g} k_B (T_e - T_g) n_e v_e dV + \oint_S e \mathcal{E}_w \Gamma_i \cdot d\mathbf{S} \quad (1.101)$$

In Eq. (1.101),

$$\gamma_i = \frac{\mathcal{E}_{iz} + \sum K_{ex} \mathcal{E}_{ex} / K_{iz}}{\mathcal{E}_{iz}} \quad (1.102)$$

is the ratio between the energy losses of all electron-neutral inelastic collisions and the ionization energy. \mathcal{E}_w is the mean electron energy when they reach the wall. According to Chabert and Braithwaite [27],

$$\mathcal{E}_w = 2T_e [\text{eV}] + \Delta\phi \quad (1.103)$$

where $\Delta\phi$ represents the potential difference between the plasma and wall. The potential drop ϕ_s in the sheath is given by Eq. (1.94). The plasma potential drops in the pre-sheath region to accelerate the ions by approximately $T_e [\text{eV}] / 2$. One can therefore estimate

$$\phi_s < \Delta\phi < \phi_s + T_e [\text{eV}] / 2 \quad (1.104)$$

Since the isothermal model tends to slightly overestimate the sheath drop, it is reasonable to assume

$$\Delta\phi \approx \phi_s = \frac{T_e [\text{eV}]}{2} \ln \left(\frac{m_i}{2\pi m_e} \right) \quad (1.105)$$

Hence,

$$\mathcal{E}_w = T_e [\text{eV}] \left[2 + \frac{1}{2} \ln \left(\frac{m_i}{2\pi m_e} \right) \right] \quad (1.106)$$

The second term of the right-hand side (RHS) of Eq. (1.101) is the energy transferred from the electron population to the neutral gas through elastic collisions. Its expression is given by Liard et al. [83]. The ratio m_e/m_i is very small but since the elastic collision rate is much larger than the rate for inelastic collisions, the contribution of this term can be significant. At each collision, the electrons transfer some momentum to the neutral gas and lose a fraction of their energy. The expression $3\frac{m_e}{m_g}k_B(T_e - T_g)n_e v_e$ comes from an average over Maxwellian distribution functions.

The power balance equation is represented schematically in Fig. 1.10(b).

In PIC simulation, the background gas is fixed at a given pressure. Conversely, global models allow one to consider a gas balance equation. The discharge chamber is filled at a certain rate Q_0 (in Standard Cubic Centimeters per Minute (sccm) or particles per second). The gas leaves the discharge chamber with a thermal flux through an open surface S_g . The gas population is regenerated by the ions that reach the inner walls and depleted by electron impact ionization. Moreover, the gas density is assumed uniform here, which can be a strong assumption if the power becomes too high. Following [26], the gas balance equation writes

$$\frac{dn_g}{dt} = \frac{Q_0}{V} + h n u_B \frac{S}{V} - n n_g K_{iz} - \frac{1}{4} n_g \left(\frac{8k_B T_g}{\pi m_g} \right)^{1/2} \frac{S_g}{V} \quad (1.107)$$

The balance equation for the neutral gas density is illustrated in Fig. 1.10(c).

An additional equation for the gas temperature was included in former models [26, 83]. This last equation is subject to some approximations that are not the main focus of this work, so the gas heating phenomenon is not included here.

Global models can be very efficient for the modeling of a discharge because all the physics is reduced to a system of a few temporal equations. However it has a number of limitations because it depends on parameters that are not necessarily easy to estimate. First, the reaction rates rely on more or less direct experiments or some quantum chemistry simulations, for example through the R-matrix method[120] to compute the reaction cross sections. The cross sections are then integrated over a certain distribution function to yield the reaction rates. At higher pressure (typically greater than 100 mTorr for laboratory plasmas), the Boltzmann equation can be solved in the local approximation, for example with the Bolsig+ solver. At the range

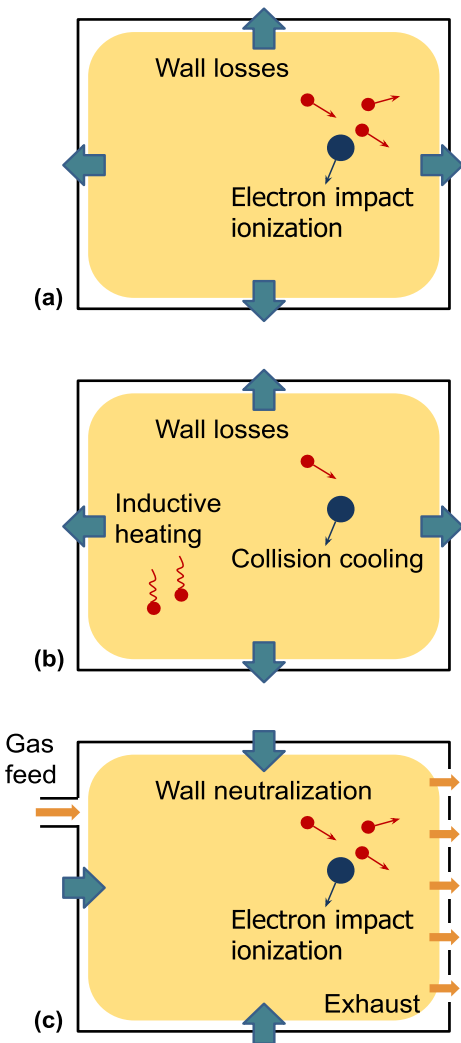


Figure 1.10: Illustration of the equations of the global models of a plasma discharge for (a) particles (electron or ion), (b) the electron temperature, and (c) the neutral gas.

of pressure of interest here, these methods do not apply. The easier assumption that was made in the global models used for this work is take Maxwellian electron distribution functions, although this is not the case in general (see Fig. 1.9(c)). A finer approach would be to feed the global model solver with distribution functions measured experimentally or found with PIC simulation. This would however break the predictive nature of the global model.

Second, some of the mechanisms at the walls are not very well known for most plasmas and wall material. Here, we have assumed that the ions that reach the walls are released in the reactor as neutral atoms. We have neglected secondary electron emission from the surface that can be the consequence of high energy electron or ion impacts. At the low electron temperature observed in the conditions simulated in this work, this effect should not be dominant but may depend on the wall material.

Finally, in the global model presented above, all the plasma transport processes are contained solely in the h factor that is not easy to estimate in general. More insights on the h factor can be provided by PIC simulation and fluid theory, as will be shown in the next Chapter.

Summary

This Chapter has mainly defined the framework in which the present work is performed. The concepts of sheath, quasineutrality, reaction rate, global models, that can vary in the literature, are defined. The results of a 2D PIC simulation of a helium ICP at low plasma density are presented and discussed. Finally, a 1D model of a polytropic sheath was proposed that provides a significant improvement to the more common isothermal model as it can account for the drop of electron temperature in the sheath.

Chapter 2

Isothermal transport models

Contents

2.1	Motivation	70
2.2	1D transport solutions	71
2.2.1	Differential equation for the plasma velocity	71
2.2.2	The problem of ion-neutral momentum transfer collision frequency	72
2.2.3	Boundary conditions and mathematical solution	74
2.2.4	The high D_a limit (low pressure <i>and</i> low magnetic field)	79
2.2.5	The low D_a limit (high pressure <i>or</i> high magnetic field)	79
2.3	2D transport modeling in the non-magnetized case	81
2.3.1	Equations of ion transport	81
2.3.2	The temperature equation	83
2.3.3	h factor in 2D	85
2.3.4	Comparison with 2D PIC simulation	88
2.3.5	Discussion	101

The transport equations of a quasineutral, isothermal plasma are solved in several conditions. We first treat the general 1D case for a wide range of pressure and magnetic field. We then focus on the non-magnetized 2D case. The 2D analytical solution is validated by PIC simulation and the general 2D h factor that represents the ion losses at the reactor walls is correctly predicted. The analytical solutions rely on the assumption of a spatially uniform collision

frequency between charged particles and neutrals. This assumption is also discussed.

2.1 Motivation

The h factor introduced in Chapter 1 is often known in the literature as the pre-sheath drop or edge-to-center density ratio and it characterizes the ratio between the plasma density in the center of a discharge and the density at the sheath edge, where the quasineutrality becomes violated. In the literature, this factor has been labeled h_L for 1D Cartesian geometries or h_R for 1D cylindrical geometries. In a 1D system, this definition coincides with the more general definition proposed in Eq. (1.97) for the 1D case. In 2D or 3D, the plasma density at the sheath edge is not necessarily the same everywhere.

We have proposed a generalization of Eq. (1.97) in a Review paper (Lucken et al., PSST 2018 [87]) and successfully implemented the corrected h factor in a simplified global model (Lucken et al. IEPC 2017)[86]).

Several authors provided theoretical estimates of the h factor in several pressure regimes, based on asymptotic solutions of the 1D transport equations of a quasineutral, isothermal plasma with no magnetic field [84, 27]. The low pressure regime was investigated in the early days of plasma physics, in the 1920s, by Tonks and Langmuir [124]. Ion and electron collisions are completely neglected in this case, and the h factor is independent of pressure. Schottky [107] studied the higher pressure regime where the ion thermal velocity dominates over the ion fluid velocity and found that the plasma density profile follows a Helmholtz equation

$$n'' = -\frac{v_{iz}}{D} n \quad (2.1)$$

where v_{iz} is the electron impact ionization frequency and D is a diffusion coefficient that is inversely proportional to the pressure. It can be shown that the h factor decreases in $1/p$ as well in this case. The intermediate pressure regime is of particular interest because ion collisions cannot be neglected in this regime but the typical velocity of the ions is driven by the mean fluid velocity and not by the thermal velocity of the ions. V. Godyak successfully described this transport regime and found that the h factor should be proportional to $p^{-1/2}$ [54]. The effect of neutral gas depletion in this intermediate transport regime was studied by J.-L. Raimbault et al. [97]. Lafleur and Chabert [79] confirmed by PIC simulation the validity of heuristic models over the entire pressure range for weakly-ionized 1D plasmas.

All these theories are some limit cases of the *ambipolar* 1D transport of the plasma. In the next paragraph, we introduce the *ambipolar* transport of an isothermal plasma with one ion species, in a quite general context.

2.2 1D transport solutions

2.2.1 Differential equation for the plasma velocity

One of the fundamental assumption of ambipolar transport is the plasma neutrality

$$n_e = n_i = n \quad (2.2)$$

It is assumed that the plasma properties only depend on the x direction, and that the magnetic field $\mathbf{B} = B\mathbf{e}_z$ is uniform and along z . Both electrons and ions can be magnetized, and can potentially drift in the y direction.

The continuity equation (Eq. (1.54)) is in 1D

$$(nv_{ix})' = (nv_{ex})' = nv_{iz} \quad (2.3)$$

the prime ' denotes the derivative with respect to x . Eq. (2.3) says that the electric current $en(v_i - v_e)$ is constant. We further assume that no current is drawn at the discharge center. By symmetry, electron and ion fluid velocities are equal to 0 at the discharge center. It follows then that

$$nv_i = nv_e \quad (2.4)$$

everywhere. The fact that $v_{ex} = v_{ix} = v_x$ is called the *ambipolarity* condition, and it is a simple consequence of quasineutrality in 1D.

The projections of Eq. (1.55) on the x and y axis with constant electron and ion temperatures are respectively

$$-k_B T_e \frac{n'}{n} - eE - ev_{ey} B - m_e v_e v_x = 0 \quad (2.5)$$

$$ev_x B - m_e v_e v_{ey} = 0 \quad (2.6)$$

for the electrons, and

$$-k_B T_i \frac{n'}{n} + eE + ev_{iy} B - m_i v_{i,tot} v = m_i v_x v'_x \quad (2.7)$$

$$-ev_x B - m_i v_{i,tot} v_{iy} = 0 \quad (2.8)$$

for the ions. In Eqs. (2.7) and (2.8), $v_{i,tot}$ is the total momentum loss term for the ion population. This term includes momentum transfer due to elastic collisions (both isotropic and backscattering) with the neutral atoms, and the inertia of newly created ions, produced by electron impact ionization [27]:

$$v_{i,tot} = v_i + v_{iz} \quad (2.9)$$

The y component of electron and ion velocities can be eliminated to yield

$$-k_B T_e \frac{n'}{n} - eE - m_e v_e (1 + \eta_e^2) v = 0 \quad (2.10)$$

and

$$-k_B T_i \frac{n'}{n} + eE - m_i v_{i,tot} (1 + \eta_i^2) v = m_i v v' \quad (2.11)$$

where we have replaced v_x by v since it is now the only velocity variable, and where

$$\eta_e = \frac{\omega_{ce}}{v_e} = \frac{eB}{m_e v_e} \quad (2.12)$$

and

$$\eta_i = \frac{\omega_{ci}}{v_{i,tot}} = \frac{eB}{m_i v_{i,tot}} \quad (2.13)$$

are the Hall parameters of electrons and ions respectively. By introducing the Bohm speed

$$u_B = \left[\frac{k_B(T_e + T_i)}{m_i} \right]^{1/2} \quad (2.14)$$

Eqs. (2.10) and (2.11) can be summed up to eliminate the electric field,

$$-\frac{n'}{n} - \frac{v}{D_a} = \frac{v v'}{u_B^2} \quad (2.15)$$

where

$$D_a = \frac{k_B(T_e + T_i)}{m_e v_e (1 + \eta_e^2) + m_i v_{i,tot} (1 + \eta_i^2)} \quad (2.16)$$

is a general *ambipolar diffusion* coefficient. This equation is combined with the continuity equation $(nv)' = nv_{iz}$ to yield

$$\left(1 - \frac{v^2}{u_B^2} \right) v' = v_{iz} + \frac{v^2}{D_a} \quad (2.17)$$

2.2.2 The problem of ion-neutral momentum transfer collision frequency

The integration of Eq. (2.17) is possible when the ambipolar diffusion coefficient is assumed constant. If the magnetic field is uniform, the only question is on the collision frequencies which are given by Eq. (1.25). We will assume that the gas density is uniform which is a reasonable approximation for weakly ionized plasmas. The rate for momentum transfer between electrons and neutrals is a function of

the electron temperature, which is assumed uniform. For the momentum transfer between ions and neutral atoms, the rate depends on the cross section, which is almost constant within the range of energy considered (typically 0.03 - 0.3 eV), and on the typical velocity of the ions. The latter quantity should in general depend on the plasma fluid velocity v . By assuming that the neutral atoms are at rest,

$$v_i \approx n_g \sigma_i \langle \|\mathbf{v}_i\| \rangle \quad (2.18)$$

Computing the mean velocity for a Maxwellian distribution function shifted by a drift velocity \mathbf{v}_0

$$f(\mathbf{v}) = n \left(\frac{m}{2\pi k_B T} \right)^{3/2} \exp \left[-\frac{m(\mathbf{v} - \mathbf{v}_0)^2}{2k_B T} \right] \quad (2.19)$$

is thus useful for the accurate modeling of ion collisions in fluid simulations. The integral is

$$\langle \|\mathbf{v}\| \rangle = \left(\frac{m}{2\pi k_B T} \right)^{3/2} \iiint \|\mathbf{v}\| \exp \left[-\frac{m(\mathbf{v} - \mathbf{v}_0)^2}{2k_B T} \right] d^3 v. \quad (2.20)$$

Assuming that \mathbf{v}_0 is along the z axis of spherical coordinates,

$$\langle \|\mathbf{v}\| \rangle = \frac{1}{v_T^3 \sqrt{2\pi}} \int_0^{+\infty} \int_0^\pi v^3 \exp \left[-\frac{v^2 + v_0^2 - 2vv_0 \cos \theta}{2v_T^2} \right] \sin \theta d\theta dv. \quad (2.21)$$

where $v_0 = \|\mathbf{v}_0\|$ and $v = \|\mathbf{v}\|$. By introducing the normalized velocities $u = v/v_T$ and $u_0 = v_0/v_T$,

$$\langle \|\mathbf{v}\| \rangle = \frac{v_T}{\sqrt{2\pi}} \int_0^{+\infty} \int_0^\pi u^3 \exp \left[-\frac{u^2 + u_0^2 - 2uu_0 \cos \theta}{2} \right] \sin \theta d\theta du. \quad (2.22)$$

Since

$$\int_0^\pi e^{uu_0 \cos \theta} \sin \theta d\theta = \frac{e^{uu_0} - e^{-uu_0}}{uu_0}, \quad (2.23)$$

$$\langle \|\mathbf{v}\| \rangle = \frac{v_T e^{-u_0^2/2}}{u_0 \sqrt{2\pi}} \int_0^{+\infty} u^2 e^{-u^2/2} (e^{uu_0} - e^{-uu_0}) du. \quad (2.24)$$

We find

$$\langle \|\mathbf{v}\| \rangle = v_T \left[\frac{1 + u_0^2}{u_0} \operatorname{erf} \left(\frac{u_0}{\sqrt{2}} \right) + \left(\frac{2}{\pi} \right)^{1/2} e^{-u_0^2/2} \right] \quad (2.25)$$

which satisfies the limits

$$\langle \|\mathbf{v}\| \rangle \approx \left(\frac{8}{\pi} \right)^{1/2} v_T \quad \text{when } u_0 \ll 1, \quad (2.26)$$

$$\langle \|\mathbf{v}\| \rangle \approx v_0 \quad \text{when } u_0 \gg 1. \quad (2.27)$$

The gas velocity was neglected here. The derivation could also be done by integrating over a given gas velocity distribution function, for example a Maxwellian distribution function at temperature T_g .

2.2.3 Boundary conditions and mathematical solution

In order to make analytical derivations, we now assume a constant ambipolar diffusion coefficient D_a and that v_i is uniform. Eq. (2.17) has separate variables

$$\frac{(1 - v^2/u_B^2)dv}{v_{iz} + v^2/D_a} = dx \quad (2.28)$$

and can be integrated into

$$\left(1 + \frac{v_{iz} D_a}{u_B^2} \right) \arctan \left[\frac{v}{(v_{iz} D_a)^{1/2}} \right] - \frac{(v_{iz} D_a)^{1/2}}{u_B^2} v = \left(\frac{v_{iz}}{D_a} \right)^{1/2} x \quad (2.29)$$

This equation can be inverted numerically to yield a plasma velocity profile $v(x)$. The plasma density is also retrieved by arranging Eqs. (2.15) and (2.17):

$$\frac{n'}{n} = -\frac{v}{u_B^2 - v^2} \left(\frac{u_B^2}{D_a} + v_{iz} \right) \quad (2.30)$$

Under integral form

$$n(x) = N \exp \left[- \int_0^x \frac{v(X)}{u_B^2 - v(X)^2} \left(\frac{u_B^2}{D_a} + v_{iz} \right) dX \right] \quad (2.31)$$

$$= N \exp \left[- \left(1 + \frac{v_{iz} D_a}{u_B^2} \right) \int_0^{v(x)} \frac{\zeta d\zeta}{v_{iz} D_a + \zeta^2} \right] \quad (2.32)$$

This integral is

$$n(x) = N \left(1 + \frac{v(x)^2}{v_{iz} D_a} \right)^{-\frac{1}{2} \left(1 + \frac{v_{iz} D_a}{u_B^2} \right)} \quad (2.33)$$

To be consistent with the isothermal approximation, the polytropic coefficient has to be equal to 1, such that the sheath criterion applicable here is the simple Bohm criterion $v = u_B$. If the sheath thickness is neglected, Eq. (2.29) becomes at the sheath edge defined by $x = l/2$

$$f \left(\frac{u_B}{(v_{iz} D_a)^{1/2}} \right) = \frac{u_B l}{2 D_a} \quad (2.34)$$

where the function f is defined by

$$f(x) = \left(x + \frac{1}{x} \right) \arctan(x) - 1 \quad (2.35)$$

The graph of f is provided in Appendix C. Eq. (2.34) can be seen as the equation for the electron temperature, which will play the role of an eigen value of the system. f has the following asymptotes

$$f(x) \underset{x \rightarrow 0}{\sim} \frac{2}{3} x^2 + \mathcal{O}(x^4) \quad (2.36)$$

$$f(x) \underset{x \rightarrow +\infty}{\sim} \frac{\pi}{2} x - 2 + \mathcal{O}(x^{-1}) \quad (2.37)$$

The inverse function f^{-1} therefore has the following asymptotic developments

$$f^{-1}(x) \underset{x \rightarrow 0}{\sim} \left(\frac{3}{2} x \right)^{1/2} + \mathcal{O}(x^{3/2}) \quad (2.38)$$

$$f^{-1}(x) \underset{x \rightarrow +\infty}{\sim} \frac{2}{\pi} (x + 2) + \mathcal{O}(x^{-1}) \quad (2.39)$$

and is plotted in Fig. 2.1(a) in logarithmic scales. The two asymptotic limits can provide the following approximate equation

$$f^{-1}(x) \approx \left[\frac{4}{\pi^2} x^2 + \frac{3}{2} x \right]^{1/2} \quad (2.40)$$

that preserves the first term of each asymptotic development. The formula provided by Eq. (2.40) approximates the numerical solution shown in Fig. 2.1(a) with a relative error of only 0.77% in the interval $[10^{-3}, 10^4]$. Similarly, estimating Eq. (2.33) at the sheath edge provides an estimate of the h factor in 1D

$$h = \left(1 + \frac{u_B^2}{v_{iz} D_a} \right)^{-\frac{1}{2} \left(1 + \frac{v_{iz} D_a}{u_B^2} \right)} \quad (2.41)$$

where $\frac{u_B^2}{v_{iz} D_a}$ is given by Eq. (2.34). The function

$$g(x) = \left(1 + \frac{1}{x}\right)^{-\frac{1}{2}(1+x)} \quad (2.42)$$

has the following asymptotes

$$g(x) \underset{x \rightarrow 0}{\sim} x^{1/2} + \mathcal{O}(x^{3/2} \ln(x)) \quad (2.43)$$

$$g(x) \underset{x \rightarrow +\infty}{\sim} e^{-1/2} + \mathcal{O}(x^{-1}) \quad (2.44)$$

Using the function

$$F : x \rightarrow g\left(\left[f^{-1}(x)\right]^{-2}\right) \quad (2.45)$$

the h parameter is

$$h = F\left(\frac{u_B l}{2D_a}\right) \quad (2.46)$$

The function F has the limits

$$F(x) \underset{x \rightarrow 0}{\sim} e^{-1/2} \quad (2.47)$$

$$F(x) \underset{x \rightarrow +\infty}{\sim} \frac{\pi}{2x} \quad (2.48)$$

F is very well approximated by

$$F(x) \approx \left[\exp(1) + 2x + \left(\frac{2x}{\pi}\right)^2\right]^{-1/2} \quad (2.49)$$

with a relative error of less than 1.3 % in the interval $[10^{-3}, 10^4]$. The function F is plotted in Fig. 2.1(b) together with its asymptotes.

This implies for the h factor that

$$h \approx e^{-1/2} \quad \text{when } \frac{u_B l}{2D_a} \ll 1 \quad (2.50)$$

$$h \approx \frac{\pi D_a}{u_B l} \quad \text{when } \frac{u_B l}{2D_a} \gg 1 \quad (2.51)$$

and

$$h \approx \left[\exp(1) + \frac{u_B l}{D_a} + \left(\frac{u_B l}{\pi D_a}\right)^2\right]^{-1/2} \quad (2.52)$$

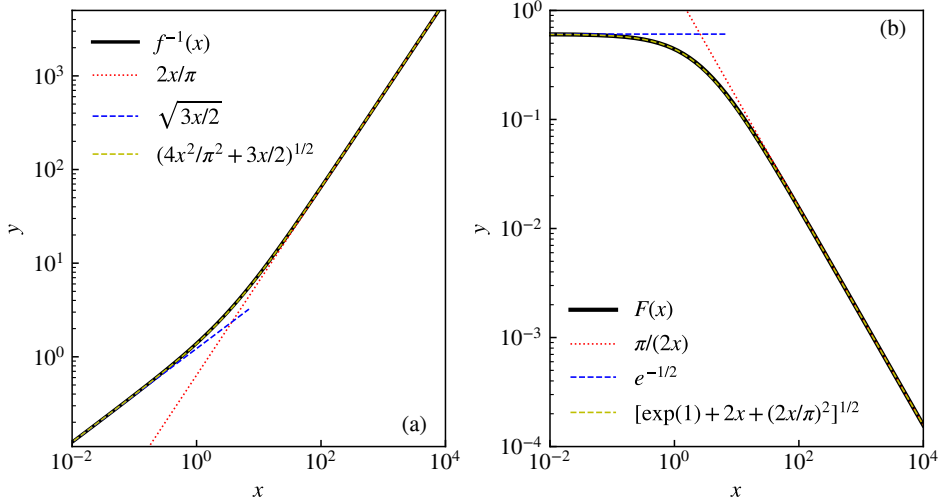


Figure 2.1: Graphs of the mathematical solutions of the quasineutral transport model with the asymptotes and the approximate formulas.

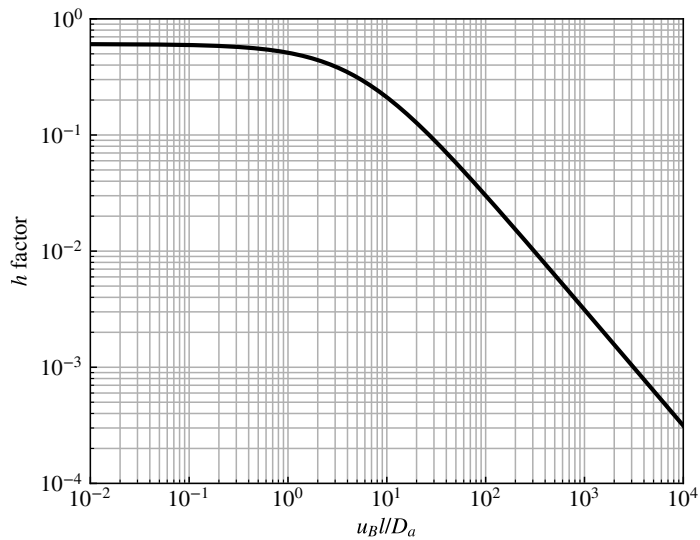


Figure 2.2: Graphs of the numerical solution for the h factor as a function of $u_B l / D_a$.

The mean normalized density profile

$$\tilde{n} = \frac{2}{l} \int_0^{l/2} n(x) dx \quad (2.53)$$

also has a simple general expression. Integrating the 1D continuity equation $(nv)' = nv_{iz}$ between the center and the edge gives

$$hu_B = v_{iz}\tilde{n}l/2 \quad (2.54)$$

which is of course equivalent to the particle balance used in global models (see Eq. (1.99)) and yields

$$\tilde{n} = \frac{2hu_B}{lv_{iz}} \quad (2.55)$$

The numerical solution of h is shown in Fig. 2.2. We would like to emphasize the fact that Eq. (2.52) includes the electron and ion collisions, ion temperature, and the magnetic field effects through the general ambipolar diffusion coefficient D_a given by Eq. (2.16). Since the h factor is sometimes difficult to measure directly, knowing a general expression between the ambipolar diffusion coefficient and the h factor can be very useful. This expression can also be applied to turbulent transport regimes, provided that we assume an instability-enhanced diffusion coefficient, as will be seen in Chapter 3. This expression is consistent with more classical heuristic formulas as the ones given by Chabert et al. [27] that incorporates in particular the intermediate pressure regime studied by Godyak [54]

$$h = h_0 = 0.86 \left[3 + 0.5 \frac{l}{\lambda_i} + 0.2 \frac{T_i}{T_e} \left(\frac{l}{\lambda_i} \right)^2 \right]^{-1/2}. \quad (2.56)$$

where λ_i is the ion mean free path. The second term of Eq. (2.56) accounts for an ion collision frequency that incorporates the ion fluid velocity, as it was suggested with Eq. (2.25). Few direct measurements of the h factor exist. To the knowledge of the author, only Kim et al. [70] provided some experimental values of the h factor in argon ICP discharges for pressures between 3 and 30 mTorr. The experimental values were in good agreement with the classical models. Eq. (2.56) was also validated using 1D PIC simulations of ICP and CCP discharges by T. Lafleur. [79]. The main difference between the models described above and the classical models is that no assumption was made on any particular form of the ambipolar diffusion coefficient. All the terms of Eq. (2.16) were retained. In particular, D_a depends on the ionization frequency at low pressure, which makes comparison with other models not so straightforward.

We now investigate two limit cases: $D_a/(u_B l) \gg 1$ and $D_a/(u_B l) \ll 1$

2.2.4 The high D_a limit (low pressure and low magnetic field)

The low pressure non-magnetized limit is slightly intricate because the ambipolar diffusion coefficient depends on the electron impact ionization frequency through $\nu_{i,tot}$ (Eq. (2.9)). By neglecting ion magnetization, the ambipolar coefficient is written

$$D_a = \frac{u_B^2}{\nu_m + \nu_{iz}} \quad (2.57)$$

where ν_m accounts for both ion and electron transport processes

$$\nu_m = \nu_i + \frac{m_e}{m_i} \nu_e (1 + \eta_e^2) \quad (2.58)$$

Instead of treating D_a as a parameter, Eqs. (2.34) and (2.57) can be seen as two equations for the two variables ν_{iz} and D_a , that can be re-arranged into

$$\frac{\nu_m D_a}{u_B^2} f \left(\left[1 - \frac{\nu_m D_a}{u_B^2} \right]^{-1/2} \right) = \frac{l \nu_m}{2 u_B} \quad (2.59)$$

At very low pressure, the *collisionless ambipolar diffusion coefficient* involves $f(1) = \pi/2 - 1$ and is

$$D_a = \frac{l u_B}{\pi - 2}. \quad (2.60)$$

This expression is quite interesting because it gives a diffusion coefficient that represents only the inertia of the newly created ions that are instantly coupled to the electrons through the ambipolar electric field. The diffusion coefficient is quite large at low pressure such that the second term of the left-hand side (LHS) in Eq. (2.15) is rather small, but not negligible. Since we also have $D_a = u_B^2 / \nu_{iz}$ in this low pressure regime, we find a very simple equation for the electron temperature

$$\nu_{iz} = (\pi - 2) u_B / l \quad (2.61)$$

In this regime, Eq. (2.41) yields

$$h = 0.5 \quad (2.62)$$

which is consistent with the low pressure limit of Eq. (2.56).

2.2.5 The low D_a limit (high pressure or high magnetic field)

At high pressure ($l \nu_m / u_B \gg 1$), Eq. (2.59) yields

$$D_a = u_B^2 / \nu_m \quad (2.63)$$

This is consistent with classical non-magnetized diffusion coefficients in the high pressure case [84], where $T_i \ll T_e$ and $v_i = (8/\pi)^{1/2} v_{Ti}/\lambda_i$

$$D_a = (\pi/8)^{1/2} u_B \lambda_i (T_e/T_i)^{1/2} \quad (2.64)$$

Finally, the low D_a limit provides an interesting behavior at the sheath edge because the electric field has a finite value in $1/D_a$. If $v_{iz} D_a / u_B^2 \ll 1$, Eq. (2.29) yields

$$v = (v_{iz} D_a)^{1/2} \tan \left(\frac{v_{iz}^{1/2}}{D_a^{1/2}} x \right) = -D_a \frac{n'}{n} \quad (2.65)$$

Therefore,

$$n = N \cos \left(\frac{v_{iz}^{1/2}}{D_a^{1/2}} x \right) \quad (2.66)$$

so the density n is the solution of a Helmholtz equation. Moreover, the electron temperature equation Eq. (2.34) provides the boundary condition

$$v_{iz} = \pi^2 D_a / l^2 . \quad (2.67)$$

which is equivalent to the so-called *Schottky boundary condition* that states that the plasma density drops to zero at the wall. In this case,

$$v' = \frac{v_{iz}}{\cos^2 \left(\frac{v_{iz}^{1/2}}{D_a^{1/2}} x \right)} = \frac{v^2 / D_a}{\sin^2 \left(\frac{v_{iz}^{1/2}}{D_a^{1/2}} x \right)} \quad (2.68)$$

So at the sheath edge ($v = u_B$), the plasma acceleration is

$$v'_s = u_B^2 / D_a \quad (2.69)$$

Hence, Eqs. (2.10) and (2.11) taken at the sheath edge provide a system of equations for the electric field E_s and the density gradient length $\Lambda_s = -n/n'|_s$ at the sheath edge

$$k_B T_e \Lambda_s^{-1} - e E_s - m_e v_e (1 + \eta_e^2) u_B = 0 \quad (2.70)$$

$$k_B T_i \Lambda_s^{-1} + e E_s - m_i v_{i,tot} (1 + \eta_i^2) u_B = m_i u_B^3 / D_a \quad (2.71)$$

This system leads to

$$\Lambda_s = \frac{D_a}{2 u_B} \quad (2.72)$$

and

$$E_s = \frac{m_i u_B^3}{e D_a} \left(1 + \left[1 + \frac{m_e v_e (1 + \eta_e^2)}{m_i v_i (1 + \eta_i^2)} \right]^{-1} - \frac{2 T_i}{T_e + T_i} \right) \quad (2.73)$$

The second term of this expression is equal to 1 when the transport is limited by the ions, as it is usually the case in non-magnetized plasmas, and is small when the transport is limited by the electrons, as in a strongly magnetized plasma for example. The third term is just a correction related to the ion temperature and can be neglected in most cases.

$$E_s = \begin{cases} 2m_i u_B^3 / (e D_a) & \text{at high pressure} \\ m_i u_B^3 / (e D_a) & \text{at high magnetic field} \end{cases} \quad (2.74)$$

2.3 2D transport modeling in the non-magnetized case

In this section, we first go on with the analytical description of the quasineutral isothermal plasma transport, but now in a 2D Cartesian geometry in a non magnetized case. The electron collisions are usually negligible in this case so they will be neglected. The plasma is bounded by walls located at $x = \pm l_x/2$ and $y = \pm l_y/2$. The analysis is quite analogous to the work performed by Sternberg and Godyak [115] in cylindrical coordinates but with several validations and improvements enabled by the use of the *LPPic* code.

2.3.1 Equations of ion transport

The electron momentum conservation is just the Boltzmann equation

$$-k_B T_e \nabla n / n - e \mathbf{E} = 0 \quad (2.75)$$

It is important to note that the electron fluid velocity does not appear in this equation. The ion momentum conservation equation is projected along both x and y axis

$$m_i (v_x \partial_x + v_y \partial_y) v_x = e E_x - k_B T_i \partial_x n / n - m_i (v_i + v_{iz}) v_x \quad (2.76)$$

$$m_i (v_x \partial_x + v_y \partial_y) v_y = e E_y - k_B T_i \partial_y n / n - m_i (v_i + v_{iz}) v_y \quad (2.77)$$

where \mathbf{v} is now the *fluid velocity of the ions*. Combined with the electron momentum equation, this leads to

$$(v_x \partial_x + v_y \partial_y) v_x / u_B^2 = -\partial_x n / n - v_x / D_a \quad (2.78)$$

$$(v_x \partial_x + v_y \partial_y) v_y / u_B^2 = -\partial_y n / n - v_y / D_a \quad (2.79)$$

where the ambipolar diffusion coefficient D_a is here $u_B^2 / (v_i + v_{iz})$. Moreover, the 2D ion continuity equation is

$$\partial_x (n v_x) + \partial_y (n v_y) = v_{iz} n \quad (2.80)$$

The plasma is not ambipolar in this case and we do not need to use the electron continuity equation. Eqs. (2.78) to (2.80) form a set of 3 first order partial differential equation (PDE) for the 3 unknown variables v_x , v_y , and n . The boundary condition is fixed by the Bohm criterion. By neglecting the sheath thickness, we also assume that the ions are always accelerated perpendicularly to the walls, such that

$$\mathbf{v} \left(x = \pm \frac{l_x}{2}, y = 0 \right) = \begin{pmatrix} \pm u_B \\ 0 \end{pmatrix} \quad (2.81)$$

$$\mathbf{v} \left(x = 0, y = \pm \frac{l_y}{2} \right) = \begin{pmatrix} 0 \\ \pm u_B \end{pmatrix} \quad (2.82)$$

The plasma density cannot be calculated without the power balance equation. So the solution of the model will be a density profile that can be multiplied by a any constant, depending on the power conditions. We look for solutions by separation of variables

$$n = N n_x(x) n_y(y) \quad (2.83)$$

$$\mathbf{v} = \begin{bmatrix} v_x(x) \\ v_y(y) \end{bmatrix} \quad (2.84)$$

where n_x and n_y are arbitrary dimensionless functions of x and y respectively, and N is the plasma density at the discharge center ($x = y = 0$). The normalization implies that $n_x(0) = n_y(0) = 1$. Due to the symmetry of the system, n_x and n_y are even functions, and v_x and v_y are odd functions, with $v_x(0) = v_y(0) = 0$. Eq. (2.80) becomes

$$v_x \frac{n'_x}{n_x} + v'_x + v_y \frac{n'_y}{n_y} + v'_y = v_{iz} \quad (2.85)$$

All the functions have only one variable, so the prime ' denotes here the derivative with respect to x for the functions that depend on x and y for the functions that depend on y . By taking the derivatives of Eq. (2.85) with respect to x and y :

$$\left[v_x \frac{n'_x}{n_x} + v'_x \right]' = 0 \quad (2.86)$$

$$\left[v_y \frac{n'_y}{n_y} + v'_y \right]' = 0 \quad (2.87)$$

We can therefore introduce the constants v_x and v_y such that

$$v_x \frac{n'_x}{n_x} + v'_x = v_x \quad (2.88)$$

$$v_y \frac{n'_y}{n_y} + v'_y = v_y \quad (2.89)$$

and

$$v_x + v_y = v_{iz} \quad (2.90)$$

With the assumption of Eq. (2.84), the second term of the LHS drops for Eq. (2.78) and the first term of the LHS drops for Eq. (2.79). Combined with Eqs. (2.88) and (2.89), Eqs. (2.78) and (2.79) yield to first order differential equations for v_x and v_y

$$(1 - v_x/u_B^2)v'_x = v_x + v_x^2/D_a \quad (2.91)$$

$$(1 - v_y/u_B^2)v'_y = v_y + v_y^2/D_a \quad (2.92)$$

which have exactly the same form as the equation that describes the 1D case (Eq. (2.17)) and can be solved by the exact same way, for uniform D_a , v_x and v_y :

$$\left(1 + \frac{v_x D_a}{u_B^2}\right) \arctan \left[\frac{v_x}{(v_x D_a)^{1/2}} \right] - \frac{(v_x D_a)^{1/2}}{u_B^2} v_x = \left(\frac{v_x}{D_a}\right)^{1/2} x \quad (2.93)$$

$$\left(1 + \frac{v_y D_a}{u_B^2}\right) \arctan \left[\frac{v_y}{(v_y D_a)^{1/2}} \right] - \frac{(v_y D_a)^{1/2}}{u_B^2} v_y = \left(\frac{v_y}{D_a}\right)^{1/2} y \quad (2.94)$$

2.3.2 The temperature equation

As in the 1D case, the boundary conditions (Bohm criterion) impose that

$$f \left(\frac{u_B}{(v_x D_a)^{1/2}} \right) = \frac{u_B l_x}{2 D_a} \quad (2.95)$$

$$f \left(\frac{u_B}{(v_y D_a)^{1/2}} \right) = \frac{u_B l_y}{2 D_a} \quad (2.96)$$

and the electron temperature equation is given by Eq. (2.90):

$$\left[f^{-1} \left(\frac{u_B l_x}{2 D_a} \right) \right]^{-2} + \left[f^{-1} \left(\frac{u_B l_y}{2 D_a} \right) \right]^{-2} = \frac{v_{iz} D_a}{u_B^2} \quad (2.97)$$

The density profiles can also be integrated

$$n_x(x) = \left(1 + \frac{v_x^2}{v_x D_a} \right)^{-\frac{1}{2} \left(1 + \frac{v_x D_a}{u_B^2} \right)} \quad (2.98)$$

$$n_y(x) = \left(1 + \frac{v_y^2}{v_y D_a} \right)^{-\frac{1}{2} \left(1 + \frac{v_y D_a}{u_B^2} \right)} \quad (2.99)$$

As discussed before, D_a may also depend on the ionization frequency at low pressure, which makes Eq. (2.97) harder to solve, especially since it depends here on two parameters l_x and l_y . In the low pressure limit, the only collision type that is important is ionization, so $\frac{v_{iz} D_a}{u_B^2} = 1$. Let us introduce the angle θ such that

$$\tan^2 \theta = l_y/l_x \quad (2.100)$$

and the variable

$$\delta = \frac{2D_a}{u_B(l_x + l_y)} \quad (2.101)$$

such that Eq. (2.97) becomes

$$[f^{-1}(\cos^2 \theta/\delta)]^{-2} + [f^{-1}(\sin^2 \theta/\delta)]^{-2} = 1 \quad (2.102)$$

This equation can be inverted to give δ as a function of θ . As shown in Fig. 2.3, the solution is very well approximated by

$$\delta = \frac{\sin^2(2\theta)}{2f(\sqrt{2})} \quad (2.103)$$

where $f(\sqrt{2}) \approx 1.027$.

So for D_a :

$$D_a = \frac{u_B(l_x + l_y)}{\beta_{xy}} \quad (2.104)$$

where

$$\beta_{xy} = \frac{4f(\sqrt{2})}{\sin^2 [2 \arctan (\sqrt{l_y/l_x})]} \approx \frac{4.11}{\sin^2 [2 \arctan (\sqrt{l_y/l_x})]} . \quad (2.105)$$

contains the role of the aspect ratio at low pressure. The properties of the sin and arctan functions imply that $\beta_{xy} = \beta_{yx}$. Moreover, β_{xy} becomes large for large aspect ratios.

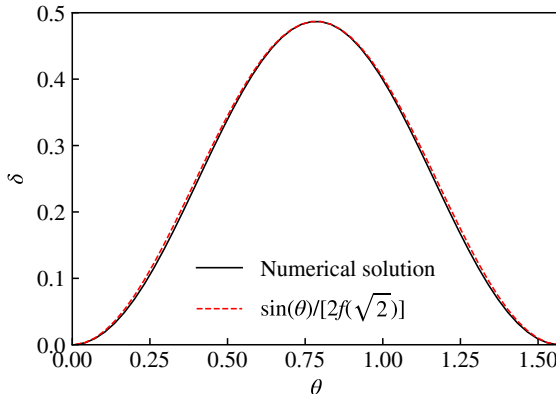


Figure 2.3: Graph of the geometrical dependence of the collisionless ambipolar diffusion coefficient. See Eqs. (2.100) and (2.101) for the definitions of the dimensionless axis.

At higher pressure, the dimensions l_x and l_y does not affect the ambipolar diffusion coefficient. We hence propose the following heuristic formula

$$D_a = \frac{u_B^2}{v_i} \left[1 + \frac{u_B \beta_{xy}}{v_i (l_x + l_y)} \right]^{-1} \quad (2.106)$$

that matches very well the numerical solution of the model for all pressure and aspect ratios (see Fig. 2.11). This general formula is injected in Eq. (2.97), that gives directly v_{iz} as a function of the discharge parameters, and the Bohm speed. For convenience, this solution is also approximated by

$$v_{iz} = v_i \left[\frac{v_i (l_x + l_y)}{\beta_{xy} u_B} + \frac{v_i^2}{\pi^2 u_B^2 (1/l_x^2 + 1/l_y^2)} \right]^{-1} \quad (2.107)$$

This heuristic formula is shown in Fig. 2.11 and compared with the numerical solution. This expression is a quite simple electron temperature equation for the 2D Cartesian system with no magnetic field.

2.3.3 *h* factor in 2D

Now that the interdependence between the x and the y direction is solved thanks to the low pressure limit of the ambipolar diffusion coefficient, we can give some useful estimates of the *h* factor as a function of the ion collision frequency.

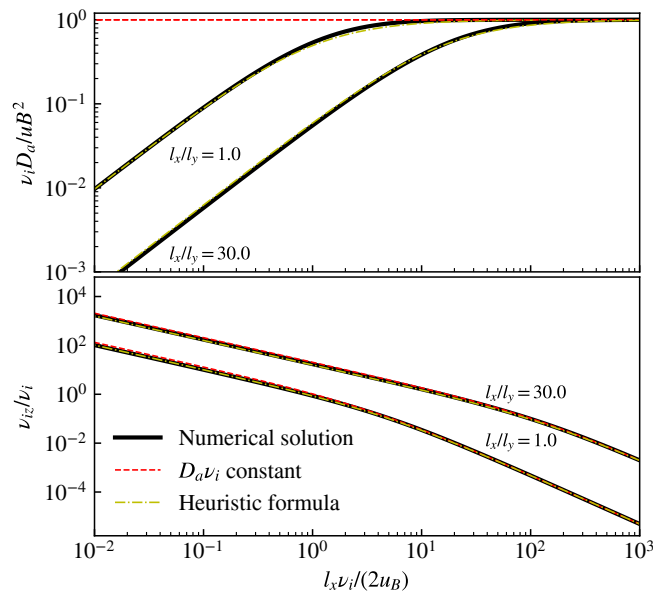


Figure 2.4: Comparison between the numerical solution, the heuristic formula, and the simple high pressure model for the ambipolar diffusion coefficient. (a) Normalized ambipolar diffusion coefficient, (b) normalized ionization frequency.

First, we should notice that the ion flux collected at a wall, for example at $x = l_x/2$, is not uniform

$$\Gamma_i(l_x/2, y) = N n_{xs} n_y(y) u_B \quad (2.108)$$

where $n_{xs} = n_x(l_x/2)$ (similarly $n_{ys} = n_y(l_y/2)$) is the edge-to-center density ratio in the x direction. Therefore,

$$\int_{-l_y/2}^{l_y/2} \Gamma_i(l_x/2, y) dy = N n_{xs} u_B \int_{-l_y/2}^{l_y/2} n_y(y) dy \quad (2.109)$$

Integrating , as it was made to obtain Eq. (2.55), leads to

$$\int_{-l_y/2}^{l_y/2} \Gamma_i(l_x/2, y) dy = 2 N u_B^2 n_{xs} n_{ys} / v_y \quad (2.110)$$

According to the definition of Eq. (1.97), in 2D Cartesian coordinates, the h factor is

$$h_{2D} = \frac{2 u_B n_{xs} n_{ys}}{l_x + l_y} \left(\frac{1}{v_x} + \frac{1}{v_y} \right) \quad (2.111)$$

Using Eqs. (2.95) and (2.96) and the approximate formula of f^{-1} ,

$$\frac{1}{v_x} = \frac{l_x^2}{\pi^2 D_a} + \frac{3}{4} \frac{l_x}{u_B} \quad (2.112)$$

$$\frac{1}{v_y} = \frac{l_y^2}{\pi^2 D_a} + \frac{3}{4} \frac{l_y}{u_B} \quad (2.113)$$

Replacing D_a from Eq. (2.106),

$$\frac{1}{v_x} = \frac{l_x^2 v_i}{\pi^2 u_B^2} + \frac{l_x}{u_B} \left(\frac{3}{4} + \frac{\beta_{xy}}{\pi^2} \right) \quad (2.114)$$

$$\frac{1}{v_y} = \frac{l_y^2 v_i}{\pi^2 u_B^2} + \frac{l_y}{u_B} \left(\frac{3}{4} + \frac{\beta_{xy}}{\pi^2} \right) \quad (2.115)$$

The solutions of the 1D model can be rigorously applied to each direction x and y , provided that the ambipolar diffusion coefficient D_a is taken from the solution of

the 2D electron temperature equation. Therefore,

$$n_{xs} = \left[\exp(1) + \frac{u_B l_x}{D_a} + \left(\frac{u_B l_x}{\pi D_a} \right)^2 \right]^{-1/2} \quad (2.116)$$

$$n_{ys} = \left[\exp(1) + \frac{u_B l_y}{D_a} + \left(\frac{u_B l_y}{\pi D_a} \right)^2 \right]^{-1/2} \quad (2.117)$$

Replacing again D_a ,

$$\begin{aligned} n_{xs} = & \left[\exp(1) + \frac{\beta_{xy} l_x^2}{(l_x + l_y)^2} \left(1 + \beta_{xy} + \frac{l_y}{l_x} \right) \right. \\ & \left. + \frac{v_i l_x^2}{u_B (l_x + l_y)} \left(1 + \frac{2\beta_{xy}}{\pi^2} + \frac{l_y}{l_x} \right) + \frac{v_i^2 l_x^2}{\pi^2 u_B^2} \right]^{-1/2} \end{aligned} \quad (2.118)$$

$$\begin{aligned} n_{ys} = & \left[\exp(1) + \frac{\beta_{xy} l_y^2}{(l_x + l_y)^2} \left(1 + \beta_{xy} + \frac{l_x}{l_y} \right) \right. \\ & \left. + \frac{v_i l_y^2}{u_B (l_x + l_y)} \left(1 + \frac{2\beta_{xy}}{\pi^2} + \frac{l_x}{l_y} \right) + \frac{v_i^2 l_y^2}{\pi^2 u_B^2} \right]^{-1/2} \end{aligned} \quad (2.119)$$

2.3.4 Comparison with 2D PIC simulation

Input parameters

In order to validate this new 2D model, we run several PIC simulations for a rectangular argon discharge of an ICP with a uniform heating electric field, corresponding to the configuration of Fig. 1.6(a). In order to satisfy quasineutrality over most of the simulation domain, the Debye length, that is supposed to be a fraction of the sheath thickness [84], should be much smaller than the size of the discharge. Hence, the aim is to simulate a plasma at reasonably high density, typically higher than 10^{16} m^{-3} . As explained in the discussion relative to global models, the density in a weakly ionized plasma is typically controlled by the absorbed power, which is an input of the simulation. It is here fixed to 19.1 kW/m^{-3} . Since we are not focusing on the heating process but more on the transport, this parameter is kept constant. The mesh has between 4×10^4 and 4×10^5 cells. The most relevant input parameters are provided in Table 2.1.

Physical parameters			
Gas type		Ar	
Discharge size in x direction	l_x	7.5–75	mm
Discharge size in y direction	l_y	30	mm
Neutral pressure	p	0.3–100	mTorr
Neutral density	n_g	$9.6 \times 10^{18} – 3.2 \times 10^{21}$	m^{-3}
Neutral temperature	T_g	0.026	eV
Frequency	f_{RF}	13.56	MHz
Power density	w	19.1	kW/m^3
Physical time of the simulation	$t_{\text{simulation}}$	12–48	μs
Averaging time	t_{average}	0.03 – 0.09	μs
Initial conditions			
Plasma density	$n_e = n_i$	1×10^{15}	m^{-3}
Electron temperature	T_e [eV]	4.0	eV
Ion temperature	T_i [eV]	0.026	eV
Particles per cell	$N_{\text{part./cell}}$	100	
Heating electric field amplitude	E_0	1.0	kV/m
Numerical parameters			
Cell size	Δx	75	μm
Time step	Δt	$1 \times 10^{-11} – 3 \times 10^{-11}$	s
Steps to execute	$N_{\text{simulation}}$	> 450 000	
Steps to average	N_{average}	3 000	
Weighting factor	q_f	$1.5E \times 10^6 – 3.75 \times 10^6$	m^{-1}
Number of Central Processing Unit (CPU)	N_{CPU}	200–400	
Initial number of super-particles	$N_{\text{part,0}}$	$1.5 \times 10^5 – 1.2 \times 10^6$	

Table 2.1: Main physical and numerical input parameters of the 2D PIC simulation.

Verification of the assumptions of the model

We summarize here the assumptions made in the model and verify it against the PIC simulation results.

1. The sum of the electron temperature and the ion temperature is the same everywhere in the plasma bulk.
2. The plasma is quasineutral in the region where the ion speed is lower than the Bohm speed.
3. The plasma density and the velocity profiles can be described by separation of variables (see Eqs. (2.83) and (2.84))
4. The sheath thickness is small.
5. Electron and ion collision frequencies are uniform in the bulk plasma.

First, the pressure is varied from 0.3 to 100 mTorr for a square geometry where $l_x = l_y = 3$ cm. The electron and ion density profiles are plotted in Fig. 2.5(a). The electrons and the ions have almost exactly the same densities, except in the sheath region which is localized very close to the walls. In this region, the electron density becomes lower than the ion density, as predicted by the classical sheath theory (see Section 1.5). The quasineutral assumption seems reasonable for the bulk plasma region. As shown in Fig. 2.5(b), the plasma potential, which is set to zero at the walls, decreases from the center to the edge, and it accelerates the ions.

Fig. 2.6 shows the region of the discharge close to the wall for $y = l_y/2$. The plasma is quasineutral with a good approximation up to the location where the ions reach the Bohm speed. The Bohm speed is computed at each cell using the local electron temperature. The electron fluid velocity is more sensitive to the numerical noise and was here averaged over 10 cells around $y = l_y/2$. The quantities shown in this figure are averaged over 8 μ s at steady-state. The sheath thickness is approximately $s = 2$ mm in this case. When we apply the model equations the dimension of the plasma should not be $l_x \times l_y$ but $(l_x - 2s) \times (l_y - 2s)$. In Fig. 2.8 we aim at justifying the assumption made in the model that the plasma density could be described by variable separation. Here, we compute the ion density along both slices $x = l_x/2$ and $y = l_y/2$ and reconstruct a 2D map as a convoluted solution

$$n_{conv} = \frac{n\left(x, \frac{l_y}{2}\right) n\left(\frac{l_x}{2}, y\right)}{n\left(\frac{l_x}{2}, \frac{l_y}{2}\right)} \quad (2.120)$$

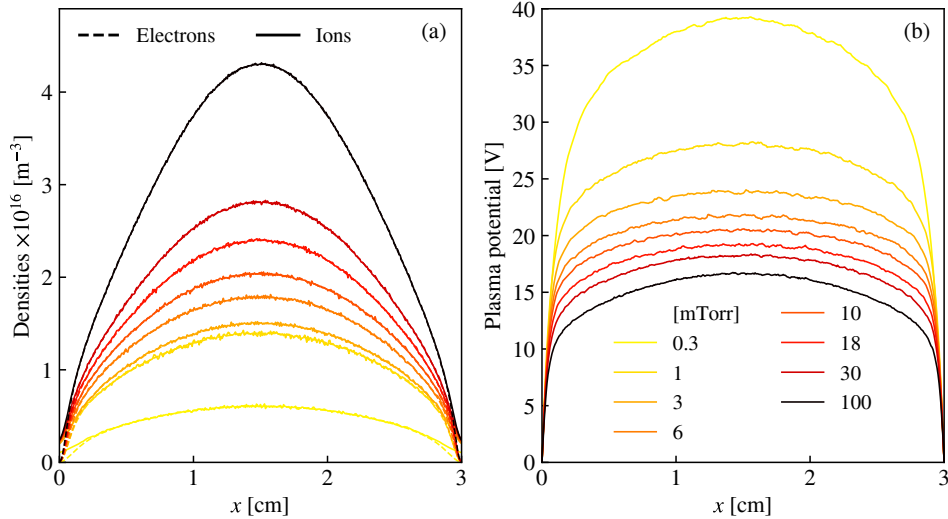


Figure 2.5: Properties of the plasma at steady-state for a square box (3×3 cm), at $y = l_y/2$, and 19.1 kW of absorbed power. The pressure is varied from 0.3 to 100 mTorr. (a) Electron and ion densities, (b) plasma potential.

The convoluted solution and the real solution should of course be equal in the slices $x = l_x/2$ and $y = l_y/2$. In Fig. 2.8, the convoluted solution is compared with the real solution at 1.5 mm from the wall, near the sheath edge, where the discrepancy is the largest (we are not interested in the sheath behavior as the model is quasineutral). The convoluted solution tends to slightly underestimate the density at the sheath edge but in general shows a very good agreement with the real solution.

The temperature profiles are analyzed in Fig. 2.7 at low pressure (0.3 mTorr) and relatively high pressure (100 mTorr). The ion temperature was multiplied by ten to scale with the electron temperature – it always remains below the electron temperature. The sum of the two temperatures is approximately constant in the plasma bulk and the isothermal assumption seems reasonable. The model could perhaps be improved by adding a polytropic coefficient γ , as it was done in the description of the sheath in Section 1.5, but the isothermal assumption is much more accurate in the bulk than in the sheath. At high pressure, the ion temperature reaches 0.6 eV near the wall because a large part of the directional kinetic energy of the ions gained by the sheath electric field is transferred to thermal energy through collisions. This effect is also visible at low pressure, but less acute.

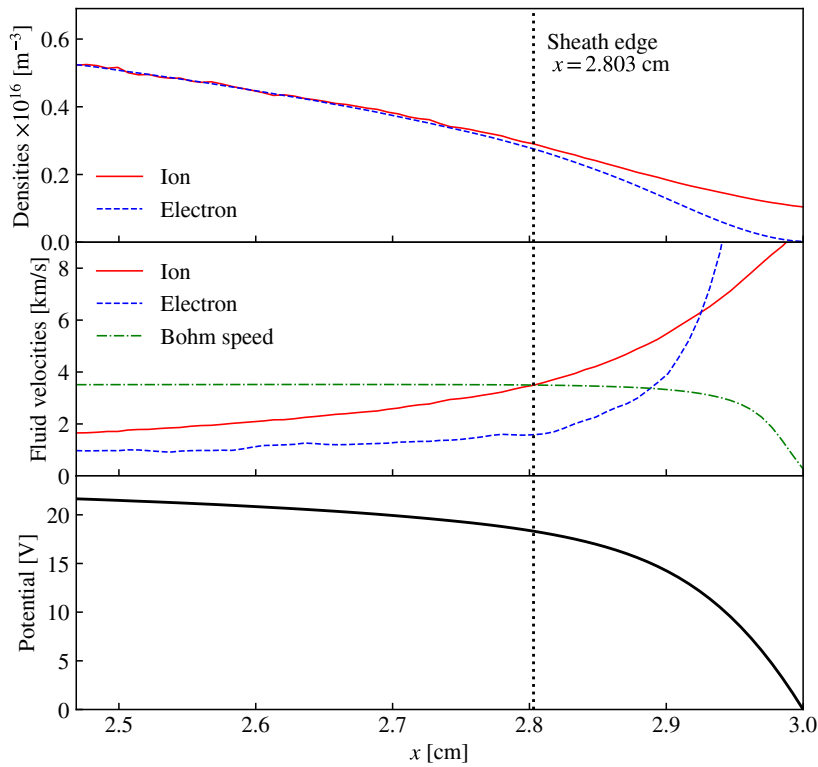


Figure 2.6: Sheath profiles at $y = l_y/2$ for a square (3×3 cm) discharge at 3 mTorr. In this case, the power is 9.6 kW/m^3 .

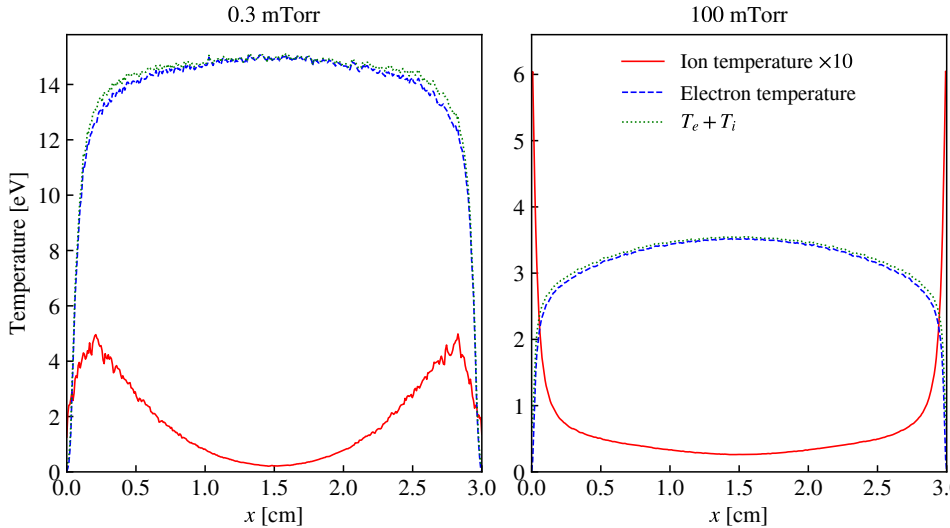


Figure 2.7: Electron and ion temperature profiles at $y = l_y/2$ for a 3×3 cm discharge at 0.3 mTorr (left) and 100 mTorr (right) of gas pressure. The ion temperature was multiplied by a factor ten to scale with the electron temperature.

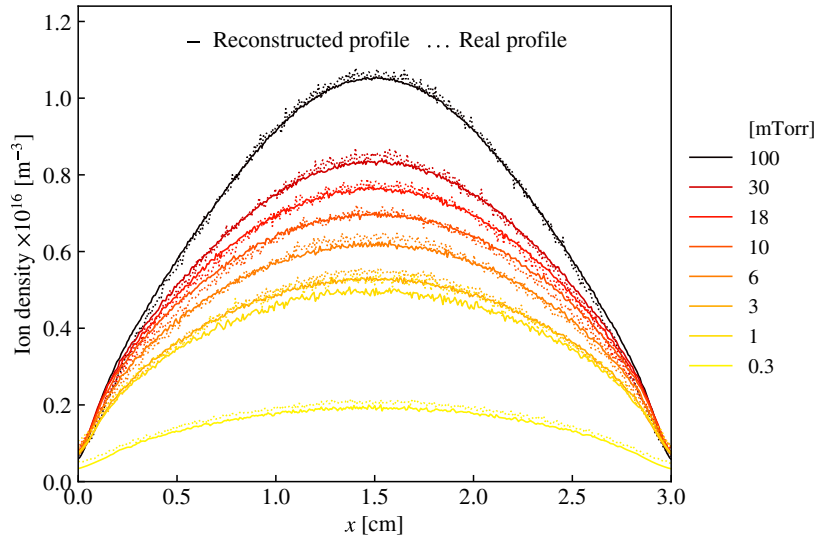


Figure 2.8: Plasma density profiles at steady-state for discharges between 0.3 and 100 mTorr, at 1.5 mm from the wall. The real simulation profiles (solid line) of ion density are compared with the convoluted profiles (dotted line). The simulation conditions are: 3×3 cm, at 19.1 kW/m^3 .

Parametric study with pressure

We now investigate the role of pressure on the discharge properties, in order to verify the solutions of the model. The ions have more difficulty to reach the walls at higher pressure due to collisions with neutrals. The losses are hence reduced and the electron temperature needed to sustain the discharge through ionization decreases, as predicted by the theory. The quantity measured in the PIC simulation is based on the mean energy of the electrons inside the simulation domain, including the beam energy, multiplied by 2/3. This effective electron temperature is hence slightly higher than the kinetic temperature of Eq. (1.19). Since the electron fluid velocity is neglected in the fluid model, we will compare the electron temperature of the fluid model with this effective electron temperature measured in the PIC simulation. The effective electron temperature drops from 18.7 eV at 0.3 mTorr to 3.21 eV at 100 mTorr. Below 0.3 mTorr, the discharge was very difficult to sustain and would require a smaller time step to preserve the CFL condition for the energetic electrons. Since the plasma is better confined at high pressure for the same injected power, the plasma density rises at high pressure. This result matches the general picture that was established in the section on global models.

To allow comparison with theory, we need to make a choice for the ion neutral collision frequency. The easiest way to evaluate the typical ion-neutral momentum transfer collision frequency is to assume a constant cross section (10^{-18} m^2 for argon) and multiply it by the mean thermal velocity:

$$\nu_i = n_g \sigma_i \bar{v}_i \quad (2.121)$$

where

$$\bar{v}_i = \left(\frac{8k_B T_{i0}}{\pi m_i} \right)^{1/2} \quad (2.122)$$

Here, $T_{i0} = 300 \text{ K}$ is the injection ion temperature in the PIC simulation, which is also the ion temperature measured at the discharge center. However, Fig. 2.7 shows that the ion temperature increases away from the discharge center. Moreover, the ions are accelerated, such that their fluid velocity also has an important role in the mean velocity (see Eq. (2.25)). The typical ion velocity is therefore significantly affected by the electric field, as they have to reach the Bohm speed at the sheath edge. At high pressure, the acceleration is very localized at the sheath edge, but at low pressure it is much smoother, such that the typical ion fluid velocity in the bulk is a fraction of the Bohm speed at low pressure. We have proposed [87] to correct this effect by introducing a dependence of the typical ion velocity $v_{i,\text{ref}}$ on the Bohm speed

$$\nu_i = n_g \sigma_i v_{i,\text{ref}} \quad (2.123)$$

The reference velocity should be typically \bar{v}_i at high pressure where the ion energy is dominated by the thermal motion, and of the order of $u_B/2$ at low pressure where most of the ion energy is directional (towards the wall). We chose

$$v_{i,ref} = \bar{v}_i + b(\alpha)u_B/2 \quad (2.124)$$

where $\alpha = 4\lambda_i^2/(l_x l_y)$ is inversely proportional to the pressure squared, and

$$b(\alpha) = \tanh^{0.2}(\alpha) \quad (2.125)$$

satisfies the conditions $b(0) = 0$ and $\lim_{\alpha \rightarrow \infty} b(\alpha) = 1$. This way we, do not need to solve the non-linear equation where Eq. (2.25) is taken into account, and we still have a model that has a good prediction capability. The model equations can also be used with experimental data of the mean ion energy.

In Fig. 2.10, the electron temperature and the h factor are plotted against the inverse Knudsen number in the x direction l_x/λ_i , which is proportional to the pressure. Here, l_x is fixed to 3 cm, at the ion mean free path is

$$\lambda_i = (\sigma_i n_g)^{-1} \quad (2.126)$$

As shown in Fig. 2.10(a) the electron temperature is very well predicted by the model and the choice for the ion collision frequency does not play a major role. There is however a significant discrepancy at high pressure, probably because the isothermal assumption is less valid at pressures of the order of 100 mTorr, see Fig. 2.7. The h factor is not very well predicted by the model with $v_{i,ref} = \bar{v}_i$ for pressures higher than 10 mTorr because the ion collision frequency is badly predicted. The low pressure regime is correctly described because it corresponds to a collisionless model where the only momentum loss in the ion momentum conservation equation comes from the newly created ions, and is hence proportional to v_{iz} and not v_i anymore. Using Eq. (2.124) yields good prediction of the h factor.

The heuristic formula proposed by Chabert and Braithwaite [27] (Eq. (2.56)) can be corrected to take into account the first order corrections induced by the 2D geometry. The correction factor essentially depends on the mean density profile in the direction perpendicular to the ion velocity vector. At high pressure, as in the 1D case, the density profile has a cosine shape in both directions, such that the mean normalized density profile is $2/\pi$. The corrected heuristic formulas hence become

$$h_{L,heur,x} = 0.55 \left[3 + 0.5 \frac{l_y}{\lambda_i} + 0.2 \frac{T_i}{T_e} \left(\frac{l_y}{\lambda_i} \right)^2 \right]^{-1/2} \quad (2.127)$$

$$h_{L,heur,y} = 0.55 \left[3 + 0.5 \frac{l_x}{\lambda_i} + 0.2 \frac{T_i}{T_e} \left(\frac{l_x}{\lambda_i} \right)^2 \right]^{-1/2} \quad (2.128)$$

where $0.55 \approx (2/\pi) \times 0.86$. It should be noted that $h_{L,heur,x}$ – which is the h factor relative to the flux of ions collected on $y = \pm l_y/2$ – depends on l_y , and not l_x . The global heuristic h factor is then

$$h_{2D,heur} = \frac{l_x h_{L,heur,x} + l_y h_{L,heur,y}}{l_x + l_y} \quad (2.129)$$

For a square, ($l_x = l_y = l$)

$$h_{2D,heur} = 0.55 \left[3 + 0.5 \frac{l}{\lambda_i} + 0.2 \frac{T_i}{T_e} \left(\frac{l}{\lambda_i} \right)^2 \right]^{-1/2}. \quad (2.130)$$

This formula was also compared with the PIC simulation results and the solutions of the model in Fig. 2.10. It shows a good agreement for the whole range of pressures investigated. In Eqs. (2.127) and (2.128), the electron temperature is the solution of Eq. (2.107).

The local currents collected at the walls of the PIC simulation domain are plotted in Fig. 2.9. The discharge is clearly not ambipolar as the electron and ion fluxes differ very significantly. The electron tend to move towards low electrostatic potential regions, while the ions are accelerated straight to the walls. The profile for the ion flux resembles the density profile in the center of the discharge. On the contrary, the electron current profile is flatter at high pressure, where it reminds of the plasma potential profile, and features a minimum in the center for pressures below 18 mTorr. At low pressure, the electron current has very sharp peaks near the corner of the simulation domain. However, the spatially integrated electron and ion currents are equal, which is a necessary condition for the steady-state.

We noted that the h factor determined by PIC simulation slightly decreases from 1 mTorr to 0.3 mTorr. At low pressure, the EEDF is strongly anisotropic, which might affect the sheath formation and hence the ion flux.

Parametric study with dimension l_x

We now perform a parametric study with the aspect ratio while keeping the pressure fixed to 10 mTorr. The size l_y is set to 3 cm and the size l_x is varied from 0.75 to 7.5 cm. The density profiles are plotted in Fig. 2.13. The density generally increases with the size of the discharge. In the case where $l_x = 0.75$ cm, the plasma potential is not uniform across y such that quasineutrality is not satisfied anymore in most of the simulation domain. The sheath dimension becomes of the same order of magnitude as the discharge size, which gives the concave shape to the electron density profile at $l_x = 0.75$ cm in Fig. 2.13(a). The quasineutral model does not seem to

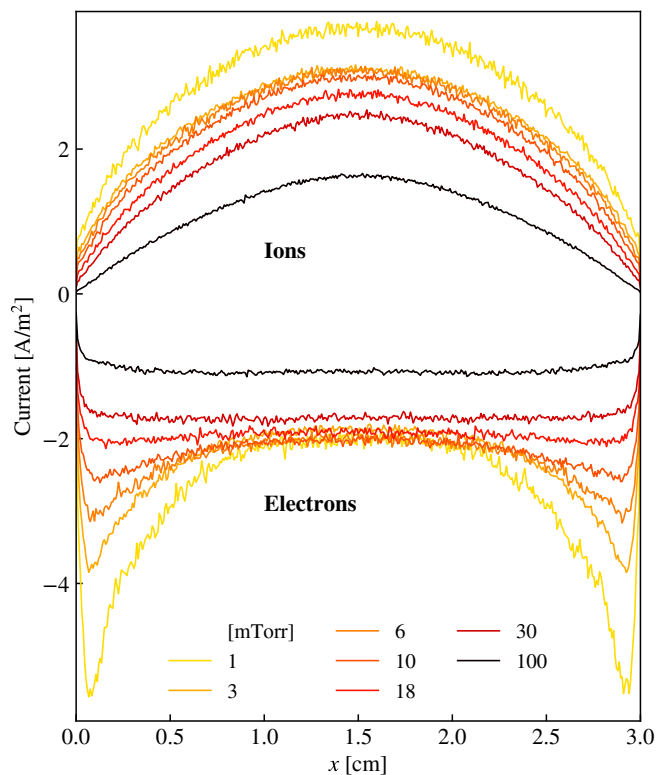


Figure 2.9: Electron (bottom, negative) and ion (top positive) currents collected at the bottom wall ($y = 0$) of the simulation domain for simulation cases between 1 and 100 mTorr.

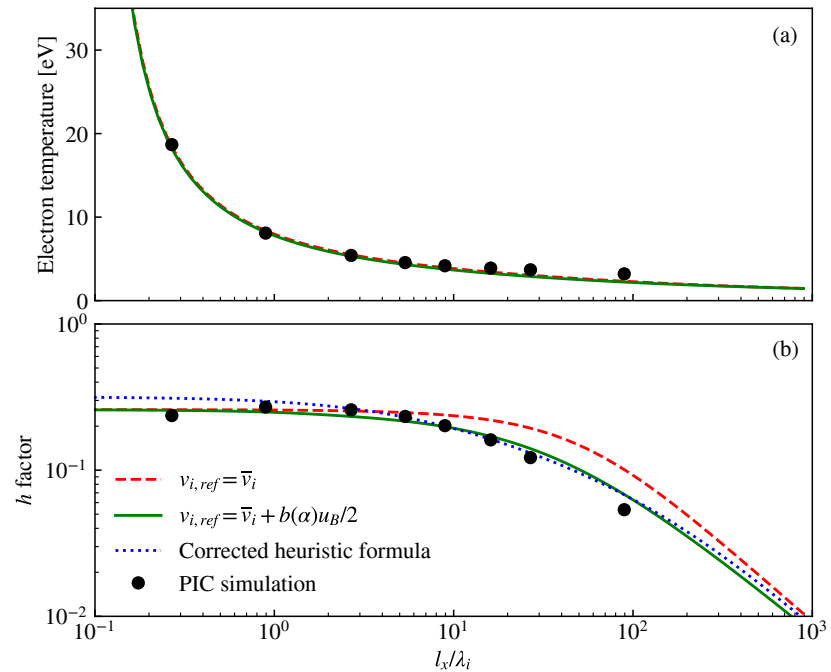


Figure 2.10: Parametric study with pressure varying from 0.3 to 100 mTorr for 3×3 cm argon discharge. (a) Electron temperature. (b) *h* factor. The PIC simulation results (black circles) are compared with the solutions of the fluid model, with Eq. (2.121) (red dashed line) and Eq. (2.124) (green solid line).

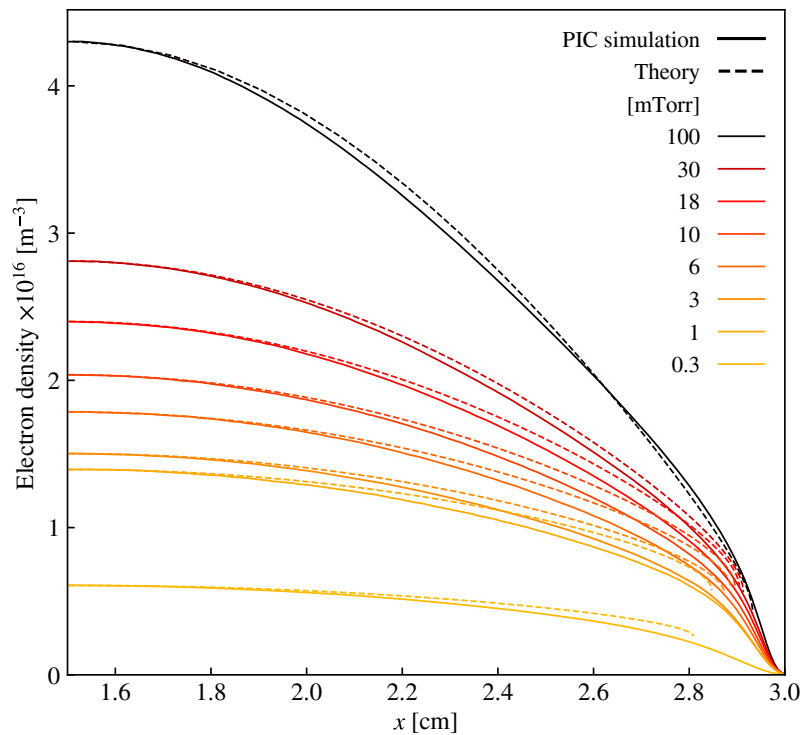


Figure 2.11: Comparison between the simulation results and the theoretical solution with predicted electron temperature and profiles. The electron density is plotted at $y = l_y/2$ of a square discharge with pressure varying between 0.3 and 100 mTorr.

strictly apply for aspect ratios greater than 4. However, as the aspect ratio increases, the 2D effects become minor and the plasma can essentially be described with the single x direction. As confirmed by the good agreements found in Fig. 2.10, the 2D quasineutral model derived above accounts for the large aspect ratio limit correctly.

As emphasized by the ratio l/λ_i that characterizes the properties of a non-magnetized 1D discharge, increasing the size of the system should play approximately the same role as increasing the pressure, such that the electron temperature should decrease for larger systems. Fig. 2.12(a) shows that this is also generally true for a 2D system. The h factor measured from the PIC simulation is compared with the solutions of the model and the corrected heuristic formula described in the previous paragraph in Fig. 2.12(b). For l_x/λ_i higher than 4, the h factor decreases with the system size and the three formulas are reasonably accurate. However, below typically $l_x/\lambda_i = 4$, and for an aspect ratio higher than 2, the effect of the coupling of x and y direction through the β_{xy} factor becomes important and the h factor decreases again. This effect seems to be well captured by the model, both with $v_{i,ref} = \bar{v}_i$ and $v_{i,ref} = \bar{v}_i + b(\alpha)u_B/2$, but the corrected heuristic formula does not show this trend, although the order of magnitude seems correct for all the conditions investigated.

2.3.5 Discussion

The ambipolar assumption is not necessary to derive the equation of the plasma transport as long as electron inertia and collisions are neglected. *A posteriori*, we can verify if the ion and the electron fluxes are equal. Fig. 2.9 has already shown that this is not the case for the particles collected at the wall. We now examine the ambipolar nature of the plasma outside of the sheath. Therefore, Fig. 2.14 presents the electron and ion currents in the bulk plasma. We can observe the same patterns as in the curve of the currents collected at the walls of the discharge: while the ions are going straight to the walls with short streamlines, the electrons tend to first escape towards the corners where the potential is higher. They still enter the sheath with a velocity vector that is almost everywhere perpendicular to the sheath surface.

The assumption of variable separation can also be questioned for large aspect ratio discharges. Fig. 2.15(a) and (b) show the profiles of the electron and ion density along the x and y axis respectively for a 10 mTorr argon discharge with $l_x = 0.75$ cm and $l_y = 3$ cm. While the plasma is quasineutral in the main direction (y), the space charge sheaths are quite large in the x direction. It seems that the larger the dimension, in a given axis, the smaller the sheath. The space charge sheaths are relatively large and cover almost half of the discharge. This observation affects very much the reconstructed plasma density profiles shown in Fig. 2.15(c) and (d). The reconstructed profiles seem to match the electron density (in red) quite accurately but the

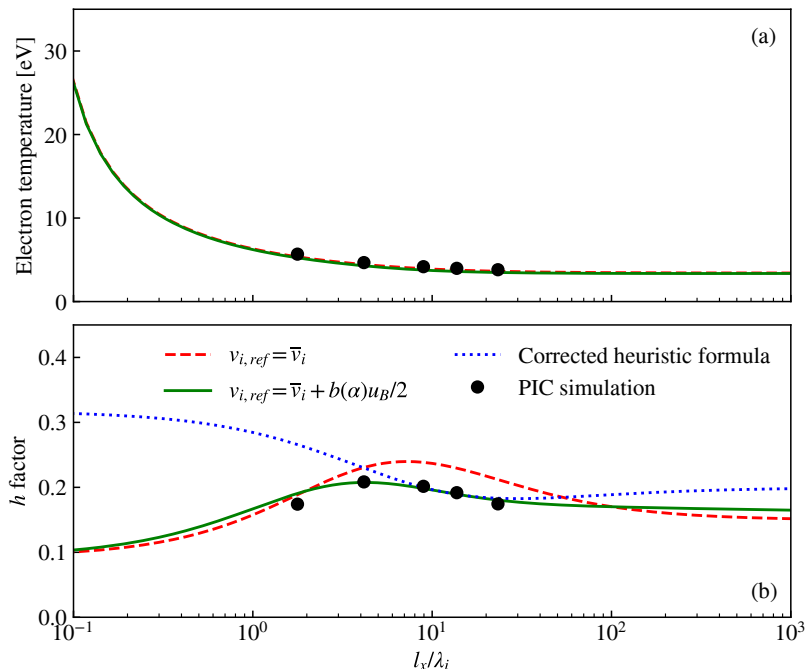


Figure 2.12: Electron temperature (a) and h factor (b) investigated for different discharge geometries. l_y is fixed to 3 cm and l_x varied from 0.75 to 7.5 cm. The pressure is 10 mTorr. The PIC simulation results (black circles) are compared with the solutions of the fluid model, with Eq. (2.121) (red dashed line) and Eq. (2.124) (green solid line).

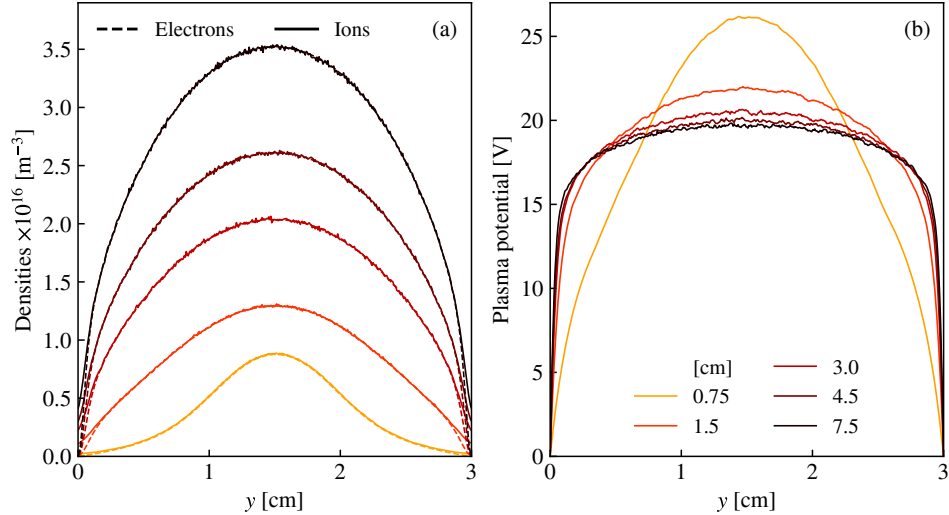


Figure 2.13: Properties of a 10 mTorr plasma at steady-state at $x = l_x/2$, and 19.1 kW of absorbed power. l_y is fixed to 3 cm and l_x is varied between 0.75 and 7.5 cm. (a) Electron and ion densities, (b) plasma potential.

assumption of variable separation seems to break up for the ions. A more accurate model of this type of plasma would require to solve the Poisson's equation in 2D, as it is done in the PIC simulation.

The limitation of the model being acknowledged, it is probably of some interest to mention the 3D generalization of the method developed in this section. If one assumes that the variable separation method is applicable in 3D, the model equations can be solved exactly the same way and provide a 3D electron temperature equation for an isothermal, quasineutral, electropositive plasma bounded by space charge sheaths with no magnetic field:

$$\left[f^{-1} \left(\frac{u_B l_x}{2 D_a} \right) \right]^{-2} + \left[f^{-1} \left(\frac{u_B l_y}{2 D_a} \right) \right]^{-2} + \left[f^{-1} \left(\frac{u_B l_z}{2 D_a} \right) \right]^{-2} = \frac{\nu_{iz} D_a}{u_B^2} \quad (2.131)$$

which is a generalization of Eq. (2.97). Again, this equation can be solved if some assumptions are made about the ambipolar diffusion coefficient D_a . For inverse Knudsen number l_x/λ_i higher than 1, and if the aspect ratio is not too large. The 2D analysis suggests that $D_a = u_B^2/\nu_i$ is a good approximation. It would be however useful to perform some probe measurements to check these predictions experimentally.

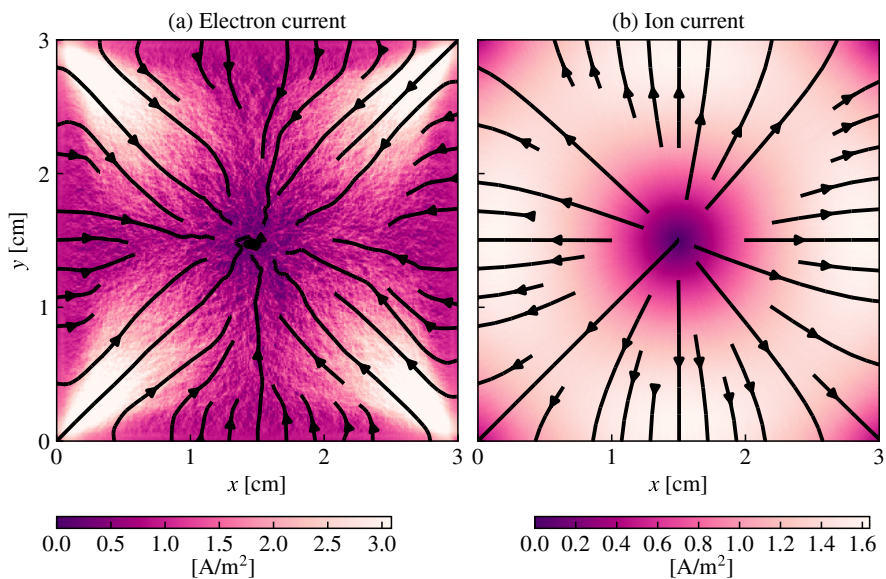


Figure 2.14: Maps of the norm of the electric current generated by electron (a) and ion (b) motion, for a pressure of 3 mTorr. The arrows represent the streamlines.

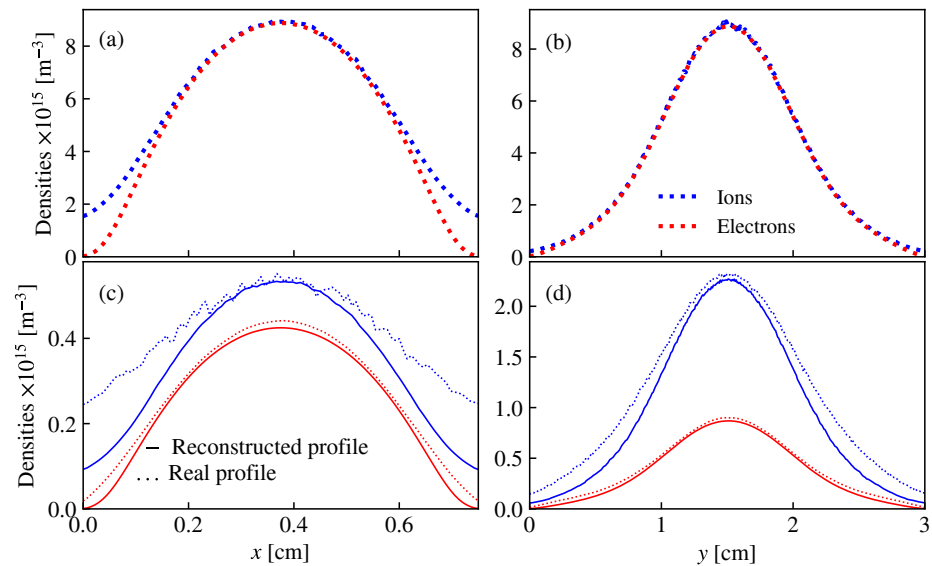


Figure 2.15: Plasma density profiles for a discharge at 10 mTorr with $l_x = 3$ cm and $l_y = 0.75$ cm. The following slices are shown: (a) $y = l_y/2$, (b) $x = l_x/2$, (c) $y = 0.052$ cm, (d) $x = 0.225$ cm. In (c) and (d), the real ion and electron density profiles (dotted lines) are compared with the reconstructed ones (solid lines) $n(x, l_y/2)n(l_x/2, y)/n(l_x/2, l_y/2)$.

Summary

In this Chapter, we have presented a set of isothermal models for quasineutral, weakly ionized plasmas. In 1D, the discharge is ambipolar and analytical solutions can always be found to these models, under the assumption of constant ion mobility. In 2D, the discharge is non-ambipolar and no general solution exists. However, assuming a Boltzmann electron distribution, a solution can be found by variable separation when no magnetic field is applied. These solutions compare very well with the PIC simulation results and the model allows for a generalization of the so-called h factor.

Chapter 3

Cross field transport in a uniform magnetic field

Contents

3.1	2D PIC simulation of a magnetized plasma column	108
3.1.1	Context	108
3.1.2	Simulation parameters	109
3.1.3	Description of the steady state	109
3.1.4	Magnetic drifts	112
3.1.5	Magnetized sheath	114
3.1.6	Parametric studies with the magnetic field and the pressure	116
3.2	The collisional resistive drift instability	122
3.2.1	Model introduction	122
3.2.2	Dispersion relation in a homogeneous plasma	123
3.2.3	Dispersion relation in an inhomogeneous plasma	127
3.2.4	Solutions of the dispersion relations	132
3.2.5	Comparison with the PIC simulations	133
3.3	Transport theory at high magnetic field	145
3.3.1	2D isothermal model	145
3.3.2	Saturation of the magnetic confinement	151
3.3.3	Instability-enhanced transport	159
3.3.4	Discussion on the marginal stability	162

This Chapter contains the core of the theoretical results of this work. A magnetized plasma column with a uniform magnetic field pointing in the direction perpendicular is simulated in order to study the cross-field plasma transport. We investigate the instabilities predicted by uniform and non-uniform fluid plasma theories and propose a theory of the instability-enhanced plasma transport.

3.1 2D PIC simulation of a magnetized plasma column

3.1.1 Context

The magnetized plasma column is a classic of plasma physics. Experimentally, several methods exist to sustain a magnetized plasma column. Among them, one can cite the Penning discharge that features an external electron source, or inductive discharges. An experimental study on the combination of both plasma generation techniques was recently performed by V. Desangles [43]. Our work focuses on ICP generation. In a magnetized plasma column, the length of the axis is typically larger than the radial dimensions, such that 2D simulations in the plane perpendicular to the main axis are well-suited to the geometry. The magnetic field is along the main axis of the magnetized plasma column (z).

The magnetized low-temperature plasma column has been investigated by a number of theoretical and experimental studies. Fruchtman et al. [50] performed an experimental study of the 2D (radial-axial) transport in a cylindrical discharge. In the configuration of this paper, the ion losses along the axis (and along the magnetic field lines) are thought to be dominant. The classical fluid model developed does not show a good agreement with the experiments. When an empirical Bohm mobility is included, the model predictions yield a correct order of magnitude for the plasma density, but still with up to 100% discrepancy with the experimental results at magnetic fields between 10 and 20 mT. Curreli and Chen [39] provided a comprehensive review of the historical studies on crossfield diffusion. The classical theories are presented together with their limits, and the qualitative effects of the resistive drift wave instability are described. The resistive drift instability can be triggered by collisions in systems where the axial dimension is extremely long or where the magnetic surfaces are closed, as shown already by Birdsall in 1953 [14]. However,

- the conditions needed for collisions to trigger an instability are not clearly identified in the literature.
- Moreover, few theories were able to quantify the corresponding instability-enhanced transport.

The main results of this Chapter were published in Lucken et al. PoP 2019 [89] and Lucken et al. PSST 2019 [].

3.1.2 Simulation parameters

In our configuration, the cross section of the magnetized plasma column is a square that has the same dimensions as the system that was described in the previous Chapter. The walls remain conductive and we keep the same cross section set for argon as previously. The simulation parameters used for the results presented in this Chapter are reported in Table 3.1. Most of the runs were performed on 220 CPU and last between 12 and 24 hours on the OCCIGEN machine (CINES, Montpellier, France) so the parallel capability of the *LPPic* code is fully used.

The typical lengths and frequencies that characterize the simulation conditions are summarized in Tables 3.2 and 3.3. The ion mean free path is a fraction of the size of the discharge, which is a characteristic of intermediate pressure regimes. The Larmor radius for the ions thermalized at 300 K can be as low as 5 mm at 40 mT. The typical ion speed however increases away from the discharge center, both due to ion collisional heating, and ion flow acceleration, in a similar fashion as in the non-magnetized case. These effects cause the typical ion Larmor radius to increase as well. In general, the ion mean free path is not smaller than the size of the discharge and can often be neglected. In most of the simulation runs, the Lorentz force on the ions is neglected. Some tests were performed with magnetized ions as well, with minor effects on the discharge properties.

3.1.3 Description of the steady state

We have seen in the 1D model described in Chapter 2 that a permanent magnetic field perpendicular to the direction of the transport can considerably confine the plasma, and hence reduce the wall losses. Magnetic field is however known for generating plasma instabilities that can in turn have an influence on the plasma transport. There are hence two time scales to be considered. The larger time-scale is the one that corresponds to the equilibrium observed in experiments. At this time-scale, for each value of the magnetic field, one can define the mean values of the plasma properties, for example ϕ , n_e , n_i , Γ_e , Γ_i , T_e and T_i , at each position in space. On the shorter time-scale, these properties may fluctuate with a wide range of frequencies, and with more or less spatial structures. When only the longer time-scale is considered, and for reasonable values of the magnetic field (this will be specified later), some of the discharge characteristics have qualitatively the same aspect as the non-magnetized equilibrium. For example, the discharge domain can still be split into a quasineutral region near the center, and a sheath region near

Physical parameters			
Gas type		Ar	
Discharge size in x direction	l_x	30	mm
Discharge size in y direction	l_y	30	mm
Neutral pressure	p	3.0, 6.0, 12.0	mTorr
Transverse magnetic field	B	0–40	mT
Neutral density	n_g	$0.96 \times 10^{20} – 3.83 \times 10^{20}$	m^{-3}
Neutral temperature	T_g	0.026	eV
Frequency	f_{RF}	13.56	MHz
Power density	w	9.6	kW/m^3
Physical time of the simulation	$t_{\text{simulation}}$	27–98	μs
Averaging time	t_{average}	0.033–0.099	μs
Initial conditions			
Plasma density	$n_e = n_i$	1×10^{15}	m^{-3}
Electron temperature	T_e [eV]	4.0	eV
Ion temperature	T_i [eV]	0.026	eV
Particles per cell	$N_{\text{part./cell}}$	7–50	
Heating electric field amplitude	E_0	0.1–1	kV/m
Numerical parameters			
Cell size	Δx	75	μm
Time step	Δt	3.3×10^{-11}	s
Steps to execute	$N_{\text{simulation}}$	> 818 000	
Steps to average	N_{average}	1 000–3 000	
Weighting factor	q_f	$2.53E \times 10^6 – 1.05 \times 10^7$	m^{-1}
Number of CPU	N_{CPU}	220	
Initial number of super-particles	$N_{\text{part},0}$	$8 \times 10^6 – 3.2 \times 10^7$	

Table 3.1: Main physical and numerical input parameters for the parametric study in pressure and magnetic field of the magnetized plasma column.

<i>Lengths</i>	[mm]
Typical wavelength , λ	0.6 – 3
Ion Debye length , λ_{Di}	$7 - 14 \times 10^{-3}$
Ion mean free path , λ_i	2.6 – 10
Thermal ion Larmor radius , ρ_{Li}	5 – ∞
Electron Debye length , λ_{De}	0.08 – 0.2
Electron mean free path (elastic) , λ_e	30 – 120
Thermal electron Larmor radius , ρ_{Le}	0.4 – ∞
Discharge sizes , $l_x = l_y$	30
Cell size , dX	0.075

Table 3.2: Characteristic lengths of the system, in mm.

<i>Frequencies</i>	[Hz]
Drift wave , $\omega/2\pi$	$1 - 10 \times 10^6$
Electron impact ionization , ν_{iz}	$1 - 7 \times 10^4$
Ion collision , ν_i	$1 - 4 \times 10^4$
Ion cyclotron , $\omega_{ci}/2\pi$	$0 - 8 \times 10^3$
Ion plasma , $\omega_{pi}/2\pi$	$0.5 - 1 \times 10^7$
Electron elastic collision , ν_e	$0.5 - 2 \times 10^7$
Electron cyclotron , $\omega_{ce}/2\pi$	$0 - 1 \times 10^9$
Electron plasma , $\omega_{pe}/2\pi$	$1 - 2 \times 10^9$
RF heating antenna , f_{RF}	1.356×10^7
Sampling frequency , $1/(N_A dT)$	$0.3 - 1 \times 10^7$
Time resolution , $1/dT$	3×10^{10}

Table 3.3: Characteristic frequencies of the system, in Hz.

the wall where the electron density becomes lower than the ion density. As in the non-magnetized case, the ion and electron densities decrease from the center to the walls and the electron temperature is almost uniform in the plasma bulk and decreases significantly in the sheath. The mean plasma potential also decreases smoothly from the center to the walls, which indicates that the space charge always remains positive.

In the simulations performed in this work, instabilities in the range of 1 to 5 MHz were observed. The two time scales that are investigated are hence typically 50 ns for the shorter one and 10 μ s for the longer one. Fig. 3.1 shows the maps of the electron density and the electron current for a run at 3 mTorr of pressure and 20 mT of magnetic field. We can see in Fig. 3.1(a) that the time-averaged electron density looks qualitatively similar to the non-magnetized case, in spite of the strong electron magnetization. On the shorter time-scale, the map of the electron density features a very distinct instability pattern that rotates in the anti-clockwise direction, with a motion that is close to a solid body motion. The typical wavelength seems to be about 2 mm. As shown in Fig. 3.1(c), the electron fluid rotates in the same direction as the instability. This drift motion is typical from magnetized plasma, and it is here opposed to the $E \times B$ drift.

3.1.4 Magnetic drifts

Similarly to what was done to obtain Eq. (1.5) for the $E \times B$ drift, the collisionless momentum conservation equation

$$m_e \frac{d\mathbf{v}_e}{dt} = -e(\mathbf{E} + \mathbf{v} \times \mathbf{B}) - \frac{\nabla p_e}{n_e} \quad (3.1)$$

can be written

$$\frac{d(v_e - v_{E \times B} - v_*)}{dt} = -\frac{e}{m_e}(v_e - v_{E \times B} - v_*) \times \mathbf{B} \quad (3.2)$$

where

$$v_* = \frac{\nabla p_e \times \mathbf{B}}{en_e B^2} \quad (3.3)$$

is the diamagnetic drift. Eq. (3.2) implies that the electron fluid velocity can be split into a translation by $v_{E \times B} + v_*$ and a cyclotron motion at a frequency $\omega_{ce} = eB/m_e$. The diamagnetic drift v_* is only present in the fluid momentum conservation equations and not in the equation of motion of a single particle. This term cannot be interpreted as a transport of particles but it can be captured in the PIC simulation without difficulty due to grid discretization. The reader can refer to the monograph

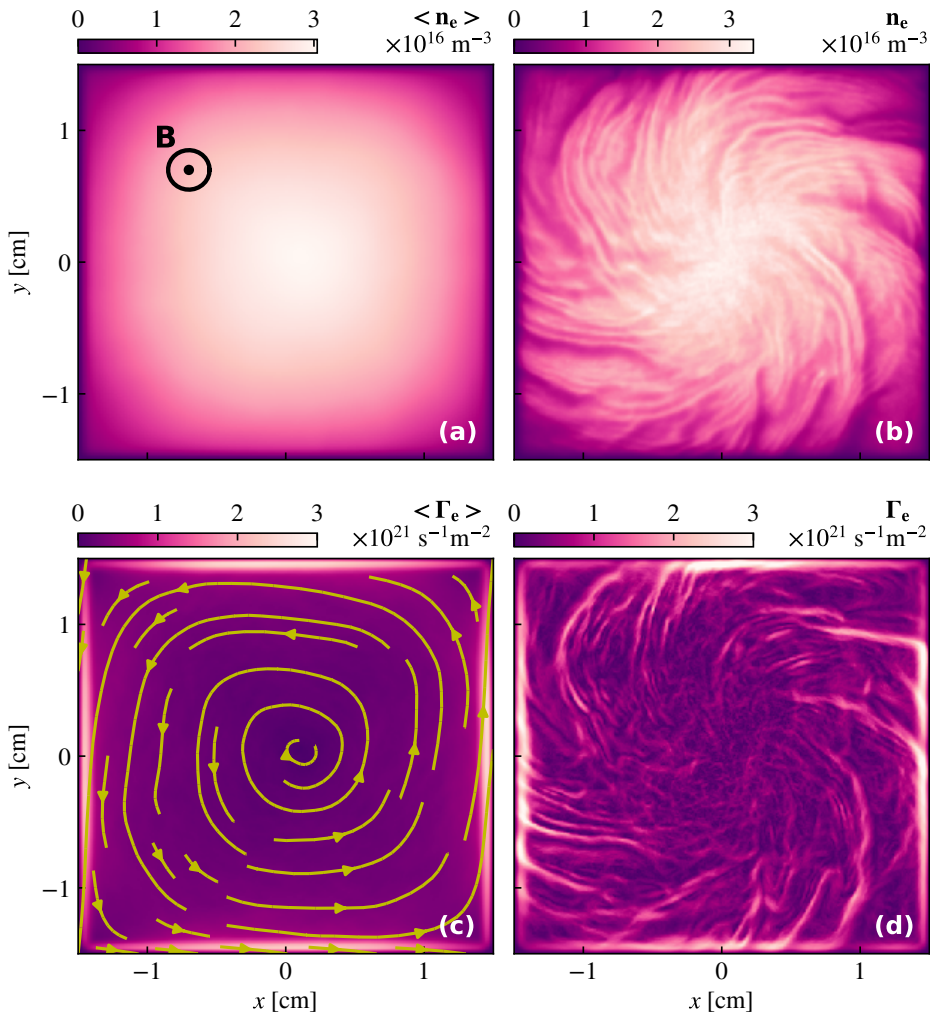


Figure 3.1: Electron density and norm of the electron flux at $91 \mu\text{s}$ (b, d), and averaged over the last $27 \mu\text{s}$ of the simulation (a, c). In (c), the spiral streamlines represent the electron flux. The data come from a $3 \text{ mTorr}, 20 \text{ mT}$ LPPic simulation.

by Chen [31] for more details about the interpretation and the measurement of the diamagnetic drift. The electron flux found in Fig. 3.1(c) is in the same direction as the diamagnetic drift and has the same order of magnitude.

To validate the idea that the electron fluid motion is driven by the diamagnetic drift, the electron fluid velocity along y measured from the PIC simulation at $y = l_y/2$ is plotted as a function of x together with the $E \times B$ drift and the diamagnetic drift in Fig. 3.2. The $E \times B$ and the diamagnetic drifts were computed using Eqs. (1.5) and (3.3) respectively. The gas pressure is 3 mTorr and the power is 9.6 kW/m³. The velocity terms are averaged over more than 4 μ s since we are interested in the properties of the plasma equilibrium here. To cases are investigated:

- (a) 2.5 mT. At low magnetic field, both the $E \times B$ and the diamagnetic drifts are very large because of the $1/B$ dependency but cancel each other to produce a total drift that is typically one order of magnitude lower.
- (b) 20 mT. At higher magnetic field, the $E \times B$ drift becomes negligible and the electron drift velocity is almost equal to the diamagnetic drift velocity everywhere in the bulk plasma.

Both in Fig. 3.2(a) and (b), the sum of the diamagnetic drift and the $E \times B$ drift represented with a cyan dotted line matches the measured fluid velocity in the plasma bulk. In the sheath, this condition breaks because the electron fluid velocity becomes very high so the electron inertia can no longer be neglected.

On the shorter time-scale, the electron fluid velocity is also perturbed by the instability, as illustrated in Fig. 3.1(d). The amplitude of the instability seems lower in the central region of the discharge and increases closer to the walls.

3.1.5 Magnetized sheath

Before further development, it may be useful to focus on the sheath that characterizes the plasma equilibrium. Fig. 3.3 is analog to Fig. 2.6 with a magnetic field of 20 mT. Again, all the quantities are averaged over more than 5 μ s. One can first notice that the plasma density is generally higher for the same injected power so the magnetic field does have a significant confining effect. The plasma density is typically 3 to 4 times higher at 20 mT than at 0 mT. This discrepancy translates into a smaller sheath region near the wall. The qualitative descriptions of section Section 3.1.3 are generally validated. The axial electron velocity is very much perturbed by the instability such that a smooth electron velocity profile could not be obtained at 20 mT, even when large temporal averages are considered. It is suspected that these patterns partially remain at steady-state, as will be indicated later when the wall currents will be studied. The plasma potential is quite flat far away from the walls and the ions accelerate smoothly towards the walls.

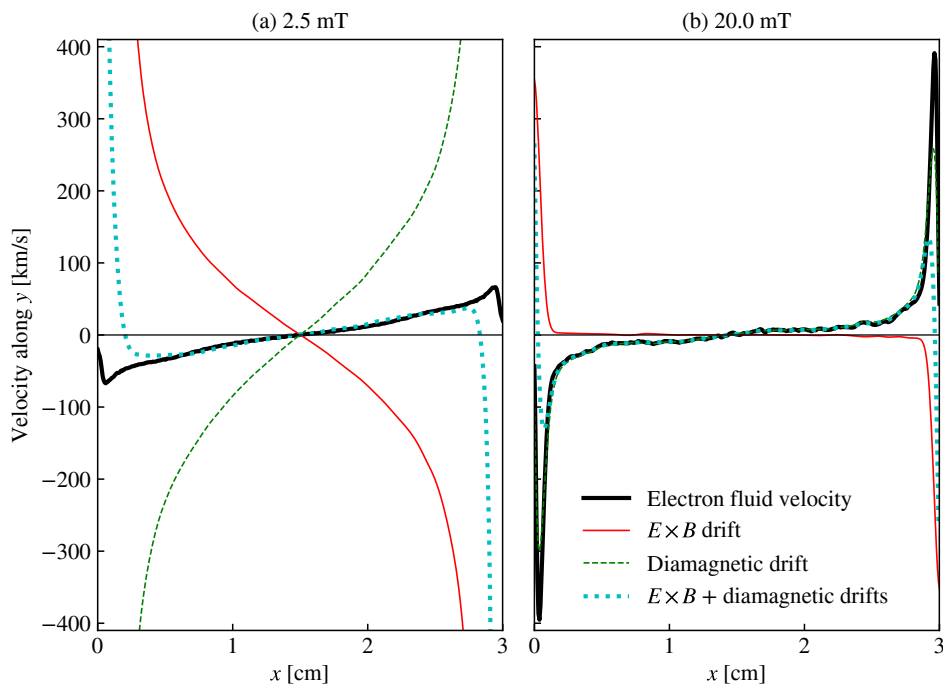


Figure 3.2: The electron fluid velocity along y extracted from the PIC simulation (solid black line) is compared to the diamagnetic drift (green dashed line) and the $E \times B$ drift (solid red line). The sum of the diamagnetic drift and the $E \times B$ drift is represented in cyan dotted line. The simulation data are averaged over a time greater than $4\ \mu\text{s}$. The pressure is 3 mTorr and the magnetic field is 2.5 mT (a) and 20 mT (b).

We have seen in Chapter 2 that the Bohm criterion that states that the ion velocity should be equal to the Bohm speed at the sheath edge is a necessary condition that appears naturally in the 1D quasineutral fluid model. This can be seen for example in Eq. (2.30) which is completely valid in the magnetized case. The Bohm sheath criterion was observed experimentally in magnetized plasma already in the original studies of Bohm [40]. Several authors have investigated the validity of the Bohm sheath criterion in magnetized plasmas. Allen has investigated the 1D cylindrical case with a fluid model and has retrieved the usual Bohm criterion from a Boltzmann gradient condition for the electrons [4]. The effect of the angle between the magnetic field vector and the wall was also studied separately by Chodura [32], Stangeby (1994) [112], and Yankun et al. (2011) [130]. The situation investigated in the present work is restricted to the case where the magnetic field is parallel to the wall, but the plasma unstable behavior is taken into account here, which was not possible with the equilibrium fluid models employed in former studies.

The Bohm criterion is supposed to define the boundary between the quasineutral plasma region and the sheath region. Fig. 3.3 shows that the electron density is already about 30% lower than the ion density when the ion velocity reaches the Bohm speed. This is in contrast with the non-magnetized case where the electron density is only about 6% lower than the ion density at the sheath edge (see Fig. 2.6), and it suggests that the accuracy of quasineutral models could be improved by selecting as a boundary condition a pre-sheath velocity that would be slightly lower than the Bohm speed.

3.1.6 Parametric studies with the magnetic field and the pressure

Already earlier than Bohm, it was found that collisions were not the right mechanism to describe the transport of the electrons away from the magnetic field lines where they are trapped. The high frequency oscillations in more or less random directions were suspected to be responsible for local electric fields that generate drifts pushing the electrons to the discharge walls. This effect was first described qualitatively by experimentalists [40]. In a paper by Yoshikawa and Rose [132] it is assumed that the direction of plasma oscillations is completely random and that the relative density fluctuations do not depend on the magnetic field at strong magnetic field. Under these conditions, the diffusion coefficient is inversely proportional to the magnetic field, which seemed in reasonable agreement with experimental observations. The conclusion of these former works is that the effective Hall parameter for the electrons should saturate at a value that is of the order of 10 or 100. The value of 16 is often used in the literature [132, 84].

In Fig. 3.4(a, b, c), the time averaged electron density is plotted as a function

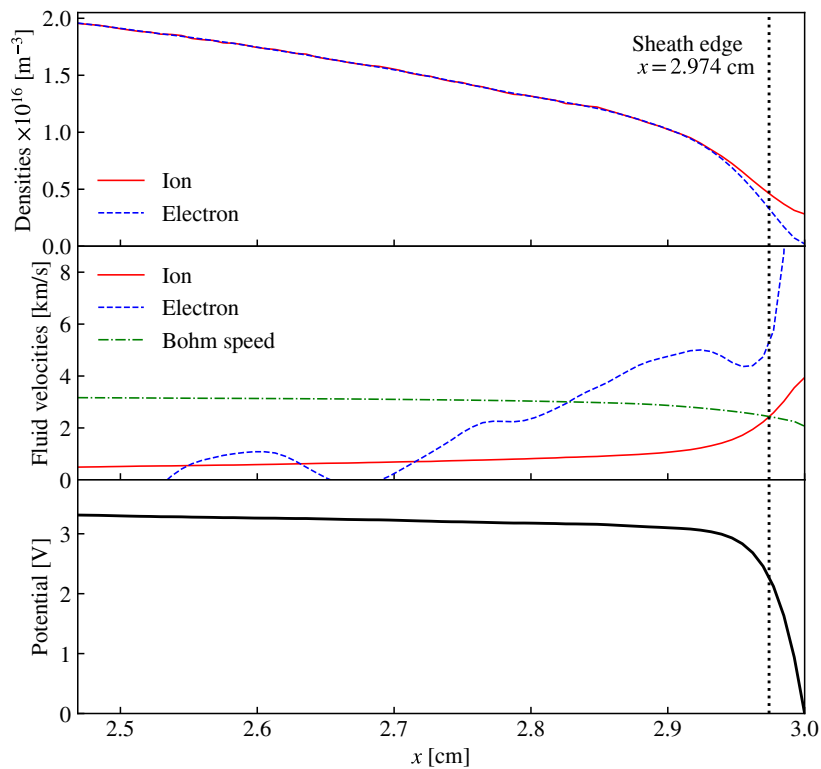


Figure 3.3: Magnetized sheath profiles at $y = l_y/2$ for a square (3×3 cm) discharge at 3 mTorr, 9.6 kW/m^3 and with a uniform magnetic field of 20 mT along z .

of x , at the discharge center ($y = l_y/2 = 1.5$ cm) for many values of the magnetic field and three values of the pressure. At low magnetic field, the electron density increases with the magnetic field, and then seems to saturate. Moreover, the shape of the profile is not much affected, and the typical cosine profile seems to be a reasonable solution. The electron temperature profiles are shown in Fig. 3.4(d, e, f). The assumption that the electron temperature is uniform in the bulk plasma seems to be satisfied as well. The electron temperature first decreases with the magnetic field, which is in agreement with the classical theory, and then saturates to a certain value that weakly depends on the pressure. When the magnetic field is above 30 mT, fluctuations are visible in the electron temperature. According to the global particle balance equation taken at steady-state (Eq. (1.99)), the fact that the plasma density saturates at high magnetic field is a hint that the h factor, and therefore the diffusion coefficient have minimum values, whatever the magnetic field.

Fig. 3.5 shows the electric currents collected along the bottom wall of the simulation domain due to electrons (negative currents) and ions (positive currents) for various simulation runs at 6 mTorr. The ion current features a cosine shape that resembles the density profiles of Fig. 3.4. The ion current is remarkably constant with the magnetic field. The magnetic confinement tends both to increase the plasma density and to reduce the ion speed at the sheath edge because the electron temperature decreases. These two effects seem to cancel out in the ion flux. This unexpected feature could be subject to further investigations. The profiles of electron currents are much more complex. First, the mean electron current over all the walls of the discharge is always exactly opposite to the mean ion current, which ensures that the plasma has reached a steady-state. This condition can be called a *global ambipolarity* condition. At low magnetic field, we could find the same patterns as in previous works [78, 87]. In the high pressure limit with no magnetic field, one could show that the electron flux should be uniform along the wall, except near the corner where the sheath is distorted. At high magnetic field, the electrons rotate in the azimuthal direction. The mean motion of the particles is in the $E \times B$ direction, while the electron *fluid* current is always in the direction of the diamagnetic drift. The simulations showed that at high magnetic field, the electron flux at the wall is locally equal to the ion flux, which is equivalent to the ambipolar condition found in former publications [78, 74]. In between these two asymptotic regimes, the electrons are magnetized but they do not yet dominate the transport process, such that the electron flux is distorted with surprising patterns that look like stationary waves. As shown in Fig. 3.3 (center), these patterns can also be detected with the electron current diagnostics in volume, but the noise is quite large due to both the large drift velocity in the azimuthal direction, and the instability.

The 2D maps of the normalized density are plotted in Fig. 3.6 for various values of the pressure and the magnetic field. The instability seems to play an important

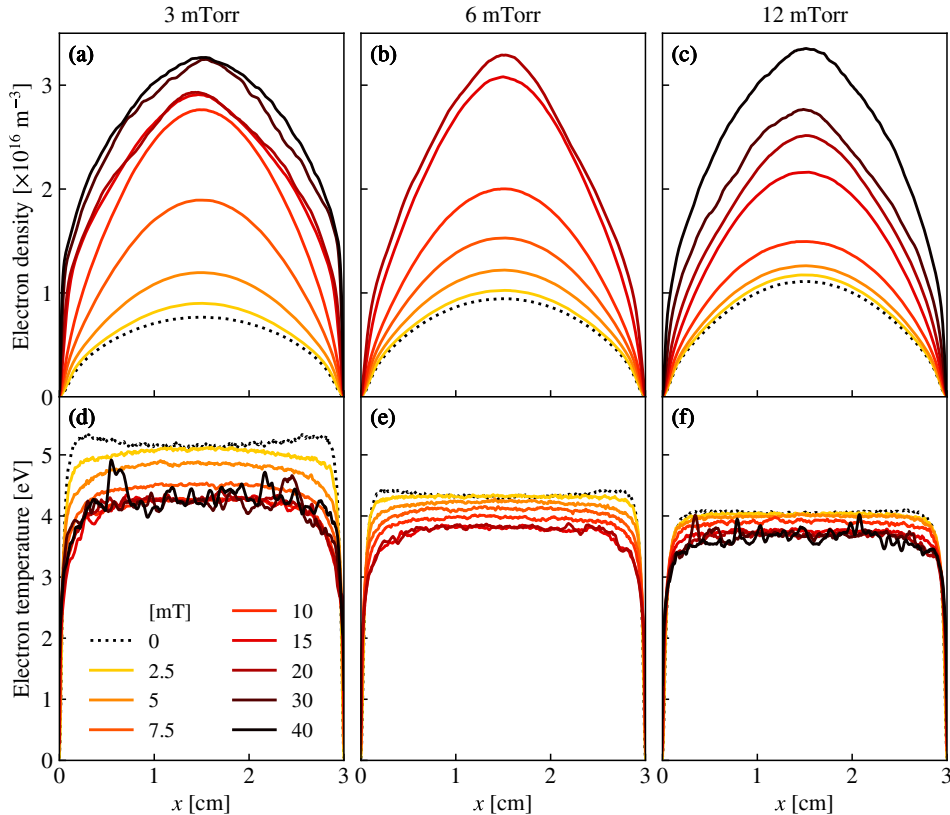


Figure 3.4: Curves of the time-averaged electron density (a, b, c) and the electron temperature (d, e, f) at $y = 1.5 \text{ cm}$. The density is averaged over at least $5 \mu\text{s}$ of simulation while the electron temperature is only averaged over $N_{\text{average}}dT \approx 0.1 \mu\text{s}$.

role in the discharge aspect only when the magnetic field is higher than a certain threshold that depends on the pressure. Once the threshold is passed, the 2D density profiles are more and more distorted by the magnetic field. The instability develops first mainly in the azimuthal direction. When the magnetic field further increases, more complex structures with smaller wavelengths appear.

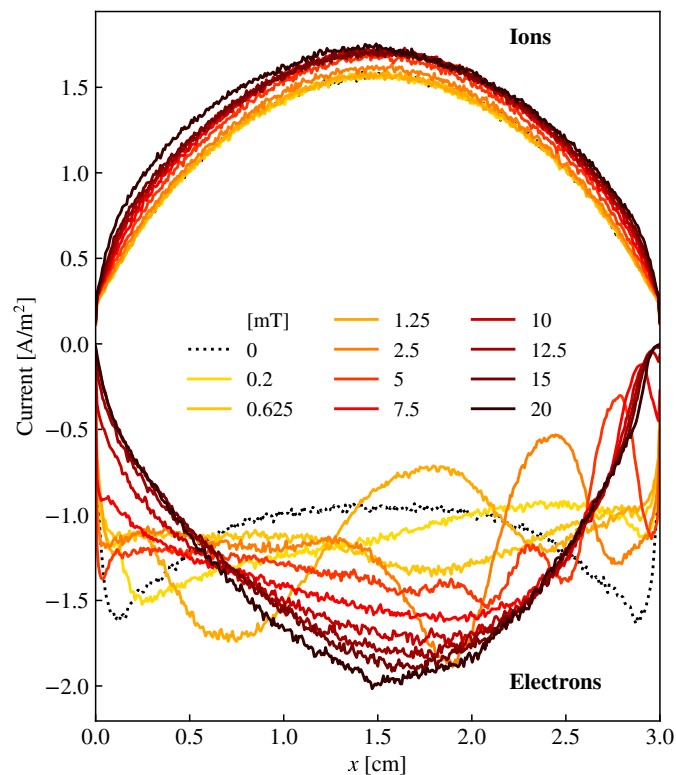


Figure 3.5: Electron currents (bottom, negative) and ions (top, positive) collected at the bottom wall of the simulation ($y = 0 \text{ cm}$) and averaged over at least $5 \mu\text{s}$ of simulation.

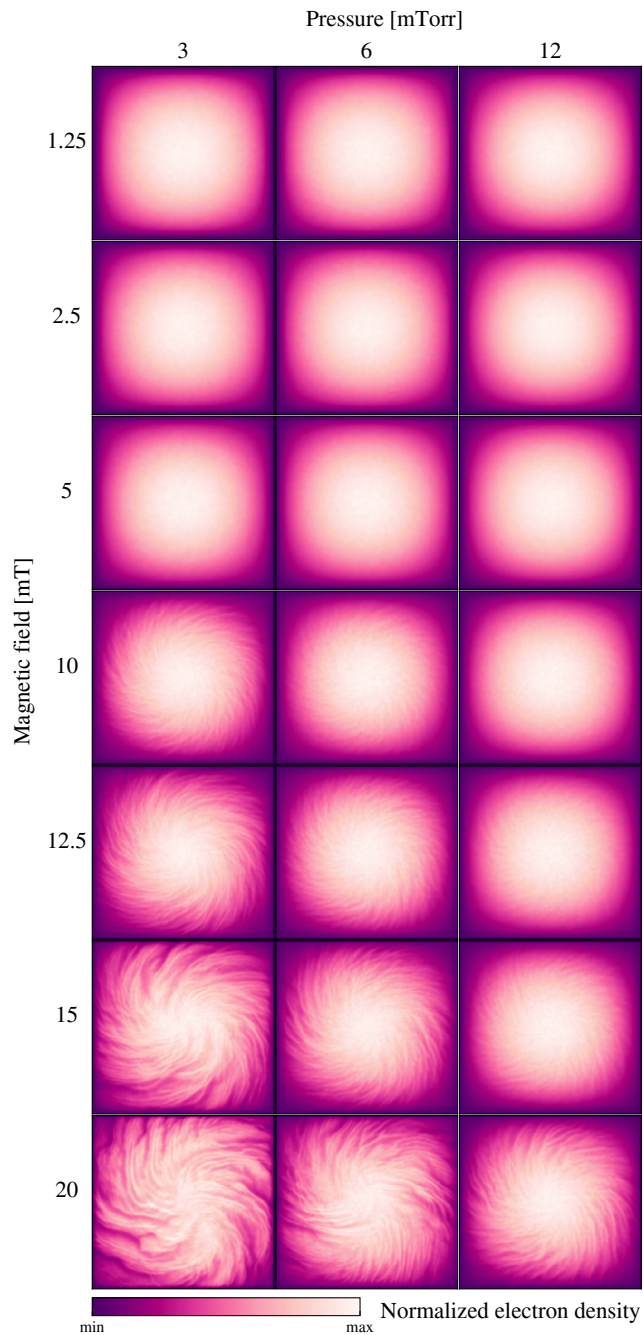


Figure 3.6: Normalized density map for 21 *LPPic* simulation runs after instability saturation for various values of the pressure (vertical axis) and the magnetic field (horizontal axis).

3.2 The collisional resistive drift instability

The aim of this section is to describe the linear propagation of oscillatory modes in the direction of the electron drift using isothermal fluid theory.

3.2.1 Model introduction

The effect of curvature is neglected and it is assumed that the wave propagation is purely 1D. The electron temperature is assumed uniform and the ion temperature is neglected. It is further assumed that the ions are not magnetized.

All the frequencies are normalized to the electron cyclotron frequency and the distances are normalized to the thermal electron Larmor radius. The plasma potential is normalized to the electron temperature in volts. The plasma density is normalized to the plasma density in the discharge center n_0 . The whole set of normalized quantities is listed below.

$$\begin{aligned}
 \tilde{n} &= n/n_0 \\
 \tilde{l} &= l/\rho_{Le} \\
 \tilde{v}_e &= v_e/\omega_{ce} \\
 \tilde{v}_i &= v_i/\omega_{ce} \\
 \tilde{\omega}_{ce} &= 1 \\
 \tilde{\omega}_{ci} &= m_e/m_i \\
 \tilde{t} &= \omega_{ce} t \\
 \tilde{\omega}_{pe} &= \omega_{pe}/\omega_{ce} \\
 \tilde{\mathbf{k}} &= \rho_{Le} \mathbf{k} \\
 \tilde{\mathbf{x}} &= \mathbf{x}/\rho_{Le} \\
 \tilde{\mathbf{v}} &= \mathbf{v}/v_{Te} \\
 \tilde{\nabla} &= \rho_{Le} \nabla
 \end{aligned} \tag{3.4}$$

Poisson's equation in normalized units is

$$\frac{\tilde{\nabla}^2 \tilde{\phi}}{\tilde{\omega}_{pe}} = \tilde{n}_e - \tilde{n}_i \tag{3.5}$$

We consider small perturbations of the plasma potential and the electron and ion densities:

$$\tilde{n}_e = \tilde{n}_{e0}(\tilde{x}) + \tilde{n}_{e1}(\tilde{y}, \tilde{t}); \quad \tilde{n}_i = \tilde{n}_{i0}(\tilde{x}) + \tilde{n}_{i1}(\tilde{y}, \tilde{t}); \quad \tilde{\phi} = \tilde{\phi}_0(\tilde{x}) + \tilde{\phi}_1(\tilde{y}, \tilde{t}) \tag{3.6}$$

with $n_{e1} \ll n_{e0}$, $n_{i1} \ll n_{i0}$ and $\tilde{\phi}_1 \ll \tilde{\phi}_0$, and n_1 and $\tilde{\phi}_1$ proportional to $\exp(-i\tilde{\omega}\tilde{t} + i\tilde{k}\tilde{y})$.

To the first order, Eq. (3.5) implies

$$-\frac{\tilde{k}^2}{\tilde{\omega}_{pe}^2} \tilde{\phi}_1 = \tilde{n}_{e1} - \tilde{n}_{i1} \quad (3.7)$$

which can be written under the form

$$1 + \chi_e + \chi_i = 0 \quad (3.8)$$

where

$$\chi_e = \frac{\tilde{\omega}_{pe}^2 \tilde{n}_{e1}}{\tilde{k}^2 \tilde{\phi}_1} \text{ and } \chi_i = -\frac{\tilde{\omega}_{pe}^2 \tilde{n}_{i1}}{\tilde{k}^2 \tilde{\phi}_1} \quad (3.9)$$

are the electron and ion susceptibilities.

3.2.2 Dispersion relation in a homogeneous plasma

In this paragraph, it is assumed that the equilibrium quantities \tilde{n}_{e0} , \tilde{n}_{i0} and $\tilde{\phi}_1$ have slow variations with respect to \tilde{x} .

The ion momentum conservation equation is

$$\mu \frac{d\tilde{\mathbf{v}}_i}{d\tilde{t}} = -\tilde{\nabla} \tilde{\phi} - \tilde{v}_i \tilde{\mathbf{v}}_i. \quad (3.10)$$

where $\frac{d}{d\tilde{t}}$ is the total time derivative. The \tilde{y} axis projection of Eq. (3.10) yields to the first order, in the referential of the drift motion of the ions ($\tilde{\mathbf{v}}_i = 0$)

$$-i\mu\tilde{\omega}\tilde{v}_{iy1} = -i\tilde{k}\tilde{\phi}_1 - \tilde{v}_i \tilde{v}_{iy1} \quad (3.11)$$

We assume that the frequency of the perturbations is much greater than the electron impact ionization frequency, such that the ion continuity equation is

$$\partial_t \tilde{n}_i + \tilde{\nabla} \cdot (\tilde{n}_i \tilde{\mathbf{v}}_i) = 0 \quad (3.12)$$

which becomes to the first order

$$-i\tilde{\omega}\tilde{n}_{i1} + i\tilde{k}\tilde{n}_{i0}\tilde{v}_{iy1} = 0 \quad (3.13)$$

Eqs. (3.11) and (3.13) are combined and lead to

$$\chi_i = -\frac{\mu\tilde{\omega}_{pe}^2}{\tilde{\omega}(\tilde{\omega} + i\tilde{v}_i)} \quad (3.14)$$

The picture is similar for the electrons but the resolution is slightly more complicated due to the magnetic field and the pressure term. In normalized quantities, the electron momentum conservation equation is

$$\frac{d\tilde{\mathbf{v}}_e}{d\tilde{t}} = \tilde{\nabla}\tilde{\phi} - \tilde{\mathbf{v}}_e \times \mathbf{b} - \frac{\tilde{\nabla}\tilde{n}_e}{\tilde{n}_e} - \tilde{v}_e \tilde{\mathbf{v}}_e. \quad (3.15)$$

where \mathbf{b} is a unit vector in the direction of the magnetic field. The analysis is first performed in the electron reference frame where $\tilde{\mathbf{v}}_e = 0$. The two components of Eq. (3.15) are to the first order

$$-i\tilde{\omega}\tilde{v}_{ex1} = -\tilde{v}_{ey1} - \tilde{v}_e \tilde{v}_{ex1} \quad (3.16)$$

$$-i\tilde{\omega}\tilde{v}_{ey1} = i\tilde{k}\tilde{\phi}_1 + \tilde{v}_{ex1} - \frac{i\tilde{k}\tilde{n}_{e1}}{\tilde{n}_{e0}} - \tilde{v}_e \tilde{v}_{ey1} \quad (3.17)$$

Eliminating \tilde{v}_{ex1} ,

$$(i\tilde{\omega} - \tilde{v}_e)\tilde{v}_{ey1} + i\tilde{k}\tilde{\phi}_1 + \frac{\tilde{v}_{ey1}}{i\tilde{\omega} - \tilde{v}_e} - \frac{i\tilde{k}\tilde{n}_{e1}}{\tilde{n}_{e0}} = 0 \quad (3.18)$$

The continuity equation writes exactly the same way as for the ions (Eq. (3.13)) and leads to

$$\chi_e = -\frac{\tilde{\omega}_{pe}^2(\tilde{\omega} + i\tilde{v}_e)}{(\tilde{\omega} + i\tilde{v}_e)^2\tilde{\omega} - \tilde{k}^2(\tilde{\omega} + i\tilde{v}_e) - \tilde{\omega}} \quad (3.19)$$

Let us now assume that the wave frequency and the collision frequency are both smaller than the electron cyclotron frequency

$$|\tilde{\omega} + i\tilde{v}| \ll 1 \quad (3.20)$$

The computation will be performed to the first order in $|\tilde{\omega} + i\tilde{v}|$. In this approximation

$$\chi_e = \frac{\tilde{\omega}_{pe}^2(\tilde{\omega} + i\tilde{v}_e)}{\tilde{k}^2(\tilde{\omega} + i\tilde{v}_e) + \tilde{\omega}} \quad (3.21)$$

Let us now assume that the electrons are drifting with respect to the ions with a velocity \tilde{v}_d . If $\tilde{\omega}$ is the wave frequency in the ion referential, it has to be shifted to $\tilde{\omega} - \tilde{\omega}_d$ in the referential of the ions, where $\tilde{\omega}_d = \tilde{k}\tilde{v}_d$, such that the electron susceptibility is $\chi_e = -\frac{\tilde{\omega}_{pe}^2(\tilde{\omega} - \tilde{\omega}_d + i\tilde{v}_e)}{\tilde{k}^2(\tilde{\omega} - \tilde{\omega}_d + i\tilde{v}_e) + \tilde{\omega}}$. In this case, the perturbed Poisson's equation (3.8) is

$$P(\tilde{\omega}) = P_0(\tilde{\omega}) + i\tilde{v}Q(\tilde{\omega}) + i\tilde{v}_iQ_i(\tilde{\omega}) - \tilde{v}\tilde{v}_iR(\tilde{\omega}) = 0 \quad (3.22)$$

where

$$P_0(\tilde{\omega}) = (\tilde{\omega} - \tilde{\omega}_d) [(1 + \tilde{k}^2 + \tilde{\omega}_{pe}^{-2})\tilde{\omega}^2 - \mu \tilde{\omega}_{pe}^2(1 + \tilde{k}^2)] ; \quad (3.23)$$

$$Q(\tilde{\omega}) = (\tilde{k}^2 + \tilde{\omega}_{pe}^{-2})\tilde{\omega}^2 - \mu \tilde{\omega}_{pe}^2 \tilde{k}^2 ; \quad (3.24)$$

$$Q_i(\tilde{\omega}) = \tilde{\omega}(\tilde{\omega} - \tilde{\omega}_d)(1 + \tilde{k}^2 + \tilde{\omega}_{pe}^{-2}) ; \quad (3.25)$$

$$R(\tilde{\omega}) = (\tilde{k}^2 + \tilde{\omega}_{pe}^{-2})\tilde{\omega} . \quad (3.26)$$

If there are no collisions, the modes that can exist in the plasma are the roots of P_0 :

$$\tilde{\omega}_0 = \tilde{\omega}_d \text{ and } \tilde{\omega}_{\pm} = \pm \tilde{\omega}_{pe} \left[\frac{\mu(1 + \tilde{k}^2)}{1 + \tilde{k}^2 + \tilde{\omega}_{pe}^{-2}} \right]^{1/2} \quad (3.27)$$

which are purely harmonic modes. Since the phase velocity of the $\tilde{\omega} = \tilde{\omega}_d$ mode is the electron drift velocity, it is called an electron beam mode. Three asymptotic regimes are of interest for the $\tilde{\omega}_{\pm}$ mode:

- If $\tilde{k} \ll 1$, $\tilde{\omega}_{\pm} = \pm \frac{\mu^{1/2}}{(1 + \tilde{\omega}_{pe}^{-2})^{1/2}}$, which corresponds to the lower hybrid modes.
- If $1 \ll \tilde{k} \ll \tilde{\omega}_{pe}$, $\tilde{\omega}_{\pm} = \pm \tilde{k}\mu^{1/2}$, which corresponds to the ion acoustic modes.
- If $\tilde{k} \gg \tilde{\omega}_{pe}$, $\tilde{\omega}_{\pm} = \pm \tilde{\omega}_{pe}\mu^{1/2}$, which corresponds to the ion plasma frequency.

We are now interested in the perturbation of these modes by collisions, under the assumption $\tilde{v}, \tilde{v}_i \ll \tilde{\omega}$. In general the electron collision frequency is higher than the ion collision frequency, due to the higher electron speed. Except in very special cases, $Q(\tilde{\omega})$ and $Q_i(\tilde{\omega})$ are of the same order. So the contribution of Q_i can be neglected. Since $\tilde{v}_i < \tilde{v}$, the contribution of $R(\tilde{\omega})$ is of order 2. The only perturbation of P_0 taken into account comes therefore from the electron collisions. Let $\tilde{\omega}_r$ be a root of P_0 , and $\tilde{\omega}_r + i\tilde{v}\delta$ the corresponding perturbed root of P (when there are no collisions $P = P_0$ and the roots are equal).

$$0 = P(\tilde{\omega}_r + i\tilde{v}\delta) \quad (3.28)$$

$$= P_0(\tilde{\omega}_r) + i\tilde{v}\delta P'_0(\tilde{\omega}_r) + i\tilde{v}Q(\tilde{\omega}_r) + \mathcal{O}(\tilde{v}^2) \quad (3.29)$$

To the 0-th order in \tilde{v} ,

$$\delta = -\frac{Q(\tilde{\omega}_r)}{P'_0(\tilde{\omega}_r)} \quad (3.30)$$

The stability of the perturbed mode $\tilde{\omega}_r$ is hence determined by the sign of δ . If $\delta > 0$, the mode is unstable, and if $\delta < 0$, the mode is stable.

$$\begin{aligned} P'_0(\tilde{\omega}_d) &= (1 + \tilde{k}^2 + \tilde{\omega}_{pe}^2)\tilde{\omega}_d^2 - \mu\tilde{\omega}_{pe}^2(1 + \tilde{k}^2) \\ &= (1 + \tilde{k}^2 + \tilde{\omega}_{pe}^2)(\tilde{\omega}_d^2 - \tilde{\omega}_+^2) \end{aligned} \quad (3.31)$$

$$P'_0(\tilde{\omega}_\pm) = 2\tilde{\omega}_+(1 + \tilde{k}^2 + \tilde{\omega}_{pe}^2)(\tilde{\omega}_+ \mp \tilde{\omega}_d) \quad (3.32)$$

Moreover,

$$Q(\tilde{\omega}_d) = (\tilde{k}^2 + \tilde{\omega}_{pe}^2)\tilde{\omega}_d^2 - \mu\tilde{\omega}_{pe}^2\tilde{k}^2 \quad (3.33)$$

$$Q(\tilde{\omega}_\pm) = \frac{\mu\tilde{\omega}_{pe}^4}{1 + \tilde{k}^2 + \tilde{\omega}_{pe}^2} > 0 \quad (3.34)$$

We define

$$\delta_0 = -\frac{Q(\tilde{\omega}_d)}{P'_0(\tilde{\omega}_d)} \text{ and } \delta_\pm = -\frac{Q(\tilde{\omega}_\pm)}{P'_0(\tilde{\omega}_\pm)} \quad (3.35)$$

δ_+ has the sign of $\tilde{\omega}_d - \tilde{\omega}_+$ and δ_- has the sign of $-\tilde{\omega}_d - \tilde{\omega}_+$. Hence:

- If $\tilde{\omega}_d^2 > \tilde{\omega}_+^2$, either the $\tilde{\omega}_+$ mode or the $\tilde{\omega}_-$ mode is unstable.
- If $\tilde{\omega}_d^2 < \tilde{\omega}_+^2$, then $\tilde{\omega}_+$ and $\tilde{\omega}_-$ modes are both stable. Furthermore,

$$\delta_0 = \frac{\mu\tilde{\omega}_{pe}^2\tilde{k}^2 - (\tilde{k}^2 + \tilde{\omega}_{pe}^2)\tilde{\omega}_d^2}{(1 + \tilde{k}^2 + \tilde{\omega}_{pe}^2)(\tilde{\omega}_d^2 - \tilde{\omega}_+^2)} \quad (3.36)$$

has the same sign as $(\tilde{k}^2 + \tilde{\omega}_{pe}^2)\tilde{\omega}_d^2 - \mu\tilde{\omega}_{pe}^2\tilde{k}^2$. Hence, $\tilde{\omega} = \tilde{\omega}_d$ mode is stable if

$$\tilde{\omega}_d^2 < \frac{\mu\tilde{\omega}_{pe}^2\tilde{k}^2}{\tilde{k}^2 + \tilde{\omega}_{pe}^2} \quad (3.37)$$

In summary, since $\frac{\mu\tilde{\omega}_{pe}^2\tilde{k}^2}{\tilde{k}^2 + \tilde{\omega}_{pe}^2} < \tilde{\omega}_+^2$, the plasma is stable if and only if condition (3.37)

$$\tilde{\omega}_d < \frac{\mu^{1/2}\tilde{k}}{(1 + k^2/\tilde{\omega}_{pe}^2)^{1/2}} \quad (3.38)$$

where the sign of \tilde{k} is chosen to match \tilde{v}_d 's sign. In the case where the drift velocity is higher than the Bohm speed ($\tilde{v}_d^2 > \mu$), this condition is never satisfied and the plasma is unstable for all wavenumbers. This instability is not an ion acoustic wave, in the sense that its phase velocity is not constant and is not equal to the Bohm speed. If the drift velocity is lower than the Bohm speed, stability occurs for low wavenumbers

$$\tilde{k}^2 < \tilde{\omega}_{pe}^2 \left(\frac{\mu}{\tilde{v}_d^2} - 1 \right) \quad (3.39)$$

3.2.3 Dispersion relation in an inhomogeneous plasma

The situation derived above corresponds to the ideal situation of a uniform plasma. When plasma inhomogeneities are to be taken into account, one cannot decouple the perturbed motion to the 0-th order drift motion.

It is assumed that a steady-state solution is perturbed by a harmonic wave propagating in the y direction such that the first order densities \tilde{n}_{e1} and \tilde{n}_{i1} for electrons and ions respectively, and the first order potential $\tilde{\phi}_1$ are proportional to $\exp(-i\tilde{\omega}\tilde{t} + i\tilde{k}\tilde{y})$, where $\tilde{\omega}$ is the complex wave frequency (normalized to $\tilde{\omega}_{ce}$), and \tilde{k} is the wavenumber (normalized to ρ_L^{-1}).

It is now assumed that

$$\tilde{v}, d/dt = \mathcal{O}(\epsilon) \quad (3.40)$$

$$\tilde{\phi}, \tilde{n}, |\tilde{\nabla}| = \mathcal{O}(1) \quad (3.41)$$

where ϵ is a small parameter, we can expand $\tilde{\mathbf{v}}$ with respect to ϵ . To the 0-th order, Eq. (3.15) is

$$\tilde{\nabla}\tilde{\phi} - \tilde{\mathbf{v}} \times \mathbf{b} - \tilde{\nabla}\tilde{n}/\tilde{n} = 0 \quad (3.42)$$

which yields the $E \times B$ and diamagnetic drifts, respectively

$$\tilde{\mathbf{v}}_{E \times B} = \mathbf{b} \times \tilde{\nabla}\tilde{\phi} \quad \text{and} \quad \tilde{\mathbf{v}}_* = \frac{\tilde{\nabla}\tilde{n}}{\tilde{n}} \times \mathbf{b}. \quad (3.43)$$

Eq. (3.15) is then to the first order

$$\frac{d}{dt}(\tilde{\mathbf{v}}_{E \times B} + \tilde{\mathbf{v}}_*) = -\tilde{\mathbf{v}}^{(1)} \times \mathbf{b} - \tilde{v}(\tilde{\mathbf{v}}_{E \times B} + \tilde{\mathbf{v}}_*) \quad (3.44)$$

where $\tilde{\mathbf{v}}^{(1)} = \tilde{\mathbf{v}} - \tilde{\mathbf{v}}_{E \times B} - \tilde{\mathbf{v}}_*$ is the first order term of the electron velocity. Hence,

$$\tilde{\mathbf{v}}^{(1)} = \tilde{\mathbf{v}}_p + \tilde{\mathbf{v}}_{dp} \quad (3.45)$$

where

$$\tilde{\mathbf{v}}_p = \left(\frac{d}{d\tilde{t}} + \tilde{v} \right) \tilde{\mathbf{v}}_{E \times B} \times \mathbf{b} = \left(\frac{d}{d\tilde{t}} + \tilde{v} \right) \tilde{\nabla}\tilde{\phi} \quad (3.46)$$

and

$$\tilde{\mathbf{v}}_{dp} = \left(\frac{d}{d\tilde{t}} + \tilde{v} \right) \tilde{\mathbf{v}}_* \times \mathbf{b} = - \left(\frac{d}{d\tilde{t}} + \tilde{v} \right) \frac{\tilde{\nabla}\tilde{n}}{\tilde{n}} \quad (3.47)$$

are the polarization drift terms due to the $E \times B$ and the diamagnetic drifts, respectively (including the friction force). It is useful to derive the divergence of the fluxes corresponding to each of the drift terms.

$$\tilde{\nabla} \cdot (\tilde{n}\mathbf{v}_{E \times B}) = (\mathbf{b} \times \tilde{\nabla}\tilde{\phi}) \cdot \tilde{\nabla}\tilde{n} + \tilde{n}\tilde{\nabla} \cdot (\mathbf{b} \times \tilde{\nabla}\tilde{\phi}) \quad (3.48)$$

The second term is zero due to the general formula

$$\nabla \cdot (u \times v) = -u \cdot (\nabla \times v) + v \cdot (\nabla \times u). \quad (3.49)$$

Thus,

$$\tilde{\nabla} \cdot (\tilde{n}\tilde{\mathbf{v}}_{E \times B}) = (\mathbf{b} \times \tilde{\nabla}\tilde{\phi}) \cdot \tilde{\nabla}\tilde{n} \quad (3.50)$$

Using again Eq. (3.49),

$$\tilde{\nabla} \cdot (\tilde{n}\tilde{\mathbf{v}}_*) = 0. \quad (3.51)$$

By neglecting all particle source and loss terms ($\tilde{v}_{iz} \ll \tilde{\omega}$), the electron continuity equation is

$$\partial_{\tilde{t}}\tilde{n} + \tilde{\nabla} \cdot (\tilde{n}\tilde{\mathbf{v}}) = 0. \quad (3.52)$$

So to the first order in ϵ ,

$$\partial_{\tilde{t}}\tilde{n} + \tilde{\nabla} \cdot [\tilde{n}(\tilde{\mathbf{v}}_{E \times B} + \tilde{\mathbf{v}}_* + \tilde{\mathbf{v}}_p + \tilde{\mathbf{v}}_{dp})] = 0, \quad (3.53)$$

or

$$\partial_{\tilde{t}}\tilde{n} + (\mathbf{b} \times \tilde{\nabla}\tilde{\phi}) \cdot \tilde{\nabla}\tilde{n} + \tilde{\nabla} \cdot \left[\tilde{n} \left(\frac{d}{d\tilde{t}} + \tilde{v} \right) \left(\tilde{\nabla}\tilde{\phi} - \frac{\tilde{\nabla}\tilde{n}}{\tilde{n}} \right) \right] = 0 \quad (3.54)$$

The only term contributing to the motion of the electron guiding centers is the $E \times B$ drift [129]

$$\frac{d}{d\tilde{t}} = \partial_{\tilde{t}} + \tilde{\mathbf{v}}_{E \times B} \cdot \tilde{\nabla} \quad (3.55)$$

Using the property

$$\tilde{\nabla} \cdot [(\tilde{\mathbf{v}}_{E \times B} \cdot \tilde{\nabla})\tilde{\nabla}\tilde{\phi}] = (\tilde{\mathbf{v}}_{E \times B} \cdot \tilde{\nabla})\tilde{\nabla}^2\tilde{\phi}, \quad (3.56)$$

$$\begin{aligned} \tilde{\nabla} \cdot (\tilde{n}\tilde{\mathbf{v}}_p) &= \tilde{n} \left(\partial_{\tilde{t}} + \tilde{\mathbf{v}}_{E \times B} \cdot \tilde{\nabla} + \tilde{v} \right) \nabla^2\tilde{\phi} \\ &\quad + \tilde{\nabla}\tilde{n} \cdot \left(\partial_{\tilde{t}} + \mathbf{v}_{E \times B} \cdot \tilde{\nabla} + \tilde{v} \right) \tilde{\nabla}\tilde{\phi}. \end{aligned} \quad (3.57)$$

For the density gradient polarization drift,

$$\begin{aligned} \tilde{\nabla} \cdot (\tilde{n}\tilde{\mathbf{v}}_{dp}) &= \tilde{\nabla} \cdot \left[\frac{\tilde{\nabla}\tilde{n}}{\tilde{n}} \left(\partial_{\tilde{t}} + \tilde{\mathbf{v}}_{E \times B} \cdot \tilde{\nabla} \right) \tilde{n} \right] \\ &\quad - \left(\partial_{\tilde{t}} + \tilde{v} \right) \tilde{\nabla}^2\tilde{n} - \tilde{\nabla} \cdot [(\tilde{\mathbf{v}}_{E \times B} \cdot \tilde{\nabla})\tilde{\nabla}\tilde{n}]. \end{aligned} \quad (3.58)$$

We assume

$$\tilde{n} = \tilde{n}_0(\tilde{x}) + \tilde{n}_1(\tilde{y}, \tilde{t}) \quad ; \quad \tilde{\phi} = \tilde{\phi}_0(\tilde{x}) + \tilde{\phi}_1(\tilde{y}, \tilde{t}) \quad (3.59)$$

with $n_1 \ll n_0$ and $\tilde{\phi}_1 \ll \tilde{\phi}_0$, and \tilde{n}_1 and $\tilde{\phi}_1$ proportional to $\exp(-i\tilde{\omega}\tilde{t} + i\tilde{k}\tilde{y})$. To the first order in $\tilde{\phi}_1$ and \tilde{n}_1 :

$$\begin{aligned}\tilde{\nabla} \cdot (\tilde{n}\tilde{\mathbf{v}}_p) &= \tilde{n}_0 [\partial_{\tilde{t}} + (\mathbf{b} \times \tilde{\nabla} \tilde{\phi}_0 \cdot \tilde{\nabla}) + \tilde{v}] \tilde{\nabla}^2 \tilde{\phi}_1 \\ &\quad + \tilde{v}\tilde{n}_1 \tilde{\nabla}^2 \tilde{\phi}_0 + n_0 (\mathbf{b} \times \tilde{\nabla} \tilde{\phi}_1 \cdot \tilde{\nabla}) \tilde{\nabla}^2 \tilde{\phi}_0 \\ &\quad + \nabla n_0 \cdot (\mathbf{b} \times \nabla \phi_1 \cdot \nabla) \nabla \phi_0\end{aligned}\quad (3.60)$$

$$\begin{aligned}\tilde{\nabla} \cdot (\tilde{n}\tilde{\mathbf{v}}_p) &= i\tilde{n}_0 \tilde{k}^2 (\tilde{\omega} + \tilde{\omega}_0 + i\tilde{v}) \tilde{\phi}_1 + \tilde{v}\tilde{n}_1 \tilde{\phi}_0'' \\ &\quad - i\tilde{k}\tilde{n}_0 \tilde{\phi}_0''' \tilde{\phi}_1 + i\tilde{\omega}_* \tilde{n}_0 \tilde{\phi}_0'' \tilde{\phi}_1\end{aligned}\quad (3.61)$$

where $\tilde{\omega}_* = -\tilde{k}\tilde{n}_0'/n_0$ and $\tilde{\omega}_{E \times B} = -\tilde{k}\tilde{\phi}_0'$. Similarly,

$$\begin{aligned}\tilde{\nabla} \cdot (\tilde{n}\tilde{\mathbf{v}}_{dp}) &= \tilde{\nabla} \cdot \left\{ \frac{\tilde{\nabla}\tilde{n}_0}{\tilde{n}_0} [\partial_{\tilde{t}} + (\mathbf{b} \times \tilde{\nabla} \tilde{\phi}_0 \cdot \tilde{\nabla})] \tilde{n}_1 \right\} \\ &\quad + \tilde{\nabla} \cdot \left[\frac{\tilde{\nabla}\tilde{n}_0}{\tilde{n}_0} (\mathbf{b} \times \tilde{\nabla} \tilde{\phi}_1 \cdot \tilde{\nabla}) \tilde{n}_0 \right] \\ &\quad - (\partial_{\tilde{t}} + \nu) \tilde{\nabla}^2 \tilde{n}_1 - \tilde{\nabla} \cdot [(\mathbf{b} \times \tilde{\nabla} \tilde{\phi}_0 \cdot \nabla) \tilde{\nabla} \tilde{n}_1] \\ &\quad - \tilde{\nabla} \cdot [(\mathbf{b} \times \tilde{\nabla} \tilde{\phi}_1 \cdot \tilde{\nabla}) \tilde{\nabla} \tilde{n}_0] \\ &= -i\tilde{n}_1 (\tilde{\omega} + \tilde{\omega}_{E \times B}) \left(\frac{\tilde{n}_0''}{\tilde{n}_0} - \frac{\tilde{\omega}_*^2}{\tilde{k}^2} \right) - i\tilde{n}_1 \tilde{\omega}_* \tilde{\phi}_0'' \\ &\quad + i\tilde{\omega}_* \tilde{n}_0 \tilde{\phi}_1 \left(2 \frac{\tilde{n}_0''}{\tilde{n}_0} - \frac{\tilde{\omega}_*^2}{\tilde{k}^2} \right) \\ &\quad - i\tilde{k}^2 (\tilde{\omega} + \tilde{\omega}_{E \times B} + i\tilde{v}) \tilde{n}_1 + i\tilde{k}\tilde{\phi}_1 \tilde{n}_0''.\end{aligned}\quad (3.62)$$

Finally, Eq. (3.50) yields

$$\tilde{\nabla} \cdot (\tilde{n}\tilde{\mathbf{v}}_{E \times B}) = -i\tilde{\omega}_{E \times B} \tilde{n}_1 + i\tilde{\omega}_* \tilde{n}_0 \tilde{\phi}_1 \quad (3.64)$$

To the first order in $\tilde{\omega}_*$, and neglecting second and third order derivatives of \tilde{n}_0 and $\tilde{\phi}_0$ (no shear),

$$\tilde{\nabla} \cdot (\tilde{n}\tilde{\mathbf{v}}_p) = i\tilde{n}_0 \tilde{k}^2 (\tilde{\omega} + \tilde{\omega}_{E \times B} + i\tilde{v}) \tilde{\phi}_1 \quad (3.65)$$

$$\tilde{\nabla} \cdot (\tilde{n}\tilde{\mathbf{v}}_{dp}) = -i\tilde{k}^2 (\tilde{\omega} + \tilde{\omega}_{E \times B} + i\tilde{v}) \tilde{n}_1 \quad (3.66)$$

Eq. (3.52) is therefore:

$$\begin{aligned}-i\tilde{\omega}\tilde{n}_1 - i\tilde{\omega}_{E \times B}\tilde{n}_1 + i\tilde{\omega}_* \tilde{n}_0 \tilde{\phi}_1 + i\tilde{n}_0 \tilde{k}^2 (\tilde{\omega} + \tilde{\omega}_{E \times B} + i\tilde{v}) \tilde{\phi}_1 \\ - i\tilde{k}^2 (\tilde{\omega} + \tilde{\omega}_{E \times B} + i\tilde{v}) \tilde{n}_1 = 0\end{aligned}\quad (3.67)$$

Hence,

$$\frac{\tilde{n}_1}{\tilde{n}_0} = \frac{\tilde{\omega}_* + \tilde{k}^2(\tilde{\omega} + \tilde{\omega}_{E \times B} + i\tilde{v})}{\tilde{\omega} + \tilde{\omega}_{E \times B} + \tilde{k}^2(\tilde{\omega} + \tilde{\omega}_{E \times B} + i\tilde{v})} \tilde{\phi}_1. \quad (3.68)$$

It follows then that the electron susceptibility is

$$\chi_e \equiv \frac{\tilde{\omega}_{pe}^2}{\tilde{k}^2} \frac{\tilde{n}_e 1}{\tilde{\phi}_1} = \frac{\tilde{\omega}_{pe}^2}{\tilde{k}^2} \frac{\tilde{\omega}_* + \tilde{k}^2(\tilde{\omega} + \tilde{\omega}_{E \times B} + i\tilde{v})}{(\tilde{\omega} + \tilde{\omega}_{E \times B}) + \tilde{k}^2(\tilde{\omega} + \tilde{\omega}_{E \times B} + i\tilde{v})} \quad (3.69)$$

where

$$\tilde{\omega}_{E \times B} = -\tilde{k}\tilde{\phi}' \quad , \quad \tilde{\omega}_* = -\tilde{k}\tilde{n}'/\tilde{n}. \quad (3.70)$$

The formula for the electron susceptibility should be compared with Eq. (3.21). The $E \times B$ drift plays a role that is similar to the fluid drift velocity of the homogeneous plasma approach. However, the diamagnetic drift plays a role that is completely different because of the contribution of the density gradient. Eq. (3.69) was also introduced by the gyroviscosity formalism in Smolyakov et al. [110].

Since the ions are non magnetized, the derivation of their susceptibility does not require a special treatment, and Eq. (3.14) is retained [8]. The assumption that $\tilde{v}_i \ll \tilde{v}$ is made again.

The first order Poisson's equation Eq. (3.8) provides a new dispersion relation. Introducing the polynomial

$$P_{0,I}(\tilde{\omega}) = (\tilde{\omega} + \tilde{\omega}_{E \times B}) [(1 + \tilde{k}^2 + \tilde{\omega}_{pe}^2)\tilde{\omega}^2 - \mu\tilde{\omega}_{pe}^2(1 + \tilde{k}^2)] + \tilde{\omega}^2\tilde{\omega}_{pe}^2\tilde{\omega}_*/\tilde{k}^2 \quad (3.71)$$

the dispersion relation is

$$P_I(\tilde{\omega}) = P_{0,I}(\tilde{\omega}) + i\tilde{v}Q(\tilde{\omega}) = 0. \quad (3.72)$$

where the Q polynomial is the same as in Section 3.2.2 (Eq. (3.24)). Interestingly,

$$P_{0,I}(\tilde{\omega}) = P_0(\tilde{\omega}) + \tilde{\omega}^2\tilde{\omega}_{pe}^2\tilde{\omega}_*/\tilde{k}^2 \quad (3.73)$$

under the assumption that $\tilde{\omega}_{E \times B} = \tilde{\omega}_d$. Eq. (3.72)) is valid as long as the frequency of the instability is smaller than the electron cyclotron harmonics, where a kinetic description of the Bernstein modes is required [5, 106, 8, 77]. Inspecting the following table, $P_{0,I}$ has always two negative roots and one positive root:

$\tilde{\omega}$	$-\infty$	$-\tilde{\omega}_{E \times B}$	0	$+\infty$
$P_{0,I}(\tilde{\omega})$	< 0	> 0	< 0	> 0

Let $\tilde{\omega}_r$ be the positive root. Since $\tilde{v} \ll 1$, collisions can be treated as a perturbation term. Once again, the perturbed solution being $\tilde{\omega}_r + i\tilde{v}\delta$, to the first order in \tilde{v} ,

$$P_I(\tilde{\omega}_r + i\tilde{v}\delta) = 0 \Leftrightarrow \delta = -Q(\tilde{\omega}_r)/P'_{0,I}(\tilde{\omega}_r) \quad (3.74)$$

Since $P'_{0,I}(\tilde{\omega}_r) > 0$, the mode stability is determined by the sign of $Q(\tilde{\omega}_r)$. If $\tilde{\omega}_* = \tilde{\omega}_{E\times B} = 0$, the positive root is

$$\tilde{\omega}_r = \mu^{1/2} \left(\frac{1}{\tilde{\omega}_{pe}^2} + \frac{1}{1 + \tilde{k}^2} \right)^{-1/2}, \quad (3.75)$$

a mode transiting from the lower hybrid frequency at low \tilde{k} 's to the ion plasma frequency at high \tilde{k} 's, and damped by collisions. If $\tilde{\omega}_{E\times B} = 0$, but $\tilde{\omega}_* \neq 0$, the solution is

$$\tilde{\omega}_r = \frac{\tilde{\omega}_* \tilde{\omega}_{pe}^2 \left\{ \left[1 + \frac{4\mu\tilde{k}^4(1+\tilde{k}^2)(1+\tilde{k}^2+\tilde{\omega}_{pe}^2)}{\tilde{\omega}_{pe}^2 \tilde{\omega}_*^2} \right]^{\frac{1}{2}} - 1 \right\}}{2\tilde{k}^2(1 + \tilde{k}^2 + \tilde{\omega}_{pe}^2)} \quad (3.76)$$

The general instability criterion is found by solving jointly $P_0(\tilde{\omega}) = 0$ (the mode exists) with $Q(\tilde{\omega}) = 0$ (the mode is at stability limit):

$$\tilde{\omega}_* - \tilde{\omega}_{E\times B} = \tilde{\omega} = \frac{\mu^{1/2}\tilde{k}}{(1 + \tilde{k}^2/\tilde{\omega}_{pe}^2)^{1/2}}. \quad (3.77)$$

This criterion is exactly the same one as in the homogeneous fluid model (see Eq. (3.37)) when $\tilde{\omega}_d = \tilde{\omega}_* - \tilde{\omega}_{E\times B}$. This confirms that the plasma is unstable when the total fluid electron drift is higher than the ion sound speed. The numerical resolution of the two other roots of P_I shows that they are all stable in the regime of interest here. Moreover, the equilibrium electron momentum conservation equation (Eq. (2.10)) in normalized quantities is

$$-\tilde{\phi}' = -\frac{\tilde{n}'}{\tilde{n}} - \tilde{v}_x \left(\frac{1}{\tilde{v}} + \nu \right). \quad (3.78)$$

Using Eqs. (3.70) and (3.78) for low wavenumbers, the plasma is unstable if:

$$\tilde{v}_x (1/\tilde{v} + \tilde{v}) > \mu^{1/2}. \quad (3.79)$$

At the sheath edge, $\tilde{v}_x = \mu^{1/2}$, and $1/\tilde{v} + \tilde{v}$ is greater than 1 for all $\tilde{v} > 0$. Therefore, the plasma is always unstable, at least at the sheath edge, as long as the electrons are magnetized ($l \gg 1$). The destabilization of similar modes by collisions was first found experimentally [14, 64] and explained theoretically by Chen [30] as a particular type of resistive drift mode [29].

3.2.4 Solutions of the dispersion relations

Figs. 3.7 and 3.8 show the solutions of the dispersion relations for $\tilde{\omega}_{pe} = 2$ and $\tilde{v}_{E \times B} = 0.2\mu^{1/2}$. $\tilde{v}_{E \times B}$ is here equal to $\tilde{\omega}_{E \times B}/\tilde{k}$, such that $\tilde{\mathbf{v}}_{E \times B} = -\tilde{v}_{E \times B}\mathbf{e}_y$. We remind that all the dispersion relations investigated here correspond to the high magnetic field approximation ($\tilde{\omega} \ll 1$). In every case, at high wavenumbers \tilde{k} , two modes represent the ion plasma oscillations $\tilde{\omega} = \pm\mu^{1/2}\tilde{\omega}_{pe}$ and the third mode represents the electron beam mode $\tilde{\omega} = \tilde{\omega}_d$. At low wavenumbers, the ion plasma oscillations become lower hybrid modes $\tilde{\omega} = \mu^{1/2}$. The collisionless case is illustrated in Fig. 3.8(b) in the case where $\tilde{v}_* = 1.3\mu^{1/2}$. In the collisionless case, only the inhomogeneous plasma theory can predict the anti-drift mode [110] at low wavenumber, where the frequency is proportional to $-\tilde{k}^{-1}$. In the present models, the growth rate is always zero without collisions, but we are aware that other mechanisms can cause instabilities to form in experimental plasmas, such as a non-zero component of the wavevector in the direction parallel to the magnetic field for example. The latter mechanism triggers the well-known *flute mode* [31].

Adding collisions to the models leads to non-zero imaginary parts of the solutions of the dispersion relations. In most cases, collisions result in a damping of plasma oscillations (negative imaginary part), but the plasma can also become unstable in some cases. We first notice that the homogeneous plasma model where the drift velocity is equal to the $E \times B$ drift predicts that the plasma is always stable for $E \times B$ drifts lower than the Bohm speed, while PIC simulations showed that the plasma unstable behavior appeared even at relatively low electric fields. In the homogeneous plasma model, the instability can be interpreted as a wave mixing between the electron beam mode and the lower hybrid / ion plasma mode. In the frame of the inhomogeneous plasma theory, the potentially unstable mode is the only mode that propagates in the drift direction (positive real part).

Stability criteria were established in Sections 3.2.2 and 3.2.3 in the frame of homogeneous and inhomogeneous plasma theories. It was found that the homogeneous plasma theory yields the same stability criterion as the inhomogeneous plasma theory, provided that the drift velocity is the sum of the $E \times B$ and the diamagnetic drift. However, the electron beam mode predicted by the inhomogeneous plasma theory corresponds to $\tilde{\omega} = -\tilde{\omega}_{E \times B}$, which is not in agreement with the electron beam mode found in the homogeneous case $\tilde{\omega} = \tilde{\omega}_* - \tilde{\omega}_{E \times B}$. This discrepancy is visible when comparing the phase diagrams of Fig. 3.7(b): the electron beam mode is correctly predicted by the homogeneous theory with $\tilde{v}_d = -\tilde{v}_{E \times B}$ but the instability criterion corresponds better to $\tilde{v}_d = \tilde{v}_* - \tilde{v}_{E \times B}$. Nevertheless, the growth rate is overestimated in the latter case.

Fig. 3.8(b) shows the harmonic solutions for the different dispersion relations in the collisionless case. In the limit of low collisionality, the most unstable mode in

the framework of homogeneous plasma theory comes from the intersection between two harmonic modes $\tilde{\omega}_d = \tilde{\omega}_+$ (see Eq. (3.27)). The corresponding wavenumber \tilde{k}_{\max} is a root of a second order polynomial but does not have any simplified expression. Considering the inhomogeneous plasma theory, the maximum growth rate cannot be estimated by Eq. (3.30) because $P'_0(\tilde{\omega}_d) = P'_0(\tilde{\omega}_+) = 0$ at $\tilde{k} = \tilde{k}_{\max}$. The Taylor expansion with respect to the solution perturbation has to be taken to the second order. The dispersion relation $P(\tilde{\omega}) = 0$ is equivalent to

$$(\tilde{\omega} - \tilde{\omega}_d)(\tilde{\omega} - \tilde{\omega}_+)(\tilde{\omega} + \tilde{\omega}_+) = -\frac{i\tilde{v} [(\tilde{k}_{\max}^2 + \tilde{\omega}_{pe}^2)\tilde{\omega}^2 - \mu\tilde{\omega}_{pe}^2\tilde{k}_{\max}^2]}{1 + \tilde{k}_{\max}^2 + \tilde{\omega}_{pe}^2} \quad (3.80)$$

The perturbation of the mode intersection writes $\tilde{\omega} = \tilde{\omega}_+ + i\tilde{v}\delta_{\max} = \tilde{\omega}_d + i\tilde{v}\delta_{\max}$, which yields

$$2\tilde{\omega}_+\tilde{v}^2\delta_{\max}^2 = \frac{i\tilde{v} [(\tilde{k}_{\max}^2 + \tilde{\omega}_{pe}^2)\tilde{\omega}^2 - \mu\tilde{\omega}_{pe}^2\tilde{k}_{\max}^2]}{1 + \tilde{k}_{\max}^2 + \tilde{\omega}_{pe}^2} \quad (3.81)$$

Hence,

$$\delta_{\max} = \frac{e^{i\pi/4}}{2\tilde{v}^{1/2}} \left[\frac{\mu\tilde{\omega}_{pe}^6}{(1 + \tilde{k}^2)(1 + \tilde{k}^2 + \tilde{\omega}_{pe}^2)^3} \right]^{1/4} \quad (3.82)$$

It means in particular that the growth rate $\Re(\tilde{v}\delta)$ is proportional to $\tilde{v}^{1/2}$ and not \tilde{v} as for most perturbed solutions, including the most unstable solution predicted by the inhomogeneous plasma theory. As a consequence, the homogeneous plasma theory tends to overestimate the growth rate of the instability, as it is shown in Fig. 3.9(a). The discrepancy between the growth rate predicted by the mode intersection and the numerical solution of the dispersion relation comes from the approximation $\tilde{v}^{1/2} \ll \tilde{\omega}$ which is necessary to apply the perturbation theory on the solution of the homogeneous plasma dispersion relation, but can be difficult to satisfy. Fig. 3.9(b) shows the most unstable modes predicted by the various models as a function of the diamagnetic drift normalized to the Bohm speed. The homogeneous plasma theory predicts that the normalized wavenumber of the most unstable mode goes to zero for very high diamagnetic drifts, which is in disagreement with the inhomogeneous plasma theory that predicts that a minimum \tilde{k}_{\max} should exist.

3.2.5 Comparison with the PIC simulations

Until Section 3.3.4, the de-normalized physical quantities are used again.

On the shorter time-scale, the spectrum of the grid data extracted from the PIC simulation can be computed and compared with the simple 1D models described

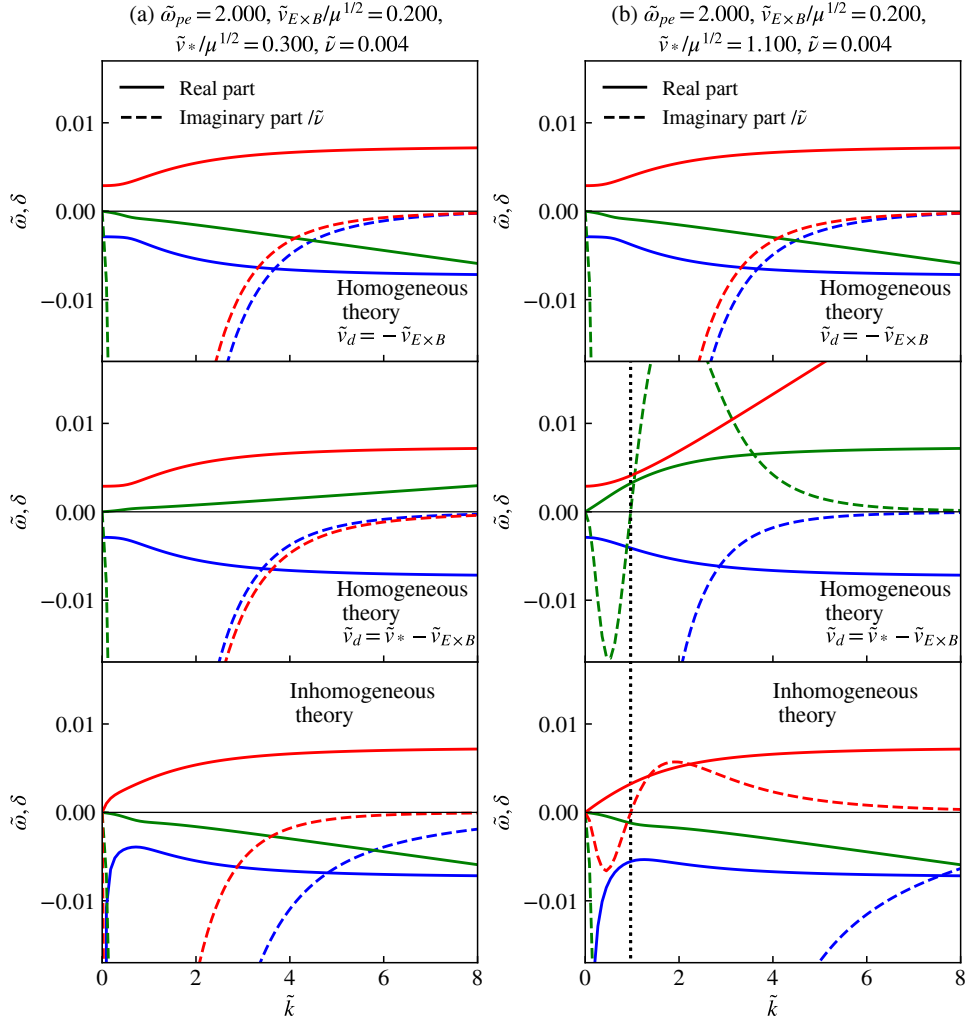


Figure 3.7: Phase diagrams for the 3 solutions of the polynomial dispersion relations $(\tilde{\omega}, \tilde{k})$ in normalized units plotted using various theories. The top diagrams correspond to the homogeneous plasma theory where the $E \times B$ drift is taken as the drift velocity. The diagrams in the middle present the homogeneous plasma theory with a drift velocity equal to the sum between the $E \times B$ and the diamagnetic drifts. The diagrams in the bottom represent the more accurate inhomogeneous plasma theory. (a) Stable configuration ($\tilde{v}_* - \tilde{v}_{E \times B} < \mu^{1/2}$) ; (b) Transition to unstable plasma. The vertical dotted line represents the transition to unstable wavenumbers.

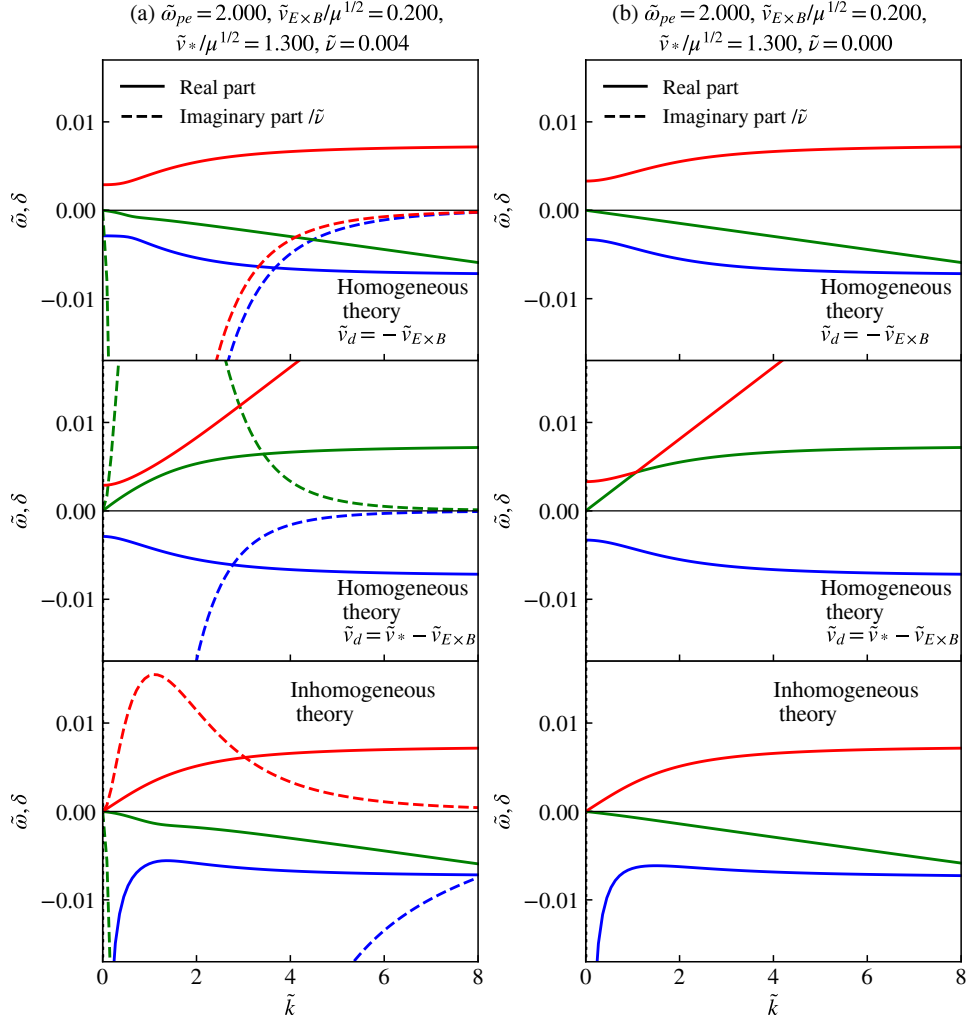


Figure 3.8: Phase diagrams for the 3 solutions of the polynomial dispersion relations $(\tilde{\omega}, \tilde{k})$ in normalized units plotted using various theories. The top diagrams correspond to the homogeneous plasma theory where the $E \times B$ drift is taken as the drift velocity. The diagrams in the middle present the homogeneous plasma theory with a drift velocity equal to the sum between the $E \times B$ and the diamagnetic drifts. (a) Unstable configuration ($\tilde{v}_* - \tilde{v}_{E \times B} > \mu^{1/2}$). (b) Collisionless case (harmonic waves).

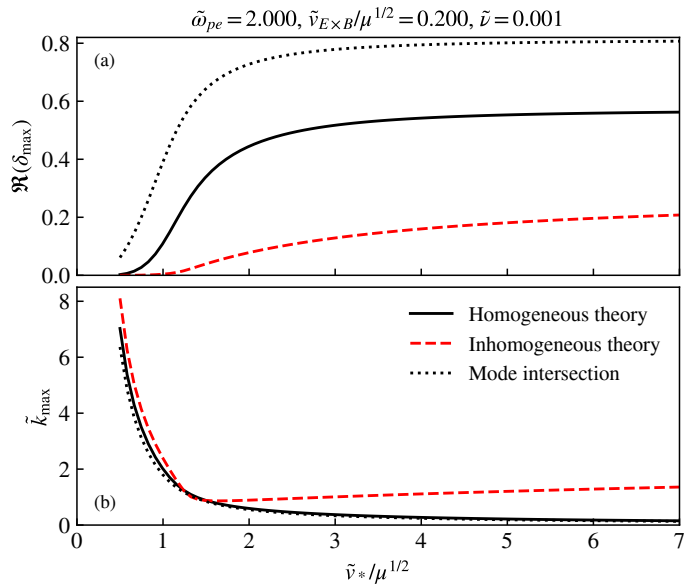


Figure 3.9: The most unstable modes are computed numerically using the homogeneous plasma theory where $\tilde{\nu}_d = \tilde{\nu}_* - \tilde{\nu}_{E \times B}$ (black solid lines) and the inhomogeneous plasma theory (red dashed lines). (a) Maximum growth rate divided by the collision frequency $\Re(\delta_{\max})$. (b) Corresponding wavenumber \tilde{k}_{\max} . The black dotted lines correspond to the intersection between the harmonic modes $\tilde{\omega} = \tilde{\omega}_d$ and $\tilde{\omega} = \tilde{\omega}_+$ in the homogeneous plasma case ("wave mixing").

above. The variable that is selected is the azimuthal electric field

$$E_\theta = \cos \theta E_y - \sin \theta E_x \quad (3.83)$$

where the polar angle θ is defined from the center of the discharge

$$\tan \theta = \frac{y - l_y/2}{x - l_x/2} \quad (3.84)$$

The advantage of this variable is that it should be approximately 0 in a stable plasma, away from the corners, even if the electrons are drifting, so the measured signal is either noise or an instability pattern. The distance from the center

$$r = (x - l_x/2)^2 + (y - l_y/2)^2 \quad (3.85)$$

is also introduced. The azimuthal electric field $E(r, \theta, t)$ contains the temporal and spatial spectra in t and θ respectively, at a given radial position r . The analogy with the 1D model is performed by assuming that the direction called y in the previous section is now represented by the distance along a circle of radius r , namely $r\theta$. Fig. 3.10 shows the map of the azimuthal electric field at 3 Torr and 20 mT. Of course the 1D pseudo-cylindrical model cannot apply near the corners where the equilibrium azimuthal electric field is not zero anymore. In particular, one can observe that the azimuthal electric field becomes very high in the sheaths. This of course a feature of the plasma equilibrium and does not come from the instability. At the center of the discharge, the amplitude of the instability is significantly lower. Since we have seen that the drift velocity was much lower at the discharge center, this is in agreement with the fact that the instability can develop only when the drift velocity is high enough. At low magnetic field, the drift velocity is higher than the Bohm speed only near the sheath edge. When the magnetic field increases, the instability penetrates inside the discharge until a certain penetration lengths. However, since the instability pattern is not purely azimuthal, the waves tend to travel radially, such that measuring a penetration length of the instability is not so easy.

In Fig. 3.11, the 2D maps of the azimuthal electric field are represented for a discharge at 3 mTorr in the non magnetized case (a), and with magnetic fields of 10 mT (b) and 20 mT (c). The color scale is saturated in Fig. 3.11(c) to allow qualitative comparison with the noise detected in the non-magnetized case.

For a given radial position equal to 9 mm, the signal E_θ is plotted as a function of θ and t in Fig. 3.12(a) when the discharge has reached a steady-state (for $t > 35 \mu\text{s}$ in this case). The instability pattern has a quite distinct structure with several modes that can be appreciated by eye. The angular phase velocity can here be estimated

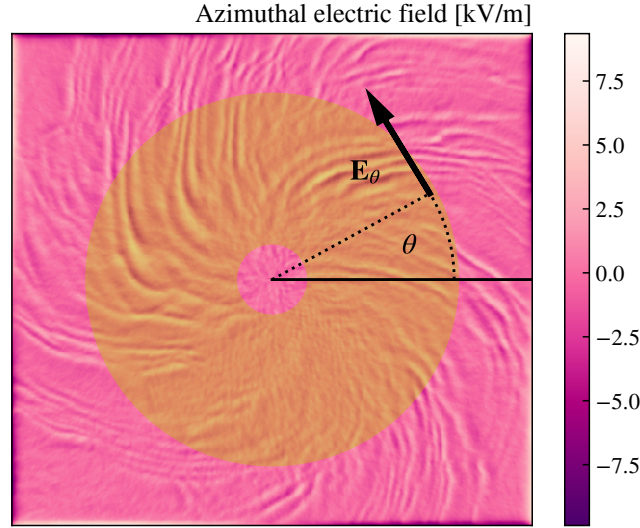


Figure 3.10: Map of the azimuthal electric field for a run at 3 mTorr and 20 mT. The Fourier transforms are perform in the azimuthal direction using $E_\theta(\theta)$.

to about 4.7×10^5 rad/s which corresponds to 4.2 km/s at a distance of 9 mm from the center, which is significantly higher than the Bohm speed (typically 2.7 km/s at $T_e = 3$ eV).

In order to be more accurate and to capture the different modes that develop in the plasma, Fourier transforms of E_θ for a given value of r can be performed, using the `scipy` fast Fourier transform algorithm. The 2D Fourier transform (FT) of $E_\theta(r\theta, t)$ for the typical run at 3 mTorr and 20 mT is plotted in Fig. 3.12(b). The original data were extracted with a rate of 30 ns to achieve the 2D FT but the result remains quite noisy. To allow for comparisons with the theoretical spectra, a 2D Gaussian filter was applied to the signal with a standard deviation $\sigma = 12.5$ (in both directions). The time-averaged and θ -averaged steady-state plasma properties at $r = 9$ mm are summarized in Table 3.4. These numerical values can be inserted into the dispersion relation found with the inhomogeneous plasma theory (Eq. (3.72)) to provide a theoretical spectrum. This theoretical spectrum is plotted in cyan solid line in Fig. 3.12(b) and matches well the transformed PIC data. The approximate formulae of Eq. (3.72) and Eq. (3.75) show good agreement with the simulated spectrum as well. Although it is not shown directly here, the solution of the dispersion relation coming from the homogeneous plasma theory with a drift velocity $\tilde{v}_d = \tilde{v}_* - \tilde{v}_{E \times B}$ also shows a good agreement at least for the real part. The transition from the lower hybrid mode to the ion plasma mode is also clearly visible

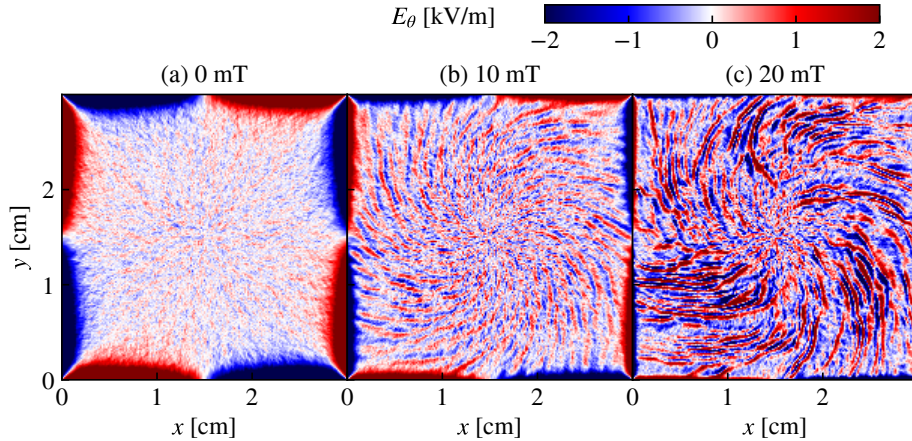


Figure 3.11: Snapshots of the azimuthal electric field in polar coordinates. Simulations were run at 3 mTorr of gas pressure.

in the transformed PIC data.

The 1D Fourier transforms are also presented in Fig. 3.13 in time (a) and in space (b) for magnetic fields of 5, 10, 20 and 40 mT. Both series of curves feature clear maxima at the typical frequency and wavenumber of the instability. Once the instability is triggered, the typical frequency and the wavenumber remain of the same order of magnitude. The temporal Fourier transform is averaged in θ and the spatial Fourier transform is averaged in time, such that the original curves are not so noisy even for sampling rates up to 100 ns. Gaussian filters (with $\sigma = 2$ and 3) were still employed to yield better estimates of the maxima of the curves.

The advantage of the inhomogeneous plasma theory compared to the homogeneous plasma approximation is revealed when looking at the growth rates of the various modes. As explained above (see for example Fig. 3.9), the growth rates and the most unstable wavenumbers predicted by both approaches are very different. The instability growth rate was also estimated in the PIC simulation. This requires particular care because the plasma equilibrium builds up at the same time as the instability develops. At every sampling time, the spatial Fourier transform was computed for a given mode whose amplitude can hence be tracked over time. The result is shown in Fig. 3.14 for wavenumbers corresponding to ρ_{Le} , $\rho_{Le}/2$, and $3\rho_{Le}/4$. The data was initially very noisy and had to be smoothed with a quite broad Gaussian filter ($\sigma = 30$). The mode amplitude is very small during the first few microseconds of the simulation. This onset time which corresponds to the time needed for the discharge to build up from the initial uniform situation was fitted manually and estimated to be about 4.2 μ s. The mode amplitudes then seem to sat-

urate. The exponential growths predicted by the linear perturbation theory are plotted in dotted lines in Fig. 3.14 (the y axis is in log scale so the exponential growth appears as a straight line). The growth rates are reasonably well predicted by the linear theories when the instability develops. Of course, the linear theory cannot capture the saturation of the instability. We are aware that the latter data analysis is at the limit of what can be extracted from the PIC simulations performed within the project. A more detailed investigation of the instability growth could be performed for example by starting a simulation with specially prepared initial electron and ion distributions that would correspond to a time-averaged plasma equilibrium under the same conditions. The number of particles should also be increased to reduce the noise level. Finally, a purely cylindrical simulation code could be used to remove the effects of the corners.

Using a series of data generated the same way as for Fig. 3.13(b) we could identify the dominant mode in the PIC data and compare it with the most unstable mode predicted by the fluid theory for a wide range of conditions of pressure and magnetic field. The comparison is presented in Fig. 3.15, which is analogous to Fig. 3.9 but with

$$\tilde{\omega}_{E \times B} = 0, \quad \tilde{\omega}_{pe} \rightarrow \infty, \quad \text{and } \tilde{v} \rightarrow 0. \quad (3.86)$$

These assumptions are only roughly valid in the PIC simulations but they do not have a major contribution on the solution and allow to plot all the data on the same graph. Based on the numerical determination of the most unstable mode with assumption (3.86), the following power was found

$$\tilde{k}_{\max} = 0.709 \left(\frac{\tilde{v}_*}{\mu^{1/2}} \right)^{0.362}. \quad (3.87)$$

The drift velocity is measured directly from the simulation at a distance of 9 mm from the discharge center. The drift velocity decreases with the magnetic field, so the runs at higher magnetic field are on the LHS of the curve. Considering the data quality and the methods employed to treat it, a typical error of 15 to 20% should be assumed on the estimates of the dominant modes. At high magnetic field, the agreement between the dominant mode in the simulation and the most unstable mode predicted by the inhomogeneous plasma theory of linear perturbations is satisfactory. In our low temperature plasma conditions, when the ratio between the diamagnetic drift and the Bohm speed is larger than about 10, the instability is not really present in the simulation and the dominant mode departs from the prediction of the linear perturbation theory. The homogeneous plasma theory predicts that the wavenumber of the most unstable mode should decrease with the diamagnetic drift, which does not seem to match the simulation data.

Magnetic field	20	mT
Pressure	3	mTorr
Plasma density	1.8×10^{16}	m^{-3}
Electron temperature	3.84	eV
Diamagnetic drift	17.3	km/s
$E \times B$ drift	-4.3	km/s

Table 3.4: Numerical quantities of the simulation used to solve the dispersion relation in Fig. 3.12. The plasma density and the diamagnetic drift are measured at steady-state for the run at 20 mT and 3 mTorr, at $r = 9$ mm from the discharge center, and averaged over time and over θ .

As will be seen in the next Section, the $E \times B$ drift becomes negligible at high magnetic field, such that the part of the graph that corresponds to $\tilde{v}_*/\mu^{1/2} < 1$ would correspond to a stable configuration. This could define a condition of marginal stability that may be of interest to describe the plasma for magnetic fields higher than those investigated in the present work. This condition will be partially discussed in Section 3.3.4.

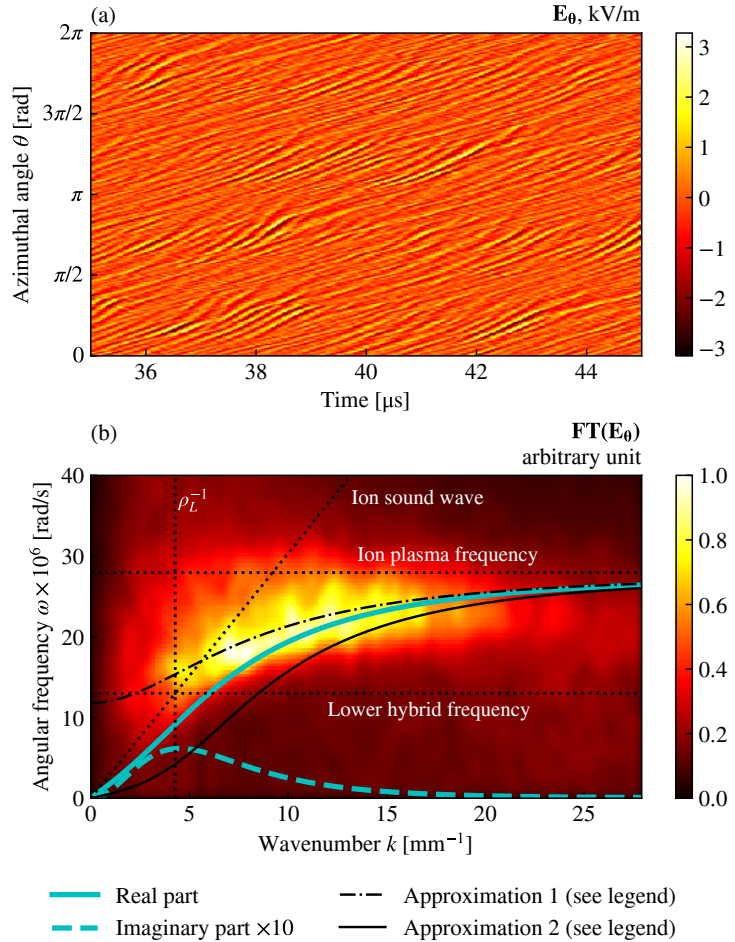


Figure 3.12: (a) Azimuthal electric field obtained at 3 mTorr, and 20 mT, at a distance of 9 mm from the center of the simulation domain. (b) The corresponding spatio-temporal FT (colorplot) with a numerical solution of Eq. (3.72) in cyan, approximate solutions in dashed (Eq. (3.75)) and solid black lines (Eq. (3.76)), with the parameters of Table 3.4.

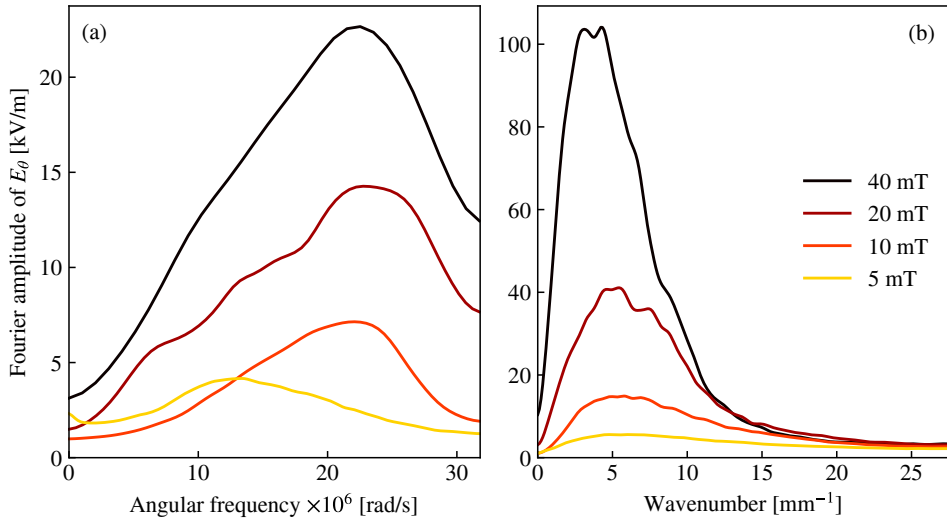


Figure 3.13: Fourier spectra of the azimuthal electric field $E_\theta(\theta, t)$ at a distance $r = 9$ mm from the discharge center for several values of the magnetic field, at 3 mTorr of gas pressure. (a) Temporal Fourier transform averaged in θ with a Gaussian filter ($\sigma = 2$). (b) Spatial Fourier transform averaged in time with a Gaussian filter ($\sigma = 3$). The spatial coordinate is $r\theta$.

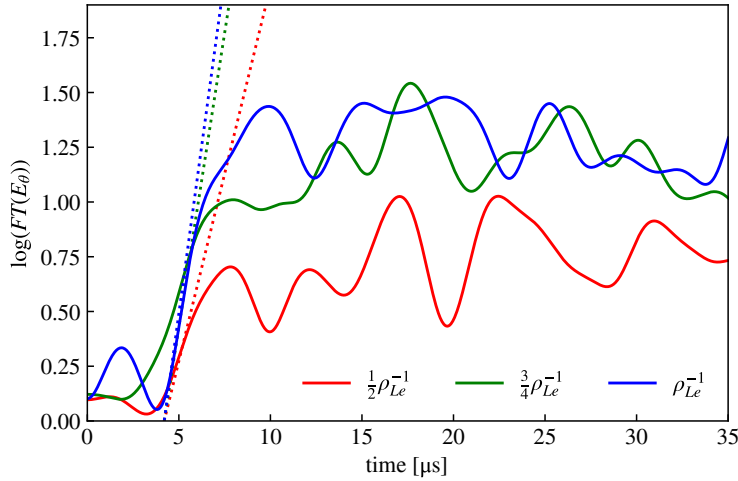


Figure 3.14: Instability growth rates at 3 mTorr and 20 mT, at a distance $r = 9$ mm from the discharge center for various wavenumbers. The data extracted from the PIC simulation (solid lines) is compared with the predictions of the inhomogeneous plasma theory (dotted lines).

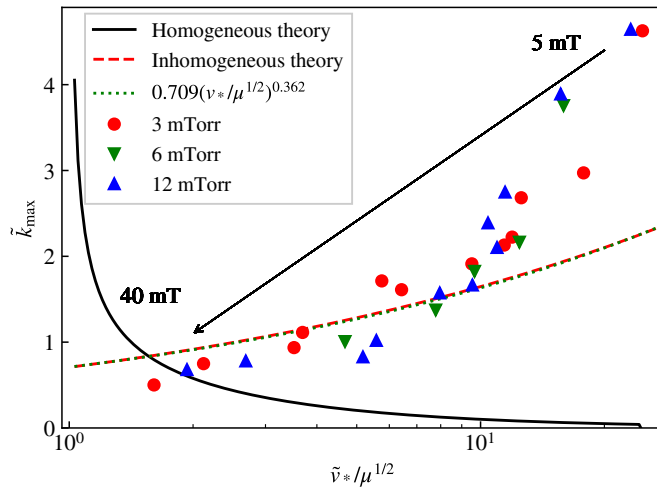


Figure 3.15: Comparison between the most unstable mode $\tilde{k}_{\max} = k_{\max}\rho_{Le}$ predicted by the inhomogeneous (red dashed line) and homogeneous (solid black line) fluid linear theories with simplifying assumptions of Eq. (3.86), and the Fourier spectrum of the PIC simulation data (solid markers) at a distance $r = 9$ mm from the discharge center. The x axis is the diamagnetic drift normalized to the Bohm speed. The magnetic field of the PIC simulation is varied from 5 to 40 mT. The fit (green dotted line) is given by Eq. (3.87)

3.3 Transport theory at high magnetic field

The general 1D model of the plasma transport described in Chapter 2 was based on the ambipolar assumption in the transport direction. While this assumption is perfectly justified in 1D, it cannot be made in 2D. The non-magnetized 2D case could be treated by assuming Boltzmann electrons in Section 2.3, but this assumption does not hold either at high magnetic field. The general two-fluid Magnetohydrodynamics (MHD) equations do not seem to have analytical solutions, even in a quasineutral isothermal plasma. In this Section, we will show that the electric field becomes weak at high magnetic field and that, under these conditions, the properties of the plasma equilibrium can be estimated with very simple formulae.

3.3.1 2D isothermal model

Low electric field assumption

The approximation where the electric field is neglected was already used by Sternberg et al. [116] to model the radial profile of a magnetized plasma column. The behavior of the electric field can be explained by observing that the electric field always accelerates the ions to the walls, and does not change sign at high magnetic field. Then, looking at the steady-state electron momentum balance equation along x as it was done to obtain Eq. (2.10)

$$-k_B T_e \frac{n'}{n} - eE - m_e v_e (1 + \eta_e^2) v = 0$$

with $E > 0$, $n'/n < 0$ and $v > 0$ in the region where $x \in [0, l_x/2]$ where x is here defined from the discharge center. As observed in the simulations, the density profiles keep a familiar shape such that

$$n'/n = 1/L \quad (3.88)$$

where L is a gradient length that remains of the order of the system size (except near the center). As the Hall parameter increases with the magnetic field, the electric field term does not have the right sign to balance the velocity term. The increase of the velocity term can only be balanced by the pressure term. Since the electron temperature and the gradient length remain bounded, the velocity also has to go to zero.

More formally, the electric field can be estimated in the 1D model using the ion momentum balance equation (Eq. (2.11)), such that the ratio between the electric field term and the velocity term in the electron momentum conservation equation

(Eq. (2.10)) is

$$\frac{eE}{m_e v_e (v_x (1 + \eta_e^2))} = \frac{m_i}{m_e v_e (1 + \eta_e^2)} \left[\frac{v_{iz} + \frac{v_x^2}{D_a} - \frac{T_i}{T_e} \left(\frac{u_B^2}{D_a} + v_{iz} \right)}{1 - v^2/u_B^2} + v_{i,tot} (1 + \eta_i) \right] \quad (3.89)$$

At high magnetic field, the ionization frequency can be estimated by Eq. (2.67) such that v_{iz} goes to zero. Moreover, the ratio $\frac{m_i v_{i,tot} (1 + \eta_i^2)}{m_e v_e (1 + \eta_e^2)}$ is equal to $(m_e v_e)/(m_i v_{i,tot})$ at high magnetic field, which is very small. Finally,

$$D_a \approx \frac{m_i u_B^2}{m_e v_e (1 + \eta_e^2)} \quad (3.90)$$

at high magnetic field. Therefore,

$$\frac{eE}{m_e v_e (v_x (1 + \eta_e^2))} = \frac{\left(\frac{v_x}{u_B} \right)^2 - \frac{T_i}{T_e}}{1 - \left(\frac{v_x}{u_B} \right)^2} \quad (3.91)$$

We can see here that the electric field might reverse because of the ion temperature. This was however not observed in the simulations. At high magnetic field, the tangent velocity profile found in Chapter 2 is retained and the velocity is much lower than the Bohm speed everywhere except at the sheath edge. Everywhere in the plasma bulk, the ratio between the electric field term and the velocity term is hence $-T_i/T_e$ whose absolute value is much smaller than 1 in low temperature plasma conditions. The electric field term can hence be neglected in the transport equations of magnetized low temperature plasmas.

The model above is 1D and the assumption of small electric field has to be validated in 2D. This can be done using the PIC simulation data. Fig. 3.16 shows the ratio between the electric field term and the electron pressure term in many simulated conditions, for $y = l_y/2$. When there is no magnetic field, the ratio is approximately 1 (or -1) everywhere in the plasma bulk, which corresponds to the Boltzmann equilibrium. When the magnetic field increases, both terms tend to decrease but the electric field term decreases much faster than the pressure term. For gas pressures of 3 and 6 mTorr, the electric field term is less than 15% of the pressure term when the magnetic field is higher than 15 mT. The effect is less visible at 12 mTorr as a higher magnetic field is required to reach the strongly magnetized regime.

Although 2D effects and the instability onset make the interpretation of the PIC data more intricate than with the simple 1D model described above, the low electric

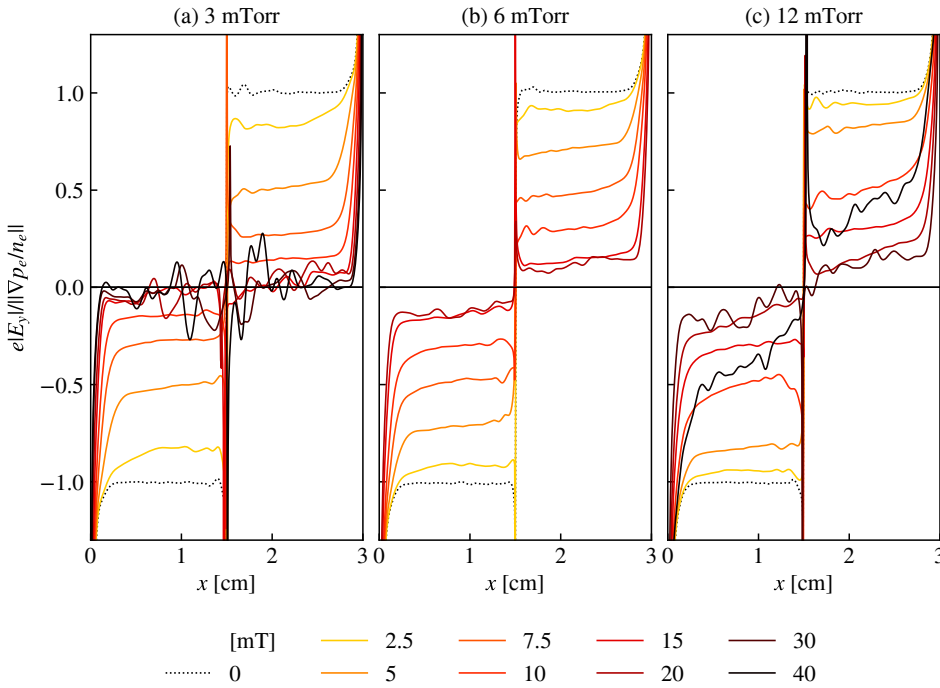


Figure 3.16: Ratio between the electric field term and the pressure term in the electron momentum conservation equation as a function of x , for $y = l_y/2$. The magnetic field is varied from 0 to 40 mT, for $p = 3$ mTorr (a), 6 mTorr (b) and 12 mTorr (c).

field assumption seems legitimate to describe the high magnetic field regime of the plasma column studied here.

Introduction of the effective collision frequency

The effect of the instability on the time-averaged transport is difficult to predict. However, the momentum conservation equations can be written at the shorter time scale and then averaged in time to evidence the formal contribution of the instability. This was done for example by T. Lafleur for the study of the electron drift instability in Hall thrusters [76]. The electric field, the electron density and the electron velocity can be split into a time-averaged ($\langle \cdot \rangle$) term and a fluctuating term:

$$n_e = \langle n_e \rangle + n_{e1} ; \mathbf{v}_e = \langle \mathbf{v}_e \rangle + \mathbf{v}_{e1} ; \mathbf{E} = \langle \mathbf{E} \rangle + \mathbf{E}_1 \quad (3.92)$$

By neglecting the electron inertia, the electron momentum conservation equation is

$$\begin{aligned} & m_e (\langle n_e \rangle \partial_t \mathbf{v}_{e1} + n_{e1} \partial_t \mathbf{v}_{e1}) \\ & + k_B T_e (\nabla \langle n_e \rangle + \nabla n_{e1}) + e (\langle n_e \rangle \langle \mathbf{E} \rangle + \langle n_e \rangle \mathbf{E}_1 + n_{e1} \langle \mathbf{E} \rangle + n_{e1} \mathbf{E}_1) \\ & + e [(\langle n_e \rangle \langle \mathbf{v}_e \rangle + \langle n_e \rangle \mathbf{v}_{e1} + n_{e1} \langle \mathbf{v}_e \rangle + n_{e1} \mathbf{v}_{e1}) \times \mathbf{B}] \\ & + m_e v_e (\langle n_e \rangle \langle \mathbf{v}_e \rangle + n_{e1} \langle \mathbf{v}_e \rangle + \langle n_e \rangle \mathbf{v}_{e1} + n_{e1} \mathbf{v}_{e1}) = 0. \end{aligned} \quad (3.93)$$

Since the time average of the fluctuating quantities is 0, the average of the equation above yields

$$\begin{aligned} 0 = & -k_B T_e \nabla \langle n_e \rangle - e (\langle n_e \rangle \langle \mathbf{E} \rangle + \langle n_e \rangle \langle \mathbf{v}_e \rangle \times \mathbf{B}) - m_e v_e \langle n_e \rangle \langle \mathbf{v}_e \rangle \\ & - m_e \langle n_{e1} \partial_t \mathbf{v}_{e1} \rangle - e \langle n_{e1} \mathbf{E}_1 \rangle - e \langle n_{e1} \mathbf{v}_{e1} \rangle \times \mathbf{B} - m_e v_e \langle n_{e1} \mathbf{v}_{e1} \rangle \end{aligned} \quad (3.94)$$

The four last terms of Eq. (3.94) are of second order with respect to the perturbation and account for the effects of the instability on the time-averaged plasma transport.

The same process can be applied to the electron continuity equation

$$\nabla \cdot (\langle n_e \rangle \langle \mathbf{v}_e \rangle + n_{e1} \langle \mathbf{v}_e \rangle + \langle n_e \rangle \mathbf{v}_{e1} + n_{e1} \mathbf{v}_{e1}) = (\langle n_e \rangle + n_{e1}) v_{iz} \quad (3.95)$$

The average yields

$$\nabla \cdot (\langle n_e \rangle \langle \mathbf{v}_e \rangle + \langle n_{e1} \mathbf{v}_{e1} \rangle) = \langle n_e \rangle v_{iz} \quad (3.96)$$

Subtracting Eqs. (3.95) and (3.96),

$$\nabla \cdot (\langle n_e \rangle \mathbf{v}_{e1} + n_{e1} \mathbf{v}_{e1}) = n_{e1} v_{iz} \quad (3.97)$$

For a specific wavevector \mathbf{k} , this yields

$$\mathbf{v}_{e1} \cdot \mathbf{k} = (v_{iz} - \langle \mathbf{v}_e \rangle \cdot \mathbf{k}) \frac{n_{e1}}{\langle n_e \rangle} \quad (3.98)$$

which means that \mathbf{v}_{e1} and n_{e1} always fluctuate with the same phase. Hence,

$$\langle n_{e1} \mathbf{v}_{e1} \rangle = 0 \quad (3.99)$$

Thus, the fluctuations do not affect the equilibrium electron continuity equation and the only term with fluctuations that remains in Eq. (3.94) is $\langle n_{e1} \mathbf{E}_1 \rangle$. According to Eq. (3.69), the phase shift between the fluctuations of density and electric field is $\pi/2$ without collisions, in which case $\langle n_{e1} \mathbf{E}_1 \rangle = 0$. So only collisions can introduce

a term coming from fluctuating quantities in the equilibrium momentum conservation equation. The equilibrium continuity and momentum conservation equations are therefore

$$\nabla \cdot (\langle n_e \rangle \langle \mathbf{v}_e \rangle) = \langle n_e \rangle v_{iz} \quad (3.100)$$

and

$$0 = -k_B T_e \nabla \langle n_e \rangle - e (\langle n_e \rangle \langle \mathbf{E} \rangle + \langle n_e \rangle \langle \mathbf{v}_e \times \mathbf{B} \rangle) - m_e v_e \langle n_e \rangle \langle \mathbf{v}_e \rangle - e \langle n_e \rangle \langle \mathbf{E}_1 \rangle \quad (3.101)$$

The last term of Eq. (3.101) cannot be estimated without investigating the saturation mechanism of the instability. In the work of T. Lafleur on Hall thrusters [76, 77], it was shown that the saturation came from ion trapping, such that an estimate of the term $\langle n_e \rangle \langle \mathbf{E}_1 \rangle$ was provided. A slightly different approach is proposed here. It is assumed that the two last terms of the RHS of Eq. (3.101) can be represented in the form of a collision term, with different effective collision frequencies in each direction. In the following, we get rid of the brackets $\langle \cdot \rangle$ for the time averaged quantities, and write

$$m_e v_e n_e \mathbf{v}_e + e \langle n_e \rangle \langle \mathbf{E}_1 \rangle = m_e n_e \underline{\nu}_{\text{eff}} \mathbf{v}_e \quad (3.102)$$

where

$$\underline{\nu}_{\text{eff}} = \nu_x \mathbf{e}_x \otimes \mathbf{e}_x + \nu_y \mathbf{e}_y \otimes \mathbf{e}_y + \nu_z \mathbf{e}_z \otimes \mathbf{e}_z \quad (3.103)$$

is a diagonal effective collision tensor. It accounts both for the collisional processes and for the effects of temporal fluctuations on the mean plasma transport.

Solution of the model

At high magnetic, the equilibrium electric field is neglected, such that the stationary momentum conservation equation is

$$0 = -k_B T_e \nabla n_e - e n_e \mathbf{v}_e \times \mathbf{B} - m_e n_e \underline{\nu}_{\text{eff}} \mathbf{v}_e \quad (3.104)$$

It is assumed that the plasma is quasineutral, hence $n_e = n_i = n$. The projections in the plane perpendicular to the magnetic field are therefore

$$-\omega_{ce} \Gamma_{ey} - v_{Te}^2 \partial_x n - \nu_x \Gamma_{ex} = 0 \quad (3.105)$$

$$\omega_{ce} \Gamma_{ex} - v_{Te}^2 \partial_y n - \nu_y \Gamma_{ey} = 0 \quad (3.106)$$

where Γ_{ex} and Γ_{ey} are the components of the equilibrium electron flux $\mathbf{\Gamma}_e = n \mathbf{v}_e$. The electron flux is then

$$\Gamma_{ex} = -\frac{v_{Te}^2}{\omega_{ce}^2 + \nu_x \nu_y} (\nu_y \partial_x n - \omega_{ce} \partial_y n) \quad (3.107)$$

$$\Gamma_{ey} = -\frac{v_{Te}^2}{\omega_{ce}^2 + \nu_x \nu_y} (\nu_x \partial_y n + \omega_{ce} \partial_x n) \quad (3.108)$$

We now make the assumption that v_x and v_y are independent of space. This is not strictly true but it allows to solve the set of equations and will later be justified by the PIC simulations. Injecting these expressions in the steady-state continuity equation,

$$v_y \partial_x^2 n + v_x \partial_y^2 n = -(\omega_{ce}^2 + v_x v_y) \frac{v_{iz}}{v_{Te}^2} n. \quad (3.109)$$

Eq. (3.109) is a generalized Helmholtz equation that has solutions under the form

$$\begin{aligned} n = n_0 \cos & \left[(\omega_{ce}^2 + v_x v_y)^{\frac{1}{2}} \left(\frac{v_{iz}}{v_y} \right)^{\frac{1}{2}} \frac{x}{v_{Te}} + \varphi_x \right] \\ & \times \cos \left[(\omega_{ce}^2 + v_x v_y)^{\frac{1}{2}} \left(\frac{v_{iz}}{v_x} \right)^{\frac{1}{2}} \frac{y}{v_{Te}} + \varphi_y \right] \end{aligned} \quad (3.110)$$

where n_0 is the maximum density, and φ_x and φ_y are integration constants that depend on the initial conditions. Since the maximum density is reached at the center of the domain, $\varphi_x = \varphi_y = 0$. We have already seen in Section 2.2.5 that the Bohm criterion at high magnetic field is equivalent to Schottky's boundary conditions: $n = 0$ at the walls. Using the latter condition:

$$n = n_0 \cos \left(\frac{\pi x}{l_x} \right) \cos \left(\frac{\pi y}{l_y} \right) \quad (3.111)$$

where

$$\pi^2 v_{Te}^2 \left(\frac{v_y}{l_x^2} + \frac{v_x}{l_y^2} \right) = v_{iz} (\omega_{ce}^2 + v_x v_y). \quad (3.112)$$

is the electron temperature equation.

When the electric field is neglected the electron and ion equations are completely decoupled, such that the plasma density is found using only the fluid equations for the electrons: the transport is limited by the electron confinement. At the walls, the electron flux is

$$\Gamma_{ex} \left(x = \pm \frac{l_x}{2}, y \right) = \frac{\pi n_0 v_{Te}^2 v_y}{(\omega_{ce}^2 + v_x v_y) l_x} \cos \left(\frac{\pi y}{l_y} \right) \quad (3.113)$$

$$\Gamma_{ey} \left(x, y = \pm \frac{l_y}{2} \right) = \frac{\pi n_0 v_{Te}^2 v_x}{(\omega_{ce}^2 + v_x v_y) l_y} \cos \left(\frac{\pi x}{l_x} \right). \quad (3.114)$$

It is not clear which collision frequency should be taken for each direction, since the instability is rotating, with a wavevector that is mainly azimuthal but with a significant radial contribution as well. However, we have seen that the instability

develops mainly in the azimuthal direction, and the local electric field fluctuations are expected to push the electrons in the $E \times B$ direction [40]. To estimate v_x and v_y , the simulation domain is split into 4 regions as illustrated in Fig. 3.17. For each section of the wall, the anisotropic collision frequency is either ν_e when the instability is perpendicular to the wall, or equal to a scalar ν_{eff} when it is parallel to it. Since at steady-state, the total current leaving the plasma is zero ($\oint_S \Gamma_i \cdot d\mathbf{S} = \oint_S \Gamma_e \cdot d\mathbf{S}$), the h factor of the discharge defined by Eq. (1.97) can directly be estimated through the electron flux

$$h_B = \frac{(m_i/m_e)^{1/2} v_{Te}(\nu_e + \nu_{\text{eff}})}{(\omega_{ce}^2 + \nu_e \nu_{\text{eff}})(l_x + l_y)} \left(\frac{l_y}{l_x} + \frac{l_y}{l_x} \right) \quad (3.115)$$

which reduces to

$$h_B = \frac{v_{Te}(\nu_e + \nu_{\text{eff}})}{(\omega_{ce}^2 + \nu_e \nu_{\text{eff}})l} \left(\frac{m_i}{m_e} \right)^{1/2} \quad (3.116)$$

for a square ($l_x = l_y = l$). The index B indicates that this equation is valid at high magnetic field only, otherwise the assumption of low electric field cannot be made.

If the instability has no effect on the transport, then $\nu_{\text{eff}} = \nu_e$ and the h factor decreases as B^{-2} with the magnetic field, which corresponds to the classical regime found by Sternberg et al. [116]. However, as will be shown in the next paragraph, the Hall parameter cannot be arbitrarily large, which sets boundaries for the possible values of h and ν_{eff} .

3.3.2 Saturation of the magnetic confinement

Upper bound for the Hall parameter

At $y = 0$, $\partial_y n = 0$ such that Eq. (3.106) becomes

$$\Gamma_{ey} = \frac{\omega_{ce}}{v_y} \Gamma_{ex} \quad (3.117)$$

If the instability propagates approximately in the y direction, then $v_y = \nu_{\text{eff}}$ such that the Hall parameter for the electrons is

$$\eta_e = \frac{\Gamma_y}{\Gamma_x} \approx \frac{\omega_{ce}}{\nu_{\text{eff}}} \quad (3.118)$$

which also writes

$$v_{ey} = \eta_e v_{ex} \quad (3.119)$$

Fig. 3.18 shows the profiles of v_y/v_{Te} at $y = 0$, where v_{Te} is computed from the volume-averaged electron energy at 3 mTorr and 12 mTorr, for several values of the

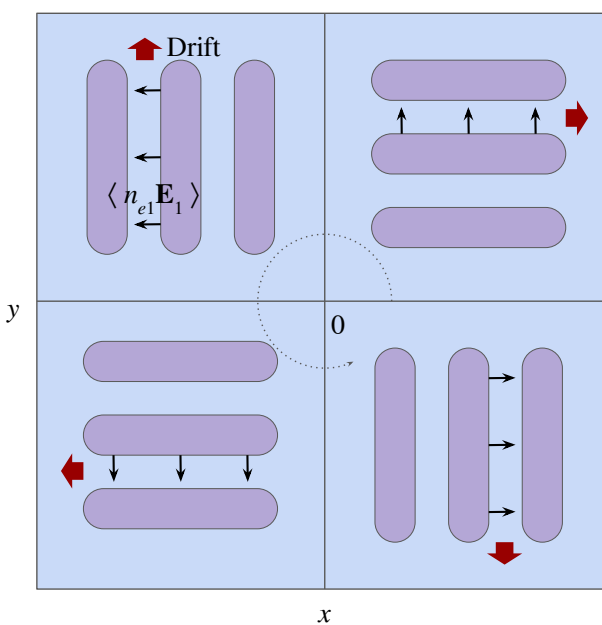


Figure 3.17: Sketch of the model where the domain is split into 4 sub-domains. The instability is always either parallel to the wall, or perpendicular to it.

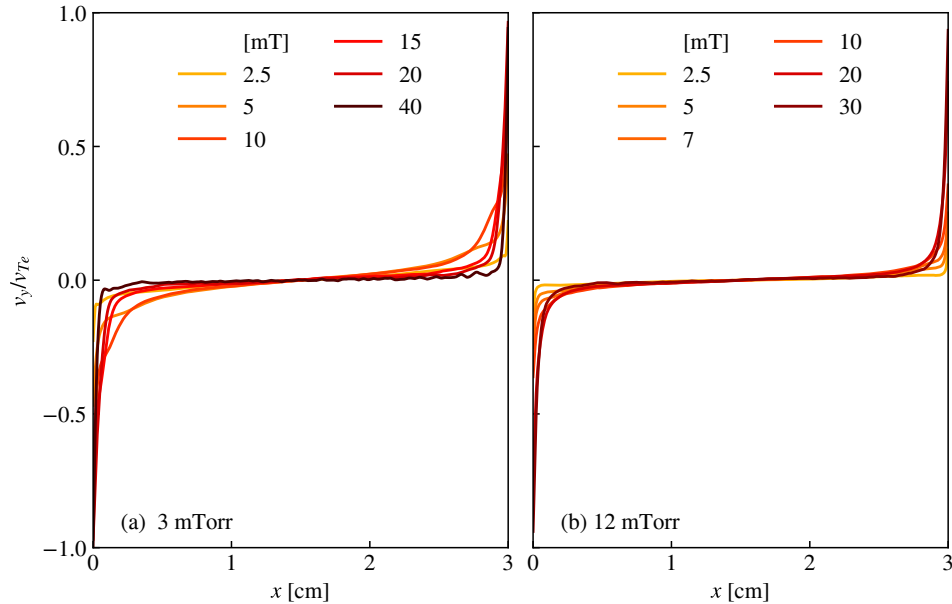


Figure 3.18: Profiles of electron fluid velocity along y as a function of x , measured at $y = l_y/2$, and normalized to the electron thermal velocity for various values of the magnetic field at 3 mTorr (a) and 12 mTorr (b).

magnetic field. Of course, these profiles are averaged over the larger time-scale. The electron drift velocity v_y always remains lower than the electron thermal velocity, and becomes very close to it at the wall (which is consistent with the thermal electron flux at the wall) at high magnetic field. In the plasma bulk, v_y is always only a fraction of the thermal velocity. This seems consistent with the fact that the electron drift velocity is dominated by the diamagnetic drift at high magnetic field. The diamagnetic drift is purely a fluid drift, it is not related to the motion of the electron guiding centers¹ and should in principle remain lower than the electron thermal velocity.

$$v_* < v_{Te} \quad (3.120)$$

The paragraph below is an attempt to provide a qualitative interpretation to this observation.

In Fig. 3.19, the electron density gradient is in the vertical direction. The elec-

¹A diamagnetic drift higher than the thermal velocity would not necessarily break the PIC CFL conditions since it comes from a strong density gradient and not necessarily from a high gyration velocity or a high guiding center velocity. We must however ensure that the Larmor radius is well resolved by the grid.

tron density decreases from the top to the bottom. We assume that all the electrons have a gyration velocity of $\pi v_0/2$ such that the mean velocity over half a gyration is v_0 . The Larmor radius is

$$\rho_{Le} = \frac{\pi v_0 m_e}{2eB} \quad (3.121)$$

Let us consider a slice of thickness $2\rho_{Le}$.

- If the density gradient is 0, there are as many electrons whose velocity contribution along x is v_0 as electrons whose velocity contribution along x is $-v_0$. The diamagnetic drift is therefore 0, which is in agreement with Eq. (3.3) when there is no pressure gradient.
- If the density gradient is $n/(4\rho_{Le})$, there are half less electrons after a distance of $2\rho_{Le}$. In Fig. 3.19, the resulting fluid velocity is $\frac{4v_0 - 2v_0}{6} = \frac{v_0}{3}$.
- If the density gradient is greater than $n/(2\rho_{Le})$, it means that all the electrons have disappeared after a distance of $2\rho_{Le}$. The mean velocity is therefore v_0 .

This means that the diamagnetic drift velocity should be limited by the electron gyration velocity, that is of the order of v_{Te} in an isotropic plasma. More precisely, since for an isotropic Maxwellian electron distribution function the mean absolute velocity is

$$\langle \|\mathbf{v}_e\| \rangle = \left(\frac{8}{\pi} \right)^{1/2} v_{Te} \quad (3.122)$$

where $v_{Te} = (k_B T_e / m_e)^{1/2}$. The mean v_0 is

$$\langle v_0 \rangle = \frac{2}{\pi} \langle \|\mathbf{v}\| \rangle \approx 1.016 v_{Te} \quad (3.123)$$

The diamagnetic drift velocity should typically be lower than $1.016 v_{Te}$. However, the single particle approach should be generalized to a population of electrons using the kinetic theory, which could be the focus of a future study.

It is assumed in the following that the drift velocity is limited by the electron thermal velocity, such that

$$v_x \eta_e < v_{Te} \quad (3.124)$$

In the sheath, the ion flux remains equal to the electron flux in average (global ambipolarity condition), and the electron density drops more rapidly than the ion density. The electron fluid velocity is therefore typically higher than the ion velocity in the sheath.

$$v_{ix} < v_{ex} \quad (3.125)$$

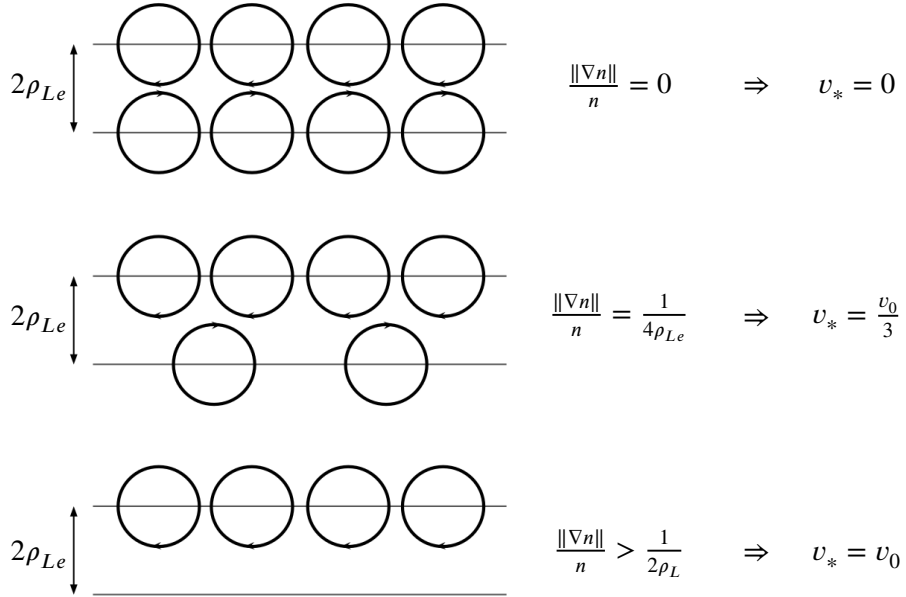


Figure 3.19: Sketch of the electron gyration motion for several values of the density gradient.

Hence,

$$\eta_e < \frac{v_{Te}}{v_{ix}} \quad (3.126)$$

For moderate magnetic fields, the density gradient and the space charge electric field terms are so strong in the sheath that electrons can be described with a Boltzmann factor. Using an isothermal sheath model, the ions are accelerated by the sheath potential ϕ_s defined by Eq. (1.94). Provided that they enter the sheath at the Bohm speed, their velocity at the wall is

$$v_{ix,w} = u_B \left[1 + \ln \left(\frac{m_i}{2\pi m_e} \right) \right]^{1/2} \quad (3.127)$$

This yields an upper bound for the Hall parameter

$$\eta_e < \eta_{c1} = \left\{ \frac{m_i}{m_e \left[1 + \ln \left(\frac{m_i}{2\pi m_e} \right) \right]} \right\}^{1/2}. \quad (3.128)$$

For argon,

$$\eta_{c1} \approx 84 \quad (3.129)$$

On the $y = l_y/2$ axis, the Hall parameter can be measured from the PIC simulation data using

$$\eta_e = \frac{\Gamma_{ey}}{\Gamma_{ex}}. \quad (3.130)$$

In order to reduce the noise level, an azimuthal average is performed, such that

$$\bar{\eta}_e = \frac{\langle \Gamma_{e\theta} \rangle}{\langle \Gamma_{er} \rangle} \quad (3.131)$$

where $\Gamma_{e\theta}$ and Γ_{er} are respectively the azimuthal and radial components of the electron flux, and $\langle \cdot \rangle$ denotes the average in time and along the θ coordinate.

Consequently, Eq. (3.128) can be validated against the PIC simulation data. Fig. 3.20 shows the Hall parameter measured in polar coordinates in the PIC simulations at 3 and 12 mTorr for various magnetic field strengths. The error bars correspond to the minimum and maximum values found when varying the radial position where the fluxes are estimated from 3 mm to 12 mm. Given the relatively small size of the error bars, the approximation of a uniform Hall parameter seems reasonable. The Hall parameter reaches a maximum η_c of approximately $0.72 \eta_{c1}$ in the 3 mTorr case and $0.37 \eta_{c1}$ in the 12 mTorr case, and decreases at high magnetic field. The x axis is the electron drift velocity at the wall divided by the electron thermal velocity. In order to determine η_{c1} , it was assumed that the drift velocity was equal to v_{Te} at the wall. If this rough estimate is corrected by using the value found in the PIC simulation, the predicted Hall parameter would be the one given by the black dashed line in Fig. 3.20.

A minimum h factor?

Let us introduce an *instability-enhanced* collision frequency ν_B such that

$$\nu_B^2 = \nu_{\text{eff}}^2 - v_e^2 \quad (3.132)$$

Since $\eta_e = \omega_{ce}/v_{\text{eff}}$ decreases at high magnetic field, it means that ν_B and v_{eff} increase with the magnetic field and $\nu_B \approx v_{\text{eff}}$ at high magnetic field. Furthermore, we can reasonably assume that $\omega_{ce}^2 \gg v_e v_{\text{eff}}$ at high magnetic field. Using Eq. (3.116), the h factor of the discharge is in the high magnetic field limit

$$h_m = \frac{v_{Te}\nu_B}{\omega_{ce}^2 l} \left(\frac{m_i}{m_e} \right)^{1/2} \quad (3.133)$$

Hence, the h factor has a lower bound if and only if $\nu_B \underset{B \rightarrow \infty}{\sim} \omega_{ce}^2$. If this is the case, then h_m is strictly positive. Otherwise, since the h factor cannot be higher than 1, $h_m = 0$.

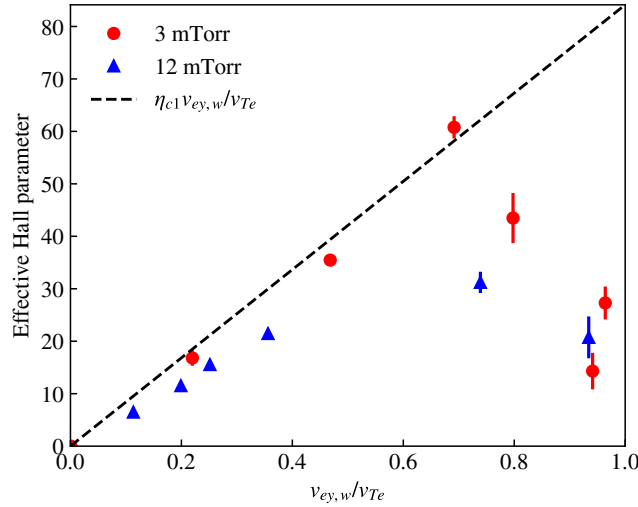


Figure 3.20: Effective Hall parameters plotted as a function of v_{ey}/v_{Te} for simulation runs at 3 and 12 mTorr, measured with Eq. (3.131). The error bars represent values extracted between 3 and 12 mm from the discharge center.

Classical ion-electron transport transition at $h_0 = h_B$

We now investigate the transition between the low magnetic field regime where the ions dominate the transport, and the high magnetic field regime where the model described above applies.

At high magnetic field, the density profiles have cosine shapes and the global particle balance equation is

$$\tilde{n}v_{iz} = 4h_B u_B/l \quad (3.134)$$

where $\tilde{n} = (2/\pi)^2$ is the 2D mean normalized electron density. Replacing v_{iz} in the electron temperature equation (3.112)

$$l\omega_{ce}^2 h_B \left(\frac{m_e}{m_i} \right)^{1/2} = v_{Te}(v_e + v_{eff}) > 2v_{Te}v_e \quad (3.135)$$

Hence;

$$\omega_{ce}^2 > \frac{2v_e v_{Te}}{lh_0} \left(\frac{m_i}{m_e} \right)^{1/2} \quad (3.136)$$

where h_0 is the non-magnetized h factor given for instance by Eq. (2.130), and where it has been assumed that $h_0 > h_B$ (the magnetic field does not enhance the transport in any case). Inequality (3.136) represents the transition between the low

magnetic field regime where the transport is limited by the ion drift-diffusion, and the high magnetic field regime where the electrons drive the transport, whatever the role of the instability². In terms of Larmos radius, this transition translates into

$$\rho_{Le,\text{ion/elec}}^2 = \frac{h_0 l \lambda_e}{2} \left(\frac{m_e}{m_i} \right)^{1/2} \quad (3.137)$$

where λ_e is the electron mean free path.

Classical / instability-enhanced transport transition at $v_e = v_B$.

In this small paragraph, the Larmor radius that corresponds to the transition to the regime where the instability dominates the plasma transport is established. We assume that this transition occurs when the maximum the Hall parameter is reached.

The effective Hall parameter η_e satisfies

$$\frac{1}{\eta_e^2} = \frac{v_e^2}{\omega_{ce}^2} + \frac{v_B^2}{\omega_{ce}^2} \quad (3.138)$$

Using Eq. (3.133),

$$\frac{1}{\eta_e^2} = \frac{v_e^2}{\omega_{ce}^2} + \frac{2h_m^2 l^2 m_e \omega_{ce}}{m_i v_{Te}^2} \quad (3.139)$$

We have seen in the simulation that the electron temperature does not vary much with the magnetic field, especially when the transport is dominated by the instability. Since $1/\eta_e$ has a lower bound that is strictly positive, h_m cannot be zero. Consequently, the derivative of Eq. (3.138) with respect to the cyclotron frequency, with constant v_{Te} and v_e is

$$\frac{d}{d\omega_{ce}} \left(\frac{1}{\eta_e^2} \right) = -\frac{2v_e^2}{\omega_{ce}^3} + \frac{2h_m^2 l^2 m_e \omega_{ce}}{m_i v_{Te}^2} \quad (3.140)$$

The maximum Hall parameter is hence reached for a magnetic field corresponding to

$$\omega_{ce0}^2 = \frac{v_e v_{Te}}{h_m l} \left(\frac{m_i}{m_e} \right)^{1/2} \quad (3.141)$$

which yields a critical Larmor radius

$$\rho_{Le,\text{stable/unstable}}^2 = h_m l \lambda_e \left(\frac{m_e}{m_i} \right)^{1/2} \quad (3.142)$$

²Inequality (3.136) does not depend on any quantity that depends on the plasma unstable behavior, such as v_B or h_m for example.

and corresponds to the transition between the classical regime and the instability-enhanced regime for the electrons. A heuristic branching under the form

$$v_{\text{eff}} = (v_e^2 + v_B^2)^{1/2} \quad (3.143)$$

was chosen to manage the transition between the classical regime and the instability-enhanced regime. As the critical magnetic field corresponds to evaluating $v_B = v_e$, we can be confident that the transition criterion does not depend on the type of heuristic branching³.

3.3.3 Instability-enhanced transport

The previous paragraph has shown that the Hall parameter was uniform in space as a first approximation, and that it had an upper bound that was lower than 84 for argon. This upper bound leads to the existence of a minimum h factor $h_m > 0$, whatever the value of the magnetic field, and an instability-enhanced collision frequency proportional to ω_{ce}^2 . Since

$$\eta_c = \frac{\omega_{ce0}}{v_e} < \eta_{c1} \quad (3.144)$$

Eq. (3.128) yields

$$h_m > \frac{2\lambda}{l} \left(\frac{m_e}{m_i} \right)^{1/2} \left[1 + \ln \left(\frac{m_i}{2\pi m_e} \right) \right] \quad (3.145)$$

At low magnetic field, we have seen that a significant fraction of the plasma can be unstable near the sheath, but the transport is still driven by the ions. The existence of a lower bound for h is fundamental: it means that the magnetic confinement of the electrons completely saturates due to the instability at high magnetic field.

Increasing the magnetic field strength, soon after the electrons start driving the transport, the unstable nature of the plasma becomes important and the Hall parameter starts decreasing. Conversely, the instability affects mainly the electron motion, so the transport cannot be instability-driven without being electron-driven. Hence

$$\rho_{Le,\text{stable/unstable}}^2 < \rho_{Le,\text{ion/elec}}^2 \quad (3.146)$$

which implies that

$$h_m < h_0/2 \quad (3.147)$$

³The critical Larmor radius would be the same for any heuristic formula under the form $v_{\text{eff}} = (v_e^\alpha + v_B^\alpha)^{1/\alpha}$ for $\alpha > 1$

In summary, it was demonstrated that

$$\frac{2\lambda}{lh_0} \left(\frac{m_e}{m_i} \right)^{1/2} \left[1 + \ln \left(\frac{m_i}{2\pi m_e} \right) \right] < \frac{h_m}{h_0} < \frac{1}{2} \quad (3.148)$$

It was found in the PIC simulations that

$$0.32 < \frac{h_m}{h_0} < 0.42 \quad (3.149)$$

for the range of pressure investigated, from 3 to 12 mTorr, such that the predictions from the theory are always satisfied. Moreover, the ratio h_m/h_0 is quite close to 0.5 and depends weakly on the pressure, which indicates that the instability starts playing an important role soon after the electrons start driving the transport. In the following, it will be assumed that the instability-dominated transport leads to a minimum h factor $h_m \approx 0.32h_0$. According to Eq. (3.133),

$$\nu_B = \frac{lh_m \omega_{ce}^2}{v_{Te}} \left(\frac{m_e}{m_i} \right)^{1/2}. \quad (3.150)$$

Fig. 3.21 shows the effective collision frequency measured from the PIC simulation

$$\nu_{\text{eff}} = \frac{\langle \Gamma_{er} \rangle}{\langle \Gamma_{e\theta} \rangle} \omega_{ce}. \quad (3.151)$$

The ν_B asymptote is verified and the heuristic formula of Eq. (3.143) shows a satisfactory agreement with the PIC data.

As it was done for the effective electron collision frequency, the regime where the electrons are strongly magnetized can be bridged heuristically to the non-magnetized case where the ions dominate the transport by writing

$$h = h_0 (1 + G + G^2)^{-1/2} \quad (3.152)$$

where

$$G = h_0/h_B \quad (3.153)$$

This heuristic formula was first proposed by Sternberg et al. [116] as a fit to 1D fluid simulation results. This formulation is compared to the 2D PIC simulation data in Fig. 3.22. The classical theory where $\nu_{\text{eff}} = \nu_e$ is depicted in Fig. 3.22(a). In the classical approximation, Eq. (3.152) correctly predicts the plasma transport properties up to the regime where the instability strongly develops. In Fig. 3.22(b), the effective collision frequency includes the effects of the instability and the h factor is correctly predicted by Eq. (3.152) for all ranges of pressure and magnetic field.

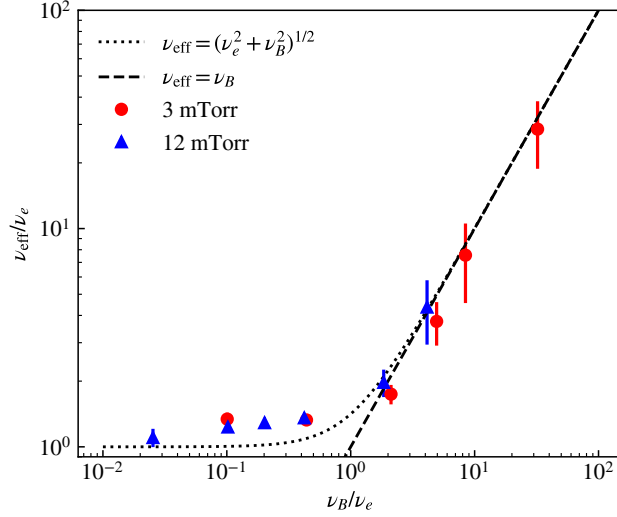


Figure 3.21: Effective collision frequency as a function of the instability-enhanced collision frequency with $h_m = 0.32h_0$, normalized by the classical collision frequency ν_e . Error bars correspond to data extracted at distances between 3 and 12 mm from the discharge center.

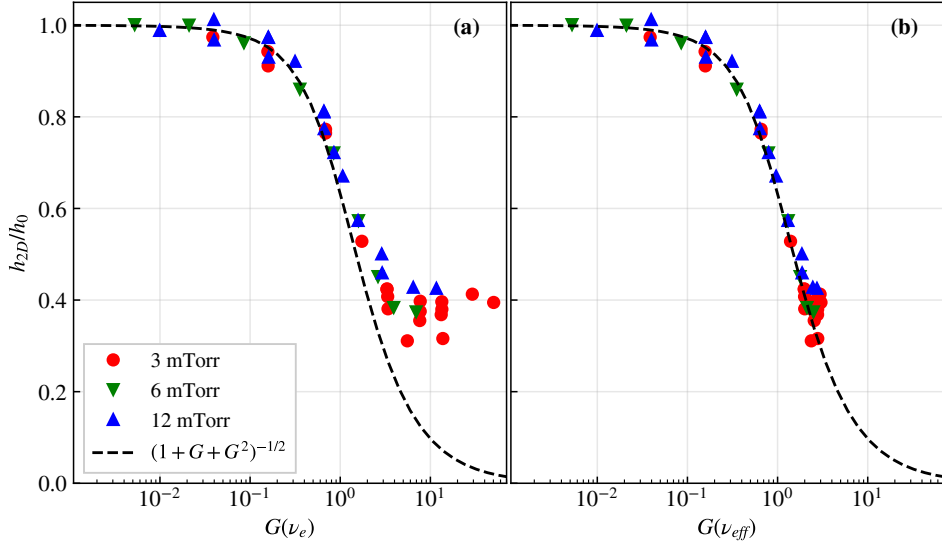


Figure 3.22: Edge-to-center plasma density ratio (h factor) plotted against the parameter $G = h_0/h_B$. In (a), only the classical collision frequency is taken into account in the computation of h_B . In (b), the effective collision frequency is computed with $h_m = 0.32h_0$.

3.3.4 Discussion on the marginal stability

It could be interesting to provide a new model of the transport using a local marginal stability condition. This could be done theoretically in 1D the same way as for the classical model described in Section 2.2, with one more equation corresponding to the marginal stability (Eq. (3.79)), and one more variable being the effective electron collision frequency. According to Eq. (3.79), at marginal stability, the total electron drift should be equal to the Bohm speed.

In this section, as the regime of interest is at high magnetic field, the normalized quantities defined in Section 3.2.1 are used again.

The behavior of the drift velocity in the PIC simulations is summarized in Fig. 3.23. In this graph, the colored dashed lines were plotted using a simplified formula for the electron drift velocity

$$\tilde{v}_\theta = \tilde{v}_r / \tilde{v}_e \quad (3.154)$$

\tilde{v}_r being the radial velocity predicted by a simple 1D, non magnetized model:

$$\tilde{v}_r = \mu^{1/2} h \tan\left(\frac{\pi x}{l}\right) \quad (3.155)$$

At high magnetic field, the solid black line represents a diamagnetic drift estimated by

$$\tilde{v}_\theta \approx \tilde{v}_* = \frac{\pi}{l} \tan\left(\frac{\pi r}{l}\right) \quad (3.156)$$

We observe in Fig. 3.23 that the electron drift first become much higher than the Bohm speed at intermediate magnetic fields, and then decreases to some value that becomes close to the Bohm speed. At very high magnetic field, the intuition is that the time-averaged drift velocity should become equal to the Bohm speed, and that the electric field cannot be neglected anymore.

The transition to this "very high magnetic field regime" occurs when the diamagnetic drift velocity is equal to the Bohm speed. If L is the pressure gradient length,

$$\frac{1}{L} = \mu^{1/2} \quad (3.157)$$

It is hard to reach this regime by 2D PIC simulations because if we make the approximation $L \approx l/\pi$ which is valid near the sheath edge, the number of cells in one direction needed to resolve the Larmor radius in one direction is at least $\pi/\mu^{1/2}$, which is equal to 850 for argon. The modeling of this regime is therefore slightly beyond the range of parameters investigated with our simulations. For example, for an argon discharge at 3 eV, with $L = l/\pi \approx 0.96 \text{ cm}$, the transition magnetic field is 117 mT. At this regime, the stability criterion of Eq. (3.79) might not hold because

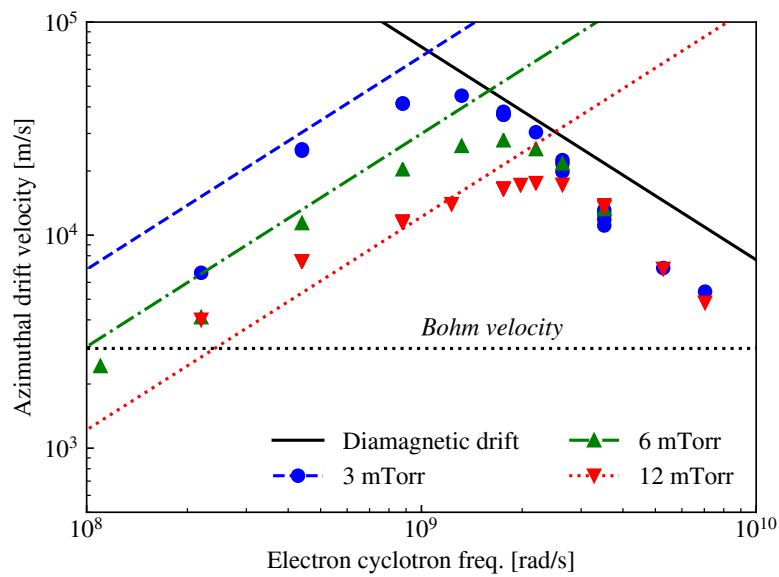


Figure 3.23: Azimuthal drift velocities measured for various values of the pressure and magnetic field, measured at $r = 9$ mm from the discharge center. The various dashed lines correspond to the classical regime (Eq. (3.154)), and the solid black line corresponds to the instability dominated regime described by Eq. (3.156).

the plasma response to electrostatic perturbations may not be isothermal anymore. Interestingly, this transition is almost equivalent to the magnetic field where the ions that travel with the Bohm velocity become magnetized. Although ion magnetization does not have a large influence in the equilibrium transport equations, it may modify the stability criterion.

The 1D differential equation of the transport is still given by Eq. (2.17). At high magnetic field, the ambipolar diffusion is driven by the electron confinement, such that in normalized units

$$\left(1 - \frac{\tilde{v}^2}{\mu} v'\right) = \tilde{v}_{iz} + \left(\tilde{v} + \frac{1}{\tilde{v}}\right) \tilde{v}^2 \quad (3.158)$$

where \tilde{v} is the effective electron collision frequency, \tilde{v} is the velocity along the x axis, and x varies from 0 to $l/2$. Using Eq. (3.154),

$$\tilde{v} = \frac{\mu^{1/2}}{\tilde{v} + 1/\tilde{v}} < \frac{\mu^{1/2}}{2} \quad (3.159)$$

which gives a corrected Bohm sheath criterion applicable to our model. Now that the variable \tilde{v} can be eliminated, the differential equation of the transport is

$$\left(1 - \frac{\tilde{v}^2}{\mu} v'\right) = \tilde{v}_{iz} + \mu^{1/2} \tilde{v} \quad (3.160)$$

which integrates into

$$x = -\frac{\tilde{v}^2}{2\mu^{3/2}} + \frac{\tilde{v}_{iz} v}{\mu^2} + \frac{1 - (\tilde{v}_{iz}/\mu)^2}{\mu^{1/2}} \ln \left(1 + \frac{\mu^{1/2} \tilde{v}}{\tilde{v}_{iz}}\right) \quad (3.161)$$

Using the boundary condition $\tilde{v} = \mu^{1/2}/2$ at $x = l/2$, the electron temperature equation is

$$\frac{l\mu^{1/2}}{2} = g \left(\frac{\tilde{v}_{iz}}{\mu} \right) \quad (3.162)$$

where the g function is defined by

$$g(x) = -\frac{1}{8} + \frac{x}{2} + (1 - x^2) \ln \left(1 + \frac{1}{2x}\right) \quad (3.163)$$

We can study the case where the magnetic field is not too high, $\tilde{v}_{iz} \gg \mu$, for which a third order Taylor development gives

$$\tilde{v}_{iz} = \frac{11}{12} \mu^{1/2} / l \quad (3.164)$$

which is to be compared with the temperature equation in the low pressure, non-magnetized case of Eq. (2.61). The confinement has the same properties as in the low pressure regime, but with a factor $11/12$ instead of $\pi - 2$, which indicates a slightly better confinement. The very high magnetic field limit yields

$$\tilde{v}_{iz} = \frac{\mu}{2} \exp\left(-\frac{l\mu^{1/2}}{2}\right) \quad (3.165)$$

The density profile can also be derived analytically

$$\tilde{n} = \tilde{n}_0 \left(1 + \frac{\mu^{1/2}\tilde{v}}{\tilde{v}_{iz}}\right)^{-1+(\tilde{v}_{iz}/\mu)^2} \exp\left(-\frac{\tilde{v}_{iz}\tilde{v}}{\mu^{3/2}}\right) \quad (3.166)$$

To be consistent with the general definition of Eq. (1.97), the h factor is here

$$h = \frac{\tilde{n}|_{\tilde{v}=\mu^{1/2}/2}}{2\tilde{n}_0} \quad (3.167)$$

which yields

$$h = \frac{1}{2} \left(1 + \frac{\mu}{2\tilde{v}_{iz}}\right)^{-1+(\tilde{v}_{iz}/\mu)^2} \exp\left(-\frac{\tilde{v}_{iz}}{2\mu}\right) \quad (3.168)$$

The h factor depends only on the ratio \tilde{v}_{iz}/μ .

- If $\tilde{v}_{iz} \gg \mu$, $h = \exp(-1/8)/2 \approx 0.44$;
- If $\tilde{v}_{iz} \ll \mu$, $h = \tilde{v}_{iz}/(4\mu)$.

For $\tilde{v}_{iz} \ll \mu$, the density profile becomes convex and the mean normalized density profile starts decreasing significantly. If the density profile had remained approximately the same, the exponential decrease found in Eq. (3.165) would have been particularly surprising as it would have meant that the confinement is better than in the classical model where it is proportional to $1/B^2$.

This model is not difficult to derive and yields some reasonable estimates of the plasma properties. However:

- We are not sure that local marginal stability is a reasonable assumption since very few studies were found on the subject for low-temperature plasmas ;
- The non-isothermal response of the plasma and ion magnetization will change the dispersion relation and affect the stability criterion in a way that we do not know.

The validity of the results is therefore arguable but the method has some interest and may give rise to more simulations and experiments.

Summary

Many 2D PIC simulations of a magnetized plasma column were performed for several values of the pressure and a wide range of magnetic field strengths. Varying the magnetic field, soon after the electron mobility becomes lower than the ion mobility, a resistive drift wave instability triggered by collisions starts playing an important role in the plasma transport. This instability is well described by the linear perturbation theory of an inhomogeneous plasma. At high magnetic field (from 10 mT) and for a given pressure, the plasma magnetic confinement is completely destroyed by the instability, and features an effective electron collision frequency that scales as B^2 , and a constant h factor. A local marginal stability condition may be incorporated in fluid models to yield self-consistent predictions of the equilibrium plasma properties.

Chapter 4

Magnetic filter theory and modeling

Contents

4.1 Why studying magnetic filters?	168
4.1.1 Applications	168
4.1.2 Literature review on magnetic filter studies	168
4.1.3 The PEGASES experiment	168
4.2 2D PIC simulations of a magnetic filter with argon	169
4.2.1 Simulation parameters	169
4.2.2 Simulation results	169
4.3 Reduced geometry	173
4.4 PIC model validation	175
4.4.1 Comparison with experiments	175
4.4.2 Comparison with previous fluid simulations	175
4.5 Identifying the main drivers of a magnetic filter	177
4.6 Influence of the localized heating	177
4.6.1 Influence of the power	177
4.6.2 Influence of dielectric boundaries	177
4.6.3 Influence of the gas pressure	184
4.6.4 Effect of the magnetic field	184
4.7 1D fluid model of a magnetic filter	184
4.7.1 Model assumptions	184
4.7.2 Model equations	184

4.7.3	Numerical scheme	188
4.7.4	First results with no heat flux	189
4.7.5	The role of the heat flux	189
4.7.6	Comparison with PIC simulations	189
4.8	The effect of instability-enhanced plasma transport in the 1D modeling of PEGASES	189
4.9	"Anomalous" heat transport	189

The fluid theory of instability-enhanced transport derived in Chapter 3 is generalized to the magnetic filter configuration with a gas of argon. PIC simulation results with localized heating and various magnetic field configurations are compared with a 1D fluid model. The simulation results are also compared with experimental data.

4.1 Why studying magnetic filters?

4.1.1 Applications

Neutral Beam Injector (NBI)

[111], [46], [63], [123], [108]

Electric propulsion concepts and applications

[95]

Space debris removal

[88], [2]

4.1.2 Literature review on magnetic filter studies

[60], [71], [72], [16]

4.1.3 The PEGASES experiment

[122], [101], [100], [20]

4.2 2D PIC simulations of a magnetic filter with argon

4.2.1 Simulation parameters

Secondary Electron Emission (SEE) are neglected.

4.2.2 Simulation results

dT	4.24×10^{-12}	[s] simulation time step
dX	20	[μm]
dX/dT	4.72×10^6	[m/s]
$N_{part/cell}$	7	Initial number of part./cell (for 1 species)
$N_{part,init}$	210 000 000	Superparticles at initialization (total)
$N_{elec,end}$	369 159 794	Electron superparticles at run end
$N_{ion,end}$	369 519 201	Ion superparticles at run end
y_{max}	5 000	number of gridpoints along y
x_{max}	6 000	number of gridpoints along x
$N_{average}$	10 000	grid diagnostics average
$loops$	71	In number of $N_{average}$
T_{simu}	3.01	[μs] physical time of the simulation
magnetized ions	True	
$N_{ionsubcycling}$	10	number of time steps for ion subcycling
Gas	Ar	
l_y	0.1	[m] system length along y
l_x	0.12	[m] system length along x
n	1.0×10^{17}	[m^{-3}] plasma density at initialization
q_f	5 714 290	particle weighting factor
T_g	300	[K] neutral gas temperature
p_g	10	[mTorr] neutral gas pressure
n_g	3.20×10^{20}	[m^{-3}] neutral gas density
B_z	2.45×10^{-2}	[T] magnetic field along y
$E_{z,amp}$	1 000	[V/m] initial amplitude of the heating E field
T_e	4.0	[eV] electron temperature
T_i	0.026	[eV] ion temperature
particle source	ionization	
ω_E	8.52×10^7	[rad/s] heating field frequency
\mathcal{W}_{abs}	0.10	[W] absorbed power
w_{abs}	125	[kW/m 3] absorbed power density
Heating	Linear, Fig. 1.6(e)	
Boundary condition	Conducting walls	
SEE model	No SEE	
N_{CPU}	3 000	Number of CPU
$V_{storage}$	259.1	[GB], run data volume
$V_{grid,snap}$	2.9	[GB], data volume per grid snapshot
Total runtime	72	[h]
Computing resource	273 000	[CPU.h]
Computing facility	OCCIGEN	

Table 4.1: LPPic simulation characteristics.

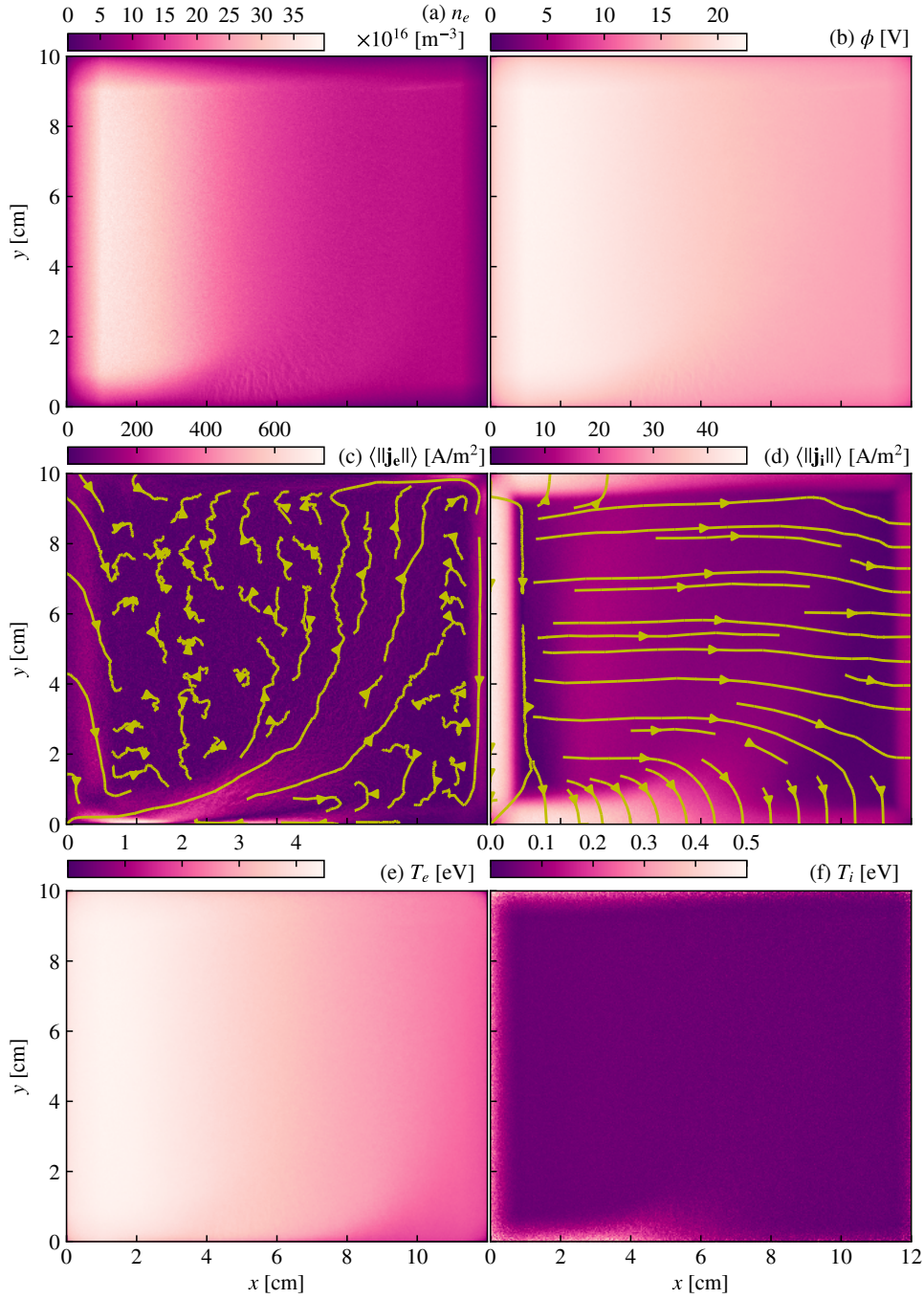


Figure 4.1: Properties of the discharge with magnetic filter after 3.1 μs of simulation. The electron and ion currents are averaged over the last 1.3 μs of the simulation.

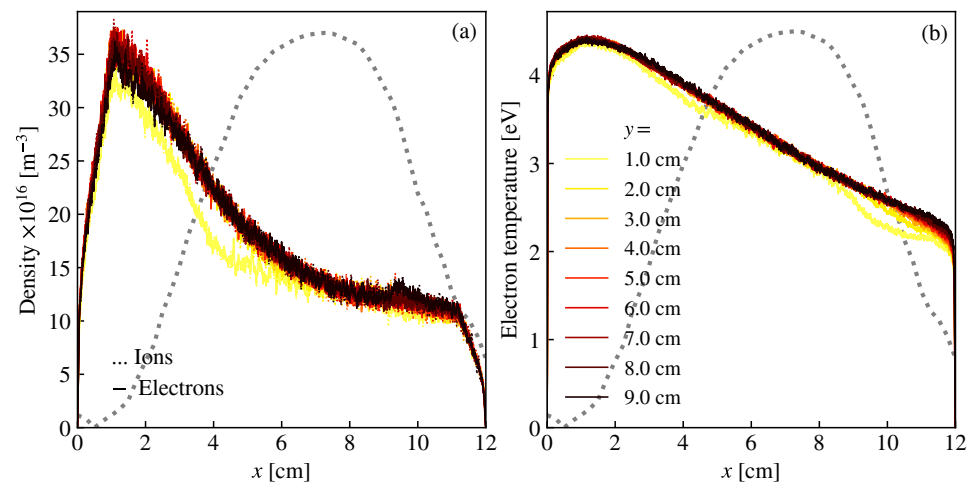


Figure 4.2: (a) plasma density and (b) electron temperature profiles along the x axis for different values of y . In (a), the dotted lines represent the ion density and the solid lines represent the electron density. The ion density profiles were smoothed with a Gaussian filter ($\sigma = 4$). The gray dotted line is the experimental magnetic field [1] profile used in the simulation. The maximum of the magnetic field is 24.5 mT.

4.3 Reduced geometry

Inpu parameters

Table 3.1 with a magnetic field up to 80 mT.

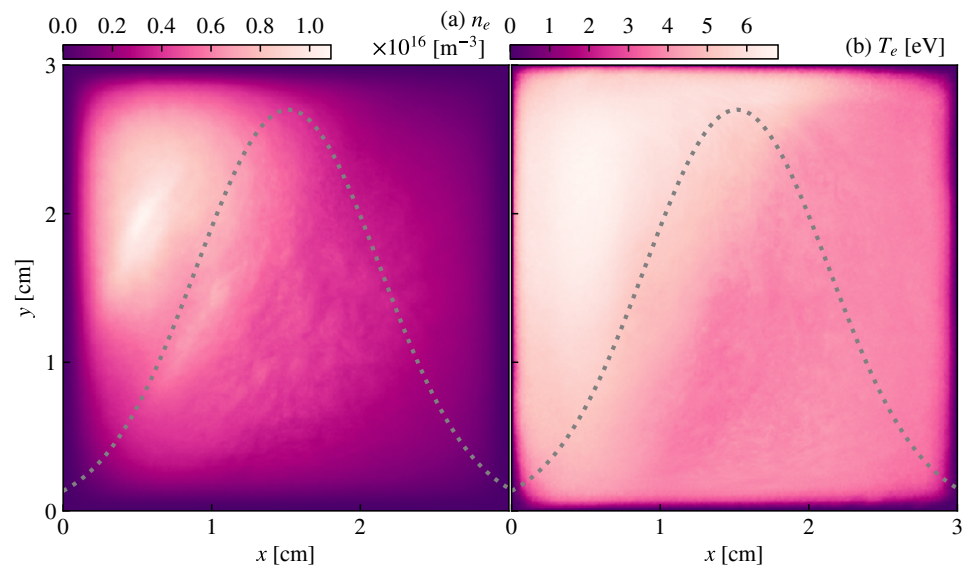


Figure 4.3: (a) Plasma density and (b) electron temperature maps at 3 mTorr along the x axis for different values of y . In (a), the dotted lines represent the ion density and the solid lines represent the electron density. The ion density profiles were smoothed with a Gaussian filter ($\sigma = 4$). The gray dotted line is the experimental magnetic field profile used in the simulation. The gray dotted line is the Gaussian magnetic field profile used in the simulation. The maximum magnetic field is 20 mT here.

4.4 PIC model validation

4.4.1 Comparison with experiments

[1], [19]

4.4.2 Comparison with previous fluid simulations

[51]

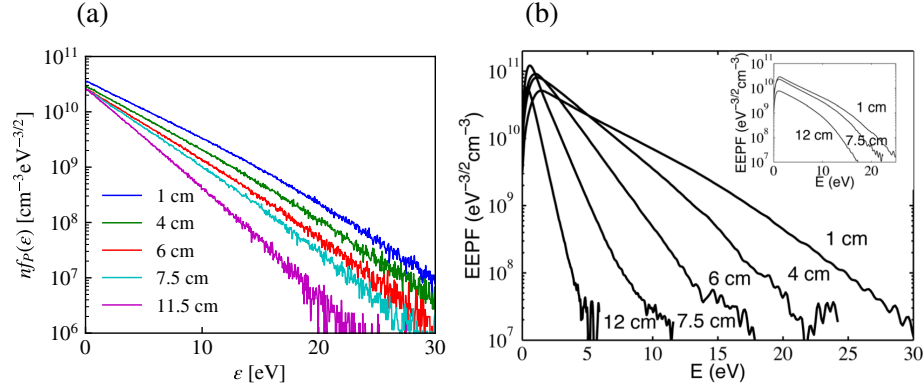


Figure 4.4: (a) EEPF measured from the PIC simulation. The distribution function is estimated by including the electrons at the given x position ± 3 mm. (b) Experimental data collected by A. Aanesland and J. Bredin in 2012 [1].

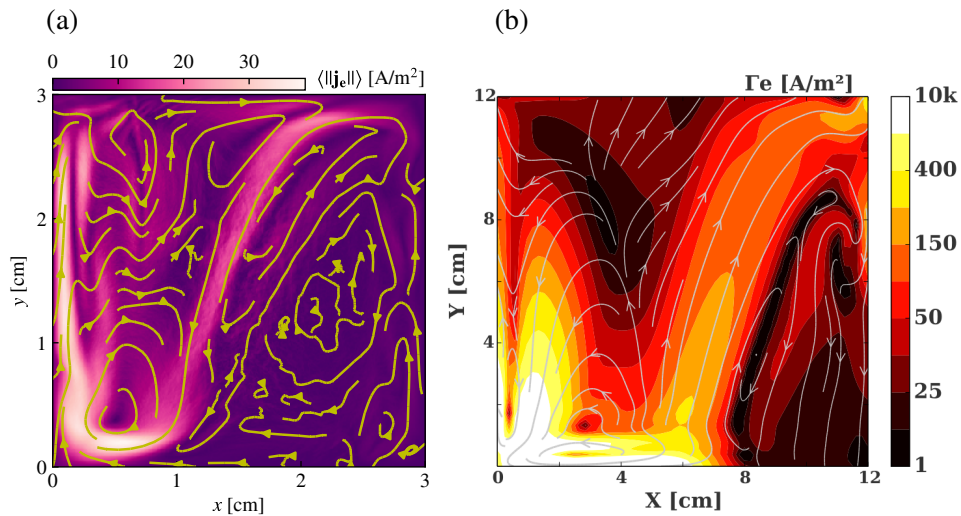


Figure 4.5: (a) Electron current measured in the PIC simulation with a maximum magnetic field of 20 mT at 3 mTorr. (b) 2D fluid simulation results by R. Fittersack [51].

4.5 Identifying the main drivers of a magnetic filter

4.6 Influence of the localized heating

Without magnetic field

Before describing the magnetic filter itself, it is important to sense the influence of heating localization, in the non-magnetized case. We have plotted the PIC simulation results for a square discharge of 3 cm with various configurations for the heating electric field in Fig. 4.7. In every case, the mean heating power density is 9.6 kW/m^3 . Configuration (A) corresponds to the case of a uniform heating electric field, as illustrated by Fig. 1.6(a). The electron density and temperature profiles are perfectly symmetrical in this case, at pressures of 3, 6 and 12 mTorr. The case where the amplitude of the heating electric field heating decreases linearly from $x = 0$ to $x = l_x$ is represented by the label (B) and corresponds to Fig. 1.6(b). In this case, the density profile is slightly shifted to the left and the electron temperature increases by about 10% inside the discharge. In case (C) (Fig. 1.6(c)), the heating is localized in the first third of the discharge. The plasma density profile is again more shifted to the left and the electron temperature increases from the center to the wall, before decreasing again in the sheath.

The heating geometry has a significant influence on the mean electron energy, both locally and in average, and the coil configuration can induce discrepancies of about 10% for the same total power absorbed by the plasma. However, the plasma density profile remains quite robust. The maximum plasma density has relative variations of only about 3%. At 12 mTorr, the profile leans towards the side where the heating is higher. At 6 mTorr and 12 mTorr, the profile is also distorted but the trend is not so clear.

With magnetic field

4.6.1 Influence of the power

4.6.2 Influence of dielectric boundaries

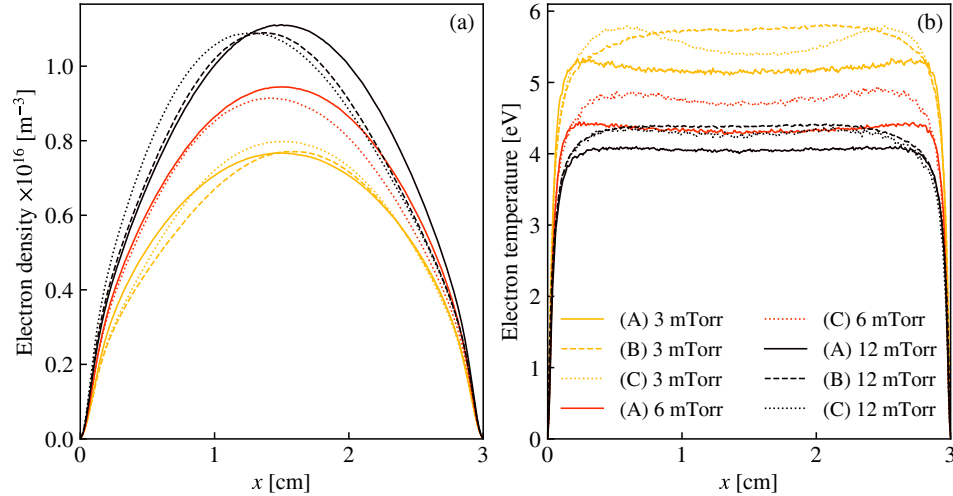


Figure 4.6: Mean electron density (a) and temperature (b) profiles at $y = l_y/2$ for non-magnetized argon discharges for 3, 6 and 12 mTorr of gas pressure. Three different heating configurations are tested: (B) corresponds to a linearly decreasing heating electric field with $\alpha = 1$ (Fig. 1.6(b)), and (C) corresponds to a heating localized only in the first third of the discharge (Fig. 1.6(c)).

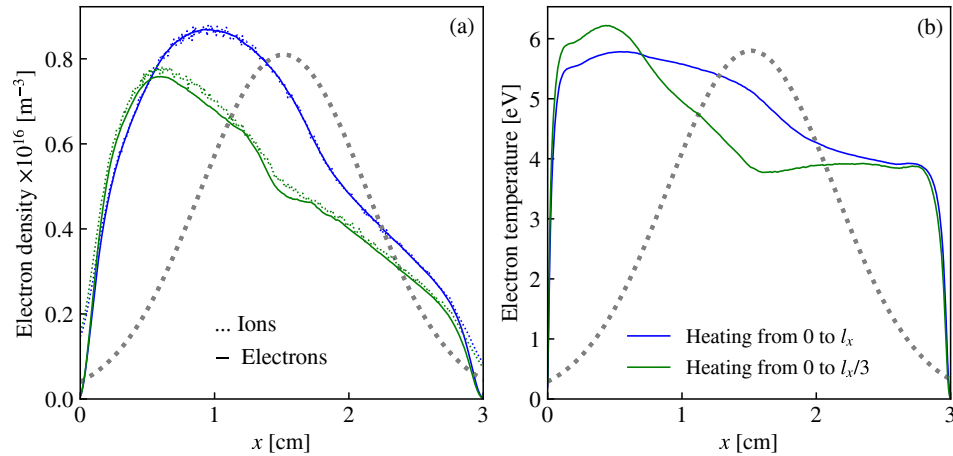


Figure 4.7: Electron density (a) and electron temperature (b) profiles at $y = l_y/2$ for magnetic filter configurations at 3 mTorr of gas pressure. Two different heating configurations are tested: linear decrease of the heating electric field from 0 to l_x (Fig. 1.6(b)), and linear decrease localized between $x = 0$ and $x = l_x/3$ (Fig. 1.6(c)).

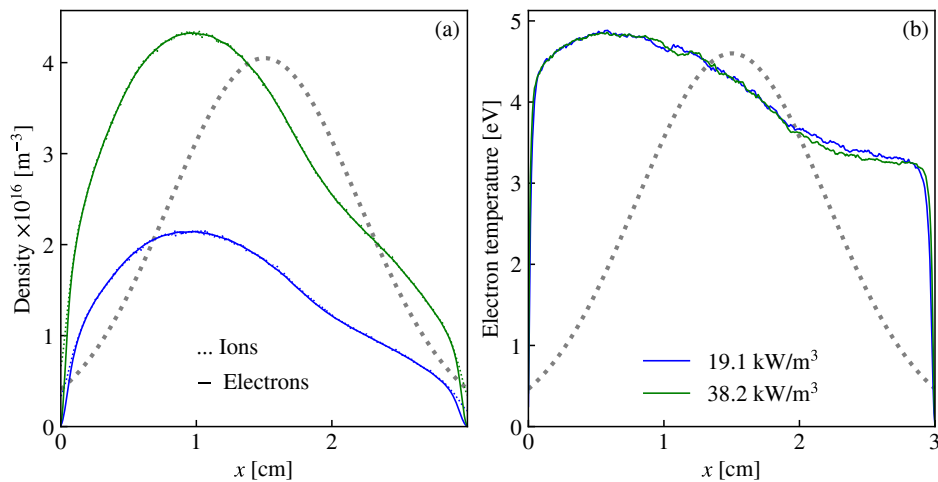


Figure 4.8: (a) Plasma density and (b) electron temperature profiles at $y = l_y/2 = 1.5 \text{ cm}$. The two runs are performed at 6 mTorr and 19.1 kW/m^3 (blue) and 38.2 kW/m^3 (green). The Gaussian magnetic field profile is indicated in gray dotted lines and the maximum value is 20 mT. In (a), the dotted lines represent the ion density and the solid lines represent the electron density. The heating electric field decreases linearly with x from 0 to l_x . The plasma density data are averaged over several μs at steady-state.

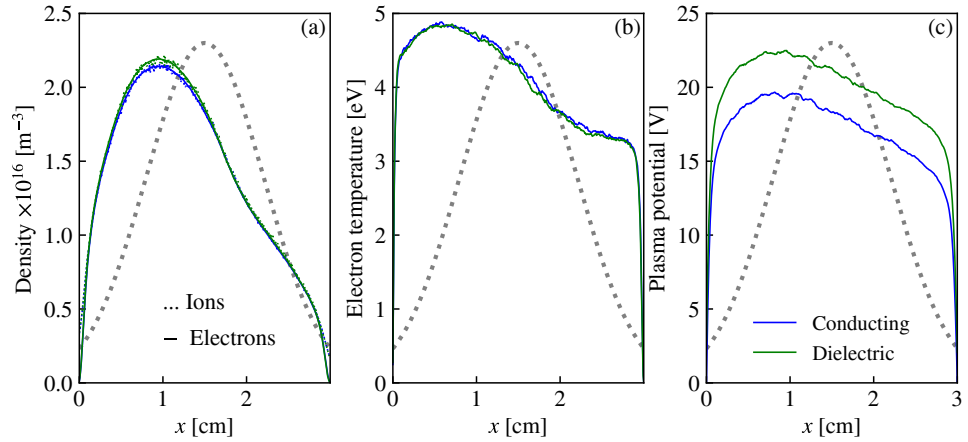


Figure 4.9: Properties along the x axis of a magnetic filter with conducting walls everywhere (blue lines), and with dielectric boundaries at the walls located at $y = 0$ and $y = l_y$ (green lines). The runs are performed at 6 mTorr of gas pressure, with a peak magnetic field of 20 mT. The Gaussian magnetic field profile is indicated with the gray dotted lines. (a) Electron and ion densities. (b) Electron temperature. (c) Plasma potential.

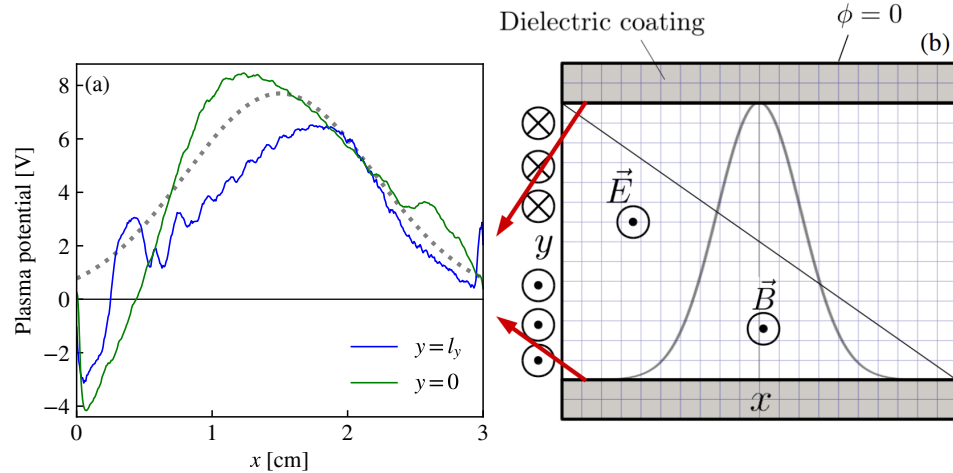


Figure 4.10: (a) Plasma potential at the inner walls of the discharge at $y = 0$ (green) and $y = l_y$ (blue). (b) Sketch of the simulation setup including the dielectric layer.

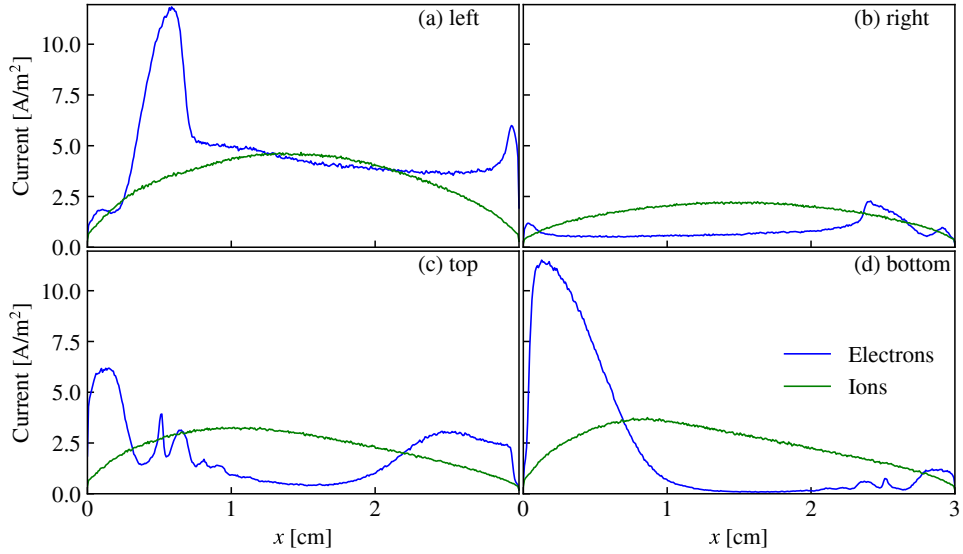


Figure 4.11: Electron and ion currents (absolute values) collected at the walls of the simulation domain at (a) $x = 0$, (b) $x = l_x$, (c) $y = l_y$, and (d) $y = 0$. The run characteristics are analogous to Fig. 4.9 with conducting walls everywhere.

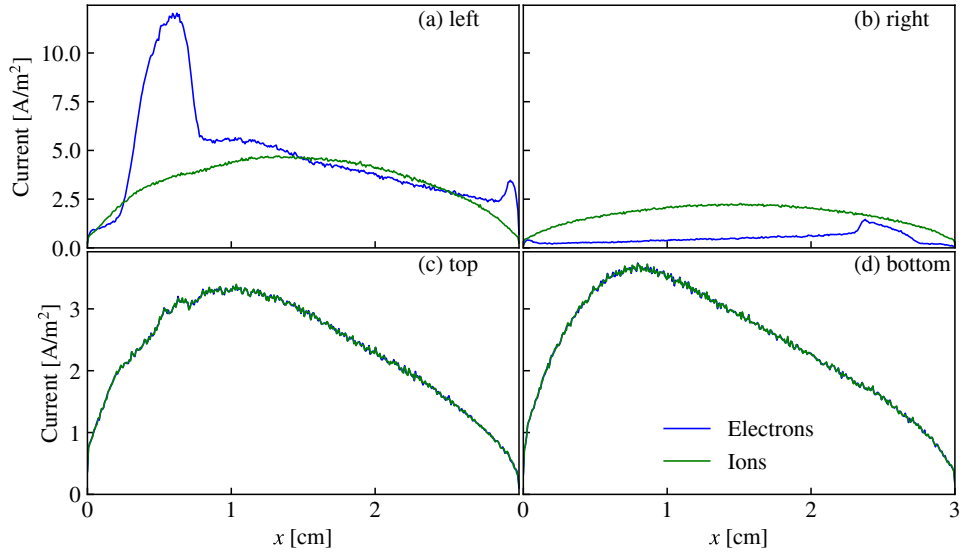


Figure 4.12: Electron and ion currents (absolute values) collected at the walls of the simulation domain at (a) $x = 0$, (b) $x = l_x$, (c) $y = l_y$, and (d) $y = 0$. The run characteristics are analogous to Fig. 4.9 with dielectric walls at $y = 0$ and $y = l_y$.

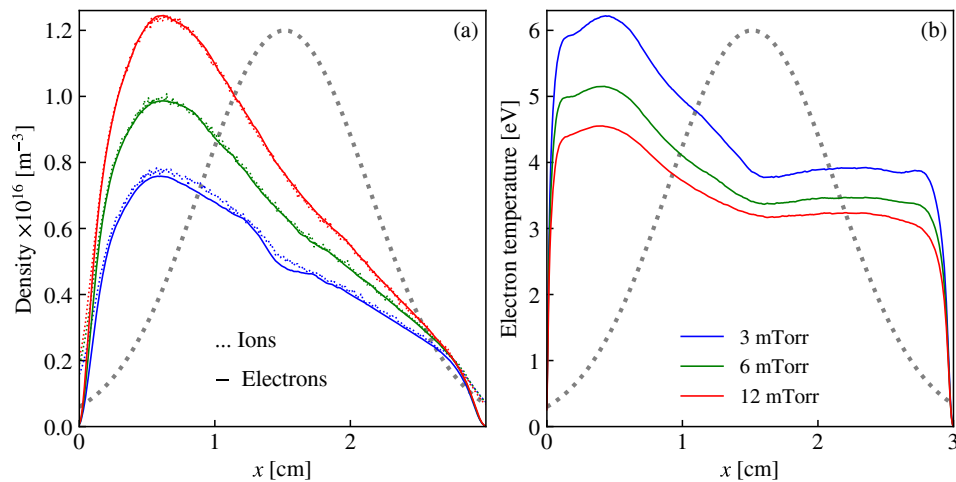


Figure 4.13: (a) Plasma density and (b) electron temperature profiles at $y = l_y/2 = 1.5$ cm for a magnetic filter at 3 mTorr (blue), 6 mTorr (green), and 12 mTorr (red). The heating power is 9.6 kW/m³ and the heating electric field decreases linearly with x from 0 to $l_x/3$. The Gaussian magnetic field profile is indicated in gray dotted lines and the maximum value is 20 mT. In (a), the dotted lines represent the ion density and the solid lines represent the electron density. Both the density and the temperature data are averaged over several μs .

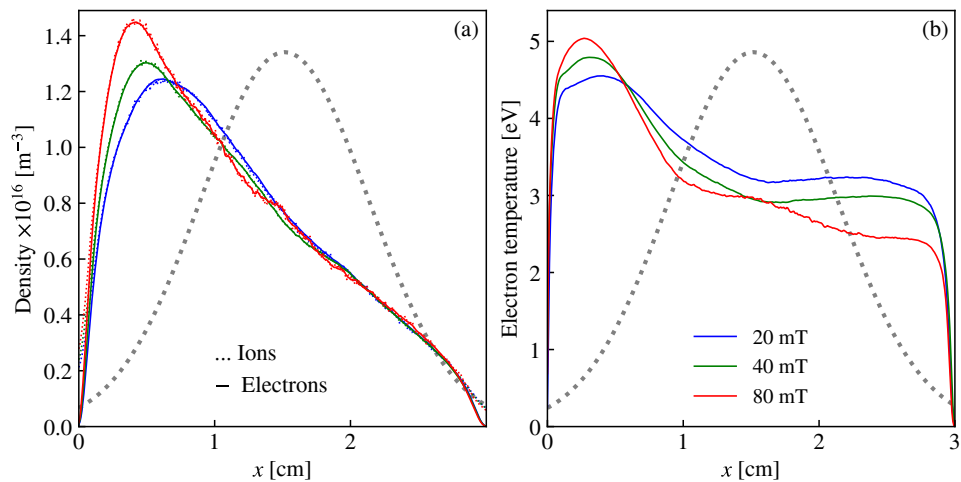


Figure 4.14: (a) Plasma density and (b) electron temperature profiles at $y = l_y/2 = 1.5$ cm for a magnetic filter at 12 mTorr. The heating power is 9.6 kW/m³ and the heating electric field decreases linearly with x from 0 to $l_x/3$. The Gaussian magnetic field profile is indicated in gray dotted lines and the maximum value varies between 20 and 80 mT. In (a), the dotted lines represent the ion density and the solid lines represent the electron density. Both the density and the temperature data are averaged over several μs .

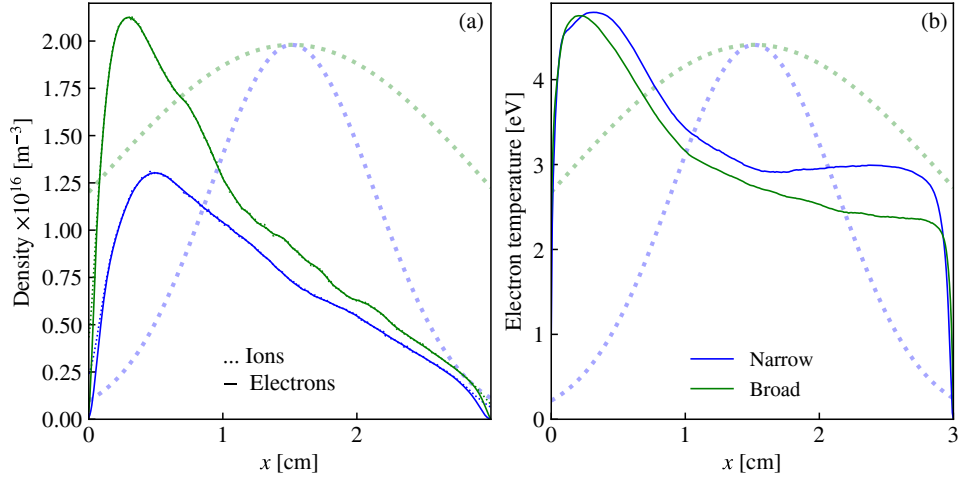


Figure 4.15: (a) Plasma density and (b) electron temperature profiles at $y = l_y/2 = 1.5 \text{ cm}$ for a magnetic filter at 12 mTorr. The heating power is 9.6 kW/m^3 and the heating electric field decreases linearly with x from 0 to $l_x/3$. The magnetic filters are modeled by Gaussian functions with a standard deviation of $0.2l_x$ (blue) and $0.5l_x$ (green), and the maximum magnetic field is 40 mT in both cases. In (a), the dotted lines represent the ion density and the solid lines represent the electron density. Both the density and the temperature data are averaged over several μs .

4.6.3 Influence of the gas pressure

4.6.4 Effect of the magnetic field

Magnetic field strength

Width of the magnetic filter

4.7 1D fluid model of a magnetic filter

4.7.1 Model assumptions

4.7.2 Model equations

As electron temperature gradients are inherent to the functioning of a magnetic filter, the electron energy equation has to be taken into account.

$$\frac{3}{2}\partial_t(n_e k_B T_e) + \frac{3}{2}\nabla \cdot (n_e k_B T_e \mathbf{v}_e) + n_e k_B T_e \nabla \cdot \mathbf{v}_e = J_e \cdot E - n_e v_{iz} e \mathcal{E}_{iz} \gamma_i - 3\mu k_B (T_e - T_g) n_e v_e \quad (4.1)$$

where

$$\mathcal{E}_{iz}\gamma_i = \mathcal{E}_{iz} + \sum K_{ex}\mathcal{E}_{ex}/K_{iz} \quad (4.2)$$

is the mean energy lost per electron created. The summation is performed over all the excitation levels included in the model. For each value of x , the fluid equations are integrated in the (yz) plane. The particle losses perpendicularly to the x axis are accounted for using a 2D h factor. In this 1D quasineutral model, it is assumed that the plasma is ambipolar along x such that

$$v_{e,x} = v_{i,x} = v \quad (4.3)$$

and $n_i = n_e = n$. The particle balance equation is

$$\partial_t n + \partial_x(nv) = nv_{iz} - \frac{hu_B n C}{S} \quad (4.4)$$

where C is the contour of the cross section at $x = cst$ and S is the cross section surface area. The projections of the momentum conservation equations along the x axis are

$$0 = -\frac{k_B \partial_x(nT_e)}{n} + e\partial_x\phi - m_e v \left(\frac{\omega_{ce}^2}{v_e} + v_e \right) \quad (4.5)$$

for the electrons and

$$m_i \partial_t v + m_i v \partial_x v = -\frac{k_B \partial_x(nT_i)}{n} - e\partial_x\phi - m_i v_i v \quad (4.6)$$

for the ions, where the ion temperature is assumed constant in time and space, and the electron inertia is neglected. We assume that the ions are not magnetized. Summing up Eqs. (4.5) and (4.6),

$$m_i \partial_t v + m_i v \partial_x v = -\frac{k_B \partial_x[n(T_e + T_i)]}{n} - \left[m_i v_i + m_e \left(\frac{\omega_{ce}^2}{v_e} + v_e \right) \right] v \quad (4.7)$$

Eq. (4.1) becomes in 1D

$$\begin{aligned} \frac{3}{2} \partial_t(nk_B T_e) + \frac{3}{2} \partial_x(nk_B T_e v) + nk_B T_e \partial_x v &= w + nm_e v_e v^2 - nv_{iz} e \mathcal{E}_{iz} \gamma_i \\ &\quad - 3\mu k_B (T_e - T_g) n v_e - \frac{hu_B n e \mathcal{E}_w C}{S} \end{aligned} \quad (4.8)$$

where w is the volume density of power absorbed by the plasma. The heating source comes from an RF induced electric field in the y and z directions and writes

$$w = \frac{ne^2 E_{\max}^2}{2m_e v_e}. \quad (4.9)$$

where E_{\max} is the the amplitude of the heating electric field. In Eq. (4.8), \mathcal{E}_w is the mean energy carried by each electron lost at the wall. Typically, \mathcal{E}_w is proportional to the electron temperature.

$$e\mathcal{E}_w = \alpha k_B T_e \quad (4.10)$$

Assuming a constant electron temperature in each plane perpendicular to the x axis,

$$\alpha = \frac{1}{2} \left[1 + \ln \left(\frac{m_i}{2\pi m_e} \right) \right] \quad (4.11)$$

The total power absorbed by the plasma is

$$\mathcal{W} = S \int_0^{l_x} w dx \quad (4.12)$$

We introduce the normalized quantities

$$N = n/n_{\mathcal{E}_{\text{ref}}} \quad (4.13)$$

$$T = T_e/T_{\mathcal{E}_{\text{ref}}} \quad (4.14)$$

$$V = v/v_{\mathcal{E}_{\text{ref}}} \quad (4.15)$$

$$\nu = \nu_e/\nu_{\mathcal{E}_{\text{ref}}} \quad (4.16)$$

$$\nu_I = \nu_i/\nu_{\mathcal{E}_{\text{ref}}} \quad (4.17)$$

$$\nu_{IZ} = \nu_{iz}/\nu_{\mathcal{E}_{\text{ref}}} \quad (4.18)$$

$$\omega_{CE} = \omega_{ce}/\nu_{\mathcal{E}_{\text{ref}}} \quad (4.19)$$

$$W = w/w_{\mathcal{E}_{\text{ref}}} \quad (4.20)$$

$$X = x/l_{\mathcal{E}_{\text{ref}}} \quad (4.21)$$

$$T = t\nu_{\mathcal{E}_{\text{ref}}} \quad (4.22)$$

$$L_X = l_x/l_{\mathcal{E}_{\text{ref}}} \quad (4.23)$$

where the reference quantities are

$$l_{\mathcal{E} \text{ ref}} = S/C \quad (4.24)$$

$$w_{\mathcal{E} \text{ ref}} = v_e e \mathcal{E}_{iz} \left(\frac{C}{S} \right)^3 \quad (4.25)$$

$$n_{\mathcal{E} \text{ ref}} = \frac{\mathcal{W}S}{C v_{\mathcal{E} \text{ ref}} e \mathcal{E}_{iz}} \quad (4.26)$$

$$T_{\mathcal{E} \text{ ref}} = e \mathcal{E}_{iz} / k_B \quad (4.27)$$

$$v_{\mathcal{E} \text{ ref}} = \left(\frac{e \mathcal{E}_{iz}}{m_i} \right)^{1/2} \quad (4.28)$$

$$\nu_{\mathcal{E} \text{ ref}} = \frac{C}{S} \left(\frac{e \mathcal{E}_{iz}}{m_i} \right)^{1/2} \quad (4.29)$$

The set of normalized equations to be solved is (Eqs. (4.4), (4.7) and (4.8))

$$\partial_T N + \partial_X (N V) = N v_{IZ} - h N T^{1/2} \quad (4.30)$$

$$\partial_T V + V \partial_X V = -\partial_X T - (T + T_I) \frac{\partial_X N}{N} - \left[v_I + \mu \left(\frac{\omega_{CE}^2}{v} + v \right) \right] V \quad (4.31)$$

$$\begin{aligned} \frac{3}{2} \partial_T (N T) + \frac{3}{2} \partial_X (N V T) + N T \partial_X V &= W + \mu N v v^2 - N v_{IZ} \gamma_i \\ &\quad - 3 \mu (T - T_g) v N - h T^{3/2} N \alpha \end{aligned} \quad (4.32)$$

The unknown variable vector of this system of equations is

$$U = \begin{pmatrix} N \\ V \\ T \end{pmatrix} \quad (4.33)$$

and the system takes the matrix form

$$\partial_T U + A \partial_X U = B \quad (4.34)$$

where

$$A = \begin{pmatrix} V & N & 0 \\ \frac{T+T_I}{N} & V & 1 \\ 0 & \frac{2}{3} T & V \end{pmatrix} \quad (4.35)$$

and

$$B = \begin{pmatrix} N v_{IZ} - h N T^{1/2} \\ -v_I V - \mu \left(\frac{\omega_{CE}^2}{v} + v \right) V \\ \left(1 - \frac{2\alpha}{3} \right) h T^{3/2} - v_{IZ} T + \frac{2W}{3N} + \frac{2\mu v V^2}{3} - \frac{2\gamma_i v_{IZ}}{3} - 2\mu (T - T_g) v \end{pmatrix} \quad (4.36)$$

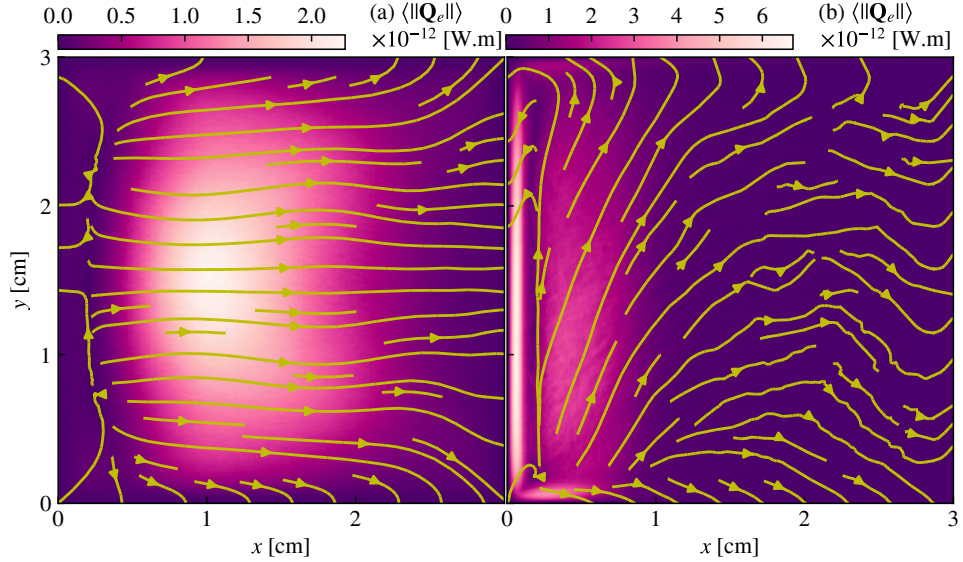


Figure 4.16: Mean electron heat fluxes found in the PIC simulations at 12 mTorr, at steady-state. The absorbed power is 9.6 kW/m³ and the amplitude of heating electric field decreases linearly with x from 0 to $l_x/3$. The arrows represent the streamlines. (a) No magnetic field. (b) Broad magnetic filter [11] with a maximum at 40 mT.

4.7.3 Numerical scheme

The system is solved using the Steger-warming scheme [82]. The reaction rates are taken from Fig. 1.4(a) for argon, with only one process describing all the inelastic collisions.

4.7.4 First results with no heat flux

4.7.5 The role of the heat flux

Heat flux in the PIC simulations

Heat flux modeling

Modified numerical scheme

4.7.6 Comparison with PIC simulations

Classical transport

Instability-enhanced transport

**4.8 The effect of instability-enhanced plasma transport in
the 1D modeling of PEGASES**

4.9 "Anomalous" heat transport

Chapter 5

Simulation of iodine discharges

Contents

5.1	Iodine for electric space propulsion	192
5.2	Iodine cross section set	193
5.2.1	Plasma species	193
5.2.2	Electron-neutral reactions	194
5.2.3	Ion-neutral reactions	195
5.2.4	Ion loss mechanisms	196
5.3	2D PIC simulation of an iodine discharge	203
5.3.1	Electronegative gas balance	203
5.3.2	Relaxation oscillations in an iodine plasma	206
5.4	A low power discharge model for iodine	212
5.5	Global model comparison	212
5.6	Simulation of negative ion production through a magnetic filter	212

Iodine is a good candidate for space electric propulsion due to its high mass, and low ionization potential. Additionally, iodine can be stored in solid state which makes pressurized vessel unnecessary in iodine plasma thruster designs. Iodine is a halogen whose mass is 126.905 amu. It can however deposit on satellite surfaces, which can cause contamination on SC surfaces. In this Chapter, we first present a comprehensive cross section set for the modeling and simulation of an ICP. Results of a global model, as well as PIC simulations of a weakly ionized plasmas in 2D are presented. Finally, a few simulations of the PEGASES thruster with the magnetic filter in reduced geometry and low

power are discussed.

Iodine is mostly available under the form of the I_2 molecule. In the PEGASES experiment carried out at LPP, the solid sample is heated up to approximately 70°C in order to be sublimated. A molecular gas of I_2 is injected in the discharge chamber, close to the antenna. The pressure inside the discharge chamber is controlled by a vacuum pump and measured by a gauge. More information on the experimental setup is available in the PhD thesis of the former students that worked on the PEGASES thruster in the past years. The experimental device operated with iodine is described in details in P. Grondein et al. [58]. P. Grondein has carried out probe experiments inside the PEGASES device and developed a global model of the discharge without the magnetic filter. Thanks to our work on the magnetized plasma column, the ion losses in the magnetized case can be estimated, such that the global model is extended to the magnetized case. More reactions are added to the model, and a minimal set of reactions was implemented in *LPPic*.

5.1 Iodine for electric space propulsion

Iodine has been contemplated for space electric propulsion since the end of the 1990s as a possible alternative to xenon. The advantage of electric space propulsion in general is to feature a very good mass consumption efficiency, with high I_{sp} designs. The mass of the full pressurized xenon tank on a typical Geostationary Earth Orbit (GEO) spacecraft is about 0.1% of the cost of the full system [127]. However, this maybe significant for satellites that cost several hundred million euros, and may not be optimal for simpler and more compact designs required for smaller satellites in Low Earth Orbit (LEO). On of the first study on the potential of iodine of electric space propulsion was performed by Dressler et al.. In a conference paper [42], the authors suggest that the performances of GIT or HT operated with iodine may be as good as equivalent designs with xenon. The authors propose a propellant handling system composed of a heating tank where iodine crystals are stored and vaporized, a porous frit that filters out crystal particles. The gas enters the discharge chamber through a heated pipe to avoid deposition and a mass flow controller. The power consumption for the heating system is found to be negligible compared to the discharge power. Barnes and Kushner [7] perfomed optical measurements on low pressure discharges in a mixture of xenon and iodine. More recently, Steinberger and Scime developed optical diagnostics to measure the proportions of the various specious inside an iodine plasma [114, 113].

At LPP, where the expertise on electronegative plasmas comes from the techniques developed for plasma etching and deposition with gases such as oxygen CF_4

mixtures [17], chlorine [41] or sulfur hexafluoride (SF_6) [20, 21], the interest for iodine electric propulsion systems is not only economical. The ultimate aim is to achieve new thruster designs where both positive and negative ions are extracted. The design could allow cathode-less thruster designs, and mutual recombination in the plume could possibly generate a neutral beam that would be very focused (low plume angle) and that would not be deflected towards the charged surfaces of the satellite. The latter aspect is particularly important since surface reactivity is a potential issue for plasma thrusters operated with iodine. The first concepts and prototypes are described in details in G. Leray's thesis [81], as well as in the work of L. Popelier [93]. The extraction was investigated experimentally by Lafleur et al. [75, 80], and the acceleration by Rafalskyi et al. [96]. In 2016, P. Grondein [59] developed a global model of an iodine GIT. There was no magnetic field in the model, so the electronegativity derived from the model was quite low. The performances were comparable with those of the xenon model.

The extraction, the acceleration, and the plume recombination are not investigated theoretically here, and are not modeled yet. In the next sections, a methodology to simulate the inside part of an GIT operated with iodine is described.

5.2 A collision cross section set for the simulation of iodine plasmas

Some of the fundamental data are missing for iodine and we do not pretend to describe the complete chemistry of an iodine plasma. All the assumptions made to gather the reaction set of Table 5.2 are made explicit in the text. Some of the assumptions come from comparisons with chlorine plasmas, but all the data are taken from the literature or from specific computations made by Quantemol Ltd. The cross sections and the reaction rates are shown in Figs. 5.1 to 5.3. The reactions that were not considered here are also presented in Table 5.3.

5.2.1 Plasma species

Iodine is very reactive and can form a variety of species depending on electron temperature conditions. We follow here the work of P. Grondein [58] and we assume that there are only six species in the plasma



In general, the gas is injected under the form of molecular iodine I_2 . Dissociation energy of I_2 is quite low (1.567 eV) such that I atoms will soon be present in the plasma. Moreover, dissociative attachment does not have a very high cross section

I atom			
Mass	126.905	amu	[109]
Ionization potential	11.64	eV	[61]
Relative polarizability	27.0		[94]

I ₂ molecule			
Mass	253.81	amu	[109]
Ionization potential	9.31	eV	[61]
Inter-atomic bond	2.7128×10^{-10}	m	[61]
Relative polarizability	69.7		[90]

Table 5.1: Physical properties of iodine

($< 2 \times 10^{-21} \text{ m}^2$) but no threshold, so I⁻ ions are also present in the mixture. Finally electron impacts on I and I₂ cause I⁺ and I₂⁺ ions to form. All the processes considered will be described in the next paragraph with more details.

We are aware that other species may appear in the plasma. Henri (1972) [65] performed a study on mass spectrometers using electronegative plasmas, with relevant experimental results on iodine. The presence of I₃⁺ and I₃⁻ ions was hence detected. Spencer and Smith found I₂⁻ ions as well [44]. Moreover, one can expect doubly-charged ions I²⁺ to form for high electron energies, as it is observed in Hall thrusters operated with xenon. The I²⁺ ion has a quite high ionization energy (19.13 eV [109]) and was not particularly observed in Hall thrusters operated with iodine [117].

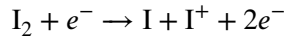
5.2.2 Electron-neutral reactions

The mechanisms that drive the balance of species in an iodine plasma is much more complex than in the case of a noble gas due to the species reactivity. The fundamental data are available on the NIST database [109] and the references therein. Iodine is an electronegative gas and Biondi and Fox showed that dissociative attachment



was the main mechanism for electron losses in experimental conditions [12]. They estimated the reaction cross section in a microwave plasma afterglow at low electron temperature [47, 13]. Positive ions I⁺ and I₂⁺ are formed from I atoms and I₂ molecules with ionization energies of 11.64 eV and 9.31 eV respectively [3]. Some of the cross sections for electron impact mechanisms were calculated by J. Hamilton [61] using the R-matrix method developed by J. Tennyson [120, 121]. This is

the case for dissociative ionization



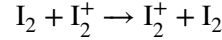
that has a threshold energy of 10.75 eV, but the branching between electron impact ionization and dissociative ionization of the I_2 molecule was extrapolated from the mass spectra of Cl_2 and Br_2 . The results of the R-matrix method were in agreement with experimental results [133] for elastic scattering of electrons on the I atom. The excitation states of the I atom are potentially very numerous, but all the excitation reactions are modeled with only one "superelastic" reaction, with a typical energy loss lower than 1 eV (0.953 eV). No excitations states of I_2 were found in the R-matrix calculation, due to the fact that the dissociation energy of the I_2 molecule is quite low (1.567 eV). As shown in Chapter 1, this reduction does not have a large influence on the EEDF. Finally, electron impact I_2 dissociation has a quite large cross section ($3.6 \times 10^{-20} m^2$ at 3.4 eV) and is generally as important as dissociative attachment for the equilibrium between I_2 and I.

5.2.3 Ion-neutral reactions

As for argon, the elastic collisions between ions and neutrals are split in two categories: isotropic scattering and backscattering. The fundamental data are sparse for noble gases and almost non-existent for iodine. The isotropic scattering was assumed to follow Langevin capture cross sections, that can be computed from atomic and molecular polarizability [84]. The data is found in the book by Radzig and Smirnov [94] for I and in a paper by Maroulis et al. for I_2 [90]. The numerical values are indicated in Table 5.1.

The resonant backscattering reaction between I and I_+ should follow the formula given by Sakabe et al. [103] (Eq. (1.29)), as it was done for krypton. The prediction of the Sakabe formula was compared to computations performed by Dressler et al. [42] based on a linear combination of atomic orbitals in Fig. 5.4. The latter computations were successfully compared to experimental data in the original paper. The Sakabe formula shows an agreement better than 6% with these computations in the range 10-1000 eV. However, the disagreement is higher at low energy, which suggests that one should not be too confident about the application of the Sakabe formula in the 0.026-10 eV energy range. Furthermore, it is assumed that the resonant charge exchange between I and I^- has the same cross section, which is somewhat arbitrary and result mainly from a lack of fundamental data. However, Karmohapatro (1965) showed that the resonant charge exchange reaction between Cl and Cl^- had a cross section only a few times higher than the resonant cross section between Cl and Cl^+ . We can therefore anticipate that the order of magnitude

should be correct for iodine. The resonant charge exchange reactions between diatomic molecules and their positive ion counterpart was the focus of a theoretical paper by Evseev et al. (1979), from which the cross section for the reaction



could be estimated.

The non-resonant charge exchange reaction



should play an significant role in the equilibrium between I_2^+ and I^+ ions. Experimentally, it was suspected to cause a significant depletion of the I^+ population [65]. In a chlorine plasma, this reaction cross section is twice lower than the resonant charge exchange reaction between Cl_2 and Cl_2^+ . We made this assumption for iodine, and estimated that the cross section for reaction (5.2) was half of the cross section for resonant charge exchange between I_2 and I_2^+ .

If the behavior is the same as for chlorine, the (non-resonant) charge exchange reaction between I and I_2^+ , and the fragmentation reaction $I_2^+ + I_2 \rightarrow I_2 + I + I^+$ should both have thresholds higher than 1 eV and their influence can be neglected in a first approximation. Collisional detachment of electrons can also be important in some electronegative gases such as oxygen but it is assumed to have a quite high threshold for iodine. Typically, the thresholds were estimated for chlorine by Huang and Gudmundsson [68] to 3.61 eV for $Cl^- + Cl_2 \rightarrow Cl + Cl_2 + e^-$ and 1.13 eV for $Cl^- + Cl \rightarrow Cl_2 + e^-$. The ion energies observed were mostly below 1 eV such that these reactions are neglected for iodine. Collisional detachment is an important mechanism for neutral beam generation in high energy ion sources. While it seems reasonable to neglect the four reactions mentioned above for the ionization and magnetic filtering stages of the PEGASES thruster, this assumption may not be valid for the acceleration stage, where the ions reach much higher energies. More insights about these reactions in a chlorine discharge can be found in a paper by Huang and Gudmundsson [68], with relevant 1D PIC simulations of a chlorine CCP.

5.2.4 Ion loss mechanisms

At low ion energies, two mechanisms are mainly responsible for negative ion loss, that are two kinds of mutual neutralization. The recombination with I_2^+



was investigated in a paper by Yeung [131]. The recombination with I^+



was studied by Greaves in the 1960s [57]. The electron detachment from I^-



is also investigated. The cross section was computed by J. Hamilton [62] and a threshold at 2.18 eV of electron energy was found. For weakly ionized plasmas, this reaction is not dominant and it was not implemented in the PIC simulation code. The electron impact dissociation of the I_2^+ molecular ion is also considered [62], with a threshold at 2.17 eV. Reactions (5.3), (5.4) and (5.5) are essential to balance negative ion production through dissociative attachment. Indeed, if no magnetic field is applied on the discharge, the negative ions are confined by the electric field of the sheath and cannot escape because $k_B T_n \ll e\phi_s$, T_n being I^- temperature. While the presence of these reactions are important, F. Marmuse has shown by uncertainty quantification methods that the value retained for the reaction rate was not critical, because it does not play a major role in the determination of the electron temperature.

Positive ions are destroyed by mutual neutralization with I^- but they are also lost at the walls, with a Bohm flux that needs to be corrected due to the presence of negative ions. The review paper by Riemann (1991) [102] provides a quite general framework to apprehend the Bohm sheath criterion. The kinetic approach that is provided allows to derive a Bohm sheath criterion with potentially several positive ion species, both positive and negative. The condition for a collisionless sheath is always that the ion kinetic energy is of the order of $k_B T_e/2$ for a plasma where all the positive ions are singly charged, except when the electronegativity becomes high at the sheath edge. This was first shown experimentally by Braithwaite and Allen (1988), and explained in details by Franklin and Snell (1999) [48]. At high electronegativity, the kinetic energy of the ions becomes of the order of $k_B T_n/2$ and the flux of negative ions leaving the plasma cannot be neglected anymore.

Reaction	Process	Threshold [eV]	Model	Reference
<i>Electron impact I</i>				
$I + e^- \rightarrow I + e^-$	Elastic	0	0D+PIC	[61]
$I + e^- \rightarrow I + 2e^-$	Ionization	11.64	0D+PIC	[61]
$I + e^- \rightarrow I^* + e^-$	Excitation	0.9529	0D+PIC	[61]
<i>Electron impact I_2</i>				
$I_2 + e^- \rightarrow I_2 + e^-$	Elastic	0	0D+PIC	[61]
$I_2 + e^- \rightarrow I_2^+ + 2e^-$	Ionization	9.31	0D+PIC	[61]
$I_2 + e^- \rightarrow I^+ + I + 2e^-$	Dissociative ionization	10.75	0D+PIC	[61]
$I_2 + e^- \rightarrow I^- + I$	Dissociative attachment	0	0D+PIC	[61]
$I_2 + e^- \rightarrow 2I + e^-$	Dissociation	1.567	0D+PIC	[61]
<i>Electron impact dissociation of I_2^+</i>				
$I_2^+ + e^- \rightarrow I^+ + I + e^-$	Dissociation	2.17	0D	[62]
<i>Electron detachment from I^-</i>				
$I^- + e^- \rightarrow I + 2e^-$	Detachment	2.1768	0D	[62]
<i>Recombination</i>				
$I^- + I_2^+ \rightarrow I + I_2$	Mutual neutralization	0	0D+PIC	[57]
$I^- + I^+ \rightarrow 2I$	Mutual neutralization	0	0D+PIC	[131]
<i>Isotropic scattering of ions</i>				
$I + I^+ \rightarrow I + I^+$	Elastic	0	PIC	Langevin
$I + I_2^+ \rightarrow I + I_2^+$	Elastic	0	PIC	Langevin
$I + I^- \rightarrow I + I^-$	Elastic	0	PIC	Langevin
$I_2 + I^+ \rightarrow I_2 + I^+$	Elastic	0	PIC	Langevin
$I_2 + I_2^+ \rightarrow I_2 + I_2^+$	Elastic	0	PIC	Langevin
$I_2 + I^- \rightarrow I_2 + I^-$	Elastic	0	PIC	Langevin
<i>Backscattering of ions</i>				
$I + I^+ \rightarrow I^+ + I$	Charge exchange	0	PIC	[103]
$I + I^- \rightarrow I^- + I$	Charge exchange	0	PIC	[103]
$I_2 + I_2^+ \rightarrow I_2^+ + I_2$	Charge exchange	0	PIC	[45]
$I_2 + I^+ \rightarrow I_2^+ + I$	Charge exchange	0	PIC	[103]+[68]
<i>Surface recombination</i>				
$I \rightarrow \frac{1}{2}I_2$	Wall process	0	0D+PIC	[41]

Table 5.2: Reactions of a low temperature iodine plasma investigated in this work.

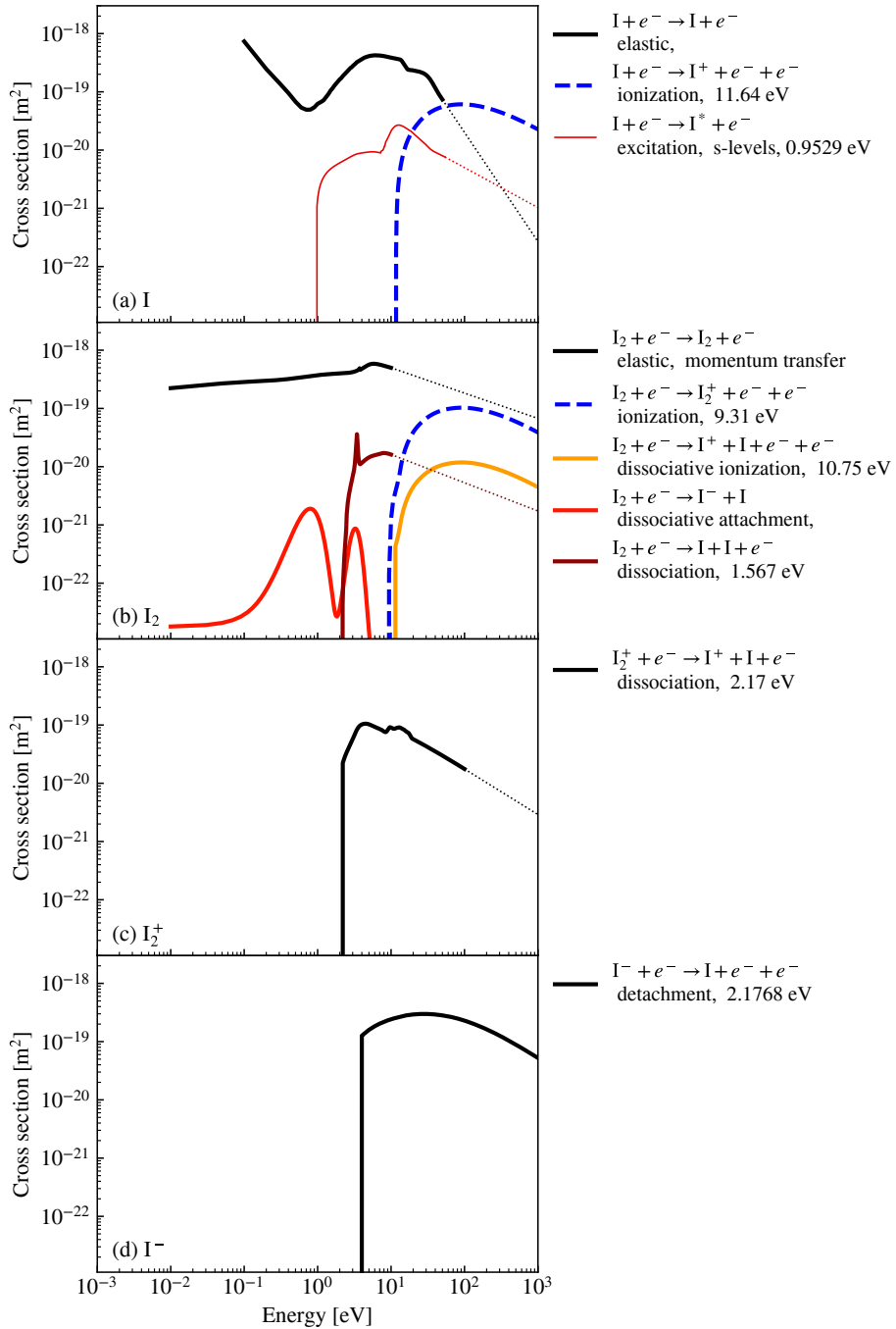


Figure 5.1: Electron-neutral collision cross sections for iodine species I, I₂, I₂⁺, and I⁻ computed by Quantemol. The dotted lines represents linear extrapolation in logarithmic scale.

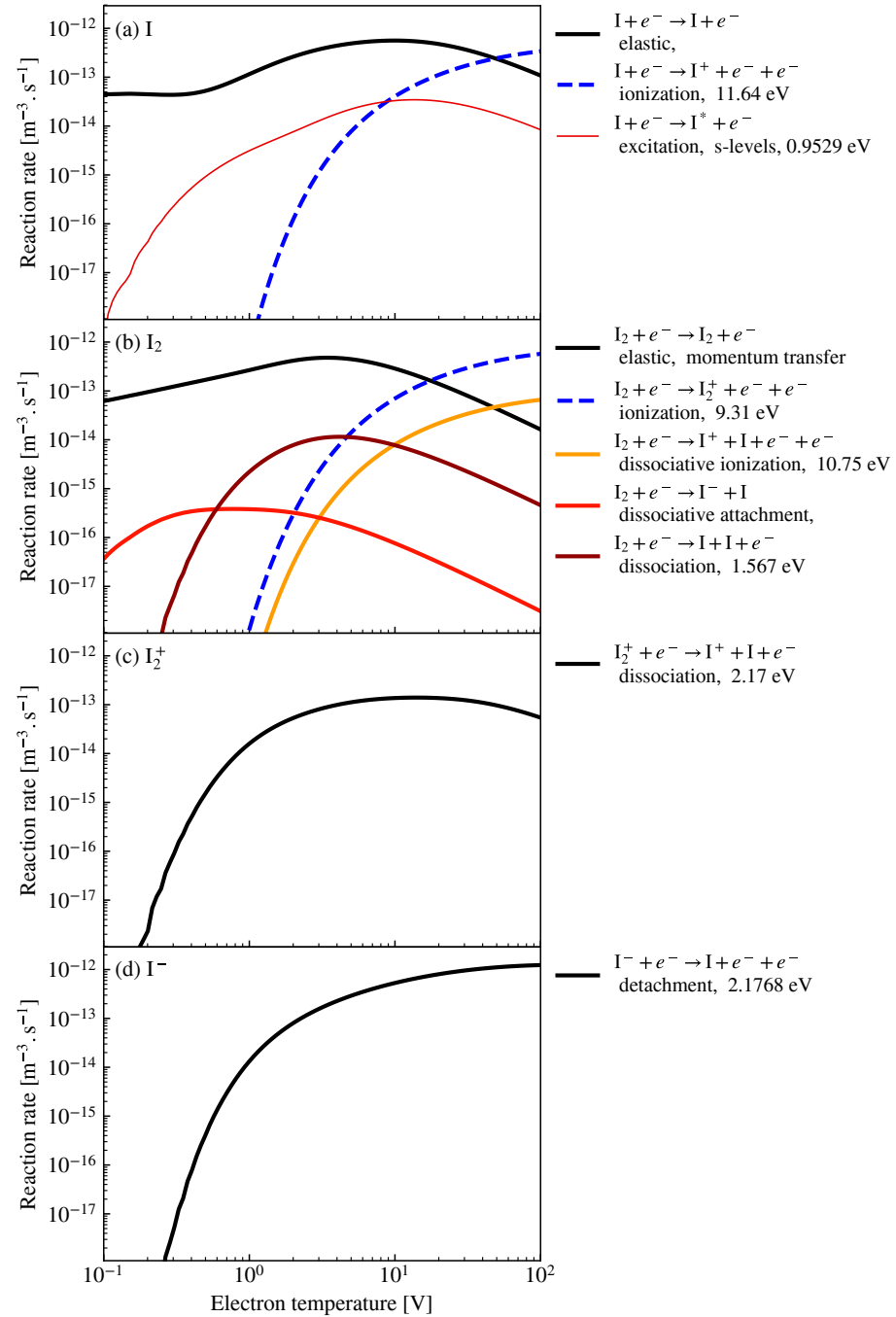


Figure 5.2: Electron-neutral reaction rates for a Maxwellian EEDF and neutral atoms at rest. Numerical integration was performed over the data of Fig. 5.1.

Reaction	Process	Reason	Reference
<i>Electron impact</i>			
$I_2 + e^- \rightarrow I_2^* + e^-$	Excitation	Threshold $> \mathcal{E}_{diss}$	[61]
$I_2 + e^- \rightarrow I^+ + I^- + e^-$	Polar dissociation	High threshold and low CS	[68, 65]
$I^- + e^- \rightarrow I^+ + 3e^-$	Electron impact detachment	Threshold > 20 eV	[68]
$I_2^+ + e^- \rightarrow 2I$	Dissociative recombination	Weakly ionized	[68]
$I_2 + e^- \rightarrow 2I^+ + 3e^-$	Dissociative double ionization	High threshold (22.5 eV)	[42]
<i>Ion impact</i>			
$I + I_2^+ \rightarrow I^+ + I_2$	Charge exchange	Threshold > 1 eV	[68]
$I_2^+ + I_2 \rightarrow I_2 + I + I^+$	Fragmentation	Threshold > 1 eV	[68]
$I^- + I_2 \rightarrow I + I_2 + e^-$	Detachment by I_2	Threshold > 1 eV	[68]
$I^- + I \rightarrow I_2 + e^-$	Detachment by I	Threshold > 1 eV	[68]

Table 5.3: Identified reactions that were neglected in the frame of this work.

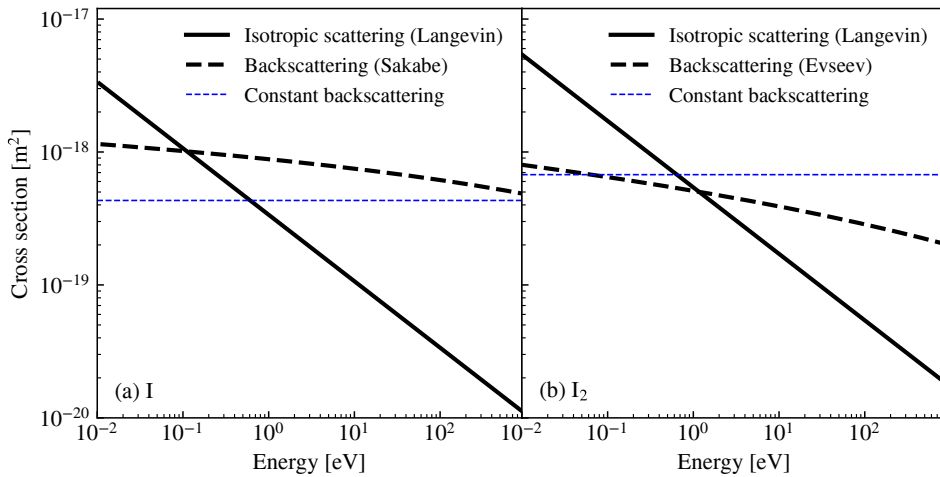


Figure 5.3: Ion-neutral collision cross sections for iodine species. The Langevin capture cross sections depend on the target only.

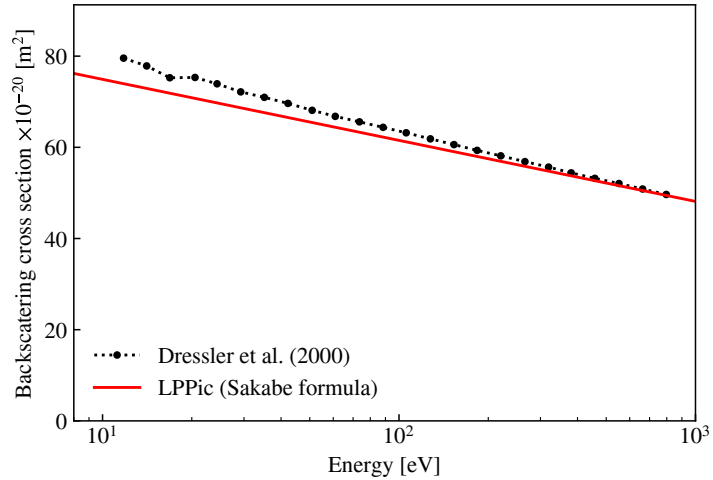


Figure 5.4: Comparison of cross sections for the resonant charge exchange between I and I^+ . The dotted line is the computation by Dressler et al. [42], and the solid line is the application of Eq. (1.29) [103] to atomic iodine. The latter is used in the *LPPic* code.

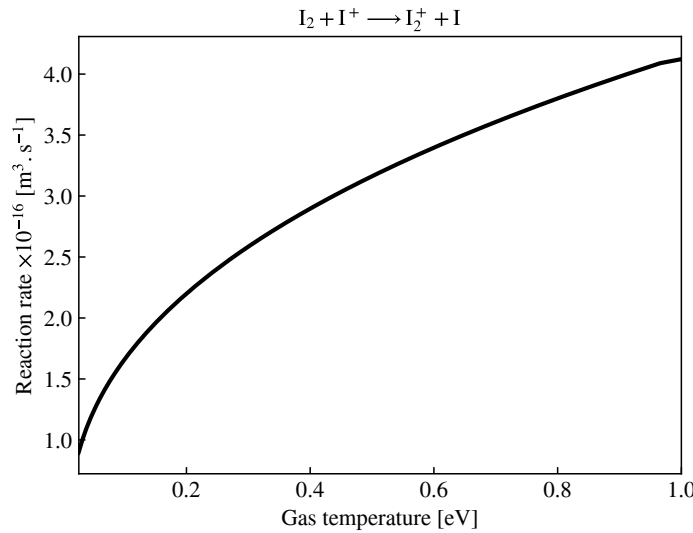


Figure 5.5: Reaction rate used in the global model for the non-resonant charge exchange reaction between I_2 and I^+ , as a function of the gas temperature.

5.3 2D PIC simulation of an iodine discharge

5.3.1 Electronegative gas balance

Most of the reactions that were discussed above are necessary to model correctly an iodine discharge via PIC simulation. Only electron impact dissociation of I_2^+ and electron detachment from I^- were neglected, because the results of the global of P. Grondein et al. [59] did not show significant discrepancies when these reactions were added, for the range of parameters we are interested in. Some of these reactions can be easily adapted from the procedures used to model noble gas discharge as described in and in V. Croes' thesis [35]. This is the case for elastic collisions, excitations, ionization and dissociative ionization reactions. The dissociative attachment is numerically treated as an ionization reaction, except that the electron is absorbed instead of producing two secondary electrons. Dissociation is treated as an excitation reaction from the point of view of the electron, with a threshold energy of 1.567 eV. However, the data structure of the *LPPic* code had to be changed in depth. Two main Fortran90 types were created, one for the population, and one for the gas. Since Fortran is not really an object oriented language, choices had to be made for the data structure of the various populations of super-particles. We chose to declare an array of fixed size `HSpecies` that contains all the populations of heavy particles tracked by the PIC algorithm:

```
integer, parameter :: N_HSpecies_max = 10
type(population), dimension(N_HSpecies_max) :: HSpecies
```

The maximum number of heavy species is hardcoded to 10 but can easily be changed if needed in a future version of the code. The population type contains mainly a allocatable array of `particle` objects. The `particle` type was not really modified from the previous versions of the code. Its definition is:

```
type population
    real(dbleprc) :: mass = 1 ! mass of
        the particles (1 for elecs)
    integer :: charge = 0 ! charge
        of the particles
    real(dbleprc) :: T_inj = -1 !
        injection temperature
    type(particle), dimension(:), allocatable :: part_tab
end type population
```

Therefore, the number of allocatable arrays of particles corresponds only to the number of heavy species that are simulated, and wasted memory is limited.

The `gas` type is defined in a similar way, except but it also contains all the grid

diagnostics relative to the reactions, as well as the collision frequencies used for the Vahedi method of null reaction [128]. Its specification is given in Appendix D.

The implementation of these two Fortran types required to modify almost the entire code and makes it more suitable for the simulation of real noble gas plasmas, where multiple ions are generated, metastable species and fast neutrals may be important to take into account, as well as mixtures and molecular plasmas.

The simulations that were performed still rely on the assumption of a weakly ionized plasma, because each gas is still treated as a uniform background, and local gas depletion is neglected. In particular, the neutral dynamics module developed by T. Charoy and D. Tordeux in 2018 was not coupled to the chemistry module. However, a gas balance equation is written globally to yield the correct fraction of I and I_2 in the gas. An effective dissociation rate was introduced such that the gas dynamics is decoupled from the ion dynamics. This dissociation rate $K_{\text{diss,eff}}(T_e)$ should represent all the processes that may turn the I_2 molecule into 2 I atoms, directly or indirectly. The effective reaction writes



The population of I atoms are repopulated by wall recombination. Indeed, wall recombination of atomic species has been identified of one of the main driver of the balance between gas species in electronegative plasmas [52]. Although the full derivation is made in a paper by Chantry (1987) on diffusion theory involving wall reflection [28], we propose a slightly different approach of the phenomenon that might be more understandable in our specific context.

Wall recombination process is described by using a wall sticking coefficient γ_s for atomic iodine, that represents the probability for an iodine atom to be stuck at the wall after a wall collision. When two atoms are collected at the same place, which always happens after a long steady-state, iodine is released under the form of a molecule I_2 . Therefore, the flux of I_2 released in the discharge due to wall recombination $\Gamma_{I_2,rec}$ is related to the flux of iodine atoms stuck at the wall surface $\Gamma_{I,s}$ by

$$\Gamma_{I_2,rec} = \frac{\Gamma_{I,s}}{2} \quad (5.7)$$

The aim is now to determine $\Gamma_{I_2,rec}$. γ_s is the probability for an individual atom to be attached to the wall, but may not necessarily be the probability for a full population of particles, provided that some of them may have already been through wall collisions. We will calculate a wall absorption frequency

$$\nu_s = \bar{v}_I / \langle \lambda \rangle_s \quad (5.8)$$

where $\langle \lambda \rangle_s$ is the average distance that an ion can go through before being attached to the wall, and \bar{v}_I is the mean velocity of the iodine atoms. Let λ_0 be the mean travel distance between two wall reflections. In the low pressure limit, the mean travel distance to the wall is $\lambda_0/2$ [28]. After it is created, an atom which is absorbed at the n^{th} wall collision has traveled a distance

$$\lambda_n = \lambda_0/2 + (n - 1)\lambda_0 \quad (5.9)$$

Moreover, the probability of being absorbed at the n^{th} wall collision is $(1 - \gamma_s)^{n-1} \gamma_s$. Therefore,

$$\langle \lambda \rangle_s = \sum_{n=1}^{+\infty} (1 - \gamma_s)^{n-1} \gamma_s \lambda_n \quad (5.10)$$

Series integration yields

$$\langle \lambda \rangle_s = \lambda_0 \frac{2 - \gamma_s}{2\gamma_s} \quad (5.11)$$

The wall absorption frequency is hence

$$\nu_s = \frac{\bar{v}_I}{\lambda_0} \frac{2\gamma_s}{2 - \gamma_s} \quad (5.12)$$

This collision frequency comes from the perspective of a single atom. If N_I atoms are present in the domain, the flow of atoms collected to the walls is

$$\Gamma_{I,s} S = N_I \nu_s \quad (5.13)$$

and of course $N_I = n_I V$, where S and V are respectively the surface area and the volume of the domain. It follows then that

$$\Gamma_{I,s} = \frac{V}{S\lambda_0} n_I \bar{v}_I \frac{2\gamma_s}{2 - \gamma_s} \quad (5.14)$$

At very low pressure, λ_0 is simply the mean geometrical distance between two points of the walls in the case of a cosine angular distribution function is $4V/S$ [24]. Therefore,

$$\Gamma_{I,s} = \frac{1}{4} n_I \bar{v}_I \frac{2\gamma_s}{2 - \gamma_s}. \quad (5.15)$$

The thermal flux

$$\Gamma_{I,thermal} = \frac{1}{4} n_I \bar{v}_I \quad (5.16)$$

appears in this equation.

At low γ_s ,

$$\Gamma_{I,s} = \gamma_s \frac{1}{4} n_I \bar{v}_I. \quad (5.17)$$

In this case, the particles may come from all the directions after potentially multiple reflections. The mean velocity is hence the 3D thermal velocity

$$\bar{v}_I = \left(\frac{8k_B T_I}{\pi m_I} \right)^{1/2} \quad (5.18)$$

Conversely, if γ_s is close to 1, no particle can come from the other parts of the walls. In this case, the source point defines the only particle direction and the particle flux corresponds to a 1D flux

$$\Gamma_{I,s} = \gamma_s \frac{1}{2} n_I \bar{v}_I \quad (5.19)$$

where

$$\bar{v}_I = \left(\frac{2k_B T_I}{\pi m_I} \right)^{1/2} \quad (5.20)$$

In both cases,

$$\Gamma_{I,s} = \frac{\gamma_s}{4} n_I \left(\frac{8k_B T_I}{\pi m_I} \right)^{1/2} \quad (5.21)$$

The gas temperature is an input parameter of the PIC simulation so we shall use the last formula. The formula that comes from Chantry's paper involves a mean velocity of the particles. It may not be relevant if the temperature is given as an input, and the flux of atoms attached to the walls is simply the sticking coefficient γ_s multiplied by the 3D thermal flux of particles. This seems reasonable at all pressure regimes and does not involve intricate considerations about the mean travel distance when collision processes are involved, as it should be the case if Chantry's approach had to be retained.

For chlorine, extensive measurements were performed to determine the recombination coefficient γ_s [73]. Values between 0.01 (silicon at room temperature) to 0.085 (stainless steel) were found, and a dependence to the wall temperature was identified. Since the surface aspect is often unknown and subject to gas deposition, comparisons between ICP experiments and simulations are required. It was shown [67, 34] that a value of $\gamma_s \approx 0.02$ yielded better predictions of the discharge properties. No fundamental values were found for iodine. In the global model developed by Grondein et al. [59], the value of $\gamma_s \approx 0.04$ was retained.

5.3.2 Relaxation oscillations in an iodine plasma

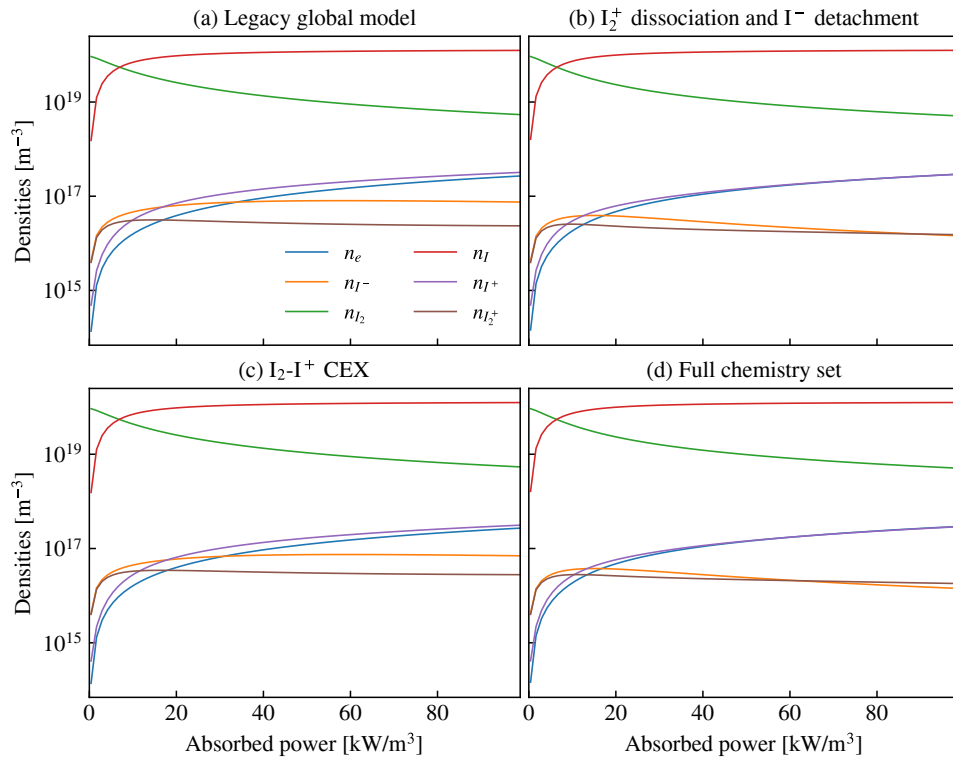


Figure 5.6: Equilibrium species densities predicted by the global model as a function of the power density absorbed for various chemical schemes. (a) legacy chemistry set (Grondein et al. [59]). The electron impact dissociation of I_2^+ and the detachment of I^- were added in (b), and the non-resonant charge exchange between I_2 and I^+ was added in (c). In (d), the full reaction set was used.

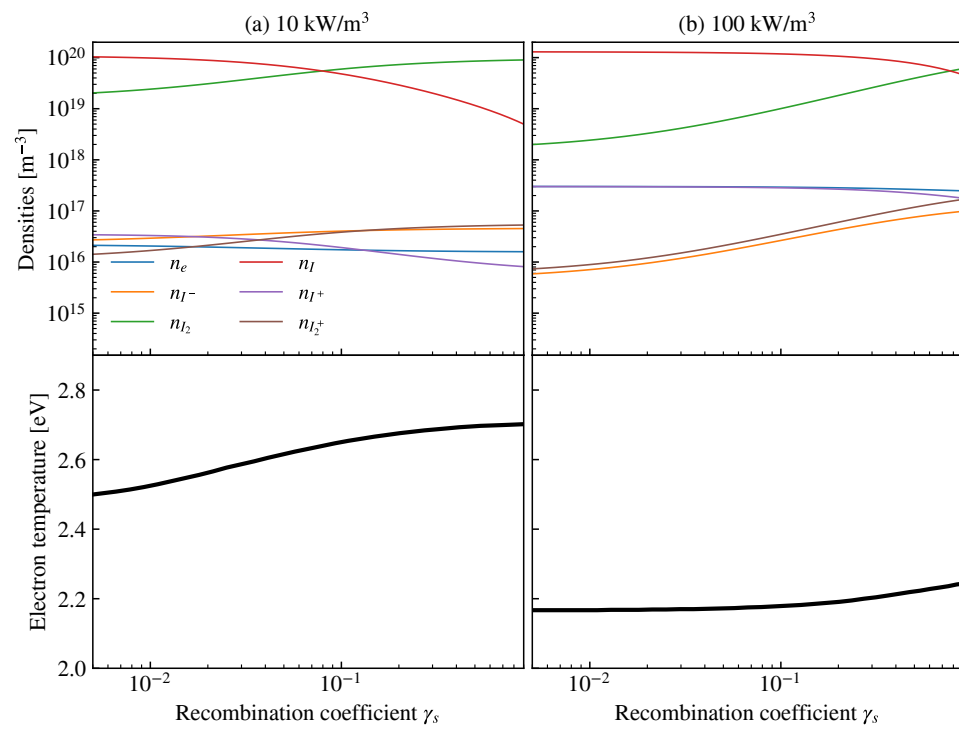


Figure 5.7: Equilibrium species densities and the electron temperature predicted by the global model as a function of the surface recombination coefficient between I and I_2 for (a) 10 kW/m^3 and (b) 100 kW/m^3 of power absorbed by the plasma. The full chemistry set is used here.

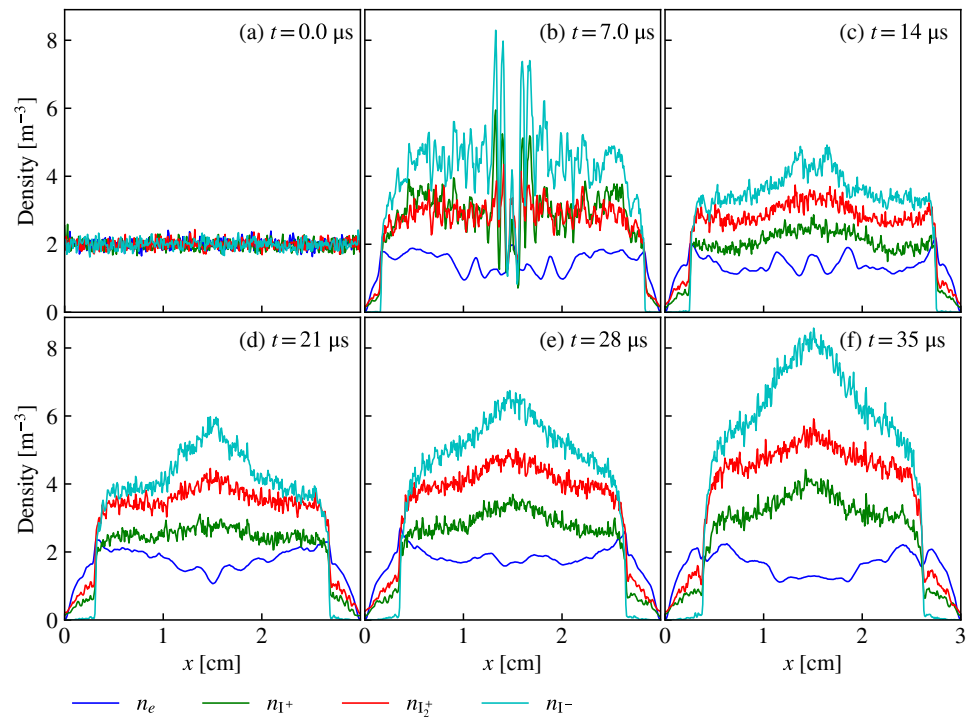


Figure 5.8: Density profiles at $y = l_y/2$ for the iodine ICP discharge in the transient regime.

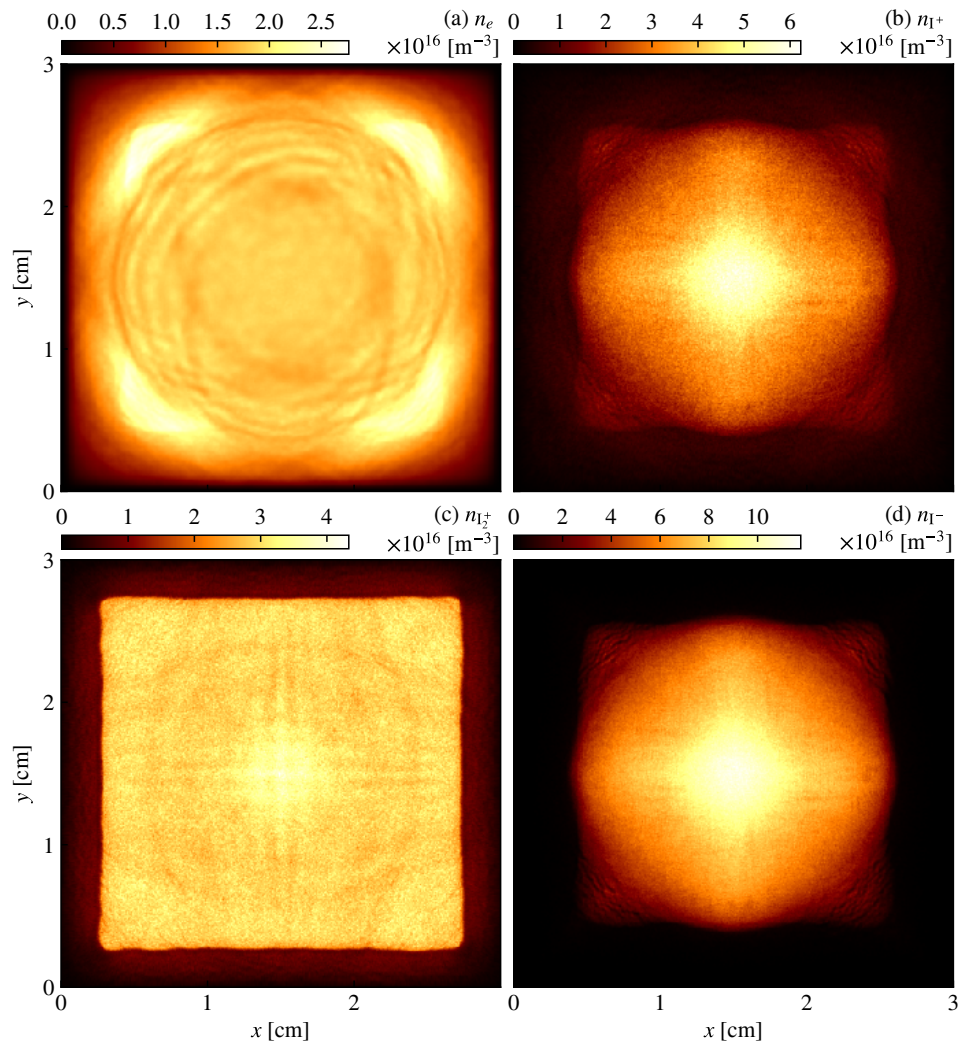


Figure 5.9: 2D maps of the densities of the various species present in the iodine plasma simulation. The snapshot performed at $t = 16.2\mu\text{s}$ corresponds to the transient and illustrates the instability perturbation.

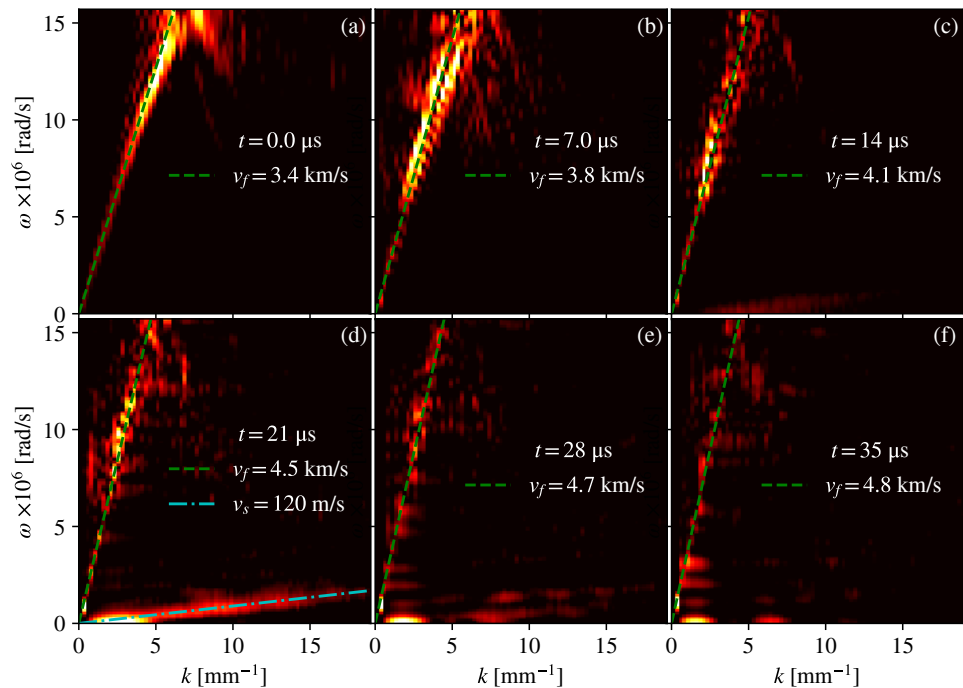


Figure 5.10: FT of the x component of the electric field in time and space, along x and for $y = l_y/2$, at several times. The fast mode (green dashed line) and the slow mode in (d) (cyan dashed-dotted line) are fitted manually to the 2D plot.

5.4 A low power discharge model for iodine**5.5 Global model comparison****5.6 Simulation of negative ion production through a magnetic filter**

Conclusion

Summary

Appendix A

Refined cross section sets for noble gases

He

- (1) $\text{He} + e^- \rightarrow \text{He} + e^-$ elastic, From Biagi's elastic momentum transfer.
- (2) $\text{He} + e^- \rightarrow \text{He}^+ + e^- + e^-$ ionization,
- (3) $\text{He} + e^- \rightarrow \text{He}^* + e^-$ excitation 1, EX 23S J=1 M ELVL=19.81961.
- (4) $\text{He} + e^- \rightarrow \text{He}^* + e^-$ excitation 2, EX 21S J=0 M ELVL=20.61577.
- (5) $\text{He} + e^- \rightarrow \text{He}^* + e^-$ excitation 3, EX 23P J= 1,0 ELVL=20.96409.
- (6) $\text{He} + e^- \rightarrow \text{He}^* + e^-$ excitation 4, EX 21P J=1 R ELVL=21.21802.
- (7) $\text{He} + e^- \rightarrow \text{He}^* + e^-$ excitation 5, EX 33S J=1 ELVL=22.71847.
- (8) $\text{He} + e^- \rightarrow \text{He}^* + e^-$ excitation 6, EX 31S J=0 ELVL=22.92032.
- (9) $\text{He} + e^- \rightarrow \text{He}^* + e^-$ excitation 7, EX 33P J= 1,0 ELVL=23.00707.
- (10) $\text{He} + e^- \rightarrow \text{He}^* + e^-$ excitation 8, EX 33D J=3, 1 ELVL=23.07365.
- (11) $\text{He} + e^- \rightarrow \text{He}^* + e^-$ excitation 9, EX 31D J=2 ELVL=23.07407.
- (12) $\text{He} + e^- \rightarrow \text{He}^* + e^-$ excitation 10, EX 31P J=1 R ELVL=23.08702.
- (13) $\text{He} + e^- \rightarrow \text{He}^* + e^-$ excitation 11, EX 43S J=1 ELVL=23.59396.
- (14) $\text{He} + e^- \rightarrow \text{He}^* + e^-$ excitation 12, EX 41S J=0 ELVL=23.67357.
- (15) $\text{He} + e^- \rightarrow \text{He}^* + e^-$ excitation 13, EX 43P J= 1,0 ELVL=23.70789.
- (16) $\text{He} + e^- \rightarrow \text{He}^* + e^-$ excitation 14, EX 41D J=2 ELVL=23.73633.
- (17) $\text{He} + e^- \rightarrow \text{He}^* + e^-$ excitation 15, EX 43D J=3, 1 ELVL=23.73609.
- (18) $\text{He} + e^- \rightarrow \text{He}^* + e^-$ excitation 16, EX 41F J=3 ELVL=23.73701.
- (19) $\text{He} + e^- \rightarrow \text{He}^* + e^-$ excitation 17, EX 43F J=3,4,2 ELVL=23.73701.
- (20) $\text{He} + e^- \rightarrow \text{He}^* + e^-$ excitation 18, EX 41P J=1 R ELVL=23.74207.
- (21) $\text{He} + e^- \rightarrow \text{He}^* + e^-$ excitation 19, EX 53S J=1 ELVL=23.97197.
- (22) $\text{He} + e^- \rightarrow \text{He}^* + e^-$ excitation 20, EX 51S J=0 ELVL=24.01121.
- (23) $\text{He} + e^- \rightarrow \text{He}^* + e^-$ excitation 21, EX 53P J= 1,0 ELVL=24.02822.

- (24) $\text{He} + e^- \rightarrow \text{He}^* + e^-$ excitation 22, EX 51D J=2 ELVL=24.04280.
- (25) $\text{He} + e^- \rightarrow \text{He}^* + e^-$ excitation 23, EX 53D J=3, 1 ELVL=24.04266.
- (26) $\text{He} + e^- \rightarrow \text{He}^* + e^-$ excitation 24, EX 513 J=3 ELVL=24.04315.
- (27) $\text{He} + e^- \rightarrow \text{He}^* + e^-$ excitation 25, EX 53F J=3,4,2 ELVL=24.04315.
- (28) $\text{He} + e^- \rightarrow \text{He}^* + e^-$ excitation 26, EX 51P J=1 R ELVL=24.04580.
- (29) $\text{He} + e^- \rightarrow \text{He}^* + e^-$ excitation 27, EX 63S J=1 ELVL=24.16900.
- (30) $\text{He} + e^- \rightarrow \text{He}^* + e^-$ excitation 28, EX 61S J=0 ELVL=24.19116.
- (31) $\text{He} + e^- \rightarrow \text{He}^* + e^-$ excitation 29, EX 63P J=1,0 ELVL=24.20081.
- (32) $\text{He} + e^- \rightarrow \text{He}^* + e^-$ excitation 30, EX 63D J=3, 1 ELVL=24.20916.
- (33) $\text{He} + e^- \rightarrow \text{He}^* + e^-$ excitation 31, EX 61D J=2 ELVL=24.20925.
- (34) $\text{He} + e^- \rightarrow \text{He}^* + e^-$ excitation 32, EX 61P J=1 R ELVL=24.21100.
- (35) $\text{He} + e^- \rightarrow \text{He}^* + e^-$ excitation 33, EX 73S J=1 ELVL=24.28456.
- (36) $\text{He} + e^- \rightarrow \text{He}^* + e^-$ excitation 34, EX 71S J=0 ELVL=24.29828.
- (37) $\text{He} + e^- \rightarrow \text{He}^* + e^-$ excitation 35, EX 73P J=1,0 ELVL=24.30429.
- (38) $\text{He} + e^- \rightarrow \text{He}^* + e^-$ excitation 36, EX 73D J=3, 1 ELVL=24.30954.
- (39) $\text{He} + e^- \rightarrow \text{He}^* + e^-$ excitation 37, EX 71D J=2 ELVL=24.30960.
- (40) $\text{He} + e^- \rightarrow \text{He}^* + e^-$ excitation 38, EX 71P J=1 R ELVL=24.31071.
- (41) $\text{He} + e^- \rightarrow \text{He}^* + e^-$ excitation 39, EX N3S SUM HIGH ELVL=24.35810.
- (42) $\text{He} + e^- \rightarrow \text{He}^* + e^-$ excitation 40, EX N1S SUM HIGH ELVL=24.36718.
- (43) $\text{He} + e^- \rightarrow \text{He}^* + e^-$ excitation 41, EX N3P SUM HIGH ELVL=24.37116.
- (44) $\text{He} + e^- \rightarrow \text{He}^* + e^-$ excitation 42, EX N1D SUM HIGH ELVL=24.37472.
- (45) $\text{He} + e^- \rightarrow \text{He}^* + e^-$ excitation 43, EX N3D SUM HIGH ELVL=24.37468.
- (46) $\text{He} + e^- \rightarrow \text{He}^* + e^-$ excitation 44, EX 81P J=1 R ELVL=24.37547.
- (47) $\text{He} + e^- \rightarrow \text{He}^* + e^-$ excitation 45, EX 91P J=1 R ELVL=24.41989.
- (48) $\text{He} + e^- \rightarrow \text{He}^* + e^-$ excitation 46, EX 101P J=1 R ELVL=24.45168.
- (49) $\text{He} + e^- \rightarrow \text{He}^* + e^-$ excitation 47, EX 111P J=1 R ELVL=24.47518.
- (50) $\text{He} + e^- \rightarrow \text{He}^* + e^-$ excitation 48, EX 121P J=1 R ELVL=24.49308.
- (51) $\text{He} + e^- \rightarrow \text{He}^* + e^-$ excitation 49, EX N1P SUM HI R ELVL=24.50708.

Ar

- (1) $\text{Ar} + e^- \rightarrow \text{Ar} + e^-$ elastic, [Ar(1S0) + e -> Ar(1S0) + e, Elastic] Phelps A V et al 1997 Yamabe C et al 1983 Phys.
- (2) $\text{Ar} + e^- \rightarrow \text{Ar}^+ + e^- + e^-$ ionization, [Ar(1S0) + e -> Ar(+,gnd) + e + e, Ionization] Rapp D and Englander-Golden P 1965 J.
- (3) $\text{Ar} + e^- \rightarrow \text{Ar}^* + e^-$ excitation 1, At. Mol.
- (4) $\text{Ar} + e^- \rightarrow \text{Ar}^* + e^-$ excitation 2, At. Mol.
- (5) $\text{Ar} + e^- \rightarrow \text{Ar}^* + e^-$ excitation 3, At. Mol.
- (6) $\text{Ar} + e^- \rightarrow \text{Ar}^* + e^-$ excitation 4, At. Mol.
- (7) $\text{Ar} + e^- \rightarrow \text{Ar}^* + e^-$ excitation 5, [Ar(1S0) + e -> Ar(4p[1/2]1) + e, Excitation] Chilton J E et al 1998 Phys. Rev. A 57

- (8) $\text{Ar} + e^- \rightarrow \text{Ar}^* + e^-$ excitation 6, [Ar(1S0) + e \rightarrow Ar(4p[5/2]3) + e, Excitation] Chilton J E et al 1998 Phys. Rev. A 57
- (9) $\text{Ar} + e^- \rightarrow \text{Ar}^* + e^-$ excitation 7, [Ar(1S0) + e \rightarrow Ar(4p[5/2]2) + e, Excitation] Chilton J E et al 1998 Phys. Rev. A 57
- (10) $\text{Ar} + e^- \rightarrow \text{Ar}^* + e^-$ excitation 8, [Ar(1S0) + e \rightarrow Ar(4p[3/2]1) + e, Excitation] Chilton J E et al 1998 Phys. Rev. A 57
- (11) $\text{Ar} + e^- \rightarrow \text{Ar}^* + e^-$ excitation 9, [Ar(1S0) + e \rightarrow Ar(4p[3/2]2) + e, Excitation] Chilton J E et al 1998 Phys. Rev. A 57
- (12) $\text{Ar} + e^- \rightarrow \text{Ar}^* + e^-$ excitation 10, [Ar(1S0) + e \rightarrow Ar(4p[1/2]0) + e, Excitation] Chilton J E et al 1998 Phys. Rev. A 57
- (13) $\text{Ar} + e^- \rightarrow \text{Ar}^* + e^-$ excitation 11, [Ar(1S0) + e \rightarrow Ar(4p'[3/2]1) + e, Excitation] Chilton J E et al 1998 Phys. Rev. A 57
- (14) $\text{Ar} + e^- \rightarrow \text{Ar}^* + e^-$ excitation 12, [Ar(1S0) + e \rightarrow Ar(4p'[3/2]2) + e, Excitation] Chilton J E et al 1998 Phys. Rev. A 57
- (15) $\text{Ar} + e^- \rightarrow \text{Ar}^* + e^-$ excitation 13, [Ar(1S0) + e \rightarrow Ar(4p'[1/2]1) + e, Excitation] Chilton J E et al 1998 Phys. Rev. A 57
- (16) $\text{Ar} + e^- \rightarrow \text{Ar}^* + e^-$ excitation 14, [Ar(1S0) + e \rightarrow Ar(4p'[1/2]0) + e, Excitation] Chilton J E et al 1998 Phys. Rev. A 57
- (17) $\text{Ar} + e^- \rightarrow \text{Ar}^* + e^-$ excitation 15, [Ar(1S0) + e \rightarrow Ar(3d[1/2]0+3d[1/2]1) + e, Excitation] Hayashi M 2003 Bibliography of Electron
- (18) $\text{Ar} + e^- \rightarrow \text{Ar}^* + e^-$ excitation 16, [Ar(1S0) + e \rightarrow Ar(3d[3/2]2) + e, Excitation] Hayashi M 2003 Bibliography of Electron
- (19) $\text{Ar} + e^- \rightarrow \text{Ar}^* + e^-$ excitation 17, [Ar(1S0) + e \rightarrow Ar(3d[7/2]4) + e, Excitation] Hayashi M 2003 Bibliography of Electron
- (20) $\text{Ar} + e^- \rightarrow \text{Ar}^* + e^-$ excitation 18, [Ar(1S0) + e \rightarrow Ar(3d[7/2]3) + e, Excitation] Hayashi M 2003 Bibliography of Electron
- (21) $\text{Ar} + e^- \rightarrow \text{Ar}^* + e^-$ excitation 19, [Ar(1S0) + e \rightarrow Ar(3d[5/2]2+5s[3/2]2) + e, Excitation] Hayashi M 2003 Bibliography of Electron
- (22) $\text{Ar} + e^- \rightarrow \text{Ar}^* + e^-$ excitation 20, [Ar(1S0) + e \rightarrow Ar(3d[5/2]3+5s[3/2]1) + e, Excitation] Hayashi M 2003 Bibliography of Electron
- (23) $\text{Ar} + e^- \rightarrow \text{Ar}^* + e^-$ excitation 21, [Ar(1S0) + e \rightarrow Ar(3d[3/2]1) + e, Excitation] Hayashi M 2003 Bibliography of Electron
- (24) $\text{Ar} + e^- \rightarrow \text{Ar}^* + e^-$ excitation 22, [Ar(1S0) + e \rightarrow Ar(3d'[5/2]2) + e, Excitation] Hayashi M 2003 Bibliography of Electron
- (25) $\text{Ar} + e^- \rightarrow \text{Ar}^* + e^-$ excitation 23, [Ar(1S0) + e \rightarrow Ar(3d'[5/2or3/2]3or2+5s'[1/2]0or1) + e, Excitation] Hayashi M 2003
- (26) $\text{Ar} + e^- \rightarrow \text{Ar}^* + e^-$ excitation 24, [Ar(1S0) + e \rightarrow Ar(3d'[3/2]1) + e, Excitation] Hayashi M 2003 Bibliography of Electron
- (27) $\text{Ar} + e^- \rightarrow \text{Ar}^* + e^-$ excitation 25, [Ar(1S0) + e \rightarrow Ar(5p[1/2]1) + e, Excitation] Weber T et al 2003 Phys. Rev. A 68

- (28) $\text{Ar} + e^- \rightarrow \text{Ar}^* + e^-$ excitation 26, $[\text{Ar}(1\text{S}0) + e^- \rightarrow \text{Ar}(5\text{p}[5/2]3) + e]$, Excitation] Weber T et al 2003 Phys. Rev. A 68
- (29) $\text{Ar} + e^- \rightarrow \text{Ar}^* + e^-$ excitation 27, $[\text{Ar}(1\text{S}0) + e^- \rightarrow \text{Ar}(5\text{p}[5/2]2) + e]$, Excitation] Weber T et al 2003 Phys. Rev. A 68
- (30) $\text{Ar} + e^- \rightarrow \text{Ar}^* + e^-$ excitation 28, $[\text{Ar}(1\text{S}0) + e^- \rightarrow \text{Ar}(5\text{p}[3/2]1) + e]$, Excitation] Weber T et al 2003 Phys. Rev. A 68
- (31) $\text{Ar} + e^- \rightarrow \text{Ar}^* + e^-$ excitation 29, $[\text{Ar}(1\text{S}0) + e^- \rightarrow \text{Ar}(5\text{p}[3/2]2) + e]$, Excitation] Weber T et al 2003 Phys. Rev. A 68
- (32) $\text{Ar} + e^- \rightarrow \text{Ar}^* + e^-$ excitation 30, $[\text{Ar}(1\text{S}0) + e^- \rightarrow \text{Ar}(5\text{p}[1/2]0) + e]$, Excitation] Weber T et al 2003 Phys. Rev. A 68
- (33) $\text{Ar} + e^- \rightarrow \text{Ar}^* + e^-$ excitation 31, $[\text{Ar}(1\text{S}0) + e^- \rightarrow \text{Ar}(5\text{p}'[3/2]1) + e]$, Excitation] Weber T et al 2003 Phys. Rev. A 68
- (34) $\text{Ar} + e^- \rightarrow \text{Ar}^* + e^-$ excitation 32, $[\text{Ar}(1\text{S}0) + e^- \rightarrow \text{Ar}(5\text{p}'[1/2]1) + e]$, Excitation] Weber T et al 2003 Phys. Rev. A 68
- (35) $\text{Ar} + e^- \rightarrow \text{Ar}^* + e^-$ excitation 33, $[\text{Ar}(1\text{S}0) + e^- \rightarrow \text{Ar}(5\text{p}'[3/2]2) + e]$, Excitation] Weber T et al 2003 Phys. Rev. A 68
- (36) $\text{Ar} + e^- \rightarrow \text{Ar}^* + e^-$ excitation 34, $[\text{Ar}(1\text{S}0) + e^- \rightarrow \text{Ar}(5\text{p}'[1/2]0) + e]$, Excitation] Weber T et al 2003 Phys. Rev. A 68
- (37) $\text{Ar} + e^- \rightarrow \text{Ar}^* + e^-$ excitation 35, $[\text{Ar}(1\text{S}0) + e^- \rightarrow \text{Ar}(4\text{d}) + e]$, Excitation] Drawin H W 1967 Fontenay-aux-Roses Report
- (38) $\text{Ar} + e^- \rightarrow \text{Ar}^* + e^-$ excitation 36, $[\text{Ar}(1\text{S}0) + e^- \rightarrow \text{Ar}(6\text{s}) + e]$, Excitation] Drawin H W 1967 Fontenay-aux-Roses Report
- (39) $\text{Ar} + e^- \rightarrow \text{Ar}^* + e^-$ excitation 37, $[\text{Ar}(1\text{S}0) + e^- \rightarrow \text{Ar}(4\text{d}') + e]$, Excitation] Drawin H W 1967 Fontenay-aux-Roses Report

Xe

- (1) $\text{Xe} + e^- \rightarrow \text{Xe} + e^-$ elastic, Elastic Momentum Transfer.
- (2) $\text{Xe} + e^- \rightarrow \text{Xe}^+ + e^- + e^-$ ionization,
- (3) $\text{Xe} + e^- \rightarrow \text{Xe}^* + e^-$ excitation 1, EX 1S5 J=2 M ELVL= 8.3153.
- (4) $\text{Xe} + e^- \rightarrow \text{Xe}^* + e^-$ excitation 2, EX 1S4 J=1 ELVL=8.436.
- (5) $\text{Xe} + e^- \rightarrow \text{Xe}^* + e^-$ excitation 3, EX 1S3 J=0 M ELVL= 9.4472.
- (6) $\text{Xe} + e^- \rightarrow \text{Xe}^* + e^-$ excitation 4, EX 1S2 J=1 R ELVL= 9.5697.
- (7) $\text{Xe} + e^- \rightarrow \text{Xe}^* + e^-$ excitation 5, EX 2P10 J=1 ELVL= 9.5802.
- (8) $\text{Xe} + e^- \rightarrow \text{Xe}^* + e^-$ excitation 6, EX 2P9 J=2 ELVL= 9.6856.
- (9) $\text{Xe} + e^- \rightarrow \text{Xe}^* + e^-$ excitation 7, EX 2P8 J=3 ELVL= 9.7207.
- (10) $\text{Xe} + e^- \rightarrow \text{Xe}^* + e^-$ excitation 8, EX 2P7 J=1 ELVL= 9.7893.
- (11) $\text{Xe} + e^- \rightarrow \text{Xe}^* + e^-$ excitation 9, EX 2P6 J=2 ELVL= 9.8211.
- (12) $\text{Xe} + e^- \rightarrow \text{Xe}^* + e^-$ excitation 10, EX 3D6 J=0 ELVL= 9.8904.
- (13) $\text{Xe} + e^- \rightarrow \text{Xe}^* + e^-$ excitation 11, EX 3D5 J=1 R ELVL= 9.9171.
- (14) $\text{Xe} + e^- \rightarrow \text{Xe}^* + e^-$ excitation 12, EX 2P5 J=0 ELVL= 9.9335.

- (15) $\text{Xe} + e^- \rightarrow \text{Xe}^* + e^-$ excitation 13, EX 3D4! J=4 ELVL= 9.9431.
- (16) $\text{Xe} + e^- \rightarrow \text{Xe}^* + e^-$ excitation 14, EX 3D3 J=2 ELVL= 9.9588.
- (17) $\text{Xe} + e^- \rightarrow \text{Xe}^* + e^-$ excitation 15, EX 3D4 J=3 ELVL=10.0391.
- (18) $\text{Xe} + e^- \rightarrow \text{Xe}^* + e^-$ excitation 16, EX 3D1!! J=2 ELVL=10.1575.
- (19) $\text{Xe} + e^- \rightarrow \text{Xe}^* + e^-$ excitation 17, EX 3D1! J=3 ELVL=10.2200.
- (20) $\text{Xe} + e^- \rightarrow \text{Xe}^* + e^-$ excitation 18, EX 3D2 J=1 R ELVL=10.4010.
- (21) $\text{Xe} + e^- \rightarrow \text{Xe}^* + e^-$ excitation 19, EX 2S5 J=2 ELVL=10.5621.
- (22) $\text{Xe} + e^- \rightarrow \text{Xe}^* + e^-$ excitation 20, EX 2S4 J=1 R ELVL=10.5932.
- (23) $\text{Xe} + e^- \rightarrow \text{Xe}^* + e^-$ excitation 21, EX SUM 3P10-5 ELVL=10.9016.
- (24) $\text{Xe} + e^- \rightarrow \text{Xe}^* + e^-$ excitation 22, EX 2P4 J=1 ELVL=10.9576.
- (25) $\text{Xe} + e^- \rightarrow \text{Xe}^* + e^-$ excitation 23, EX SUM 4D ELVL=10.9715.
- (26) $\text{Xe} + e^- \rightarrow \text{Xe}^* + e^-$ excitation 24, EX 4D5 J=1 R ELVL=10.9788.
- (27) $\text{Xe} + e^- \rightarrow \text{Xe}^* + e^-$ excitation 25, EX 2P3 J=2 ELVL=11.0547.
- (28) $\text{Xe} + e^- \rightarrow \text{Xe}^* + e^-$ excitation 26, EX 2P2 J=1 ELVL=11.0691.
- (29) $\text{Xe} + e^- \rightarrow \text{Xe}^* + e^-$ excitation 27, EX 2P1 J=0 ELVL=11.1412.
- (30) $\text{Xe} + e^- \rightarrow \text{Xe}^* + e^-$ excitation 28, EX 4D2 J=1 R ELVL=11.1626.
- (31) $\text{Xe} + e^- \rightarrow \text{Xe}^* + e^-$ excitation 29, EX 3S4 J=1 R ELVL=11.2742.
- (32) $\text{Xe} + e^- \rightarrow \text{Xe}^* + e^-$ excitation 30, EX 5D5 J=1 R ELVL=11.4225.
- (33) $\text{Xe} + e^- \rightarrow \text{Xe}^* + e^-$ excitation 31, EX 5D2 J=1 R ELVL=11.4951.
- (34) $\text{Xe} + e^- \rightarrow \text{Xe}^* + e^-$ excitation 32, EX 4S4 J=1 R ELVL=11.5829.
- (35) $\text{Xe} + e^- \rightarrow \text{Xe}^* + e^-$ excitation 33, EX 3S1! J=1 R ELVL=11.6072.
- (36) $\text{Xe} + e^- \rightarrow \text{Xe}^* + e^-$ excitation 34, EX 6D5 J=1 R ELVL=11.6828.
- (37) $\text{Xe} + e^- \rightarrow \text{Xe}^* + e^-$ excitation 35, EX 6D2 J=1 R ELVL=11.7395.
- (38) $\text{Xe} + e^- \rightarrow \text{Xe}^* + e^-$ excitation 36, EX 5S4 J=1 R ELVL=11.7521.
- (39) $\text{Xe} + e^- \rightarrow \text{Xe}^* + e^-$ excitation 37, EX 7D5 J=1 R ELVL=11.8068.
- (40) $\text{Xe} + e^- \rightarrow \text{Xe}^* + e^-$ excitation 38, EX 7D2 J=1 R ELVL=11.8403.
- (41) $\text{Xe} + e^- \rightarrow \text{Xe}^* + e^-$ excitation 39, EX 6S4 J=1 R ELVL=11.8518.
- (42) $\text{Xe} + e^- \rightarrow \text{Xe}^* + e^-$ excitation 40, EX 2S2 J=1 R ELVL=11.8778.
- (43) $\text{Xe} + e^- \rightarrow \text{Xe}^* + e^-$ excitation 41, EX 8D5 J=1 R ELVL=11.8917.
- (44) $\text{Xe} + e^- \rightarrow \text{Xe}^* + e^-$ excitation 42, EX 8D2 J=1 R ELVL=11.9082.
- (45) $\text{Xe} + e^- \rightarrow \text{Xe}^* + e^-$ excitation 43, EX 7S4 J=1 R ELVL=11.9177.
- (46) $\text{Xe} + e^- \rightarrow \text{Xe}^* + e^-$ excitation 44, EX 9D5 J=1 R ELVL=11.9416.
- (47) $\text{Xe} + e^- \rightarrow \text{Xe}^* + e^-$ excitation 45, EX 9D2 J=1 R ELVL=11.9550.
- (48) $\text{Xe} + e^- \rightarrow \text{Xe}^* + e^-$ excitation 46, EX 8S4 J=1 R ELVL=11.9621.
- (49) $\text{Xe} + e^- \rightarrow \text{Xe}^* + e^-$ excitation 47, EX 10D5 J=1 R ELVL=11.9789.
- (50) $\text{Xe} + e^- \rightarrow \text{Xe}^* + e^-$ excitation 48, EX 10D2 J=1 R ELVL=11.9886.
- (51) $\text{Xe} + e^- \rightarrow \text{Xe}^* + e^-$ excitation 49, EX 9S4 J=1 R ELVL=11.9939.

The cross section set for electron-He reactions presented here comes from the Biagi Magboltz database on LXCat [10].

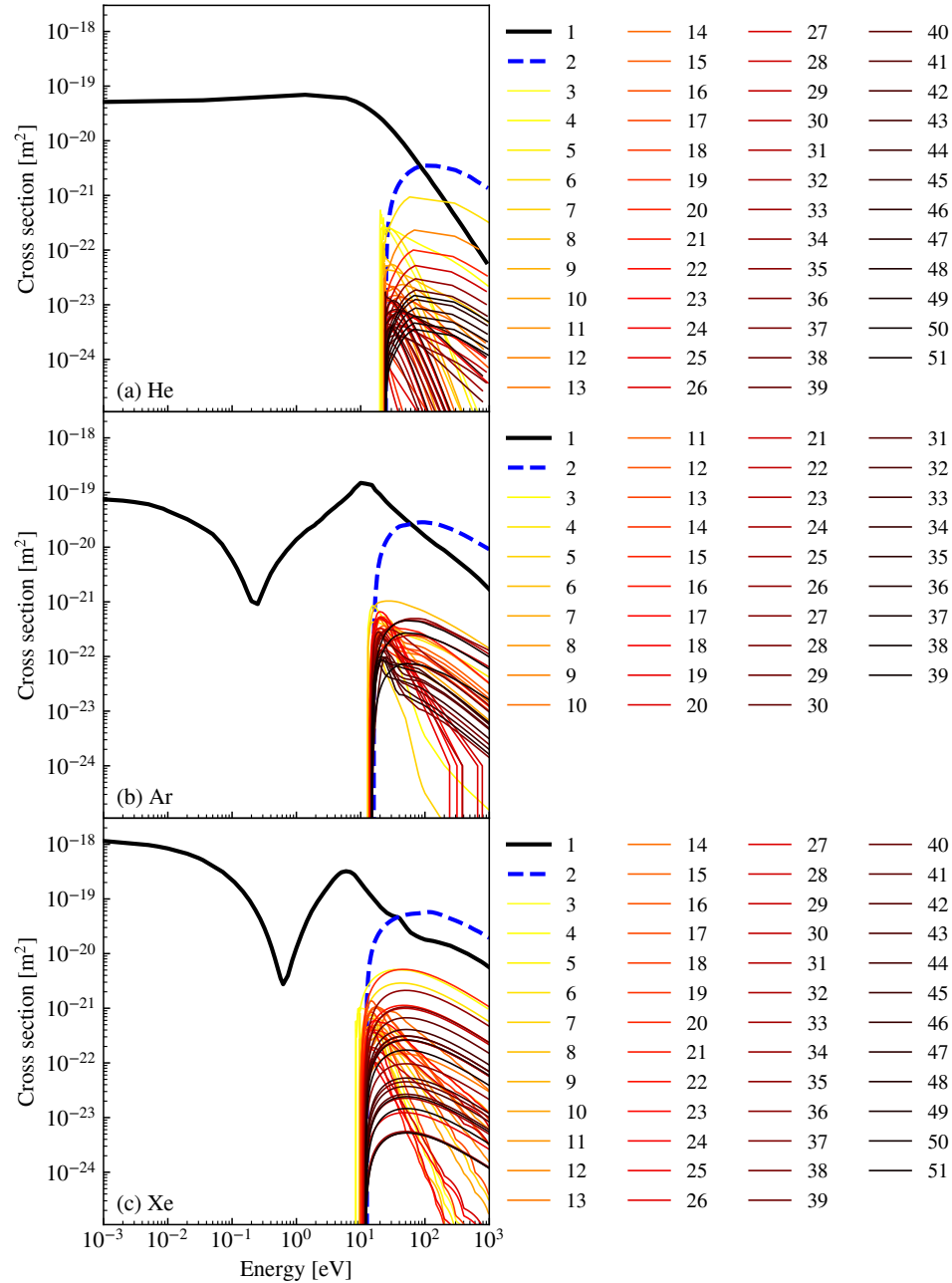


Figure A.1: Electron-neutral collision cross sections for helium, argon and xenon. [11, 6].

Appendix B

Simulations at higher magnetic field

Nothing should stop us from simulating argon plasmas at higher magnetic fields. The cell size is constrained by the Larmor radius so the computation time is larger. As shown in Fig. B.1 (also used as a front picture), the structure of the plasma instability becomes different. The instability does not look like a wave that propagates but features smaller structures that spin and rotate with the diamagnetic drift. Fig. B.1 corresponds to a run at 3 mTorr with a uniform magnetic field of 100 mT. The simulation is not converged here and the Larmor radius is badly resolved ($\rho_{Le} \approx dX$). The spin motion of the small scale structure is very fast and would require finer time sampling, which would also require more particles to reduce the statistical noise. Overall, providing consistent and converged simulations in this range of magnetic fields would require special care for convergence studies and timely runs.

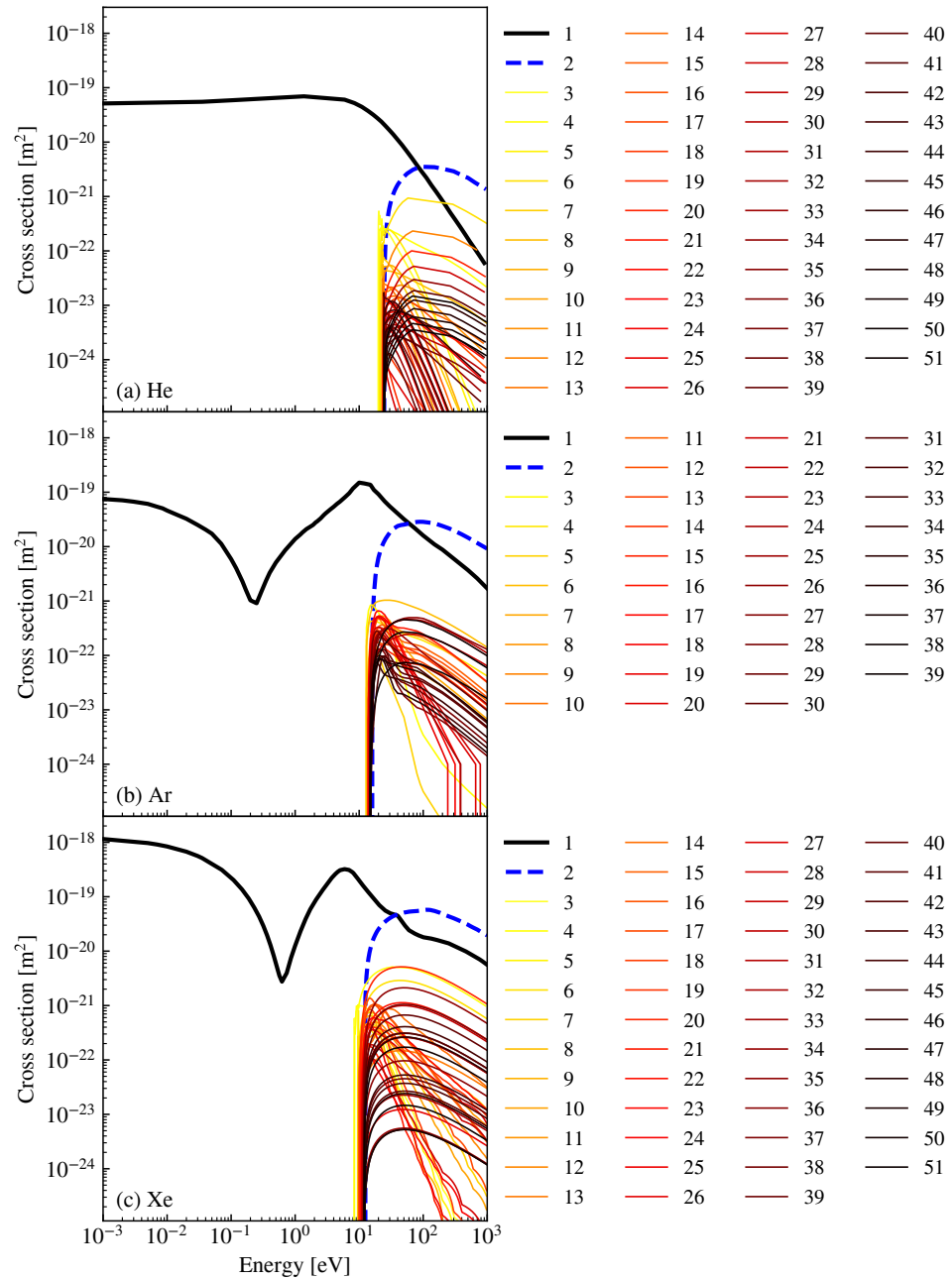


Figure B.1: Electron-neutral collision cross sections for helium, argon and xenon. [11, 6].

Appendix C

Mathematical functions

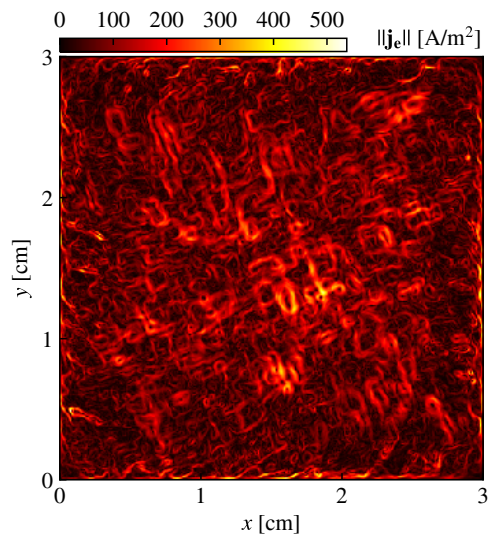


Figure C.1: Example of 2D PIC simulation at higher magnetic field: B_z is here uniform and equal to 100 mT. The pressure is 3 mT. The electron current is extracted at $t = 5.7 \mu\text{s}$, when the simulation is not converged.

Appendix D

Fortran gas type defintion

```
type gas
    character (LEN=9)                      :: formula      !
        gas formula
    real(dbleprc)                          :: mass         !
    character (LEN=256)                     :: lxcat_input_e !
        cross section file for elec
    character (LEN=256)                     :: lxcat_input_i !
        cross section file for ions
    real(dbleprc)                          :: density=0.0d0
        ! density

    ! Number of reactions for each type of process
!-----
    ! Electrons
    integer                                :: ela_elec_nb=0 ! Elastic
    integer                                :: exc_elec_nb=0 !
        Excitation
    integer                                :: iz_elec_nb=0     !
        ionization
    ! Ions
    integer                                :: i_n_nb=0 ! Elastic
        integer                                :: e_react_nb=0 ! number
            of electron processes
    integer                                :: i_react_nb=0 ! number
            of ion processes

    ! Data size for each process
    integer, allocatable, dimension(:)    :: len_ela_elec
```

```

integer, allocatable, dimension(:) :: len_exc_elec
integer, allocatable, dimension(:) :: len_iz_elec
integer, allocatable, dimension(:) :: len_i_n

! Cross section (cs) tables
! dim 1: number of reactions of the given type
! dim 2: size of the energy table
! dim 3: (1) energy [eV] / (2) cs [m^2]
real(dbleprc), ALLOCATABLE, dimension(:,:,:,:) :: ela_elec !
    electron elastic
real(dbleprc), ALLOCATABLE, dimension(:,:,:,:) :: exc_elec !
    electron excitation
real(dbleprc), ALLOCATABLE, dimension(:,:,:,:) :: iz_elec !
    electron impact ionization
real(dbleprc), ALLOCATABLE, dimension(:,:,:,:) :: i_n      !
    ion-neutral

! grid values
!
-----
! Electron-gas reactions
real(dbleprc), dimension(:,:,:), allocatable :: nu_ela_elec_temp
    ! Elastic scattering
real(dbleprc), dimension(:,:,:), allocatable :: nu_el_a_elec
real(dbleprc), dimension(:,:,:), allocatable :: nu_exc_elec_temp
    ! Excitation
real(dbleprc), dimension(:,:,:), allocatable :: nu_exc_elec
real(dbleprc), dimension(:,:,:), allocatable :: nu_iz_elec_temp !
    Ionization
real(dbleprc), dimension(:,:,:), allocatable :: nu_iz_elec
real(dbleprc), dimension(:,:,:), allocatable :: nu_dat_elec_temp
    ! Dissociative attachment
real(dbleprc), dimension(:,:,:), allocatable :: nu_dat_elec
real(dbleprc), dimension(:,:,:), allocatable :: nu_diz_elec_temp
    ! Dissociative attachment
real(dbleprc), dimension(:,:,:), allocatable :: nu_diz_elec
    ! Ion-gas reactions
real(dbleprc), dimension(:,:,:), allocatable :: nu_iso_ion_temp !
    Isotropic scattering
real(dbleprc), dimension(:,:,:), allocatable :: nu_iso_ion
real(dbleprc), dimension(:,:,:), allocatable :: nu_bsc_ion_temp !
    Backscattering
real(dbleprc), dimension(:,:,:), allocatable :: nu_bsc_ion

! Collision probability level for each reaction

```

```
real(dbleprc), allocatable, dimension(:) :: nu_e ! electrons
real(dbleprc), allocatable, dimension(:) :: nu_i ! ions

! Maximum collision probability including null collision
real(dbleprc) :: nu_prime !
    electrons
real(dbleprc) :: nu_primi ! ions

end type gas
```


Bibliography

- [1] A. Aanesland, J. Bredin, P. Chabert, and V. Godyak. Electron energy distribution function and plasma parameters across magnetic filters. *Applied Physics Letters*, 100(4):044102, Jan. 2012.
- [2] E. Ahedo, M. Merino, C. Bombardelli, H. Urrutxua, J. Pelaez, and L. Summerer. Space Debris Removal with an Ion Beam Shepherd Satellite: target-plasma interaction. In *47th AIAA/ASME/SAE/ASEE Joint Propulsion Conference & Exhibit*, San Diego, California, July 2011. American Institute of Aeronautics and Astronautics.
- [3] M. A. Ali and Y.-K. Kim. Ionization cross sections by electron impact on halogen atoms, diatomic halogen and hydrogen halide molecules. *J. Phys. B: At. Mol. Opt. Phys.*, 41(14):145202, July 2008.
- [4] J. E. Allen and J. T. Holgate. On the Bohm criterion in the presence of a magnetic field. *Nuclear Materials and Energy*, Oct. 2016.
- [5] W. P. Allis, S. J. Buchsbaum, and A. Bers. *Waves in Anisotropic Plasmas*. The MIT Press, Mar. 2003.
- [6] L. L. Alves. The ist-lisbon database on lxcat. *J. Phys. Conf. Series*, (1), 2004.
- [7] P. N. Barnes and M. J. Kushner. Reactions in the afterglow of time modulated inductive discharges of Xe and I₂ mixtures. *Journal of Applied Physics*, 84(9):4727–4730, Nov. 1998.
- [8] Bellan, P. *Fundamentals Of Plasma Physics*. Cambridge University Press, 2006.
- [9] S. F. Biagi. Programm magboltz v7.1. cross section compilation. see www.lxcat.net. retrieved on November 16, 2016, 2004.
- [10] S. F. Biagi. Programm magboltz v8.97. cross section compilation. see www.lxcat.net. retrieved on February 11, 2019, 2010.

- [11] S. F. Biagi. Programm magboltz v8.9. cross section compilation. see www.lxcat.net. retrieved on February 12, 2019, 2015.
- [12] M. A. Biondi. Dissociative Attachment of Electrons in Iodine. I. Microwave Determination of the Absolute Cross Section at 300°K. *Physical Review*, 109(6):2005–2007, Mar. 1958.
- [13] M. A. Biondi and R. E. Fox. Dissociative Attachment of Electrons in Iodine. III. Discussion. *Physical Review*, 109(6):2012–2014, Mar. 1958.
- [14] C. K. Birdsall, G. R. Brewer, and A. V. Haeff. The resistive-wall amplifier. *Proceedings of the IRE*, 41(7):865–875, 1953.
- [15] C. K. Birdsall and A. B. Langdon. *Plasma Physics via Computer Simulation*. CRC Press, Oct. 2004.
- [16] J. P. Boeuf, J. Claustre, B. Chaudhury, and G. Fubiani. Physics of a magnetic filter for negative ion sources. II. $E \times B$ drift through the filter in a real geometry. *Physics of Plasmas*, 19(11):113510, Nov. 2012.
- [17] J.-P. Booth, C. S. Corr, G. A. Curley, J. Jolly, J. Guillon, and T. Földes. Fluorine negative ion density measurement in a dual frequency capacitive plasma etch reactor by cavity ring-down spectroscopy. *Appl. Phys. Lett.*, 88(15):151502, Apr. 2006.
- [18] J. P. Boris and R. A. Shanny. Relativistic Plasma Simulation - Optimization of a Hybrid Code. Washington D.C., 1970. NRL.
- [19] J. Bredin. *Développement de diagnostics électrostatiques pour le filtrage magnétique et la formation du plasma ion-ion dans le propulseur PEGASES*. PhD thesis, École polytechnique, 2013.
- [20] J. Bredin, P. Chabert, and A. Aanesland. Langmuir probe analysis of highly electronegative plasmas. *Applied Physics Letters*, 102(15):154107, 2013.
- [21] J. Bredin, P. Chabert, and A. Aanesland. Langmuir probe analysis in electronegative plasmas. *Physics of Plasmas*, 21(12):123502, Dec. 2014.
- [22] J. Carlsson, I. Kaganovich, A. Powis, Y. Raitses, I. Romadanov, and A. Smolyakov. Particle-in-cell simulations of anomalous transport in a Penning discharge. *Physics of Plasmas*, 25(6):061201, June 2018.
- [23] J. Carlsson, A. Khrabrov, I. Kaganovich, T. Sommerer, and D. Keating. Validation and benchmarking of two particle-in-cell codes for a glow discharge. *Plasma Sources Sci. Technol.*, 26(1):014003, 2017.

- [24] K. M. Case, F. de Hoffmann, and G. Placzek. *Introduction to the theory of neutron diffusion*. Los Alamos, N. M., 1953. Section 10.1.
- [25] P. Chabert. Propulseur à Plasma électronégatif, Dec. 2005.
- [26] P. Chabert, J. Arancibia Monreal, J. Bredin, L. Popelier, and A. Aanesland. Global model of a gridded-ion thruster powered by a radiofrequency inductive coil. *Physics of Plasmas*, 19(7):073512, 2012.
- [27] P. Chabert and N. Braithwaite. *Physics of Radio-Frequency Plasmas*. Cambridge University Press, 2011.
- [28] P. J. Chantry. A simple formula for diffusion calculations involving wall reflection and low density. *Journal of Applied Physics*, 62(4):1141–1148, Aug. 1987.
- [29] F. F. Chen. Excitation of drift instabilities in thermionic plasmas. *J. Nucl. Energy, Part C Plasma Phys.*, 7(4):399, 1965.
- [30] F. F. Chen. "Universal" Overstability of a Resistive, Inhomogeneous Plasma. *The Physics of Fluids*, 8(7), 1965.
- [31] F. F. Chen. *Introduction to plasma physics and controlled fusion*. Plenum Press, New York, 2nd ed edition, 1984.
- [32] R. Chodura. Plasma–wall transition in an oblique magnetic field. *Phys. Fluids*, 25(9):1628, 1982.
- [33] E. Y. Choueiri. A Critical History of Electric Propulsion: The First Fifty Years (1906-1956). Technical Report 2004-3334, AIAA, 2004.
- [34] C. S. Corr, E. Despiau-Pujo, P. Chabert, W. G. Graham, F. G. Marro, and D. B. Graves. Comparison between fluid simulations and experiments in inductively coupled argon/chlorine plasmas. *J. Phys. D: Appl. Phys.*, 41(18):185202, Sept. 2008.
- [35] V. Croes. *Modélisation bidimensionnelle de la décharge plasma dans un propulseur de Hall*. PhD thesis, Université Paris-Saclay, Palaiseau, 2017.
- [36] V. Croes, T. Lafleur, Z. Bonaventura, A. Bourdon, and P. Chabert. 2D particle-in-cell simulations of the electron drift instability and associated anomalous electron transport in Hall-effect thrusters. *Plasma Sources Sci. Technol.*, 26(3):034001, 2017.

- [37] V. Croes, A. Tavant, R. Lucken, T. Lafleur, A. Bourdon, and P. Chabert. Study of electron transport in a Hall effect thruster with 2D $r - \theta$ Particle-In-Cell simulations. In *IEPC-2017-57*, volume 2017-57, 2017.
- [38] V. Croes, A. Tavant, R. Lucken, R. Martorelli, T. Lafleur, A. Bourdon, and P. Chabert. The effect of alternative propellants on the electron drift instability in Hall-effect thrusters: Insight from 2d particle-in-cell simulations. *Physics of Plasmas*, 25(6):063522, June 2018.
- [39] D. Curreli and F. F. Chen. Cross-field diffusion in low-temperature plasma discharges of finite length. *Plasma Sources Sci. Technol.*, 23(6):064001, 2014.
- [40] D. Bohm. *The Characteristics Of Electrical Discharges In Magnetic Fields*. R. K. Wakerling, A. Guthrie, McGraw-hill Book Company, Inc., first edition edition, 1949.
- [41] E. Despiau-Pujo and P. Chabert. Global model of instabilities in low-pressure inductive chlorine discharges. *Plasma Sources Science and Technology*, 18(4):045028, Nov. 2009.
- [42] R. Dressler, Y.-H. Chiu, and D. Levandier. Propellant alternatives for ion and Hall effect thrusters. *AIAA Paper*, 602:2000, 2000.
- [43] V. Désanglages. *Forçage à grande échelle d'une colonne de plasma faiblement magnétisée : influence d'une cathode émissive de grande taille*. PhD thesis, Nov. 2018.
- [44] K. G. Emeleus and G. A. Woolsey. *Discharges in Electronegative Gases*. Taylor and Francis LTD, London, United Kingdom, taylor and francis ltd edition, 1970.
- [45] A. V. Evseev, A. A. Radtsig, and B. M. Smirnov. Resonance charge exchange of diatomic molecular ions on molecules. *Sov. Phys. JETP*, 50(2):283, 1979.
- [46] U. Fantz, P. Franzen, W. Kraus, M. Berger, S. Christ-Koch, H. Falter, M. Fröschle, R. Gutser, B. Heinemann, C. Martens, P. McNeely, R. Riedl, E. Speth, A. Stäbler, and D. Wunderlich. Physical performance analysis and progress of the development of the negative ion RF source for the ITER NBI system. *Nucl. Fusion*, 49(12):125007, Nov. 2009.
- [47] R. E. Fox. Dissociative Attachment of Electrons in Iodine. II. Mass Spectrographic Determination of the Energy Dependence of the Cross Section. *Phys. Rev.*, 109(6):2008–2011, Mar. 1958.

- [48] R. N. Franklin and J. Snell. The positive column with negative ions in a magnetic field at low pressure. *J. Phys. D: Appl. Phys.*, 32(9):1031–1038, Jan. 1999.
- [49] S. E. R. F.R.S. LVII. The structure of the atom. *The London, Edinburgh, and Dublin Philosophical Magazine and Journal of Science*, 27(159):488–498, Mar. 1914.
- [50] A. Fruchtman, G. Makrinich, and J. Ashkenazy. Two-dimensional equilibrium of a low temperature magnetized plasma. *Plasma Sources Sci. Technol.*, 14(1):152, 2005.
- [51] R. Futtersack. *Modélisation fluide du transport magnétisé dans les plasmas froids*. PhD thesis, Université de Toulouse, Université Toulouse III-Paul Sabatier, 2014.
- [52] A. R. Gibson, M. Foucher, D. Marinov, P. Chabert, T. Gans, M. J. Kushner, and J.-P. Booth. The role of thermal energy accommodation and atomic recombination probabilities in low pressure oxygen plasmas. *Plasma Physics and Controlled Fusion*, 59(2):024004, Feb. 2017.
- [53] R. H. Goddard. Method and Means for Producing Electrified Jets of gases, Dec. 1920.
- [54] V. A. Godyak. *Soviet Radio Frequency Discharge Research*. Delphic associates inc. edition, 1986.
- [55] D. M. Goebel, G. Becatti, J. E. Polk, and P. Guerrero. Life Model for Lanthanum Hexaboride Hollow Cathodes for High-Power Hall Thrusters. 2017.
- [56] D. M. Goebel and I. Katz. *Fundamentals of electric propulsion: ion and Hall thrusters*, volume 1. John Wiley & Sons, 2008.
- [57] C. Greaves. Ion-Ion Recombination in Iodine Afterglows[†]. *Journal of Electronics and Control*, 17(2):171–180, Aug. 1964.
- [58] P. Grondein. *Investigation de l'iode comme propergol pour la propulsion ionique à grilles*. PhD thesis, École polytechnique, 2016.
- [59] P. Grondein, T. Lafleur, P. Chabert, and A. Aanesland. Global model of an iodine gridded plasma thruster. *Physics of Plasmas*, 23(3):033514, 2016.
- [60] G. J. M. Hagelaar, G. Fubiani, and J.-P. Boeuf. Model of an inductively coupled negative ion source: I. General model description. *Plasma Sources Sci. Technol.*, 20(1):015001, 2011.

- [61] J. R. Hamilton. Iodine: $I\{$_2$\}2$ molecule and I atom. Technical report, Quantemol, 2015.
- [62] J. R. Hamilton. Consultancy project for LPP. $I\{$_2^+$\}$ and $I\{$_-$\}$ data. Technical report, Quantemol ltd, 2017.
- [63] B. Heinemann, H. D. Falter, U. Fantz, P. Franzen, M. Froeschle, W. Kraus, C. Martens, R. Nocentini, R. Riedl, E. Speth, and A. Staebler. The negative ion source test facility ELISE. *Fusion Engineering and Design*, 86(6):768–771, Oct. 2011.
- [64] H. W. Hendel, B. Coppi, F. Perkins, and P. A. Politzer. Collisional Effects in Plasmas-Drift-Wave Experiments and Interpretation. *Phys. Rev. Lett.*, 18(12):439–442, Mar. 1967.
- [65] J. R. Henry. *Étude d'un plasma de gaz électronégatif. Spectrométrie de masse et propagation des ondes ioniques longitudinales*. PhD thesis, Université ParisVII, 1972.
- [66] R. W. Hockney, J. W. Eastwood, and J. W. Eastwood. *Computer Simulation Using Particles*. CRC Press, Jan. 1988.
- [67] C.-C. Hsu, M. A. Nierode, J. W. Coburn, and D. B. Graves. Comparison of model and experiment for Ar, Ar/O₂ and Ar/O₂/Cl₂ inductively coupled plasmas. *J. Phys. D: Appl. Phys.*, 39(15):3272–3284, Aug. 2006.
- [68] S. Huang and J. T. Gudmundsson. A particle-in-cell/Monte Carlo simulation of a capacitively coupled chlorine discharge. *Plasma Sources Science and Technology*, 22(5):055020, Sept. 2013.
- [69] S. Janhunen, A. Smolyakov, O. Chapurin, D. Sydorenko, I. Kaganovich, and Y. Raitses. Nonlinear structures and anomalous transport in partially magnetized E×B plasmas. *Physics of Plasmas*, 25(1):011608, Jan. 2018.
- [70] G.-H. Kim, H.-C. Lee, and C.-W. Chung. Experimental investigation of edge-to-center density ratio in inductively coupled plasmas. *Physics of Plasmas*, 17(7):073504, July 2010.
- [71] S. Kolev, G. J. M. Hagelaar, G. Fubiani, and J.-P. Boeuf. Physics of a magnetic barrier in low-temperature bounded plasmas: insight from particle-in-cell simulations. *Plasma Sources Science and Technology*, 21(2):025002, Apr. 2012.

- [72] S. Kolev, S. Lishev, A. Shivarova, K. Tarnev, and R. Wilhelm. Magnetic filter operation in hydrogen plasmas. *Plasma Physics and Controlled Fusion*, 49(9):1349–1369, Sept. 2007.
- [73] G. P. Kota, J. W. Coburn, and D. B. Graves. The recombination of chlorine atoms at surfaces. *Journal of Vacuum Science & Technology A*, 16(1):270–277, Jan. 1998.
- [74] T. Lafleur and A. Aanesland. Ambipolar and non-ambipolar diffusion in an rf plasma source containing a magnetic filter. *Physics of Plasmas*, 21(6):063510, June 2014.
- [75] T. Lafleur and A. Aanesland. Generalization of the Child-Langmuir law to the alternate extraction of positive and negative ions. *Physics of Plasmas*, 21(12):123506, Dec. 2014.
- [76] T. Lafleur, S. D. Baalrud, and P. Chabert. Theory for the anomalous electron transport in Hall effect thrusters. I. Insights from particle-in-cell simulations. *Physics of Plasmas*, 23(5):053502, May 2016.
- [77] T. Lafleur, S. D. Baalrud, and P. Chabert. Theory for the anomalous electron transport in Hall effect thrusters. II. Kinetic model. *Physics of Plasmas*, 23(5):053503, May 2016.
- [78] T. Lafleur and R. W. Boswell. Particle-in-cell simulations of ambipolar and nonambipolar diffusion in magnetized plasmas. *Physics of Plasmas*, 19(5):053505, May 2012.
- [79] T. Lafleur and P. Chabert. Edge-to-center density ratios in low-temperature plasmas. *Plasma Sources Science and Technology*, 24(2):025017, Mar. 2015.
- [80] T. Lafleur, D. Rafalskyi, and A. Aanesland. Alternate extraction and acceleration of positive and negative ions from a gridded plasma source. *Plasma Sources Science and Technology*, 24(1):015005, Nov. 2014.
- [81] G. Leray. *PEGASES: Plasma Propulsion with Electronegative Gases*. PhD thesis, Ecole Polytechnique X, 2009.
- [82] R. J. Leveque. Finite Volume Methods for Hyperbolic Problems. 2002.
- [83] L. Liard, J.-L. Raimbault, J.-M. Rax, and P. Chabert. Plasma transport under neutral gas depletion conditions. *Journal of Physics D: Applied Physics*, 40(17):5192–5195, Sept. 2007.

- [84] M. A. Lieberman and A. J. Lichtenberg. *Principles of plasma discharges and materials processing*. Wiley-Interscience, Hoboken, NJ, 2. ed edition, 2005. OCLC: 265711181.
- [85] R. Lucken. Simulation and Modelling of the Interaction between Spacecraft and Plasma Propulsion System, 2016. Master Thesis (confidential).
- [86] R. Lucken, V. Croes, T. Lafleur, J.-L. Raimbault, A. Bourdon, and P. Chabert. Global models of plasma thrusters: Insights from PIC simulation and fluid theory. In *IEPC-2017-323*, volume 2017-323, 2017.
- [87] R. Lucken, V. Croes, T. Lafleur, J.-L. Raimbault, A. Bourdon, and P. Chabert. Edge-to-center plasma density ratios in two-dimensional plasma discharges. *Plasma Sources Sci. Technol.*, 2018.
- [88] R. Lucken, N. Hubert, and D. Giolito. Systematic space debris collection using Cubesat constellation. 2017.
- [89] R. Lucken, A. Tavant, A. Bourdon, M. A. Lieberman, and P. Chabert. Instability-enhanced transport in low temperature magnetized plasma. *Physics of Plasmas*, 25(6), June 2019.
- [90] G. Maroulis, C. Makris, U. Hohm, and D. Goebel. Electrooptical Properties and Molecular Polarization of Iodine, I₂. *The Journal of Physical Chemistry A*, 101(5):953–956, Jan. 1997.
- [91] A. V. Phelps. The application of scattering cross sections to ion flux models in discharge sheaths. *Journal of Applied Physics*, 76(2):747–753, July 1994.
- [92] D. Piscitelli, A. V. Phelps, J. de Urquijo, E. Basurto, and L. C. Pitchford. Ion mobilities in Xe/Ne and other rare-gas mixtures. *Physical Review E*, 68(4), Oct. 2003.
- [93] L. Popelier. *Développement du propulseur PEGASES: source inductive à haute performance et accélération successive de faisceaux d'ions positifs et d'ions négatifs*. Physique des plasmas[physics.plasm-ph], École polytechnique X, 2012.
- [94] A. A. Radzig and B. M. Smirnov. *Reference Data on Atoms, Molecules, and Ions*. Number 31 in Chemical Physics. Springer, 1985.
- [95] D. Rafalskyi and A. Aanesland. A Neutralizer-Free Gridded Ion Thruster Embedded Into A 1u Cubesat Module. Atlanta, Georgia, USA, 2017.

- [96] D. Rafalskyi, L. Popelier, and A. Aanesland. Experimental validation of the dual positive and negative ion beam acceleration in the plasma propulsion with electronegative gases thruster. *Journal of Applied Physics*, 115(5):053301, 2014.
- [97] J.-L. Raimbault and P. Chabert. Edge-to-center plasma density ratio in high density plasma sources. *Plasma Sources Science and Technology*, 18(1):014017, Feb. 2009.
- [98] D. Rapp and W. E. Francis. Charge Exchange between Gaseous Ions and Atoms. *The Journal of Chemical Physics*, 37(11):2631, 1962.
- [99] J.-M. Rax. *Physique des Plasmas*. Dunod, 2005.
- [100] D. Renaud. *Caractérisation du propulseur PEGASES: diagnostics du filtre magnétique et du faisceau: optimisation de la géométrie*. PhD thesis, Université d'Orléans, 2016.
- [101] D. Renaud and S. Mazouffre. Investigation of the PEGASES thruster magnetic filter via laser photodetachment experiments. volume 380, Kobe, Japan, 2015.
- [102] K. U. Riemann. The Bohm criterion and sheath formation. *Journal of Physics D: Applied Physics*, 24(4):493–518, Apr. 1991.
- [103] S. Sakabe and Y. Izawa. Simple formula for the cross sections of resonant charge transfer between atoms and their positive ions at low impact velocity. *Physical Review A*, 45(3):2086, 1992.
- [104] G. Sary. *Modélisation d'une cathode creuse pour propulseur à plasma*. phd, Université de Toulouse, Université Toulouse III - Paul Sabatier, Sept. 2016.
- [105] G. Sary, L. Garrigues, and J. P. Boeuf. Hollow cathode modeling: a first approach on scaling laws. In *IEPC-2015-14*, volume 14, Kobe, Japan, 2015.
- [106] G. Schmidt. *Physics of High Temperature Plasmas: An Introduction*. Academic Press, 1966. Google-Books-ID: XqbjcigJeU4C.
- [107] W. Schottky. Diffusionstheorie der positiven Säule. *Phys. Zeits*, 25(635), 1924.
- [108] G. Serianni, V. Toigo, M. Bigi, M. Boldrin, G. Chitarin, S. Dal Bello, L. Grando, A. Luchetta, D. Marcuzzi, R. Pasqualotto, N. Pomaro, P. Zaccaria, L. Zanotto, P. Agostinetti, M. Agostini, V. Antoni, D. Aprile, M. Barbisan, M. Battistella, M. Brombin, R. Cavazzana, M. Dalla Palma, M. Dan,

- A. De Lorenzi, R. Delogu, M. De Muri, S. Denizeau, M. Fadone, F. Fellin, L. Ferbel, A. Ferro, E. Gaio, G. Gambetta, F. Gasparini, F. Gnesotto, P. Jain, A. Maistrello, G. Manduchi, S. Manfrin, G. Marchiori, N. Marconato, M. Moresco, T. Patton, M. Pavei, S. Peruzzo, N. Pilan, A. Pimazzoni, R. Piovan, C. Poggi, M. Recchia, A. Rizzolo, G. Rostagni, E. Sartori, M. Siragusa, P. Sonato, E. Spada, S. Spagnolo, M. Spolaore, C. Talierno, P. Tinti, M. Ugoletti, M. Valente, A. Zamengo, B. Zaniol, M. Zappa, C. Baltador, M. Cavenago, D. Boilson, C. Rotti, P. Veltri, T. Bonicelli, F. Paolucci, S. Muriel, A. Masiello, A. Chakraborty, H. Patel, N. Singh, U. Fantz, B. Heinemann, W. Kraus, M. Kashiwagi, and K. Tsumori. SPI-
DER in the roadmap of the ITER neutral beams. *Fusion Engineering and Design*, page S0920379619305708, Apr. 2019.
- [109] V. K. Shen, D. W. Siderius, W. P. Krekelberg, and H. W. Hatch. *NIST Standard Reference Simulation Website, NIST Standard Reference Database Number 69*. Gaithersburg MD, 20899, national institute of standards and technology edition.
- [110] A. I. Smolyakov, O. Chapurin, W. Frias, O. Koshkarov, I. Romadanov, T. Tang, M. Umansky, Y. Raitses, I. D. Kaganovich, and V. P. Lakhin. Fluid theory and simulations of instabilities, turbulent transport and coherent structures in partially-magnetized plasmas of $E \times B$ discharges. *Plasma Physics and Controlled Fusion*, 59(1):014041, Jan. 2017.
- [111] E. Speth, H. Falter, P. Franzen, U. Fantz, M. Bandyopadhyay, S. Christ, A. Encheva, M. Fröschle, D. Holtum, B. Heinemann, W. Kraus, A. Lorenz, C. Martens, P. McNeely, S. Obermayer, R. Riedl, R. Süß, A. Tanga, R. Wilhelm, and D. Wunderlich. Overview of the RF source development programme at IPP Garching. *Nuclear Fusion*, 46(6):S220–S238, June 2006.
- [112] P. C. Stangeby. The Bohm–Chodura plasma sheath criterion. *Physics of Plasmas*, 2(3):702–706, Mar. 1995.
- [113] T. E. Steinberger, M. T. Dufor, D. S. Thompson, and E. E. Scime. Zeeman splitting measurements of magnetic fields in iodine plasma. *Review of Scientific Instruments*, 89(10):10C113, Oct. 2018.
- [114] T. E. Steinberger and E. E. Scime. Laser-Induced Fluorescence of Singly Ionized Iodine. *Journal of Propulsion and Power*, 34(5):1235–1239, Sept. 2018.

- [115] N. Sternberg and V. Godyak. Two-dimensional cylindrical plasma for intermediate gas pressures. *Plasma Sources Sci. Technol.*, 20(1):015018, 2011.
- [116] N. Sternberg, V. Godyak, and D. Hoffman. Magnetic field effects on gas discharge plasmas. *Physics of Plasmas*, 13(6):063511, June 2006.
- [117] J. Szabo, M. Robin, S. Paintal, B. Pote, V. Hruby, and C. Freeman. Iodine Propellant Space Propulsion. In *IEPC-2013-311*, Washington D.C., USA, 2013.
- [118] A. Tavant, V. Croes, R. Lucken, T. Lafleur, A. Bourdon, and P. Chabert. The effects of secondary electron emission on plasma sheath characteristics and electron transport in an Ar/E_2 discharge via kinetic simulations. *Plasma Sources Sci. Technol.*, 27(12):124001, Dec. 2018.
- [119] A. Tavant, R. Lucken, A. Bourdon, and P. Chabert. Non-isothermal sheath model for low pressure plasmas. *Plasma Sources Sci. Technol.*, 2019.
- [120] J. Tennyson, D. B. Brown, J. J. Munro, I. Rozum, H. N. Varambhia, and N. Vinci. Quantemol-N: an expert system for performing electron molecule collision calculations using the R-matrix method. *Journal of Physics: Conference Series*, 86:012001, Oct. 2007.
- [121] J. Tennyson, S. Rahimi, C. Hill, L. Tse, A. Vibhakar, D. Akello-Egwel, D. B. Brown, A. Dzarasova, J. R. Hamilton, D. Jaksch, S. Mohr, K. Wren-Little, J. Bruckmeier, A. Agarwal, K. Bartschat, A. Bogaerts, J.-P. Booth, M. J. Goeckner, K. Hassouni, Y. Itikawa, B. J. Braams, E. Krishnakumar, A. Laricchiuta, N. J. Mason, S. Pandey, Z. L. Petrovic, Y.-K. Pu, A. Ranjan, S. Rauf, J. Schulze, M. M. Turner, P. Ventzek, J. C. Whitehead, and J.-S. Yoon. QDB: a new database of plasma chemistries and reactions. *Plasma Sources Science and Technology*, 26(5):055014, Apr. 2017.
- [122] M. B. Thomas, D. Rafalskyi, T. Lafleur, and A. Aanesland. Experimental investigation of electron transport across a magnetic field barrier in electronegative and electronegative plasmas. *Plasma Sources Sci. Technol.*, 25(4):045018, 2016.
- [123] V. Toigo, S. Dal Bello, E. Gaio, A. Luchetta, R. Pasqualotto, P. Zaccaria, M. Bigi, G. Chitarin, D. Marcuzzi, N. Pomaro, G. Serianni, P. Agostinetti,

- M. Agostini, V. Antoni, D. Aprile, C. Baltador, M. Barbisan, M. Battistella, M. Boldrin, M. Brombin, M. Dalla Palma, A. De Lorenzi, R. Delogu, M. De Muri, F. Fellin, A. Ferro, G. Gambetta, L. Grando, P. Jain, A. Maistrello, G. Manduchi, N. Marconato, M. Pavei, S. Peruzzo, N. Pilan, A. Pimazzoni, R. Piovan, M. Recchia, A. Rizzolo, E. Sartori, M. Siragusa, E. Spada, S. Spagnolo, M. Spolaore, C. Taliercio, M. Valente, P. Veltri, A. Zamengo, B. Zaniol, L. Zanotto, M. Zaupa, D. Boilson, J. Graceffa, L. Svensson, B. Schunke, H. Decamps, M. Urbani, M. Kushwah, J. Chareyre, M. Singh, T. Bonicelli, G. Agarici, A. Garbuglia, A. Masiello, F. Paolucci, M. Simon, L. Bailly-Maitre, E. Bragulat, G. Gomez, D. Gutierrez, G. Mico, J.-F. Moreno, V. Pilard, A. Chakraborty, U. Baruah, C. Rotti, H. Patel, M. Nagaraju, N. Singh, A. Patel, H. Dhola, B. Raval, U. Fantz, M. Fröschle, B. Heinemann, W. Kraus, R. Nocentini, R. Riedl, L. Schiesko, C. Wimmer, D. Wunderlich, M. Cavenago, G. Croci, G. Gorini, M. Rebai, A. Muraro, M. Tardocchi, and R. Hemsworth. The ITER Neutral Beam Test Facility towards SPIDER operation. *Nucl. Fusion*, 57(8):086027, Aug. 2017.
- [124] L. Tonks and I. Langmuir. A General Theory of the Plasma of an Arc. *Phys. Rev.*, 34(876), 1929.
 - [125] M. M. Turner. Collisionless electron heating in an inductively coupled discharge. *Physical review letters*, 71(12):1844, 1993.
 - [126] M. M. Turner, A. Derzsi, Z. Donkó, D. Eremin, S. J. Kelly, T. Lafleur, and T. Mussenbrock. Simulation benchmarks for low-pressure plasmas: Capacitive discharges. *Physics of Plasmas*, 20(1):013507, Jan. 2013.
 - [127] O. Tverdokhlebov and A. Semenkin. Iodine propellant for electric propulsion - To be or not to be. In *37th Joint Propulsion Conference and Exhibit*, Salt Lake City, UT, U.S.A., July 2001. American Institute of Aeronautics and Astronautics.
 - [128] V. Vahedi and M. Surendra. A Monte Carlo collision model for the particle-in-cell method: applications to argon and oxygen discharges. *Computer Physics Communications*, 87(1-2):179–198, 1995.
 - [129] J. Weiland. *Stability and Transport in Magnetic Confinement Systems*. Springer Series on Atomic, Optical, and Plasma Physics. Springer-Verlag, New York, 2012.
 - [130] J. Yankun, Z. Xiu, L. Huiping, and Q. Minghui. Bohm Criterion in a Magnetized Plasma Sheath. *Plasma Sci. Technol.*, 13(5):519, 2011.

- [131] T. H. Y. Yeung. Recombination coefficients for positive and negative ions. *Proceedings of the Physical Society*, 71(3):341, 1958.
- [132] S. Yoshikawa and D. J. Rose. Anomalous Diffusion of a Plasma across a Magnetic Field. *The Physics of Fluids*, 5(3):334–340, Mar. 1962.
- [133] O. Zatsarinny, K. Bartschat, G. Garcia, F. Blanco, L. Hargreaves, D. Jones, R. Murrie, J. Brunton, M. Brunger, M. Hoshino, and S. Buckman. Electron-collision cross sections for iodine. *Phys. Rev. A*, 83(4):042702, Apr. 2011.